# $\pi$ -Extended Ligands in Two-Coordinate Coinage Metal Complexes

Collin N. Muniz<sup>\*</sup>, Jonas Schaab<sup>\*</sup>, Anton Razgoniaev, Peter I. Djurovich; Mark E. Thompson<sup>\*</sup>

Department of Chemistry, University of Southern California, Los Angeles, CA 90089 USA

#### **Abstract**

Two-coordinate carbene-M¹-amide (cMa, M¹ = Cu, Ag, Au) complexes have emerged as highly efficient luminescent materials for use in a variety of photonic applications, due to their extremely fast radiative rates via thermally activated delayed fluorescence (TADF) from an interligand charge transfer (ICT) process. A series of cMa derivatives were prepared to examine the variables which affect the radiative rate with the goal of understanding the parameters that control the radiative TADF process in these materials. We find that blue emissive complexes with high photoluminescence efficiency ( $\Phi_{PL} > 0.95$ ) and fast radiative rates ( $k_r = 4 \times 10^6 \text{ s}^{-1}$ ) can be achieved by selectively extending the  $\pi$ -system of the carbene and amide ligands. Of note is the role played by increasing the separation between the hole and electron in the ICT excited state. Analysis of temperature dependent luminescence data along with theoretical calculations indicate that the hole-electron separation alters the energy gap between the lowest energy singlet and triplet states ( $\Delta E_{ST}$ ) while keeping the radiative rate for the singlet state unchanged. This interpretation provides guidelines for the design of new cMa derivatives with even faster radiative rates as well as those with slower radiative rates and thus extended excited state lifetimes.

<sup>≈</sup> These two authors have contributed equally to this work

<sup>\*</sup> Corresponding author, met@usc.edu

#### Introduction

The luminescent properties of coinage metal complexes ( $M^{(I)}$  = Cu, Ag and Au) were reported over fifty years ago,  $^1$  with the first report of emission from a two-coordinate  $d^{10}$  coinage metal complex in 1987. Several papers have highlighted emission in the solid state and in solution for  $M^{(I)}L_2^+$  and  $LM^{(I)}X$  complexes (L = phosphine, carbene, X = halide, acetylide, aryl, amide). Of particular interest here is the promise of (carbene) $M^{(I)}$ (amide) (cMa) complexes as efficient luminescent materials. The cMa complexes can have high photoluminescent quantum yields ( $\Phi_{PL}$ ), short luminescence decay lifetimes ( $\tau$ ) in the  $\mu$ s regime and shorter, and emission color tunable over the entire visible spectrum in solid, solution and doped films. These luminophores have properties similar to transition metal phosphors that contain Ru, Os, Ir and Pt used in a range of applications including organic electronics and LEDs<sup>3b, 4, 6</sup>, photocatalysis<sup>7</sup>, chemo- and bio-sensing<sup>8</sup> and solar energy conversion.

Unlike the noble metal phosphors which luminesce from triplet states, the majority of the reported cMa complexes emit via thermally assisted delayed fluorescence (TADF), Figure 1.9 The

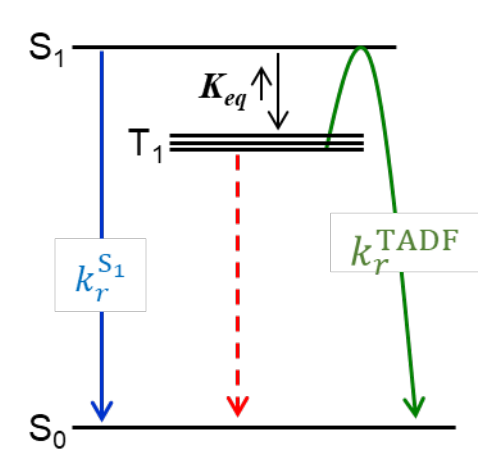


**Figure 1:** The kinetic scheme for emission via TADF, where  $k_r^{S_1}$  and  $k_r^{TADF}$  are radiative decay rates of  $S_1$  state and TADF process,  $K_{eq}$  indicates the equilibrium constant between  $T_1$  and  $S_1$  states.

carbene ligand serves as an electron acceptor (A) and amide ligand serves as an electron donor (D). The lowest energy (emitting) excited state is an interligand charge transfer (ICT) transition between the two ligands. The energy of the ICT state depends on the choice of ligands but is relatively insensitive to the identity of the metal

atom. <sup>4e</sup> The linear geometry of the cMa complexes leads to a large spatial separation between the donor and acceptor groups/ligands of ~4 Å. This spacing restricts the overlap between the  $\pi$ -orbitals of the two ligands, consequently limiting the exchange energy and thus the energy gap between lowest singlet (S<sub>1</sub>) and triplet (T<sub>1</sub>) states ( $\Delta E_{ST}$ ). A small  $\Delta E_{ST}$  enhances thermal population of the singlet state, which improves the luminescence efficiency for TADF by increasing the radiative rate for emission. <sup>9</sup> Organic TADF molecules have distinct lifetimes for prompt ( $\tau = 1$ -100 ns) and delayed ( $\tau = 1$ -1000  $\mu$ s) emission that are controlled by  $\Delta E_{ST}$  and the rate of intersystem crossing S<sub>1</sub> $\rightarrow$ T<sub>1</sub> (typically  $k_{ISC}$ < 10<sup>7</sup> s<sup>-1</sup>). <sup>10</sup> In contrast, the intersystem crossing (ISC) rates in metal containing TADF complexes are fast enough ( $k_{ISC} \ge 10^{10}$  s<sup>-1</sup>) to outcompete the radiative rates for the S<sub>1</sub> state, making delayed emission (TADF) independent of  $k_{ISC}$ . <sup>9</sup> The result is extremely fast prompt emission ( $\tau < 200$  ps) and comparatively short TADF lifetimes,  $\tau_{TADF} = 0.5$ -3  $\mu$ s, leading to high luminescence efficiency. <sup>30, 4b, 4c, 4e, 11</sup>

For compounds where the ISC rate exceeds  $k_r^{S_1}$ , a pre-equilibrium approximation can be made such that the equilibrium constant  $(K_{eq}, T_1 \rightleftarrows S_1)$  becomes a principal factor in determining  $k_r^{TADF}$  as shown in Eqn. 1:9

$$k_r^{\text{TADF}} = k_r^{S_1} \cdot K_{eq} \tag{1}$$

In this equation,  $k_r^{\rm TADF}$  is only dependent on  $k_r^{\rm S_1}$  and  $K_{eq}$ , with  $K_{eq}$  tied to  $\Delta E_{\rm ST}$ , Eqn. 2. 12

$$K_{eq}(T_1 \rightleftarrows S_1) = \frac{1}{3}e^{-\frac{\Delta E_{ST}}{k_b T}} \tag{2}$$

Therefore, predictions can be made regarding the TADF properties for TADF emitters with fast ISC (high spin orbit coupling) without prior knowledge of the ISC rates since only  $k_r^{S_1}$  and  $\Delta E_{ST}$  are needed to estimate  $k_r^{TADF}$ . Boltzmann fits of temperature dependent luminescence data can be

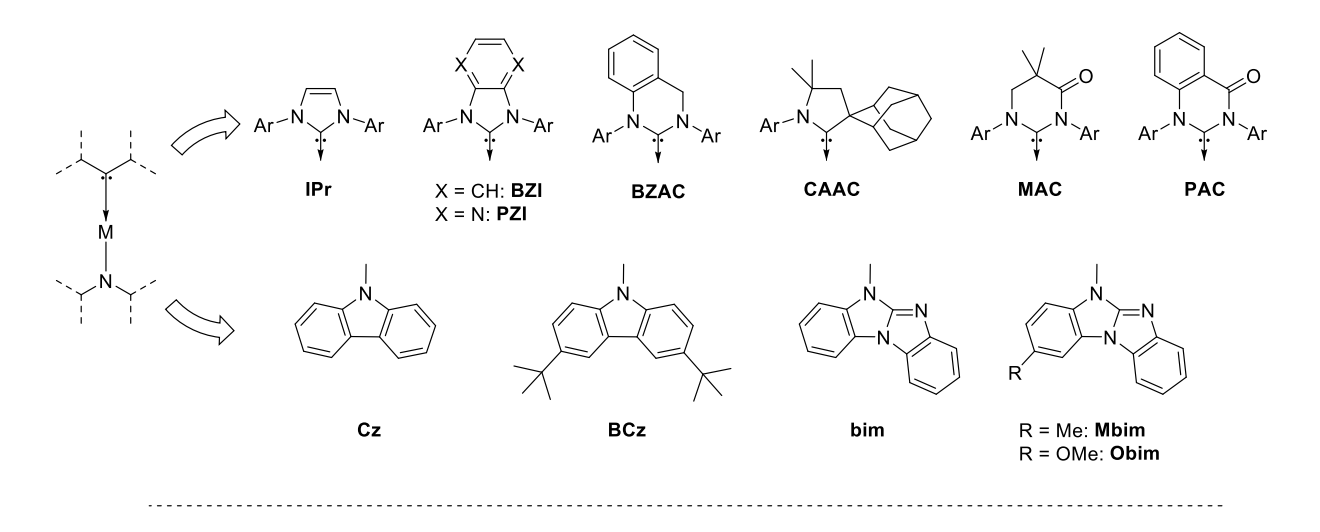
used to accurately derive  $\Delta E_{\rm ST}$  and  $k_r^{\rm S_1}$  values, and thus  $K_{eq}$  (Eqn. 2). <sup>4e, 4f, 9, 13</sup> The values of  $k_r^{\rm S_1}$  can also be estimated experimentally from absorption spectra using the Strickler-Berg analysis. <sup>14</sup>

Being able to control the rate of TADF with  $\Delta E_{\rm ST}$  and  $k_r^{\rm S_1}$  is useful when designing chromophores for different applications. A small  $\Delta E_{\rm ST}$  and large  $k_r^{\rm S_1}$  leads to a fast  $k_r^{\rm TADF}$ , 9 which is important for applications where a short excited state lifetime is important, such as organic LEDs. To that end, this paper describes cMa complexes with some of the shortest TADF lifetimes reported to date ( $\tau \sim 250$  ns). Conversely, one can design molecules where the  $\Delta E_{\rm ST}$  value is large, which will make  $K_{eq}(T_1 \rightleftarrows S_1)$  very small and push  $\tau({\rm TADF})$  in the 10-100  $\mu$ s regime. These long-lived materials could be used as sensitizers for photoelectrochemical reactions where the diffusion of the excited species to an electrocatalysis in solution is a key step in the process. A  $\Delta E_{\rm ST}$  value of 1000 cm<sup>-1</sup> is sufficient to increase the TADF lifetime to the  $\mu$ s regime, while only sacrificing  $\sim$ 100 meV in electrochemical potential for the excited state.

Both  $k_r^{S_1}$  and  $\Delta E_{ST}$  parameters are related to the degree of overlap between the hole and electron wavefunctions that describe the excited state. This overlap can be evaluated using the natural transition orbitals (NTOs) and is referred to as  $\Lambda_{NTO}$ . <sup>13, 15</sup> While  $\Lambda_{NTO}$  appears to be useful in predicting both  $k_r^{S_1}$  and  $K_{eq}$ , it affects the two parameters in opposite ways. A large  $\Lambda_{NTO}$  leads to a high value of  $k_r^{S_1}$ , but it also increases the value for  $\Delta E_{ST}$  and thus lowers  $K_{eq}$ . In a previous study we found that an  $\Lambda_{NTO} = 0.25$ -0.3 is an optimal range to give the fastest  $k_r^{TADF}$  for cMa complexes of Cu, Ag and Au with a variety of carbene and amide ligands. <sup>13</sup> The lowest  $\Lambda_{NTO}$  values were obtained for silver based cMa complexes.

In this paper we report the synthesis and characterization of a family of new cMa materials and study their photophysical properties, with an eye to further explore how ligands can tune  $\Lambda_{NTO}$ 

and how these changes affect the excited state properties. The compounds discussed here are illustrated in **Figure 2**. Neither the BZAC and PAC carbene ligands, nor the use of bim as the amide, in a cMa complex has been reported previously. We find that the choice of carbene ligand affects the excited state energy but has a weaker influence on the photophysical properties and  $\Delta E_{\rm ST}$  of the cMa complexes. Interestingly, shifting from a carbazolide to a bim ligand markedly increases  $k_r^{\rm TADF}$  even though the energy of the HOMO is effectively the same for both complexes.



 $M_X^{PAC}$ : M = Cu, Ag, Au; X = Cz, BCz and  $M_X^{BZAC}$ : M = Cu, Au; X = Cz, BCz  $Au_{am}^{carbene}$ : carbene = IPr, BZI, PZI, CAAC, MAC, PAC, BZAC; am = Cz, bim, Mbim, Obim

**Figure 2:** Compounds considered in this paper (Ar = 2.6-diisopropylphenyl).

#### **Experimental**

Detailed syntheses and full characterization data for all of the new compounds are given in the supporting information to this paper. The basic synthetic route is illustrated in Scheme 1. All of the compounds studied here are air stable in the solid state indefinitely and in solution for prolonged periods, with the exception of  $Ag_{BCZ}^{PAC}$  which decomposes in air and solution over prolonged periods.

$$\begin{array}{c} --\sqrt{\phantom{a}} \\ --\sqrt{\phantom{a}} \\ --N^{+} \end{array}$$

$$\begin{array}{c} MX \\ base \end{array}$$

$$\begin{array}{c} --\sqrt{\phantom{a}} \\ --N \end{array}$$

$$\begin{array}{c} M = Cu, Ag, Au; X = halide; Y = N, CR_{2} \end{array}$$

**Scheme 1:** synthesis of cMa complexes

The single crystal structures were determined at 100 K with Rigaku Xta LAB Synergy S, equipped with an HyPix-600HE detector and an Oxford Cryostream 800 low temperature unit, using a Cu  $K_{\alpha}$  PhotonJet-S X-ray radiation source. The structures were solved using OLEX2 with the SHELXTL software package. <sup>16</sup> Details of the data collection and structure solution are given in in supporting information. Each structure was deposited in the Cambridge Crystallographic Data Centre with the following accension codes:  $Au_{CZ}^{BZAC}$  2168084,  $Cu_{BCZ}^{PAC}$  2170320,  $Au_{bim}^{BZAC}$  2182717,  $Au_{bim}^{CAAC}$  2155241,  $Au_{bim}^{MAC}$  2167514,  $Au_{bim}^{PAC}$  2170000 and  $Au_{Mbim}^{BZI}$  2168086.

Cyclic voltammetry and differential pulsed voltammetry were performed using a VersaSTAT potentiostat measured at 100 mV/s scan. Anhydrous dimethylformamide was used as the solvent, with 0.1 M tetra(n-butyl)ammonium hexafluorophosphate as the supporting electrolyte. The redox potentials are based on values measured from differential pulsed voltammetry and are reported relative to the ferrocenium/ferrocene (Cp<sub>2</sub>Fe<sup>+</sup>/Cp<sub>2</sub>Fe) redox couple using either ferrocene or decamethylferrocene as an internal reference. Electrochemical reversibility was determined using cyclic voltammetry.

# Modeling methods

The electronic properties of the complexes were modelled using Density Functional Theory (DFT) and Time Dependent DFT (TDDFT). Geometry optimization was performed using the B3LYP functional and LACVP\* basis set using crystallographic coordinates as starting points

when possible. TDDFT calculations were performed on the geometry-optimized structures using the CAM-B3LYP exchange, LACVP effective core potential, with the random phase approximation enabled and the omega value set to 0.2 arbitrary units. The full carbene ligand, but only the parent Cz and bim ligands were investigated in these modeling studies. Natural transition orbitals (NTOs) were generated by performing a singular value decomposition on the transition density matrix using the Q-Chem v5.0 software package. <sup>17</sup>

The spatial overlap of the hole and electron NTO ( $\Lambda_{NTO}$ ) for a particular excited state is defined here by Eqn 3.

$$\Lambda_{NTO} \approx \iiint |\varphi_{h+}| |\varphi_{e-}| d\tau \tag{3}$$

where  $\phi_{h^+}$  and  $\phi_{e^-}$  are the hole and electron NTOs, respectively, for the excited state. Both  $\phi_{h^+}$  and  $\phi_{e^-}$  are orthonormal which ensures that  $\Lambda_{NTO}$  falls between 0 and 1, which represent 0% and 100% overlap respectively. Values for  $\Lambda_{NTO}$  were calculated for these compounds using a script that draws from the integration methods developed by Herman, *et al.*, <sup>18</sup> and Castro, *et al.*, <sup>19</sup> using a method reported previously (See equation S1 in the supporting info for full equation). <sup>13, 15a</sup>

The center of charge for the hole and electron NTOs of a given excited state are extracted from the expectation values of the respective wavefunction positions, Eqns. 4 and 5.

$$\langle r_{h+} \rangle = \langle \Psi_{h+} | \hat{r} | \Psi_{h+} \rangle \tag{4}$$

$$\langle r_{e-} \rangle = \langle \Psi_{e-} | \hat{r} | \Psi_{e-} \rangle \tag{5}$$

where  $|\Psi_{h+}\rangle$  and  $|\Psi_{e-}\rangle$  represent the hole and electron NTO wavefunctions. The centers of charge are calculated component-wise to extract two vectors, whose termini are the center of charge for the hole or electron,  $h^+_{xyz}$  and  $e^-_{xyz}$ , respectively. The positions of these centers of charge are

illustrated in Figure S6 by placing an atom at the coordinates of  $h^+_{xyz}$  and  $e^-_{xyz}$ . The distance between the charges  $[d(h^+, e^-)]$  for each cMa are determined algebraically from  $h^+_{xyz}$  and  $e^-_{xyz}$ .

Further details for the calculation of  $\Lambda_{NTO}$  and center of charge are given in the supporting information for this manuscript.

#### Photophysical Measurements

Samples in fluid solution were both sparged and examined under N<sub>2</sub>. Doped polystyrene thin films were prepared from a solution of polystyrene in toluene, drop cast onto a quartz substrate and measured under N<sub>2</sub>. The UV-visible spectra were recorded on a Hewlett-Packard 4853 diode array spectrometer. Steady state excitation and emission spectra were obtained using a Photon Technology International QuantaMaster spectrofluorimeter. Photoluminescence quantum yields were recorded using a Hamamatsu C9920 integrating sphere equipped with a xenon lamp. Luminescence lifetimes were measured using Time-Correlated Single Photon Counting (TCSPC) on an IBH Fluorocube apparatus interfaced to a Horiba FluoroHub+ controller.

Variable temperature photophysical measurements were carried out on a Janis SHI-4-2 (0.2 W 4K) optical cryocooler. The IBH Fluorocube was used as a detector for luminescence lifetimes and the Photon Technology International QuantaMaster spectrofluorimeter as a detector for steady state emission spectra with 375 nm LED (Thorlabs M375L4, 1270 mW) as excitation source. Doped polystyrene thin films were spin coated onto a round sapphire substrate that was used to insure good thermal conductivity at low temperatures.

#### **Results**

#### Synthesis and Characterization

A range of cMa complexes have been prepared (Figure 2). In these materials we have varied the carbene fairly extensively and looked at both *N*-carbazolide (Cz) and

*N*-benzo[d]benzo[4,5]imidazo[1,2-a]imidazolyl (bim) amides. Part of this study is to investigate two new carbene ligands for cMa complexes, *i.e.* BZAC and PAC, so the carbazolide complexes were made for these two carbenes with Cu, Ag and Au to compare to other (carbene)M(Cz) compounds. Although we were able to prepare pure samples of the PAC-based materials for all three metals, we were only able to synthesize the Cu and Au complexes with BZAC. It appears that thermal instability of  $Ag_{CZ}^{BZAC}$  and  $Ag_{BCZ}^{BZAC}$  preclude their isolation. While the BZAC and PAC carbazolide cMa complexes have not been reported, the (carbene)Au(Cz) complexes for IPr<sup>3h</sup>, BZI<sup>4k</sup>, PZI<sup>20</sup>, CAAC<sup>3l, 4a, 4e</sup> and MAC<sup>4e</sup> have been reported previously and are considered here as well. Although much of the previous work involved unsubstituted carbazole groups, we found that the addition of *t*Bu groups to the 3,6-positions of the carbazole (BCz) led to greater solubility which facilitated our solution and thin film photophysical studies. The solubility of the bim based cMa complexes are similar to their BCz analogs.

Single crystal X-ray diffraction was used to determine the molecular structures of  $Cu_{BCZ}^{PAC}$ ,  $Au_{bim}^{BZAC}$ ,  $Au_{bim}^{BZAC}$ ,  $Au_{bim}^{BZAC}$ ,  $Au_{bim}^{BAC}$  and  $Au_{bim}^{BAC}$  are shown in Figure 3. All the complexes have a coplanar conformation of carbene and amide ligands (dihedral angles = 0.7-7.3°) and close to 180° angle around the metal center (C-Au-N = 174 - 179°). The C-Au bond lengths are in the range 1.97-2.01 Å and the Au-N bond is 2.01 - 2.03 Å. Values for the C-Au and Au-N bond lengths are similar to analogous (carbene)M(Cz) complexes published previously. <sup>4a, 4d, 4c, 4h, 20a</sup> The only Cu compound structurally characterized in this report,  $Cu_{BCZ}^{PAC}$ , has C-Cu and Cu-N bond lengths of 1.89 Å and 1.85 Å, respectively, that are shorter than the Au based compounds and consistent with the difference in ionic radii of the metals. <sup>4c</sup> Two different conformers are possible for  $Au_{Bim}^{MAC}$ , one

with the carbonyl *anti* to the phenylene (pictured in Figure 3) and the other where the carbonyl is syn to the phenylene. Both conformers were present in the crystal and the diffraction data was best fit by treating the crystal as disordered with a 10% "impurity" of the syn-conformer in a crystal of the anti-conformer. Only a single conformer for  $Au_{Bim}^{BZAC}$ ,  $Au_{Bim}^{PAC}$  and  $Au_{Bim}^{CAAC}$  was observed, even though a similar stereocenter to that of  $Au_{Bim}^{MAC}$  was present in these molecules. The crystals of  $Au_{Mbim}^{BZI}$  contain two tautomers, with the major component (84%) having the methyl group closest to the Au-N bond (pictured in Figure 3). The ratio of tautomers in the single crystals is close to the 75:25 ratio observed using NMR spectroscopy.

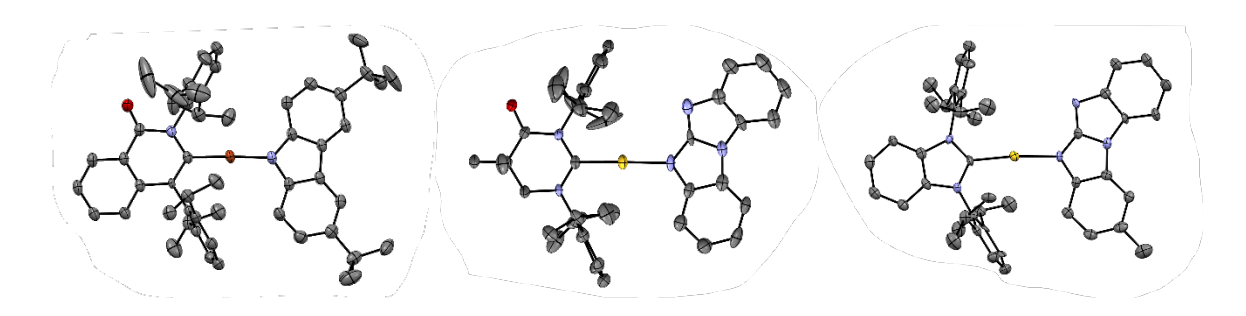


**Figure 3:** Thermal ellipsoid plots  $Cu_{BCZ}^{PAC}$  (left),  $Au_{bim}^{MAC}$  (center) and  $Au_{Mbim}^{BZI}$  (right)

The redox properties of the cMa complexes were examined by cyclic and differential pulse voltammetry in dimethylformamide (DMF), and the potentials relative to an internal ferrocene reference are listed in Table S4 and graphically presented in Figure 4. Oxidations are irreversible for all cMa complexes with Cz and bim amides. A common decomposition pathway for carbazoles upon oxidation is dimerization at the 3,6-positions. Alkyl substitution at these sites inhibits this reaction pathway,  $^{21}$  leading to reversible oxidation for the  $Au_{BCz}^{BZAC}$  and  $Au_{BCz}^{PAC}$  complexes. The oxidation potentials for silver and gold derivatives of  $M_{BCz}^{PAC}$  are similar; however, the copper analog is easier to oxidize. This is contrary to what was observed for the  $M_{Cz}^{MAC}$  and  $M_{Cz}^{CAAC}$  complexes, where the oxidation and reduction potentials were unaffected by the choice of metal

ion. <sup>4e</sup> A similar trend is observed for  $M_{BCZ}^{BZAC}$  where the oxidation potential is lower for the copper derivative than the gold analog. Addition of the tBu groups to Cz destabilizes the oxidation potential for a given complex by  $\sim 100$  mV, e.g.  $Au_{CZ}^{BZAC}/Au_{BCZ}^{BZAC}$  and  $Au_{CZ}^{PAC}/Au_{BCZ}^{PAC}$ . This effect parallels the shift observed for the energy for the longest wavelength absorption band in the two complexes, which also decreases by roughly 100 mV.

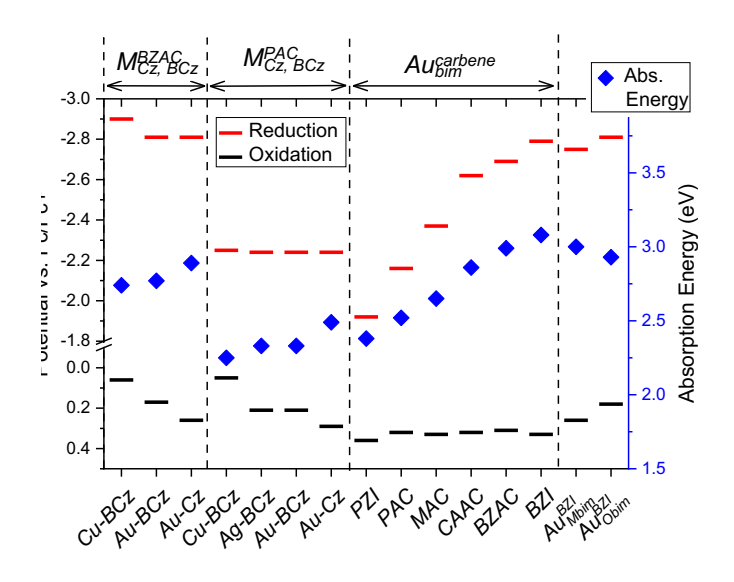


**Figure 4:** Electrochemical redox potentials and transition energies for the  ${}^{1}$ ICT state. The energy of the  ${}^{1}$ ICT state (in toluene) was estimated from the onset of the absorption band where the intensity was 0.10 the value at  $\lambda_{max}$ .

The oxidation potentials for complexes with bim ligands are ca. 60 mV greater than those of the analogous Cz based complexes, leading to a similar shift in the absorption energies. The dependence of the absorption energy on the oxidation and reduction potentials of the complex is consistent with an interligand charge transfer (ICT) transition for these complexes, as seen for other cMa complexes. Reduction waves were observed for all complexes except  $Au_{bim}^{lpr}$ , which falls outside the solvent window for DMF. All reductions are reversible, except for derivatives with BZAC ligands. The identity of the metal ion for the complex does not affect the reduction potential (see  $M_{BCz}^{PAC}$ ). A gradual shift to more negative potentials, along with a concomitant increase in energy for the lowest absorption band, is found upon going from complexes with the PZI, PAC, MAC, CAAC, BZAC and BZI carbenes, which is again consistent with an ICT assignment for the transition.

### **Computer Modeling**

The electronic properties of the complexes were modeled using Density Functional Theory (DFT) and Time Dependent DFT (TDDFT), details are given in the Experimental section. The HOMO and LUMO energies from these calculations are listed in Table 1 and representative orbital isosurfaces shown in Figure 5. TDDFT methods were used to estimate the oscillator strengths for the singlet transitions, as well as vertical energies and dipole moments for the singlet and triplet excited states. In all cases but  $Au_{bim}^{Ipr}$ , the transitions from  $S_0$  to the  $S_1$  are ICT in nature and have > 99.5% HOMO (amide)  $\rightarrow$  LUMO (carbene) character (Table S5). For the majority of the cMa complexes the  $T_1$  state is comprised of the same orbitals as the  $S_1$  state. The  $Au_{bim}^{Ipr}$  and  $Au_{Cz}^{Ipr_{22}}$ complexes are a special case where the energy of the LUMO is sufficiently destabilized that the lowest triplet state is <sup>3</sup>bim and <sup>3</sup>Cz, respectively, rather than <sup>3</sup>ICT. The dipole moments for the ground, <sup>1</sup>ICT and <sup>3</sup>ICT states are large in magnitude ( $\mu = 10\text{-}20 \text{ D}$ ); however, the excited state dipoles are antiparallel to those of the ground state (Table S6). This feature is common in cMa complexes and is a consequence of the high degree of charge transfer in the ICT excited state (Figure 5). The antiparallel alignment of dipoles gives rise to hypsochromic shifts in absorption and bathochromic shifts for emission in solvents with increasing polarity (Figures S8). The natural transition orbitals (NTOs) for the S<sub>1</sub> state were calculated using the S<sub>0</sub> optimized geometry and the overlap between the hole and electron wavefunctions ( $\Lambda_{NTO}$ ) determined as described in the experimental section (Table 1).

**Table 1:** Parameters obtained from DFT and TDDFT modeling of the cMa complexes.

	HO (eV)	LU (eV)	$\Delta E_{\text{LU-HO}}$ (eV)	$S_1 \rightarrow S_0$ (eV/f)	$T_1 \rightarrow S_0$ (eV)	$\Delta E_{\rm ST}^{\rm a}$ (eV)	$\Lambda_{NTO}\left( S_{1}\right)$
$Cu_{Cz}^{BZAC}$	-4.04	-1.39	2.65	2.95/0.12	2.76	0.19	0.36
$Au_{Cz}^{BZAC}$	-4.18	-1.41	2.76	3.10/0.19	2.87	0.23	0.39
$Cu_{Cz}^{PAC}$	-4.19	-2.20	1.99	2.43/0.13	2.21	0.22	0.36
$Ag_{Cz}^{PAC}$	-4.07	-2.29	1.78	2.39/0.09	2.27	0.11	0.26
$Au_{Cz}^{PAC}$	-4.35	-2.20	2.15	2.61/0.19	2.36	0.25	0.39
$Au_{Cz}^{PZI}$	-4.38	-2.54	1.84	2.36/0.20	2.13	0.23	0.37
$Cu_{Cz}^{MAC}$	-4.17	-1.99	2.17	2.48/0.11	2.27	0.21	0.36
$Au_{Cz}^{MAC}$	-4.32	-1.99	2.33	2.66/0.16	2.41	0.25	0.40
$Au_{Cz}^{CAAC}$	-4.29	-1.60	2.68	2.86/0.16	2.56	0.30	0.43
$Au_{Cz}^{BZI}$	-4.22	-1.46	2.76	3.09/0.20	2.87	0.22	0.40
$Au_{Cz}^{Ipr}$	-4.16	-0.81	3.35	3.44	3.15 <sup>b</sup>	0.29	0.42
$Au_{bim}^{PZI}$	-4.44	-2.58	1.85	2.45/0.16	2.29	0.16	0.32
$Au_{bim}^{PAC}$	-4.43	-2.21	2.22	2.75/0.17	2.56	0.19	0.35
$Au_{bim}^{MAC}$	-4.41	-2.0	2.41	2.81/0.14	2.63	0.18	0.35
$Au_{bim}^{CAAC}$	-4.39	-1.61	2.78	3.02/0.15	2.80	0.22	0.38
$Au_{bim}^{BZAC}$	-4.29	-1.42	2.87	3.25/0.17	3.08	0.17	0.35
$Au_{bim}^{BZI}$	-4.30	-1.50	2.80	3.22/0.21	3.04	0.18	0.35
$Au_{bim}^{Ipr}$	-4.27	-0.82	3.46	3.62/0.16	3.32 <sup>b</sup>	0.30	0.36
$H_{Cz}^{MAC}$	-3.99	-2.15	1.84	2.35/0.001	2.34	0.01	0.06
$Li_{Cz}^{MAC}$	-3.83	-2.08	1.75	2.17/0.03	2.11	0.06	0.18

 $<sup>^{</sup>a}\Delta E_{ST}$  is based on energies calculated for the  $S_{1}$  and  $T_{1}$  states.  $^{b}$  The  $T_{1}$  state for this compound has substantial  $^{3}$ amide character as opposed to the  $^{3}$ ICT state observed for the other complexes.

The transition energies in the series of Group 11 metals in  $M_{Cz}^{PAC}$  follow the same trends as reported previously for  $M_{Cz}^{CAAC}$  and  $M_{Cz}^{MAC}$ . <sup>4e</sup> The energies for the S<sub>1</sub> and T<sub>1</sub> states are independent of the metal center, whereas values for  $\Delta E_{ST}$  fall in the order Au > Cu > Ag, which mirror  $\Lambda_{NTO}$ 

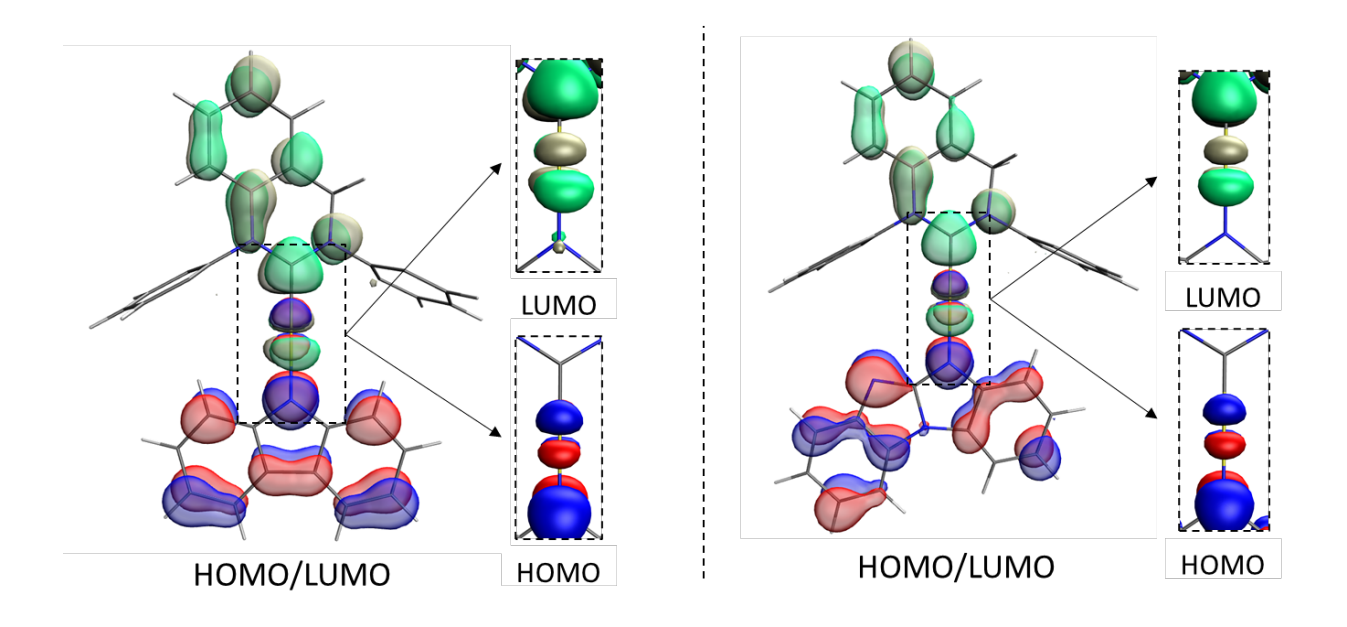


**Figure 5:** Molecular orbitals (MOs) of  $Au_{CZ}^{BZAC}$  (left) and  $Au_{Bim}^{BZAC}$  (right). The HOMO is displayed with red and blue phases and the LUMO is displayed with turquoise and cream phases (isovalue = 0.1). A magnified perspective is presented to highlight contribution of the d orbital to the HOMO and LUMO. The 2,6-isopropyl groups have been removed for clarity. values of 0.39, 0.36 and 0.26, respectively. The interligand carbene C···N distances for the three complexes fall in the order Ag > Au > Cu. A long interligand distance might be expected to give rise to a small  $\Lambda_{NTO}$ , but the higher value for the Au complex suggests a greater participation of the metal ion in the excited state than for the Cu and Ag complexes.

Examining the data for the  $Au_{bim}^{carbene}$  complexes it is apparent that the carbene ligand markedly affects the S<sub>1</sub> and T<sub>1</sub> energies, whereas the  $\Delta E_{ST}$ ,  $\Lambda_{NTO}$  and oscillator strengths for the S<sub>1</sub> state are only moderately altered by the nature of this ligand. Small differences in  $\Delta E_{ST}$  and  $\Lambda_{NTO}$  among the complexes with various carbene ligands suggests that the stabilization imparted on the carbene  $\pi$ -system by addition of electron withdrawing carbonyl groups (MAC and PAC) or benzannulated arene rings (BZI, PZI, BZAC and PAC) does not markedly alter overlap between the electron and hole wavefunctions. In contrast, both  $\Delta E_{ST}$  and  $\Lambda_{NTO}$  decrease upon shifting from a Cz to a bim donor, despite there being only a minor increase in energy for the S<sub>1</sub> and T<sub>1</sub> states.

The lowest energy excited state in these cMa complexes is best characterized as interligand, not metal-to-ligand, charge-transfer in character. In the cMa complexes the metal ion contributes equally to both the HOMO and LUMO in the ICT state, so there is no net charge transfer between the metal and the ligands. However, the metal ion is still an important participant in these transitions. This can be seen in comparing the modeling data for the complexes in Table 1 to data for  $H_{CZ}^{MAC}$  and  $Li_{CZ}^{MAC}$ . The separation between the central ion (neither of which have accessible d-orbitals available for bonding) and the ligands was kept at the same distance as for the copper ion in the geometry optimized structure of  $Cu_{CZ}^{MAC}$ . Predictably, the values for  $\Delta E_{ST}$  and  $\Delta N_{TO}$  decrease precipitously in these two complexes, illustrating the contribution of the metal ion to the valence orbitals of the cMa complexes.

### **Photophysical Properties**

The UV-visible absorption spectra of the complexes were recorded in toluene solution. Spectra for the carbazole-based cMa complexes with BZAC and PAC are shown in Figure 6(a). The absorption spectra of the  $M_{BCZ}^{BZAC}$  and  $M_{BCZ}^{PAC}$  complexes display bands at high energy ( $\lambda$  < 325 nm) that are assigned to transitions localized on the carbene and carbazolide ligands. Structured bands at 375 nm are assigned transitions on the carbazolide ligand, whereas bands assigned to absorption from the <sup>1</sup>ICT state are centered at 410 and 480 nm for the BZAC and PAC complexes, respectively. As observed for other cMa complexes, <sup>4e</sup> values for the extinction coefficients of the ICT bands fall in the order Au > Cu > Ag. Changing the methylene moiety in BZAC to carbonyl in PAC stabilizes the LUMO and leads to a marked red shift for complexes with the PAC ligand.

The absorption energies of the ICT state vary depending on the carbene ligands used here, which can best be seen by comparing spectra of the Au complexes using the bim donor

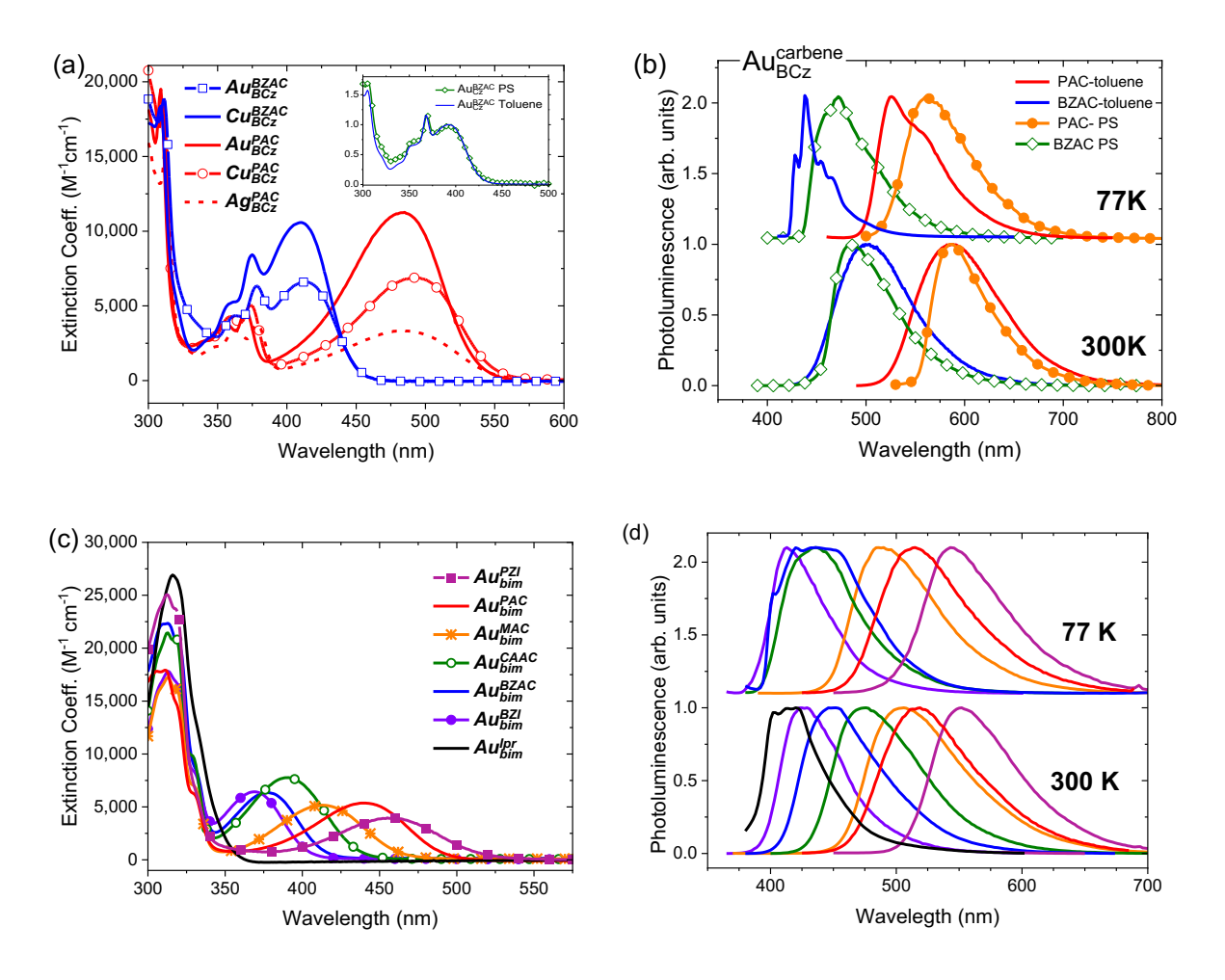


**Figure 6.** BZAC/PAC extinction (a) and emission (b) in toluene and polystyrene. Inset shows the spectra of  $Au_{CZ}^{BZAC}$  in toluene and polystyrene (1 wt %), normalized at the Cz absorbance. Extinction spectra in toluene (c) and emission spectra in polystyrene (d) of  $Au_{bim}^{carbene}$  complexes.

 $(Au_{bim}^{carbene})$ , Figure 6(c). In these complexes the absorption transitions localized on the amide (bim) ligand that appear at 310 nm ensures minimal overlap with the ICT band of the complexes. An exception is in  $Au_{bim}^{Ipr}$  where the LUMO is destabilized sufficiently to raise the energy of the ICT transition to be comparable to that of the bim ligand. For the other complexes the ICT bands are distinct and have energies that fall in the order BZI > BZAC > CAAC > MAC > PAC > PZI.

The absorption spectra of  $Au_{Cz}^{BZAC}$  in toluene, overlaid with that in polystyrene at 1 wt% loading and normalized at 375 nm, is shown in the inset to Figure 6(a). The close match in

absorption profiles confirm that the two media have similar solvation properties. However, the polystyrene matrix is expected to hinder geometric rearrangement, particularly rotation around the metal-ligand bond axis. Luminescence spectra for all cMa complexes were thus recorded in toluene and polystyrene (Figure 6(b, d); see supporting information for photoluminescence spectra in toluene). The spectra are broad and featureless at room temperature, indicative of emission from an ICT state. Spectra for complexes measured in toluene are slightly red shifted relative to the same compounds in polystyrene (Table 2), suggesting that only minor structural changes take place in the excited state; however, the shift is greater for the complexes with the bim donor. This difference in the rigidochromic effects in polystyrene suggests that the bim-based cMa complexes undergo a greater structural distortion in their ICT state than do the carbazole-based materials. The emission energies from the cMa complexes parallel values observed for the absorption energies of the ICT state (Table 2). Compounds ligated with the electrophilic PZI and PAC ligands emit orange-red whereas those with BZI and BZAC luminesce in the blue spectral region. For Au derivatives sharing a common carbene, the spectra with BCz are red-shifted relative to their Cz analogs, whereas the bim congeners emit at higher energies. Addition of methyl or methoxy groups to the bim ligand destabilizes the HOMO and leads to a concomitant red shift in emission relative to the parent  $Au_{bim}^{BZI}$  complex (Figure S9). The  $M_{BCZ}^{PAC}$  complexes display only minor variation in emission energy with respect to the identity of the metal center. The luminescence properties  $Au_{bim}^{Ipr}$  are consistent with assignment to a combined ICT/ligand-triplet transition, as observed for  $Au_{CZ}^{BZI}$ , <sup>4k</sup> leading to a slow radiative rate relative to the ICT emitters.

**Table 2:** Photophysical parameters for cMa complexes in toluene (tol) solution and polystyrene (PS) thin film (1% by weight).

	λ <sub>max</sub> (PL	L) (nm)	ФРГ	(%)	τ (	μs)	k <sub>r</sub> (1	$0^6  \mathrm{s}^{-1}$	k <sub>nr</sub> (10	0 <sup>6</sup> s <sup>-1</sup> )
	tol	PS	tol	PS	tol	PS	tol	PS	tol	PS
$Cu_{BCz}^{BZAC}$	502	459	>95	93	0.71	1.24ª	1.4		0.04	
$Au_{BCz}^{BZAC}$	500	484	>95	>95	0.56	0.72	1.7	1.4	0.07	< 0.01
$Cu_{BCz}^{PAC}$	595	594	47	75	0.56	0.95	0.84	0.79	0.95	0.26
$Ag_{BCz}^{PAC}$	610	588	10	51	0.58	0.26	0.17	1.0	1.5	0.33
$Au_{BCz}^{PAC}$	588	586	42	76	0.44	0.74	0.95	1.0	1.3	0.33
$Au_{Cz}^{PZI}$	600	570	62	92	0.41	0.45	1.5	2.0	0.94	0.22
$Au_{Cz}^{PAC}$	546	546	73	>95	0.74	0.81	1.0	1.2	0.36	0.04
$Au_{Cz}^{MAC}$ ref 4e		508		85		0.8		1.0		0.18
$Au^{\it CAAC}_{\it Cz}$ b, ref 4e		472		>95		1.14		0.88		< 0.01
$Au_{Cz}^{BZAC}$	480	479	>95	>95	0.69	1.98ª	1.5		< 0.01	
$Au_{Cz}^{BZI}$ ref 4k	448	432	94	>95	1.11	2.28 <sup>a</sup>	0.85		0.05	
$Au_{bim}^{PZI}$	600	552	31	91	0.21	0.24	1.5	3.8	3.2	0.37
$Au_{bim}^{PAC}$	562	532	30	81	0.17	0.27	1.8	3.0	4.2	0.7
$Au_{bim}^{MAC}$	548	506	19	88	0.17	0.40	1.1	2.2	4.8	0.3
$Au_{bim}^{\mathit{CAAC}}$	514	476	87	>95	0.63	0.55	1.4	1.8	0.02	< 0.01
$Au_{bim}^{BZAC}$	484	452	>95	>95	0.43	0.28	2.3	3.7	< 0.01	< 0.01
$Au_{bim}^{BZI}$	454	429	>95	>95	0.42	0.25	2.3	4.0	< 0.01	< 0.01
$Au_{bim}^{Ipr}$	340	400	<1	<5	С	13	С	0.004	С	С
$Au_{Mbim}^{BZI}$	460	436	>95	>95	0.42	0.29	2.4	3.4	< 0.01	< 0.01
$Au_{Obim}^{BZI}$	480	450	92	>95	0.37	0.38ª	2.5	 P74C	0.2	

<sup>&</sup>lt;sup>a</sup> The lifetime given is the weighted average of a biexponential fit;  $Cu_{BCZ}^{BZAC}$ : 0.79 (73%), 2.47 (27%);  $Au_{CZ}^{BZAC}$ : 0.84 (57%), 3.40 (43%);  $Au_{CZ}^{BZI}$ : 0.74 (46%); 3.6 (54%);  $Au_{Obim}^{BZI}$ : 0.25 (80%), 0.90 (20%). <sup>b</sup> The CAAC ligand on this complex has a menthyl instead of the adamantyl group. <sup>c</sup> Values cannot be accurately determined.

Cooling solutions of the  $M_{BCZ}^{BZAC}$  complexes to 77 K leads to a marked change in the luminescence spectrum with a structured band appearing to the blue of the room temperature spectrum (Figure 6(b)). This rigidochromic transformation upon freezing the solvent has previously been shown to come about from destabilization of the ICT state to an energy higher than that of the triplet state localized on the carbazolide ligand ( $^{3}$ Cz).  $^{4d, 4e, 4k}$  The ICT state is destabilized to a lesser extent in a rigid polystyrene matrix such that it remains the lowest energy state upon cooling to 77 K. Cooling both toluene and polystyrene samples of  $M_{BCZ}^{PAC}$  leads to a blue shift of the ICT band, but this change in energy is not large enough to access the  $^{3}$ Cz state. In contrast, the energy of the triplet state for bim ( $E_{T} = 365$  nm) is much higher than that of carbazole ( $E_{T} = 415$  nm) (Figure S11). The ligand localized triplet states of the carbene ligands are also in the UV region so the  $Au_{bim}^{carbene}$  complexes emit from largely featureless ICT transitions with Gaussian line shapes at all temperatures (Figure 6(d)).

The photoluminescence efficiency for several of the cMA complexes are high ( $\Phi_{PL} > 0.95$ ) in both fluid toluene and rigid polystyrene, and all have microsecond to sub-microsecond emission lifetimes. The Ag complex has a low  $\Phi_{PL}$  in solution which may be related to photodecomposition of this derivative. Lower values for  $\Phi_{PL}$  in toluene solution owe largely to increased nonradiative rates in fluid solutions, likely ligand rotation and/or excimer/exciplex formation. The radiative rates for the bim based cMa complexes are  $1.8-4 \times 10^6 \, \text{s}^{-1}$ , which are some of the highest values reported for TADF emitters and lead to radiative lifetimes as fast as 250 ns. In the cases where an analogous carbazole based complex is available for comparison, the radiative rate for the bim based cMa complexes are two-fold faster than the Cz analogs. Unfortunately, the near degeneracy in energy between the ICT and  $^3$ Cz states in  $Au_{Cz}^{BZAC}$  and  $Au_{Cz}^{BZI}$  leads to non-first order behavior

in the luminescence decay traces for these derivatives precluding direct comparisons with the bim analogs.

As discussed in the introduction, the radiative rate of TADF from luminophores with effective spin orbit coupling (SOC) is controlled by the radiative rate from the S<sub>1</sub> state and the equilibrium constant between the  $T_1$  and  $S_1$  states (Eqn. 1). For  $M_{CZ}^{MAC}$  and  $M_{CZ}^{CAAC}$  complexes, the principal factor that leads to faster TADF rates for the silver complexes over the copper and gold analogs is that the silver complex has larger equilibrium constant, owing to its smaller  $\Delta E_{\rm ST}$  (Eqn. 2). The modeling presented above suggests that the  $\Delta E_{\rm ST}$  values for bim based cMa complexes should be lower than their carbazolide counterparts, which may account for their faster TADF rates. To validate this conjecture, temperature dependent photophysical measurements were performed between 4-300 K to determine the two parameters that control  $k_r^{\rm TADF}$  (i.e.,  $k_r^{\rm S_1}$  and  $\Delta E_{\rm ST}$ ). These measurements were conducted using polystyrene thin films doped at ~1 wt% with the cMa complex. Fitting the temperature dependent lifetimes to a three-level model gives values for  $\Delta E_{ST}$ , the zero-field splitting (ZFS) and the radiative rate from the  $S_1$  and  $T_1$  states. <sup>4e, 4f, 9, 13</sup> The high  $\Phi_{PL}$  in these cMa complexes allows us to neglect nonradiative processes in our model. In this analysis, the ZFS is the energy difference between the two closely spaced triplet sublevels and the highest energy triplet sublevel. The energy spacing between the two lowest sublevels could not be determined from data obtained at temperatures down to 4 K, which is the limit of our cryogenic system. The fits to the data are shown for each complex in the supporting information, and the energy and rate data derived from the fits is given in Table 3.

The  $M_{BCZ}^{PAC}$  complexes show the same trends in TADF parameters observed previously for the MAC and CAAC analogs. <sup>4e</sup> The copper and gold complexes give similar values for  $\Delta E_{ST}$  and

**Table 3:** Energy and rate data from variable temperature photophysical measurements on 1% doped polystyrene films.

	ZFS	$\Delta E_{ m ST}$	$ au_{S_1}$	$ au_{T_1}$
	$(\text{meV}/\text{cm}^{-1})$	$(\text{meV} / \text{cm}^{-1})$	(ns)	(μs)
	± 10%	± 3%	± 9%	± 5%
$Au_{Cz}^{BZAC}$	a	65 / 520	18	a
$Cu_{BCz}^{PAC}$	ь	70 / 570	18	ь
$Ag_{BCz}^{PAC}$	ь	26 / 210	35	b
$Au_{BCz}^{PAC}$	0.9 / 7	72 / 580	14	36
$Au_{Cz}^{MAC}$	1.2 / 10	87 / 700	13	28
$Au_{Cz}^{PZI}$	0.9 / 7	54 / 440	21	82
$Au_{bim}^{PZI}$	1.1 / 9	31 / 250	26	76
$Au_{bim}^{PAC}$	1.0 / 8	45 / 360	17	38
$Au_{bim}^{MAC}$	2.0 / 16	51 / 410	14	38
$Au_{bim}^{CAAC}$	1.1 / 9	53 / 430	18	16
$Au_{bim}^{BZAC}$	1.2 / 10	41 / 330	19	19
$Au_{bim}^{BZI}$	1.5 / 12	41 / 330	15	19
$Au_{Mbim}^{BZI}$	1.5 / 12	44 / 350	16	11
$Au_{Obim}^{BZI}$	1.2 / 10	41 / 330	19	17

<sup>&</sup>lt;sup>a</sup> Luminescence from the <sup>3</sup>Cz state at temperatures below 250 K prevents accurate Boltzmann fits for the <sup>3</sup>ICT parameters. <sup>b</sup> Insufficient data was available at low temperature. Data below 4 K would be required to determine accurate values for these parameters.

 $S_1$  radiative rates, but the silver complex gives a smaller  $\Delta E_{\rm ST}$  and slower  $k_r^{S_1}$ , leading to comparable rates of TADF for complexes with the three different metals. The  $M_{bim}^{carbene}$  complexes show similar values for  $k_r^{S_1}$  to their carbazole analogs (compare the MAC and PAC derivatives in Table 3), but the  $\Delta E_{\rm ST}$  values for the bim based cMa complexes are uniformly lower than those of the analogous carbazole based materials by 30% or more. The fast  $k_r^{\rm TADF}$  for the bim based cMa complexes is thus due largely to a significant increase in  $K_{eq}$  caused by the small  $\Delta E_{\rm ST}$ . We will

discuss the origin of this decrease in  $\Delta E_{ST}$  for the bim complexes in the following discussion section, but there is a clear connection to the smaller  $\Lambda_{NTO}$  for the bim based complexes.

The values of ZFS for the  $M_{CZ}^{MAC}$  and  $M_{CZ}^{CAAC}$  complexes in Table 3 are much lower than values we presented in previous reports. <sup>4e, 4f</sup> Our earlier measurements used a cryostat that had poor thermal regulation below 80 K, which led to incorrect data collected at the low temperatures needed to extract the ZFS parameters. The present results were collected using a cryogenic system that is more reliable (see supporting information for details of the system), providing reproducible data on repeated heating and cooling cycles, which gives us confidence that the ZFS values reported here are accurate.

#### **Discussion**

The ICT transition in the cMa complexes is essentially an electron transfer from the amide group to the carbene. While the transition utilizes the full spatial extent of the HOMO and LUMO (Figure 5), one can consider the process as simply being a charge transfer from the nitrogen lone pair of the amide to the vacant p-orbital of the N-heterocyclic carbene. With this line of reasoning, it is apparent that if the amide is kept constant, the energy of the vacant p-orbital on the carbene will determine the energy of the ICT state. The energy of the LUMO in the carbene ligands chosen for the present study span a range of values (Table 1, Figure 4). The LUMO energy in N-heterocyclic carbene ligands is destabilized by electron donation from the nitrogen(s) adjacent to the p-orbital of the carbene [Figure 7(a)]. Orbital contours from DFT calculations illustrate the antibonding nature of the N-C<sup>carbene</sup> bond in the LUMO [Figure 7(b)], consistent with the energy diagram presented in 7(a). The carbene p-orbital will be destabilized by greater the participation

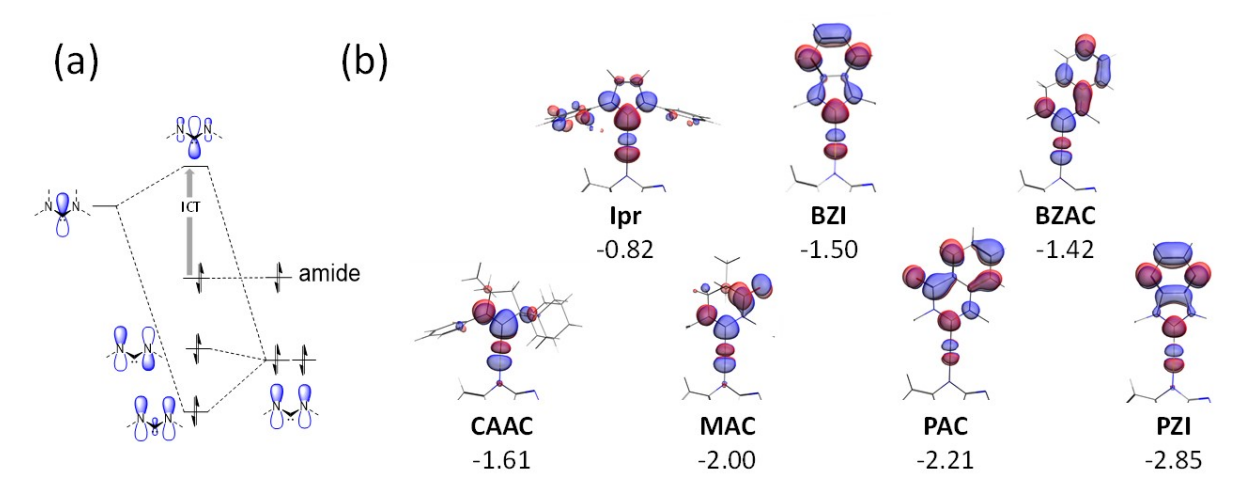


**Figure 7:** (a) The ICT transition and the nature of the interaction between the N lone pairs and carbene p-orbital of the N-heterocycle carbene (NHC) for the cMa complexes are illustrated. In this representation the plane of the NHC ligand is perpendicular to the page. (b) LUMO orbitals are shown for  $M_{bim}^{carbene}$  complexes. The dipp groups are only shown for the IPr and CAAC complexes. In the other complexes the dipp groups are not involved in the LUMO. The LUMO energies (in eV) from DFT calculations are given below the acronym of each ligand.

of the nitrogen(s) in this MO, thus raising the transition energy of the ICT state. The CAAC ligand has only a single N-atom, whereas the others have two N-atoms destabilizing the carbene p-orbital, which explains the significant stabilization of the CAAC LUMO relative to that of the closest analog (Ipr). The benzannulated phenyl ring of BZI accepts electron density from the imidazolium nitrogen atoms and leads to less mixing of the N lone pair with the carbene p-orbital, stabilizing the LUMO relative to Ipr. Nitrogen substitution into the arene ring of BZI (forming PZI) leads to even greater interaction with the imidazolium nitrogens, stabilizing the carbene LUMO further. The BZAC ligand would be expected to have a LUMO between that of Ipr and BZI, since only one nitrogen is attenuated by the benzannulation, however, the ring expansion from a five- to a six-membered ring stabilizes the carbene p-orbital, <sup>23</sup> leading to similar LUMO energies for BZI and BZAC. The carbonyl groups of MAC and PAC compete effectively for the nitrogen lone pair, therefore the LUMO energies for these two carbenes are lower than for BZAC. It is evident upon comparison of BZAC and MAC that the carbonyl group leads to a much greater stabilization of

the LUMO than does benzannulation. The LUMO energy for PAC is lowered due to stabilization of the  $\pi$ -system by both benzannulation and the carbonyl group.

An important set of observations that deserves further discussion are the short lifetimes for the cMa complexes coordinated to the bim ligand. In all cases, the radiative rate for the  $Au_{bim}^{carbene}$  complex is a factor of two faster that the analogous  $Au_{CZ}^{carbene}$  complex. This difference occurs despite both derivatives having similar excited state energies and extinction coefficients. Based on modeling studies (Table 1), the  $Au_{bim}^{carbene}$  complexes have lower  $A_{NTO}$  and  $\Delta E_{ST}$  values than their  $Au_{CZ}^{carbene}$  counterparts (excluding the Ipr complex, which emits form a <sup>3</sup>bim state). The latter trend is mirrored in the data from variable temperature photophysical measurements that show the  $Au_{bim}^{carbene}$  complexes do indeed have lower  $\Delta E_{ST}$  values than their  $Au_{CZ}^{carbene}$  analogs (Table 3). Thus, since values of  $k_r^{S_1}$  are similar for complexes with both types of amide, the principal source of the fast  $k_r^{TADF}$  values for the  $Au_{bim}^{carbene}$  complexes are the low values for  $\Delta E_{ST}$ .

A key difference between Cz and bim in the cMa complexes is the location of the center of positive charge in the ICT excited states of the two amides. The positions calculated for the electron and hole for the  $M_{amide}^{carbene}$  complexes discussed here are illustrated in Figure 8. The two charges lie within the plane of the carbene and amide ligand, respectively. For Cz the center of positive charge lies near the N atom, whereas in  $M_{bim}^{carbene}$  complexes the three nitrogen atoms of the core guanidinium unit disperse the positive charge and shift the center away from the nitrogen atom bound to the metal. The position of the electron in each carbene for the ICT excited state is nearly independent on the choice of Cz or bim, and similarly the position of the hole for each amide is unaffected by the choice of carbene. The center of electron charge resides within the C-M bond for Ipr and CAAC, whereas the charge shifts into the carbene ligand for BZI, BZAC,

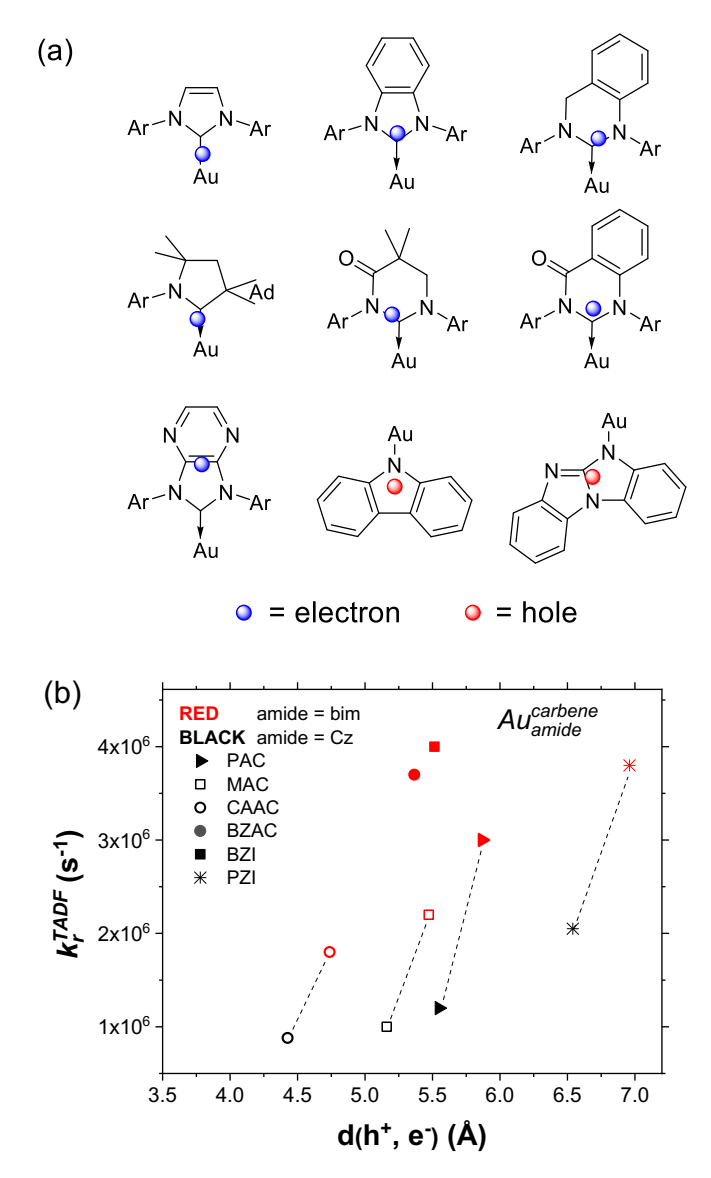


**Figure 8:** (a) The centers of negative charge (blue spheres) and positive charge (red spheres) are shown on the molecular frame for the ICT excited states. Ar = 2,6-diisopropylphenyl and Ad = adamantyl. (b) The rate of TADF emission  $(k_r^{TADF})$  at room temperature for a doped polystyrene film is plotted as a function of the hole/electron separation distance.

MAC, PAC and PZI, see Figure 8(a). This is consistent with the enhanced delocalization in the LUMO by  $\pi$ -extending the carbene backbone. The distance between the centers of positive and negative charge,  $d(h^+, e^-)$ , for each cMa is given in Table S5. Figure 8(b) shows the relationship of  $d(h^+, e^-)$  for  $M_{amide}^{carbene}$  complexes to  $k_r^{TADF}$ . Values for  $d(h^+, e^-)$  are spaced further apart for the bim complexes than the Cz-based ones.

Radiative rates for both bim and Cz complexes show a dependence on  $d(h^+, e^-)$ , with larger separations leading to faster  $k_r^{TADF}$  (Figure 8(b)); however, the degree to which  $k_r^{TADF}$  increases with  $d(h^+, e^-)$  differ for the two derivatives. In all cases where data are available for a given carbene, the  $k_r^{TADF}$ 

values are markedly faster for the bim-based cMa complexes than for the Cz-based analogs (see dashed lines in Figure 8(b)). The  $Au_{Cz}^{BZI}$  and  $Au_{Cz}^{BZAC}$  complexes were not included in Figure 8(b) because the triplet excited states for these two compounds have a mixed ICT/ligand-localized

character. 4k The energies of the ICT and 3Cz states are nearly degenerate in both of these complexes, which promotes mixing of the states and a concomitant increase in the measured lifetime, so we cannot unequivocally determine  $k_r^{TADF}$ . Although the energy separation between the  $^3$ ICT and ligand localized triplet states for the  $M_{bim}^{carbene}$  and  $M_{CZ}^{carbene}$  complexes with PAC, MAC, CAAC and PZI carbenes is large enough to prevent mixing between these excited states, the bim complexes still display a marked increase in the radiative rate relative to their carbazole analogs. The large  $d(h^+, e^-)$  separations for the bim complexes are consistent with lower  $\Lambda_{NTO}$ values, and thus the lower  $\Delta E_{ST}$  values, for the bim complexes relative to their carbazole counterparts. At first glance an increase in  $d(h^+, e^-)$  might also be expected to decrease  $k_r^{S_1}$ , as observed upon substituting Ag<sup>+</sup> (with a large ionic radius) in place of Cu<sup>+</sup> and Au<sup>+</sup> for the  $M_{BCz}^{PAC}$ complexes, as well as for the  $M_{Cz}^{MAC}$  and  $M_{Cz}^{CAAC}$  derivatives. 4e However, this is not the case for  $Au_{bim}^{carbene}$  complexes since  $k_r^{S_1}$  remains nearly constant (in the 15-20 ns range) for complexes with either carbazole or bim ligands (Table 3). Thus, the decrease in  $\Delta E_{\rm ST}$  brought about by the enhanced  $d(h^+, e^-)$  is the principal factor leading to the fast  $k_r^{TADF}$  values for the  $Au_{bim}^{carbene}$ complexes. Interestingly, considering all of the complexes other than  $Au_{bim}^{PZI}$ , values for  $k_r^{S_1}$  are near constant and do not show an increase by the cube of the emission energy as predicted by the Einstein relationship, <sup>24</sup> even though the complexes span a range of emission energies from 2.2-2.9 eV. It is also noteworthy that even though  $Au_{bim}^{PZI}$  has a substantially larger d(h<sup>+</sup>, e<sup>-</sup>) than  $Au_{bim}^{BZI}$ and  $Au_{bim}^{BZAC}$ , all three complexes have comparable rates for  $k_r^{TADF}$ . For the PZI based cMa complexes, low values for  $\Delta E_{ST}$  are compensated by S<sub>1</sub> lifetimes that are slower than the other Au(I) derivatives. This suggests that the d(h<sup>+</sup>, e<sup>-</sup>) value observed for  $Au_{bim}^{PZI}$  (6.8 Å) is approaching a limit for enhancing  $k_r^{TADF}$ , and we therefore anticipate that any further increase in  $d(h^+, e^-)$  will continue to increase the radiative lifetime for the  $S_1$  state.

#### **Conclusion**

Two-coordinate, coinage metal (carbene) $M^{(1)}$ (amide) complexes have attracted a great deal of attention recently, due in part to their excellent photophysical and electroluminescent properties. <sup>4, 20a</sup> These cMa complexes give high photoluminescent and electroluminescent efficiencies and have very short phosphorescence (TADF) lifetimes. Most of the work published to date for these complexes has focused on CAAC, MAC and BZI type ligands, with the most common amide being a carbazolide. In this paper we have explored the impact of  $\pi$ -extending the carbene and amide ligands on the physical and photophysical properties of cMa complexes. The carbene ligand was  $\pi$ -extended via benzannulation (BZI, BZAC and PAC). The amide ligand was  $\pi$ -extended via replacement of the central "pyrrole" moiety of carbazole with a guanidinium group (*i.e.*, the bim ligand). We have found that  $\pi$ -extending the carbene and amide together leads to some of the highest radiative rates observed for a triplet-controlled emission process, with rates as high as 4 x  $10^6$  s<sup>-1</sup>.

The lowest energy absorption and emission bands in the  $M_{CZ}^{carbene}$  complexes are due to transitions involving the amide (HOMO) and carbene (LUMO). The energy of the LUMO shifts significantly across the series of carbenes explored here, leading to the ordering of energies for the ICT bands of  $M_{CZ}^{carbene}$  being BZI > BZAC > CAAC > MAC > PAC. Other than this shift in energy, the choice of carbene in the  $M_{CZ}^{carbene}$  complex has a modest impact on the photophysical properties since the complexes have similar values for extinction coefficients, as well as for radiative and nonradiative decay rates. In contrast, the effect of  $\pi$ -extending the amide ligand  $(M_{CZ}^{carbene} \to M_{bim}^{carbene})$  has almost no effect on the energy of the ICT transition, but other photophysical properties are markedly altered. The radiative decay rate  $(k_r^{TADF})$  for a given

 $M_{bim}^{carbene}$  is between two-to-four times greater than the rate for the  $M_{Cz}^{carbene}$  complex of the same carbene. The principal source of the rate enhancement for bim-based cMa complexes comes from a decrease in the  $\Delta E_{\rm ST}$  for these complexes compared to the Cz counterparts. This decrease in  $\Delta E_{\rm ST}$  is related to the smaller  $\Lambda_{NTO}$  for  $M_{him}^{carbene}$  complexes, brought about by a shift of the hole density (HOMO) away from the electron localized on the carbene. While this picture explains the difference between Cz- and bim-based complexes with a common carbene ligand, it does not explain the differences in radiative rates seen for the  $M_{bim}^{carbene}$  complexes. The calculated values of  $\Delta E_{\rm ST}$  and  $\Lambda_{NTO}$  for the  $M_{bim}^{carbene}$  complexes are similar, but their radiative rates differ by more than a factor of two in comparing MAC to BZI complexes. Consistent with the experimental  $k_r^{TADF}$  data, values for  $\Delta E_{\rm ST}$  are lowest for  $M_{bim}^{carbene}$  complexes with  $\pi$ -extended carbene ligands, *i.e.* BZI, BZAC and PAC. Interestingly,  $k_r^{S_1}$  for the  $M_{bim}^{carbene}$  complexes only marginally decreases with a decrease in  $\Lambda_{NTO}$  and increase in hole/electron separation. Therefore, the increase  $k_r^{TADF}$  for  $M_{bim}^{carbene}$ complexes versus their  $M_{Cz}^{carbene}$  analogs owes primarily to a large increase in  $K_{eq}$ , rather than to a change in  $k_r^{S_1}$  (Eqn. 1), and is most prominent for the complexes with benzannulated carbene ligands. Thus,  $\pi$ -extension of both ligands (carbene and amide) imparts the most significant enhancements in radiative rate.

While this report has focused on achieving fast radiative lifetimes, it is important to stress that knowledge of  $\Lambda_{NTO}$  and d(h<sup>+</sup>, e<sup>-</sup>) can be used to tailor the ICT excited states in related compounds for use as sensitizers in photoelectrochemical processes. A small  $\Lambda_{NTO}$  will lead to a large  $\Delta E_{ST}$  value and small  $K_{eq}$ , as described above, but the large  $\Lambda_{NTO}$  will conversely improve hole/electron overlap, and thus increase extinction coefficients for light absorption. Therefore, it

should be possible to achieve both long lifetimes and high molar absorptivity from other cMa complexes.

#### Acknowledgements

The authors would like to acknowledge the Department of Energy, Office of Basic Energy Science (Award: DE-SC0016450) for support of Muniz and Thompson, the Department of Energy, Office of Energy Efficiency and Renewable Energy (Award: EE0009688) for support of Schaab and the Universal Display Corporation for support of Razgoniaev, Djurovich and Thompson. Funds were provided by the National Science Foundation (Award: CHE-2018740) to acquire the X-ray diffractometer that was used to determine the crystal structures reported here.

#### **Conflict of Interest**

One of the authors (Thompson) has a financial interest in the Universal Display Corporation.

#### **Supporting Information**

The SI includes synthetic details and characterization, X-ray structural data, electrochemical traces, details of molecular modeling, absorption and emission spectra, temperature dependent lifetime data and details of Boltzmann fitting, and <sup>1</sup>H and <sup>13</sup>C NMR spectra for compounds studied herein.

#### References

- 1. (a) Ziolo, R. F.; Lipton, S.; Dori, Z., The Photoluminescence of Phosphine Complexes of D 10 Metals. *Journal of the Chemical Society D: Chemical Communications* **1970**, (17), 1124-1125, DOI: 10.1039/c29700001124;
- (b) Antipas, A.; Dolphin, D.; Gouterman, M.; Johnson, E. C., Porphyrins. 38. Redox Potentials, Charge Transfer Transitions, and Emission of Copper, Silver, and Gold Complexes. *Journal of the American Chemical Society* **1978**, *100* (24), 7705-7709, DOI: 10.1021/ja00492a044
- 2. Sorrell, T. N.; Borovik, A. S., Absorption, Emission, and Photophysical Properties of Copper(I) Pyrazole Complexes and Their Carbonyl Adducts. *Inorganic Chemistry* **1987**, *26* (12), 1957-1964, DOI: 10.1021/ic00259a029
- 3. (a) Mercs, L.; Albrecht, M., Beyond Catalysis: N-Heterocyclic Carbene Complexes as Components for Medicinal, Luminescent, and Functional Materials Applications. *Chemical Society Reviews* **2010**, *39* (6), 1903-1912, DOI: 10.1039/b902238b;
- (b) Visbal, R.; Gimeno, M. C., N-Heterocyclic Carbene Metal Complexes: Photoluminescence and Applications. *Chemical Society Reviews* **2014**, *43* (10), 3551-3574, DOI: 10.1039/c3cs60466g;
- (c) Wang, H. M. J.; Chen, C. Y. L.; Lin, I. J. B., Synthesis, Structure, and Spectroscopic Properties of Gold(I)—Carbene Complexes. *Organometallics* **1999**, *18* (7), 1216-1223, DOI: 10.1021/om980718b;
- (d) King, C.; Khan, M. N. I.; Staples, R. J.; Fackler, J. P., Luminescent Mononuclear Gold(I) Phosphines. *Inorganic Chemistry* **1992**, *31* (15), 3236-3238, DOI: 10.1021/ic00041a013;
- (e) Hong, X.; Cheung, K.-K.; Guo, C.-X.; Che, C.-M., Luminescent Organometallic Gold(I) Complexes. Structure and Photophysical Properties of Alkyl-, Aryl- and μ-Ethynylene Gold(I) Complexes. *Journal of the Chemical Society, Dalton Transactions* **1994**, (13), 1867-1871, DOI: 10.1039/dt9940001867;
- (f) Wang, H. M. J.; Vasam, C. S.; Tsai, T. Y. R.; Chen, S.-H.; Chang, A. H. H.; Lin, I. J. B., Gold(I) N-Heterocyclic Carbene and Carbazolate Complexes. *Organometallics* **2005**, *24* (4), 486-493, DOI: 10.1021/om049221u;
- (g) Gimeno, M. C.; Laguna, A.; Visbal, R., N-Heterocyclic Carbene Coinage Metal Complexes as Intense Blue-Green Emitters. *Organometallics* **2012**, *31* (20), 7146-7157, DOI: 10.1021/om300571m;
- (h) Gomez-Suarez, A.; Nelson, D. J.; Thompson, D. G.; Cordes, D. B.; Graham, D.; Slawin, A. M.; Nolan, S. P., Synthesis, Characterization and Luminescence Studies of Gold(I)-NHC Amide Complexes. *Beilstein Journal of Organic Chemistry* **2013**, *9*, 2216-23, DOI: 10.3762/bjoc.9.260;
- (i) Romanov, A. S.; Di, D.; Yang, L.; Fernandez-Cestau, J.; Becker, C. R.; James, C. E.; Zhu, B.; Linnolahti, M.; Credgington, D.; Bochmann, M., Highly Photoluminescent Copper Carbene Complexes Based on Prompt Rather Than Delayed Fluorescence. *Chemical Communications* **2016**, *52* (38), 6379-6382, DOI: 10.1039/C6CC02349E and 10.1039/C8CC90135J;
- (j) Hamze, R.; Jazzar, R.; Soleilhavoup, M.; Djurovich, P. I.; Bertrand, G.; Thompson, M. E., Phosphorescent 2-, 3- and 4-Coordinate Cyclic (Alkyl)(Amino)Carbene (CAAC) Cu(I) Complexes. *Chemical Communications* **2017**, *53*, 9008-9011, DOI: 10.1039/C7CC02638B;
- (k) Shi, S.; Collins, L. R.; Mahon, M. F.; Djurovich, P. I.; Thompson, M. E.; Whittlesey, M. K., Synthesis and Characterization of Phosphorescent Two-Coordinate Copper(I) Complexes Bearing

- Diamidocarbene Ligands. *Dalton Transactions* **2017**, *46* (3), 745-752, DOI: 10.1039/C6DT04016K;
- (1) Romanov, A. S.; Becker, C. R.; James, C. E.; Di, D.; Credgington, D.; Linnolahti, M.; Bochmann, M., Copper and Gold Cyclic (Alkyl)(Amino)Carbene Complexes with Sub-Microsecond Photoemissions: Structure and Substituent Effects on Redox and Luminescent Properties. *Chemistry A European Journal* **2017**, *23* (19), 4625-4637, DOI: 10.1002/chem.201605891;
- (m) Yersin, H.; Czerwieniec, R.; Shafikov, M. Z.; Suleymanova, A. F., TADF Material Design: Photophysical Background and Case Studies Focusing on Cu<sup>I</sup> and Ag<sup>I</sup> Complexes. *Chemphyschem* **2017**, *18* (24), 3508-3535, DOI: 10.1002/cphc.201700872;
- (n) Gernert, M.; Balles-Wolf, L.; Kerner, F.; Müller, U.; Schmiedel, A.; Holzapfel, M.; Marian, C. M.; Pflaum, J.; Lambert, C.; Steffen, A., Cyclic (Amino)(Aryl)Carbenes Enter the Field of Chromophore Ligands: Expanded Π System Leads to Unusually Deep Red Emitting Cui Compounds. *Journal of the American Chemical Society* **2020**, *142* (19), 8897-8909, DOI: 10.1021/jacs.0c02234;
- (o) Li, T.-y.; Muthiah Ravinson, D. S.; Haiges, R.; Djurovich, P. I.; Thompson, M. E., Enhancement of the Luminescent Efficiency in Carbene-Au(I)-Aryl Complexes by the Restriction of Renner-Teller Distortion and Bond Rotation. *Journal of the American Chemical Society* **2020**, *142* (13), 6158-6172, DOI: 10.1021/jacs.9b13755
- 4. (a) Di, D.; Romanov, A. S.; Yang, L.; Richter, J. M.; Rivett, J. P. H.; Jones, S.; Thomas, T. H.; Abdi Jalebi, M.; Friend, R. H.; Linnolahti, M.; Bochmann, M.; Credgington, D., High-Performance Light-Emitting Diodes Based on Carbene-Metal-Amides. *Science* **2017**, *356* (6334), 159, DOI: 10.1126/science.aah4345;
- (b) Conaghan, P. J.; Menke, S. M.; Romanov, A. S.; Jones, S. T. E.; Pearson, A. J.; Evans, E. W.; Bochmann, M.; Greenham, N. C.; Credgington, D., Efficient Vacuum-Processed Light-Emitting Diodes Based on Carbene–Metal–Amides. *Advanced Materials* **2018**, *30* (35), 1802285, DOI: 10.1002/adma.201802285;
- (c) Romanov, A. S.; Jones, S. T. E.; Yang, L.; Conaghan, P. J.; Di, D.; Linnolahti, M.; Credgington, D.; Bochmann, M., Mononuclear Silver Complexes for Efficient Solution and Vacuum-Processed Oleds. *Advanced Optical Materials* **2018**, *6* (24), 1801347, DOI: doi:10.1002/adom.201801347;
- (d) Hamze, R.; Peltier, J. L.; Sylvinson, D.; Jung, M.; Cardenas, J.; Haiges, R.; Soleilhavoup, M.; Jazzar, R.; Djurovich, P. I.; Bertrand, G.; Thompson, M. E., Eliminating Nonradiative Decay in Cu(I) Emitters: > 99% Quantum Efficiency and Microsecond Lifetime. *Science* **2019**, *363* (6427), 601-606, DOI: 10.1126/science.aav2865;
- (e) Hamze, R.; Shi, S.; Kapper, S. C.; Muthiah Ravinson, D. S.; Estergreen, L.; Jung, M.-C.; Tadle, A. C.; Haiges, R.; Djurovich, P. I.; Peltier, J. L.; Jazzar, R.; Bertrand, G.; Bradforth, S. E.; Thompson, M. E., "Quick-Silver" from a Systematic Study of Highly Luminescent, Two-Coordinate, D10 Coinage Metal Complexes. *Journal of the American Chemical Society* **2019**, *141* (21), 8616-8626, DOI: 10.1021/jacs.9b03657;
- (f) Shi, S.; Jung, M. C.; Coburn, C.; Tadle, A.; Sylvinson M. R, D.; Djurovich, P. I.; Forrest, S. R.; Thompson, M. E., Highly Efficient Photo- and Electroluminescence from Two-Coordinate Cu(I) Complexes Featuring Nonconventional N-Heterocyclic Carbenes. *Journal of the American Chemical Society* **2019**, *141* (8), 3576-3588, DOI: 10.1021/jacs.8b12397;
- (g) Romanov, A. S.; Yang, L.; Jones, S. T. E.; Di, D.; Morley, O. J.; Drummond, B. H.; Reponen, A. P. M.; Linnolahti, M.; Credgington, D.; Bochmann, M., Dendritic Carbene Metal Carbazole

- Complexes as Photoemitters for Fully Solution-Processed Oleds. *Chemistry of Materials* **2019**, *31* (10), 3613-3623, DOI: 10.1021/acs.chemmater.8b05112;
- (h) Chotard, F.; Sivchik, V.; Linnolahti, M.; Bochmann, M.; Romanov, A. S., Mono-Versus Bicyclic Carbene Metal Amide Photoemitters: Which Design Leads to the Best Performance? *Chemistry of Materials* **2020**, *32* (14), 6114-6122, DOI: 10.1021/acs.chemmater.0c01769;
- (i) Romanov, A. S.; Jones, S. T. E.; Gu, Q.; Conaghan, P. J.; Drummond, B. H.; Feng, J.; Chotard, F.; Buizza, L.; Foley, M.; Linnolahti, M.; Credgington, D.; Bochmann, M., Carbene Metal Amide Photoemitters: Tailoring Conformationally Flexible Amides for Full Color Range Emissions Including White-Emitting Oled. *Chemical Science* **2020**, *11* (2), 435-446, DOI: 10.1039/c9sc04589a;
- (j) Feng, J.; Yang, L.; Romanov, A. S.; Ratanapreechachai, J.; Reponen, A.-P. M.; Jones, S. T. E.; Linnolahti, M.; Hele, T. J. H.; Köhler, A.; Bässler, H.; Bochmann, M.; Credgington, D., Environmental Control of Triplet Emission in Donor–Bridge–Acceptor Organometallics. *Advanced Functional Materials* **2020**, *30* (9), 1908715, DOI: 10.1002/adfm.201908715;
- (k) Hamze, R.; Idris, M.; Muthiah Ravinson, D. S.; Jung, M. C.; Haiges, R.; Djurovich, P. I.; Thompson, M. E., Highly Efficient Deep Blue Luminescence of 2-Coordinate Coinage Metal Complexes Bearing Bulky NHC Benzimidazolyl Carbene. *Frontiers in Chemistry* **2020**, *8* (401), 1-9, DOI: 10.3389/fchem.2020.00401
- 5. Conaghan, P. J.; Matthews, C. S. B.; Chotard, F.; Jones, S. T. E.; Greenham, N. C.; Bochmann, M.; Credgington, D.; Romanov, A. S., Highly Efficient Blue Organic Light-Emitting Diodes Based on Carbene-Metal-Amides. *Nature Communications* **2020**, *11* (1), 1758, DOI: 10.1038/s41467-020-15369-8
- 6. (a) Yersin, H., Triplet Emitters for Oled Applications. Mechanisms of Exciton Trapping and Control of Emission Properties. In *Transition Metal and Rare Earth Compounds. Topics in Current Chemistry*, Springer: Berlin, 2004; Vol. 241, pp 1-26, DOI 10.1007/b96858;
- (b) Thompson, M. E.; Djurovich, P. E.; Barlow, S.; Marder, S., Organometallic Complexes for Optoelectronic Applications. In *Comprehensive Organometallic Chemistry III*, 1 ed.; O'Hare, D., Ed. Elsevier Ltd.: Oxford, UK, 2007; Vol. 12, pp 102-194;
- (c) Bolink, H. J.; Coronado, E.; Costa, R. D.; Lardiés, N.; Ortí, E., Near-Quantitative Internal Quantum Efficiency in a Light-Emitting Electrochemical Cell. *Inorganic Chemistry* **2008**, *47* (20), 9149-9151, DOI: 10.1021/ic801587n;
- (d) Mahoro, G. U.; Fernandez-Cestau, J.; Renaud, J.-L.; Coto, P. B.; Costa, R. D.; Gaillard, S., Recent Advances in Solid-State Lighting Devices Using Transition Metal Complexes Exhibiting Thermally Activated Delayed Fluorescent Emission Mechanism. *Advanced Optical Materials* **2020**, *8* (16), 2000260, DOI: 10.1002/adom.202000260;
- (e) Yersin, H., Triplet Emitters for Oled Applications. Mechanisms of Exciton Trapping and Control of Emission Properties. In *Transition Metal and Rare Earth Compounds: Excited States, Transitions, Interactions Iii*, Yersin, H., Ed. Springer Berlin Heidelberg: Berlin, Heidelberg, 2004; pp 1-26.
- 7. (a) Kalyanasundaram, K., Photophysics, Photochemistry and Solar Energy Conversion with Tris(Bipyridyl)Ruthenium(Ii) and Its Analogues. *Coordination Chemistry Reviews* **1982**, *46*, 159-244, DOI: 10.1016/0010-8545(82)85003-0;

- (b) Kim, S.; Toste, F. D., Mechanism of Photoredox-Initiated C–C and C–N Bond Formation by Arylation of Iprau(I)–Cf3 and Iprau(I)–Succinimide. *Journal of the American Chemical Society* **2019**, *141* (10), 4308-4315, DOI: 10.1021/jacs.8b11273;
- (c) Jazzar, R.; Soleilhavoup, M.; Bertrand, G., Cyclic (Alkyl)- and (Aryl)-(Amino)Carbene Coinage Metal Complexes and Their Applications. *Chemical Reviews* **2020**, *120* (9), 4141-4168, DOI: 10.1021/acs.chemrev.0c00043
- 8. (a) Keefe, M. H.; Benkstein, K. D.; Hupp, J. T., Luminescent Sensor Molecules Based on Coordinated Metals: A Review of Recent Developments. *Coordination Chemistry Reviews* **2000**, 205 (1), 201-228, DOI: 10.1016/S0010-8545(00)00240-X;
- (b) Lo, K. K.-W.; Louie, M.-W.; Zhang, K. Y., Design of Luminescent Iridium(III) and Rhenium(I) Polypyridine Complexes as in Vitro and in Vivo Ion, Molecular and Biological Probes. *Coordination Chemistry Reviews* **2010**, *254* (21), 2603-2622, DOI: 10.1016/j.ccr.2010.01.014;
- (c) Liu, Q.; Wu, H.; Zhao, Z.; Wei, D., Macrometallocycle Binuclear NHC Silver(I) Complex with Bridging Azobenzene: Synthesis, Structure and Recognition for Hydrogen Sulfate. *Tetrahedron* **2019**, *75* (23), 3128-3134, DOI: 10.1016/j.tet.2019.04.066
- 9. Ravinson, D. S. M.; Thompson, M. E., Thermally Assisted Delayed Fluorescence (TADF): Fluorescence Delayed Is Fluorescence Denied. *Materials Horizons* **2020**, *7* (5), 1210-1217, DOI: 10.1039/D0MH00276C
- 10. (a) Yang, Z.; Mao, Z.; Xie, Z.; Zhang, Y.; Liu, S.; Zhao, J.; Xu, J.; Chi, Z.; Aldred, M. P., Recent Advances in Organic Thermally Activated Delayed Fluorescence Materials. *Chemical Society Reviews* **2017**, *46* (3), 915-1016, DOI: 10.1039/c6cs00368k;
- (b) Li, W.; Li, B.; Cai, X.; Gan, L.; Xu, Z.; Li, W.; Liu, K.; Chen, D.; Su, S.-J., Tri-Spiral Donor for High Efficiency and Versatile Blue Thermally Activated Delayed Fluorescence Materials. *Angewandte Chemie International Edition* **2019**, *58* (33), 11301-11305, DOI: 10.1002/anie.201904272;
- (c) Li, P.; Chan, H.; Lai, S.-L.; Ng, M.; Chan, M.-Y.; Yam, V. W.-W., Four-Coordinate Boron Emitters with Tridentate Chelating Ligand for Efficient and Stable Thermally Activated Delayed Fluorescence Organic Light-Emitting Devices. *Angewandte Chemie International Edition* **2019**, *58* (27), 9088-9094, DOI: 10.1002/anie.201903332;
- (d) Hu, J.; Li, Q.; Wang, X.; Shao, S.; Wang, L.; Jing, X.; Wang, F., Developing through-Space Charge Transfer Polymers as a General Approach to Realize Full-Color and White Emission with Thermally Activated Delayed Fluorescence. *Angewandte Chemie International Edition* **2019**, *58* (25), 8405-8409, DOI: 10.1002/anie.201902264;
- (e) Luo, Y.; Li, S.; Zhao, Y.; Li, C.; Pang, Z.; Huang, Y.; Yang, M.; Zhou, L.; Zheng, X.; Pu, X.; Lu, Z., An Ultraviolet Thermally Activated Delayed Fluorescence Oled with Total External Quantum Efficiency over 9%. *Advanced Materials* **2020**, *32* (32), 2001248, DOI: 10.1002/adma.202001248;
- (f) Izumi, S.; Higginbotham, H. F.; Nyga, A.; Stachelek, P.; Tohnai, N.; Silva, P. d.; Data, P.; Takeda, Y.; Minakata, S., Thermally Activated Delayed Fluorescent Donor–Acceptor–Donor–Acceptor π-Conjugated Macrocycle for Organic Light-Emitting Diodes. *Journal of the American Chemical Society* **2020**, *142* (3), 1482-1491, DOI: 10.1021/jacs.9b11578

- 11. Gernert, M.; Müller, U.; Haehnel, M.; Pflaum, J.; Steffen, A., A Cyclic Alkyl(Amino)Carbene as Two-Atom π-Chromophore Leading to the First Phosphorescent Linear Cui Complexes. *Chemistry A European Journal* **2017**, *23* (9), 2206-2216, DOI: 10.1002/chem.201605412
- 12. Jones, P. F.; Calloway, A. R., Temperature Effects on the Intramolecular Decay of the Lowest Triplet State of Benzophenone. *Chemical Physics Letters* **1971**, *10* (4), 438-443, DOI: 10.1016/0009-2614(71)80329-9
- 13. Li, T.-y.; Schaab, J.; Djurovich, P. I.; Thompson, M. E., Toward Rational Design of Tadf Two-Coordinate Coinage Metal Complexes: Understanding the Relationship between Natural Transition Orbital Overlap and Photophysical Properties. *Journal of Materials Chemistry C* **2022**, *10* (12), 4674-4683, DOI: 10.1039/d2tc00163b
- 14. Strickler, S. J.; Berg, R. A., Relationship between Absorption Intensity and Fluorescence Lifetime of Molecules. *The Journal of Chemical Physics* **1962**, *37* (4), 814-822, DOI: 10.1063/1.1733166
- 15. (a) Tadle, A. C.; El Roz, K. A.; Soh, C. H.; Sylvinson Muthiah Ravinson, D.; Djurovich, P. I.; Forrest, S. R.; Thompson, M. E., Tuning the Photophysical and Electrochemical Properties of Aza-Boron-Dipyridylmethenes for Fluorescent Blue Oleds. *Advanced Functional Materials* **2021**, *31* (27), 2101175, DOI: 10.1002/adfm.202101175;
- (b) Chen, T.; Zheng, L.; Yuan, J.; An, Z.; Chen, R.; Tao, Y.; Li, H.; Xie, X.; Huang, W., Understanding the Control of Singlet-Triplet Splitting for Organic Exciton Manipulating: A Combined Theoretical and Experimental Approach. *Scientific Reports* **2015**, *5*, 10923, DOI: 10.1038/srep10923
- 16. Sheldrick, G., Crystal Structure Refinement with Shelxl. *Acta Crystallographica Section C* **2015,** 71 (1), 3-8, DOI: doi:10.1107/S2053229614024218
- 17. Epifanovsky, E.; Gilbert, A. T. B.; Feng, X.; Lee, J.; Mao, Y.; Mardirossian, N., et al., Software for the Frontiers of Quantum Chemistry: An Overview of Developments in the Q-Chem 5 Package. *Journal of Chemical Physics* **2021**, *155* (8), 084801, DOI: 10.1063/5.0055522
- 18. Hermann, G.; Pohl, V.; Tremblay, J. C.; Paulus, B.; Hege, H.-C.; Schild, A., Orbkit: A Modular Python Toolbox for Cross-Platform Postprocessing of Quantum Chemical Wavefunction Data. *Journal of Computational Chemistry* **2016**, *37* (16), 1511-1520, DOI: 10.1002/jcc.24358
- 19. Castro, S. G. P.; et al. 2021 Python Wrapper for Cubature: Adaptive Multidimensional Integration, Version 0.14.8; 2021.
- 20. (a) Yang, J.-G.; Song, X.-F.; Wang, J.; Li, K.; Chang, X.; Tan, L.-Y.; Liu, C.-X.; Yu, F.-H.; Cui, G.; Cheng, G.; To, W.-P.; Yang, C.; Che, C.-M.; Chen, Y., Highly Efficient Thermally

- Activated Delayed Fluorescence from Pyrazine-Fused Carbene Au(I) Emitters. *Chemistry A European Journal* **2021**, *27* (71), 17834-17842, DOI: 10.1002/chem.202102969;
- (b) Tang, R.; Xu, S.; Lam, T.-L.; Cheng, G.; Du, L.; Wan, Q.; Yang, J.; Hung, F.-F.; Low, K.-H.; Phillips, D. L.; Che, C.-M., Highly Robust Cui-Tadf Emitters for Vacuum-Deposited Oleds with Luminance up to 222 200 Cd M-2 and Device Lifetimes (Lt90) up to 1300 Hours at an Initial Luminance of 1000 Cd M-2. *Angewandte Chemie International Edition* **2022**, *61* (33), e202203982, DOI: 10.1002/anie.202203982
- 21. Karon, K.; Lapkowski, M., Carbazole Electrochemistry: A Short Review. *Journal of Solid State Electrochemistry* **2015**, *19* (9), 2601-2610, DOI: 10.1007/s10008-015-2973-x
- 22. Tzouras, N. V.; Martynova, E. A.; Ma, X.; Scattolin, T.; Hupp, B.; Busen, H., et al., Simple Synthetic Routes to Carbene-M-Amido (M=Cu, Ag, Au) Complexes for Luminescence and Photocatalysis Applications. *Chemistry A European Journal* **2021**, *27* (46), 11904-11911, DOI: 10.1002/chem.202101476
- 23. Weinstein, C. M.; Junor, G. P.; Tolentino, D. R.; Jazzar, R.; Melaimi, M.; Bertrand, G., Highly Ambiphilic Room Temperature Stable Six-Membered Cyclic (Alkyl)(Amino)Carbenes. *Journal of the American Chemical Society* **2018**, *140* (29), 9255-9260, DOI: 10.1021/jacs.8b05518
- 24. Hilborn, R. C., Einstein Coefficients, Cross Sections, F Values, Dipole Moments, and All That. *American Journal of Physics* **1982**, *50* (11), 982-986, DOI: 10.1119/1.12937

# **Supporting Information**

# $\pi$ -Extended Ligands in Two-Coordinate Coinage Metal Complexes

Collin N. Muniz<sup>\*</sup>, Jonas Schaab<sup>\*</sup>, Anton Razgoniaev, Peter I. Djurovich; Mark E. Thompson<sup>\*</sup>

Department of Chemistry, University of Southern California, Los Angeles, CA, USA

\*These authors contributed equally to this work.

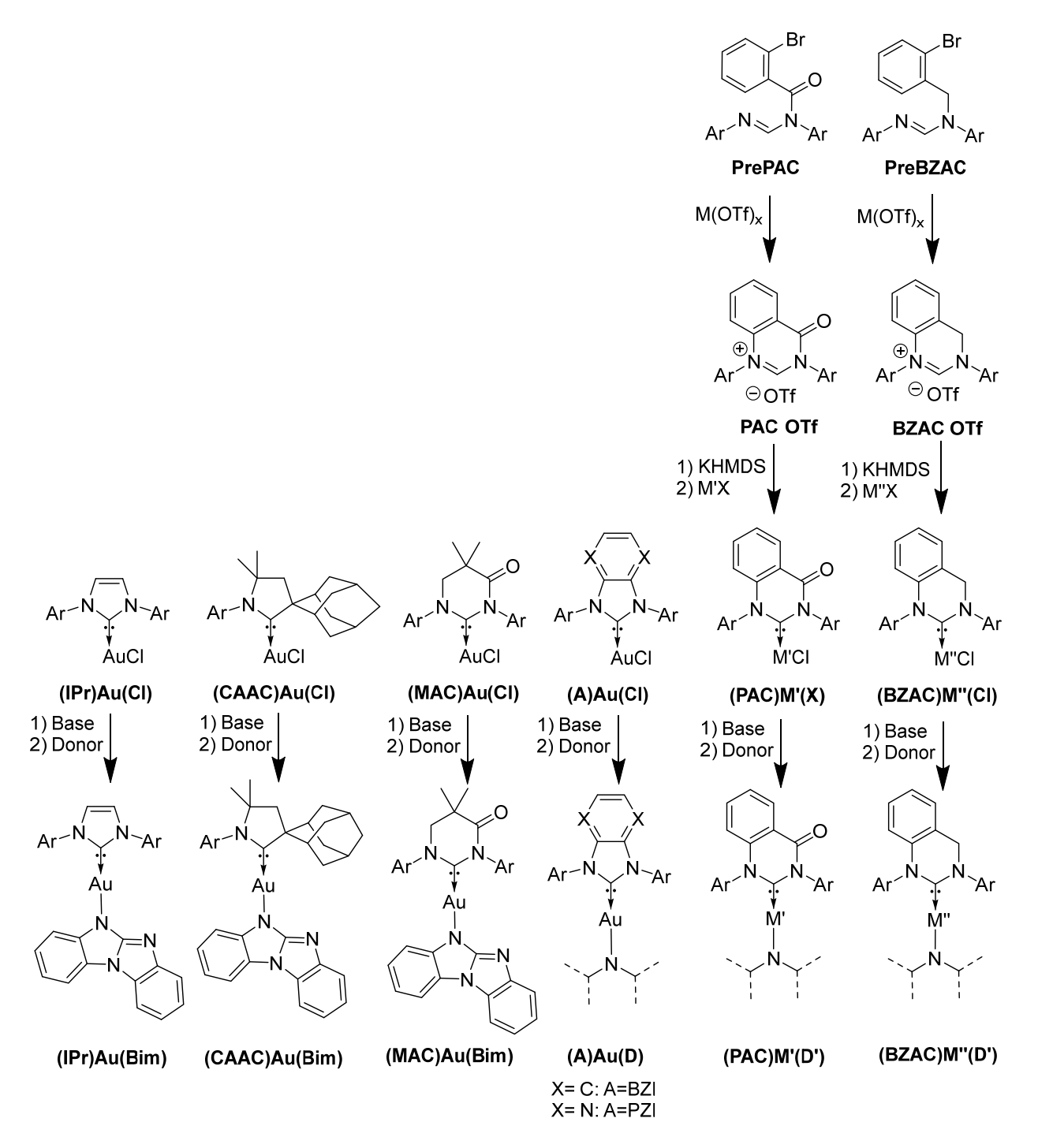
Corresponding author: met@usc.edu

# **Contents**

Synthetic details and characterization	3
Figure S1. Synthetic chart for all materials prepared in this study	3
Structural data	28
Table S1: Selected bond lengths and angles for the(carbene)M(amide) complexes	28
Table S2: Crystallographic parameters for BZAC-Au-Cz, PAC-Cu-BCz, BZAC-Au-bim a CAAC-Au-bim.	
Table S3: Crystallographic parameters for MAC-Au-bim, PAC-Au-bim and BZI-Au-Mbir	n. 30
Figure S2(a): Thermal ellipsoid drawings of BZAC-Au-Cz, PAC-Cu-BCz-, BZAC-Au-bir and CAAC-Au-bim.	
Figure S2 (b): Thermal ellipsoid drawings of MAC-Au-bim, PAC-Au-bim and BZI-Au-M	
Electrochemistry	33
Figure S3: CV and DPV traces of cMa complexes collected in DMF with 0.1 TBAPF <sub>6</sub> as a electrolyte	
Figure S3 (continued): CV and DPV traces of cMa complexes collected in DMF with 0.1 PF6 as an electrolyte.	
Table S4: Electrochemical data.	37
Molecular modeling	38
General Methodology	38
Figure S4. The S <sub>0</sub> →S <sub>1</sub> transition of	38
Figure S5. The S <sub>0</sub> →S <sub>1</sub> transition of	39
Figure S6. The NTO (left) and center of charge representation (right) for the hole and electromagnetistics of (BZAC)Au(Cz)	

Table S5: Hole/electron separation distances for (carbene)Au(amide) complexes	42
Figure S7: HOMO/LUMO images for all cMa complexes studied here	43
Table S5: Compositions of the S1 and T1 states for the cMa complexes	49
Table S6: Dipole moments of the ground, S1 and T1 states.	50
Photophysical data	51
Figure S8: Emission solvatochromism plots of cMa complexes.	51
Figure S9: Absorption and emission spectra for (BZI)Au(amide), amide = bim, Mbim and Obim.	
Figure S10: Absorption and emission spectra for (PZI)Au(Cz),	52
Figure S11: Absorption spectra	53
Figure S12: Excitation, emission and gated emission (phosphorescence) spectra of BimH, MeBimH and OBimH in 2-MeTHF	
Figure S13. Absorption spectra for (carbene)Au(Cz) and (carbene)Au(BCz) in toluene	55
Temperature dependent photophysics and Boltzmann fitting	56
Figure S14: Temperature dependent lifetime for (PAC)Cu(BCz) in PS.	58
Figure S15: Temperature dependent lifetime for (PAC)Ag(BCz) in PS.	59
Figure S16: Temperature dependent lifetime for (PAC)Au(BCz) in PS. Boltzmann fit (top and Arrhenius plot (bottom)	/
Figure S17: Temperature dependent lifetime for (BZAC)Au(Cz) in PS	61
Figure S18: Temperature dependent lifetime for (MAC)Au(Cz) in PS.	62
Figure S19: Temperature dependent lifetime for (PAC)Au(Bim) in PS.	63
Figure S20: Temperature dependent lifetime for (MAC)Au(Bim) in PS.	64
Figure S21: Temperature dependent lifetime for (CAAC)Au(Bim) in PS.	65
Figure S22: Temperature dependent lifetime for (BZAC)Au(Bim) in PS.	66
Figure S23: Temperature dependent lifetime for (BZAC)Cu(Bim) in PS	67
Figure S25: Temperature dependent lifetime for (BZI)Au(MBim) in PS.	69
Figure S26: Temperature dependent lifetime for (BZI)Au(OBim) in PS	70
Figure S27: Temperature dependent lifetime for (PZI)Au(Cz) in PS	71
Figure S28: Temperature dependent lifetime for (PZI)Au(Bim) in PS.	72
<sup>1</sup> H, <sup>13</sup> C NMR and MALDI experimental	73
<sup>1</sup> H, <sup>13</sup> C NMR and MALDI spectra or each cMa compound	74
LiteratureError! Bookmark not det	fined.

#### Synthetic details and characterization



<u>Figure S1.</u> Synthetic chart for all materials prepared in this study. Metal triflates were used to perform ring closures of PrePAC and PreBZAC where M = Cu(II), Ag(I), and  $Na^+$ . (PAC)M'(X) was achieved for M' = Cu(I), Ag(I), and Au(I) where  $X = Cl^-$  or  $BF_4$ . BZAC M''(Cl) was achieved for M'' = Cu(I) and Au(I). (BZI)Au(D) was prepared for D = Bim, MBim, and Obim. (PAC)M'(D') and (BZAC)M''(D') were isolated where D' = Cz, BCz, and Bim. Ar = 3,6 – diisopropylphenyl.

All chemicals, if not otherwise stated were used as received from chemical supplier. All inert reactions were done in dry nitrogen atmosphere. Flasks, cannula, stir bars and stoppers were dried prior usage at 140 °C.

#### **PAC-OTf:**

1,3-bis(2,6-diisopropylphenyl)- $1\lambda^4$ -quinazolin-4(3H)-one, trifluoromethanesulfonate salt (PAC-**OTf)** was synthesized based on a modification of a literature procedure. A 250 mL Schlenk flask with a stir bar was charged with 8.5 g (16.9 mmol) (E)-2-bromo-N-(2,6-diisopropylphenyl)-N-(((2,6-diisopropylphenyl)imino)methyl)benzamide (PrePAC), 4.36 g (25.34 mmol) NaOTf, and 10.8 g (29.73 mmol) Cu(OTf)<sub>2</sub> was connected to a reflux condenser and topped with a glass stopper. A vacuum of ~300 mTorr was pulled on the solids followed by backfilling with nitrogen for a total of three cycles. The glass stopper was replaced with a rubber septum against positive N2 pressure, and 100 mL of dry DMSO was canula transferred into the reaction vessel yielding a blue suspension. The reaction mixture was heated to 160 °C with an oil bath for 12 h (The suspension fully dissolved after the temperature passed 100 °C). The mixture became dark purple overnight. The mixture was raised out of the oil bath and 100 mL deionized water was added after the mixture reached room temperature. Products were extracted from the crude mixture with dichloromethane three times. The dichloromethane phases were combined and washed with 200 mL of brine a total of five times. The dichloromethane phase was further dried by mixing MgSO<sub>4</sub> and performing vacuum filtration to re-collect the dichloromethane filtrate. The solution was concentrated on the rotovap and the product was precipitated by addition of excess hexane. The product was vacuum filtered and further washed with hexane to afford PAC-OTf as a light blue powder (2.55 g, 30% yield); the light blue color likely comes from trace inorganic impurities the NMR matched the literature spectrum.

<sup>1</sup>H NMR (400 MHz, acetone-d6): 10.98, (s, 1H); 8.63, (ddd, 1H); 8.24 (ddd, 1H); 8.10 (ddd, 1H); 7.81 (m, 1H); 7.65 (m, 4H); 7.52 (m, 3H); 7.38 (ddd, 1H); 3.03 (sept, 2H); 2.92 (sept, 2H); 1.29 (dd, 12H); 1.20 (d, 6H); 1.14 (d, 6H).

#### **BZAC-OTf:**

1,3-bis(2,6-diisopropylphenyl)-3,4-dihydroquinazolin-1-ium trifluoromethanesulfonate (BZAC-OTf) was synthesized based on a modification of a literature procedure. A 250 mL Schlenk flask with a stir bar was charged with 15g (28.11 mmol) (E)-N-(2-bromobenzyl)-N,N'-bis(2,6-diisopropylphenyl)formimidamide (PreBZAC), 8.46 g NaOTf (49.19 mmol), 20.33 g Cu(OTf)<sub>2</sub> (56.22 mmol), and 7.22 g AgOTf (28.11 mmol) was connected to a reflux condenser and topped with a glass stopper. A vacuum of ~300 mTorr was pulled on the solids followed by backfilling with nitrogen for a total of three cycles. The glass stopper was replaced with a rubber septum against positive N<sub>2</sub> pressure, and 100 mL of dry DMSO was canula transferred into the reaction vessel yielding a blue suspension. The reaction mixture was heated to 160 °C with an oil bath for 12 h (The suspension fully dissolved after the temperature passed 100 °C). The mixture was cooled to room temperature and 100 mL DI water was added. The product was extracted from the crude mixture with dichloromethane three times. The dichloromethane phases were combined and washed with 200 mL of brine a total of five times. The dichloromethane phase was further dried

by mixing MgSO<sub>4</sub> and performing vacuum filtration to re-collect the dichloromethane filtrate. The solution was concentrated on the rotovap and the product was precipitated by addition of excess hexane. The product was vacuum filtered and further washed with hexane to afford a peach colored **BZAC-OTf** powder (5.93 g, 35% yield). The NMR matched the literature spectrum.

<sup>1</sup>H NMR (400 MHz, acetone-d6): 9.10 (s, 1H); 7.69 (m, 1H); 7.61 (dd, 1H); 7.54 (m, 2H); 7.50 (m, 3H); 7.45 (m, 2H); 6.60 (m, 1); 5.48 (s, 2H); 3.46 (sept, 2H); 3.17 (sept, 2H); 1.39 (d, 6H); 1.30 (dd, 12H); 1.15 (d, 6H).

#### **PZI-HCl:**

The first step was synthesized according to the publication of Chi-Ming Che.<sup>2</sup>

The second step was done similar to Chi-Ming Che's PZIPr-BF<sub>4</sub>,<sup>2</sup> but varied in the following way to yield the Cl-salt:

Pyrazine-di(2,6-diisopropylaniline) (1.29 g, 3.0 mmol, 1.0 eq) dissolved in 300 ml Triethylorthoformate and acetic acid (0.17 ml, 3 mmol, 1.0 eq). Triethylorthoformate and ethanol was slowly, over the course of 4-5 h, nearly fully distilled off at 150 °C. Reaction was cooled to room temperature, trimethylsilylchloride (43 mL, 340 mmol, 113 eq) and 50 mL of fresh triethylorthoformate was added and the reaction mixture was heated to 70 °C overnight. All solvents were removed until a solid crude was left behind, which was first washed with diethyl ether followed with ispropyl alcohol, yielding the pure off-white product in 75% yield.

<sup>1</sup>H NMR (400 MHz, CD<sub>3</sub>CN) δ 10.52 (s, 1H), 8.97 (s, 3H), 7.78 (d, J = 7.8 Hz, 2H), 7.59 (d, J = 7.9 Hz, 4H), 2.40 (sept, J = 6.8 Hz, 4H), 1.19 (dd, J = 20.5, 6.8 Hz, 24H).

#### 1H-Bim (5H-benzo[4,5]imidazo[1,2]imidazole)

This compound was synthesized based on modified literature procedure.<sup>3</sup> The following synthesis was carried out under Schlenk conditions in a 500 mL 3-neck flask with additional funnel. 2-Chloro-benzimidazole (50.0 g, 328 mmol, 1.0 eq) was charged in the flask and the system was pump-purged; N-methylpyrrolidine (180 mL) was added via cannula transfer and bubble degassed for 20 min. Under vigorously stirring, methanesulfonic acid (31.5 g, 21.3 mL, 328 mmol, 1.0 eq) was added dropwise using an additional funnel. After 1 h stirring at ambient temperature, 2-bromoaniline (56.4 g, 328 mmol, 1.0 eq) was added and heated to react at 100 °C overnight. (Tip: preheat everything which gets in contact with bromoaniline, like the beaker and funnel, which facilitates the transfer). After cooling down, the reaction was quenched with 100 mL water, and afterwards neutralized using 30 wt% aqueous KOH solution. Precipitate was filtered and dried at 90 °C in vacuum overnight. N-(2-bromophenyl)-1H-benzo[d]imidazol-2-amine was obtained NMR pure in 80% yield (76.5 g, 265 mmol). [6.93 (td, 1H); 7.01 (dd, 2H); 7.33 (dd, 2H); 7.39 (td, 1H); 7.62 (dd, 1H); 8.62 (d, 1H); 11.25 (s, 2H)]

#### 1H-Bim (5H-benzo[d]benzo[4,5]imidazo[1,2-a]imidazole)

$$\begin{array}{c|c} CuBr_2 \\ Cs_2CO_3 \\ \hline \\ N \\ H \end{array}$$

This compound was synthesized based on modified literature procedure.<sup>3</sup> N-(2-bromophenyl)-1H-benzo[d]imidazol-2-amine (76.5 g, 265 mmol, 1.0 eq), Cs<sub>2</sub>CO<sub>3</sub> (130 g, 398 mmol, 1.5 eq) and CuBr<sub>2</sub> (1.19 g, 5.3 mmol, 0.02 eq) was added to a Schlenk flask and pump purged. 275 mL dry, bubble degassed DMF was added via a cannula. After reaction at 130 °C overnight, rection was cooled down and quenched with water. Vacuum filtration yielded the crude product, which was recrystallized in hot acetic acid. The acetic acid was removed by distillation and the remaining solid was NMR pure bim and was used directly in further reactions. Alternatively, the crude bim can be sublimed in a high-vacuum sublimator starting at 230 °C with steady increase to 290 °C over 4-5 h to yield a high purity snow-white product in 90% yield (49.5 g, 265.5 mmol).

<sup>1</sup>H NMR (400 MHz, DMSO) δ 11.99 (s, 1H), 8.06 (dd, J = 7.8, 0.8 Hz, 2H), 7.46 (d, J = 7.9 Hz, 2H), 7.23 (dtd, J = 24.3, 7.5, 1.2 Hz, 4H).

#### 1H-MeBim

The following synthesis was carried out under Schlenk conditions in a 3-neck flask with additional funnel. 2-Chloro-benzimidazole (1.52 g, 10 mmol, 1.0 eq) and 2-bromo-4-methylaniline (1.86 g, 11 mmol, 1.1 eq)) was charged in the flask and the system was pump-purged; NMP was added via cannula transfer and bubble degassed for 20 min. Under vigorously stirring, methanesulfonic acid (1.06 g, 11 mmol, 1.1 eq) was added dropwise with the additional funnel and was reacted at 100°C for 48 h. After cooling down, the reaction was quenched with deionized water, and afterwards neutralized using 30 wt.% NaOH solution. Precipitate was filtered and purified on a silica column with ethylacetate and hexanes. Removing the solvent yielded N-(2-bromo-4-methylphenyl)-1H-benzo[d]imidazol-2-amine NMR pure in 46% yield (1.40 g).

N-(2-bromo-4-methylphenyl)-1H-benzo[d]imidazol-2-amine (previous step) (1.4 g, 4.6 mmol, 1.0 eq), Cs<sub>2</sub>CO<sub>3</sub> (2.25 g, 6.9 mmol, 1.5 eq) and CuBr<sub>2</sub> (51 mg, 0.23 mmol, 0.05 eq) was added to a Schlenk flask and pump purged. 30 mL dry, bubble degassed DMF was added via a cannula. After heating at 130 °C overnight, the reaction was cooled down and quenched with water. Filter off precipitate. Crude was dissolved in dry THF and loaded on a silica column and was eluted with a gradient (0-20%) dichloromethane with 5% MeOH. Hexanes were used as unipolar solvent. Remove solvent and wash with acetone yielded the snow-white product in 72% yield (742 mg).

<sup>1</sup>H NMR (400 MHz, DMSO) δ 11.86 (s, 1H), 8.04 (d, J = 7.7 Hz, 1H), 7.90 (s, 1H), 7.45 (d, J = 7.8 Hz, 1H), 7.32 (d, J = 8.1 Hz, 1H), 7.24 (tt, J = 7.8, 1.3 Hz, 1H), 7.18 (tt, J = 7.6, 1.3 Hz, 1H), 7.07 (d, J = 8.1 Hz, 1H), 2.46 (s, 3H).

#### 1H-MeO-Bim

The following synthesis was carried out under Schlenk conditions in a 50 mL 3-neck flask with additional funnel. 2-Chloro-benzimidazole (2.29 g, 15 mmol, 1.0 eq) and 2-bromo-4-methoxyaniline was charged in the flask and the system was pump-purged; N-methylpyrrolidine was added via cannula transfer and bubble degassed for 20 min. Under vigorously stirring, methanesulfonic acid (1.59 g, 1.1 mL, 16.5 mmol, 1.1 eq) was added dropwise with the additional funnel and was reacted at 100 °C for 24 h. After cooling down, the reaction was quenched with deionized water, and afterwards neutralized using concentrated KHCO<sub>3</sub> solution. Precipitate was filtered and dried at 90 °C under vacuum overnight. N-(2-bromo-4-methoxyphenyl)-1H-benzo[d]imidazol-2-amine was obtained NMR pure in 27% yield (1.30g, 4.1 mmol).

$$\begin{array}{c|c} CuBr_2 \\ Cs_2CO_3 \\ \hline \\ DMF \\ 130^{\circ}C \\ overnight \\ \end{array}$$

N-(2-bromo-4-methoxyphenyl)-1H-benzo[d]imidazol-2-amine (previous step) (820 mg, 2.58 mmol, 1.0 eq), Cs<sub>2</sub>CO<sub>3</sub> (1.26 g, 3.86 mmol, 1.5 eq) and CuBr<sub>2</sub> (12 mg, 0.052 mmol, 0.02 eq) was added to a Schlenk flask and pump purged. 15 mL dry, bubble degassed DMF was added via a cannula. After reaction at 130 °C overnight, rection was cooled down and quenched with water. Vacuum filtration yielded the snow-white product in 55% yield (340 mg, 2.58 mmol).

<sup>1</sup>H NMR (400 MHz, DMSO) δ 11.78 (s, 1H), 8.14 (d, J = 7.8 Hz, 1H), 7.69 (d, J = 2.5 Hz, 1H), 7.43 (d, J = 7.9 Hz, 1H), 7.35 (d, J = 8.7 Hz, 1H), 7.25 (td, J = 7.7, 1.3 Hz, 1H), 7.18 (td, J = 7.6, 1.2 Hz, 1H), 6.86 (dd, J = 8.7, 2.5 Hz, 1H), 3.85 (s, 3H).

## $Cu_{Cl}^{PAC}$ :

A 250 mL Schlenk flask with a stir bar was charged with 1.1g (1.78 mmol) of PAC-OTf and capped with a glass stopper. A vacuum of ~300 mTorr was pulled on the solid followed by backfilling with nitrogen for a total of three cycles. The glass stopper was replaced by a rubber septum and 100 mL of dry THF from our solvent purification system was directly added through the septum. The PAC-OTf dissolved within 5 minutes. Next, 4.6 mL (2.32 mmol) of 0.5M potassium hexamethylsilylamide in THF was added through the septum and the reaction was stirred for an additional 5 minutes. The rubber septum was removed against positive  $N_2$  pressure and 240 mg of CuCl was added (2.43 mmol). The dark green reaction mixture was covered with aluminum foil and stirred for 12 hrs. Removing the aluminum foil revealed a brown suspension which was filtered through Celite. The filtrate was concentrated on the rotovap and the product was precipitated out by addition of excess hexane to yield 1,3-bis(2,6-diisopropylphenyl)-4-oxo-3,4-dihydroquinazolin-1-ium-2-ide copper(I) chloride  $Cu_{Cl}^{PAC}$  as an off-white solid (390 mg, 39% yield). <sup>1</sup>H NMR (400 MHz, acetone-d6): 8.43 (ddd, 1H); 7.98 (ddd, 1H); 7.79 (ddd, 1H); 7.67 (m, 1H); 7.52 (m, 3H); 7.39 (m, 2H); 6.95 (ddd, 1); 2.91 (sept, 2H); 2.80 (sept, 2H); 1.33 (dd, 12H); 1.18 (d, 6H); 1.09 (d, 6H).

## $Ag_{BF_4}^{PAC}$ :

The synthesis and workup was the same as (PAC)Cu(Cl) except 318 mg (0.52 mmol) PAC-OTf was used, 129 mg (0.67 mmol) AgBF<sub>4</sub> and 1.3 mL (0.67 mmol) 0.5 M potassium hexamethylsilylamide in THF was used to yield 1,3-bis(2,6-diisopropylphenyl)-4-oxo-3,4-dihydroquinazolin-1-ium-2-ide silver(I) tetrafluoroborate  $Ag_{BF_4}^{PAC}$  (100 mg, 29% yield) (400 MHz, acetone-d6): 8.45(ddd, 1H); 8.02 (ddd, 1H); 7.83 (t, 1H); 7.68 (t, 0.95); 7.54 (m, 3H); 7.42 (m, 2H); 7.00 (m, 1H); 2.93 (sept, 2H); 2.78 (sept, 2H); 1.32 (d, 12H); 1.18 (d, 6H); 1.09 (d, 6H).

## $Au_{Cl}^{PAC}$ :

A 100 mL Schlenk flask with a stir bar was charged with 500 mg (0.81 mmol) of PAC-OTf and capped with a glass stopper. A vacuum of ~300 mTorr was pulled on the solid followed by backfilling with nitrogen for a total of three cycles. The glass stopper was replaced by a rubber septum and 50 mL of dry THF from our solvent purification system was directly added through the septum. The PAC-OTf dissolved within 5 minutes. Next, 2.1 mL (1.05 mmol) of 0.5 M potassium hexamethylsilylamide in THF was added through the septum and the reaction was stirred for an additional 5 minutes. The rubber septum was removed against positive N<sub>2</sub> pressure and 307 mg of AuS(CH<sub>3</sub>)<sub>2</sub>Cl was added (1.05 mmol). The dark red reaction mixture was covered with aluminum foil and stirred for 12 hrs. Removing the aluminum foil revealed a gold solution which was filtered through celite and dried using the Schlenk line vacuum yielding a light brown solid. The solid was washed with ethanol and vacuum filtered to yield 1,3-bis(2,6-diisopropylphenyl)-4-oxo-3,4-dihydroquinazolin-1-ium-2-ide gold(I) chloride  $Au_{Cl}^{PAC}$  as a white powder (440 mg, 78 % yield). (400 MHz, acetone-d6): 8.43 (ddt, 1H); 7.99 (dddd, 1H); 7.81 (m, 1H); 7.61 (m, 1H); 7.52 (m, 3H); 7.39 (m, 2H); 6.98 (ddd, 1H); 2.98 (sept, 2H); 2.78 (sept, 2H); 1.38 (dd, 12H); 1.17 (dd, 6H); 1.07 (d, 6H).

 $Cu_{Cl}^{BZAC}$ A 200mL Schlenk flask with a stir bar was charged with 1.0 g (1.66 mmol) of BZAC-OTf and capped with a glass stopper. A vacuum of ~300 mTorr was pulled on the solid followed by backfilling with nitrogen for a total of three cycles. The glass stopper was replaced by a rubber septum and 100 mL of dry THF from our solvent purification system was directly added through the septum. The BZAC-OTf dissolved within 5 minutes yielding a transparent solution. Next, 3.07 mL (2.14 mmol) of 0.7 M potassium hexamethylsilylamide in THF was added through the septum and the reaction was stirred for an additional 5 minutes. The solution immediately became dark green as the potassium hexamethylsilylamide was added but quickly returned to transparent. The rubber septum was removed against positive N<sub>2</sub> pressure and 223 mg of CuCl was added (2.24 mmol). The reaction mixture was covered with aluminum foil and stirred for 12 h. Removing the aluminum foil revealed an orange solution which was filtered through Celite. The filtrate was concentrated on the rotovap yielding a dark orange solid. The crude solid was washed with ethanol to afford 1,3-bis(2,6-diisopropylphenyl)-1,4-dihydroquinazolin-3-ium-2-ide copper(I) chloride  $Cu_{Cl}^{BZAC}$  as a white solid (694 mg, 76% yield). (400 MHz, acetone-d6: 7.53 (dd, 1H); 7.39 (m, 5H); 7.25 (m, 3H); 6.33 (m, 1H); 4.96 (s, 2H); 3.37 (sept, 2H); 3.17 (sept, 2H); 1.36 (m, 18H); 1.12 (dd, 6H)

## $Au_{Cl}^{BZAC}$ :

The synthesis and workup was the same as (BZAC)Cu(Cl) except with 390 mg (0.65 mmol) of BZAC-OTf, 1.0 mL (0.70 mmol) of 0.7 M potassium hexamethylsilylamide in THF, and 189 mg (0.73 mmol) of AuS(CH<sub>3</sub>)<sub>2</sub>Cl. The reaction mixture was covered with aluminum foil and stirred for 12 h. Removing the aluminum foil revealed a brown suspension which was filtered through celite to yield a clear, green filtrate. The filtrate was concentrated on the rotovap yielding a dark green solid. The crude solid was washed with ethanol to afford 1,3-bis(2,6-diisopropylphenyl)-1,4-dihydroquinazolin-3-ium-2-ide gold(I) chloride  $Au_{Cl}^{BZAC}$  as a white solid (285 mg, 60% yield). (400 MHz, acetone-d6: 7.54 (m, 1H); 7.46 (dd, 1H); 7.40 (m, 2H); 7.36 (dd, 2H); 7.27 (m, 3H); 6.35 (m, 1H); 5.00 (d, 2H); 3.35 (sept, 2H); 3.13 (sept, 2H); 1.42 (dd, 12H); 1.35 (d, 6H); 1.10 (dd, 6H).

## $Au_{Cl}^{PZI}$ :

$$\begin{array}{c|c} iPr & & & & iPr \\ \hline N & N-CI & & & Au(Me_2S)CI \\ \hline N & N & & & & \\ \hline N & N & & & \\ iPr & & iPr & & iPr \\ \hline \end{array}$$

PZI-HCl (400 mg, 0.838 mmol, 1.0 eq) were pump purged and dissolved in bubble degassed THF. 0.7 M potassium hexamethylsilylamide in THF (1.26 mL, 0.880 mmol, 1.05 eq) was added and solution steered for 1 hour. Au(Me2S)Cl (272 mg, 0.922 mmol, 1.10 eq) was added and solution was stirred overnight.

The reaction mixture was filtered through Celite to yield a dark red filtrate, the solvents were removed, and the residue was dissolved in minimal CH<sub>2</sub>Cl<sub>2</sub> and precipitated with hexanes to yield the light brown  $Au_{Cl}^{PZI}$  product in 34% yield (190 mg, 0.282 mmol)

1H NMR (400 MHz, acetone-d6: 7.54 (m, 1H); 7.46 (dd, 1H); 7.40 (m, 2H); 7.36 (dd, 2H); 7.27 (m, 3H); 6.35 (m, 1H); 5.00 (d, 2H); 3.35 (sept, 2H); 3.13 (sept, 2H); 1.42 (dd, 12H); 1.35 (d, 6H); 1.10 (dd, 6H).

## $Au_{Cz}^{PAC}$ :

A 100 mL Schlenk flask with a stir bar was charged with 57 mg (0.34 mmol) 1H-carbazole and capped with a glass stopper. A vacuum of ~300 mTorr was pulled on the solid followed by backfilling with nitrogen for a total of three cycles. The glass stopper was replaced by a rubber septum and 38 mL of dry THF from our solvent purification system was directly added through the septum. The carbazole dissolved after 5 minutes of stirring which gave a transparent solution, and 0.19 mL (0.37 mmol) of 2 M sodium *tert*-butoxide was added through the septum. The reaction was stirred for 30 minutes. The mixture went from transparent to slightly green over the duration of stirring. The rubber septum was removed against positive  $N_2$  pressure and 238 mg of  $Au_{Cl}^{PAC}$  was added (0.34 mmol). The solution was immediately yellow emissive under UV lamp upon addition of  $Au_{Cl}^{PAC}$ . The reaction stirred for an additional 12 h yielding a dark green suspension. The solution was filtered through celite and dried using the rotovap. The resultant gellike solid was redissolved in 80mL of a 50/50 dichloromethane/hexane mixture and re-dried on the rotovap three times which changed the texture of the solid from gel-like to powdery. The dried solid was washed copiously with methanol and collected via vacuum filtration to yield  $Au_{Cz}^{PAC}$  as a yellow powder (129 mg, 46% yield).

<sup>1</sup>H NMR (400 MHz, acetone-d6) δ 8.47 (ddd, J = 7.9, 1.6, 0.5 Hz, 1H), 8.02 (ddd, J = 8.6, 7.3, 1.6 Hz, 1H), 7.96 (t, J = 7.8 Hz, 1H), 7.87 – 7.77 (m, 4H), 7.72 (d, J = 7.9 Hz, 2H), 7.59 (d, J = 7.8 Hz, 2H), 7.05 (dt, J = 8.5, 0.8 Hz, 1H), 6.96 (ddd, J = 8.2, 7.0, 1.3 Hz, 2H), 6.78 (ddd, J = 7.8, 7.0, 1.0 Hz, 2H), 6.13 (dt, J = 8.1, 0.9 Hz, 2H), 3.04 (sept, J = 6.9 Hz, 2H), 2.94 (sept, J = 7.0 Hz, 2H), 1.33 (dd, J = 13.3, 6.8 Hz, 12H), 1.22 (d, J = 6.8 Hz, 6H), 1.12 (d, J = 6.8 Hz, 6H).

<sup>13</sup>C{<sup>1</sup>H} NMR (100 MHz, acetone-d6) δ 206.3, 206.3, 206.3, 201.4, 160.0, 150.6, 147.5, 147.2, 142.9, 137.9, 137.8, 132.5, 131.5, 129.9, 129.7, 127.0, 125.8, 125.0, 124.2, 120.1, 120.0, 119.8, 117.0, 115.3, 30.6, 30.4, 30.2, 30.2, 30.0, 30.0, 29.8, 29.6, 29.5, 24.9, 24.8, 24.7, 24.4.

CHN: C: 62.76%; H: 5.75%; N: 4.87%; calculated: C: 63.69%; H: 5.59%; N: 5.06%

## $Au_{Cz}^{BZAC}$ :

The same synthesis and workup as  $Au_{Cz}^{PAC}$  was used except with 61 mg (0.36 mmol) 1H-carbazole, 0.2 mL (0.4 mmol) of 2 M sodium *tert*-butoxide, and 250 mg (0.36 mmol) of (BZAC)Au(Cl). The dark grey suspension was immediately bright blue emissive under UV lamp upon addition of (BZAC)Au(Cl). The final  $Au_{Cz}^{BZAC}$  was an off-white powder (157 mg, 53% yield).

<sup>1</sup>H NMR (400 MHz, acetone-d6) δ 7.87 – 7.70 (m, 4H), 7.61 (d, J = 7.8 Hz, 2H), 7.56 (d, J = 7.7 Hz, 2H), 7.38 – 7.25 (m, 3H), 6.91 (ddd, J = 8.2, 7.0, 1.3 Hz, 2H), 6.76 (ddd, J = 7.9, 7.0, 1.0 Hz, 2H), 6.49 – 6.41 (m, 1H), 6.11 (dt, J = 8.2, 0.9 Hz, 2H), 5.12 (d, J = 0.9 Hz, 2H), 5.12 (s, 2H), 3.50 (sept, J = 6.9 Hz, 2H), 3.29 (sept, J = 6.9 Hz, 2H), 1.39 (dd, J = 12.3, 6.9 Hz, 18H), 1.17 (d, J = 6.8 Hz, 6H).

<sup>13</sup>C{<sup>1</sup>H} NMR (100 MHz, acetone-d6) δ 206.3, 206.3, 206.3, 206.2, 196.8, 150.7, 148.4, 147.0, 142.0, 138.4, 135.9, 131.4, 130.9, 130.1, 128.3, 127.5, 126.5, 124.8, 124.0, 119.7, 119.2, 117.5, 116.5, 115.2, 52.5, 30.6, 30.4, 30.2, 30.0, 29.8, 29.8, 29.7, 29.5, 25.3, 25.2, 25.1, 24.7.

## $Cu_{BCz}^{PAC}$ :

A 100 mL Schlenk flask with a stir bar was charged with 182 mg (0.65 mmol) 3,6-di-tert-butyl-9H-carbazole and 62 mg (0.65mmol) sodium *tert*-butoxide and capped with a glass stopper. A vacuum of ~300 mTorr was pulled on the solid followed by backfilling with nitrogen for a total of three cycles. The glass stopper was replaced by a rubber septum and 38 mL of dry THF from our solvent purification system was directly added through the septum. The carbazole dissolved after 5 minutes of stirring which gave a transparent solution. The reaction was stirred for 30 minutes. The rubber septum was removed against positive  $N_2$  pressure and 350 mg (0.62 mmol) of ( $Cu_{cl}^{PAC}$ was added. The solution was immediately red in color, and red emissive under UV lamp upon addition of  $Cu_{Cl}^{PAC}$ . The reaction stirred for an additional 12 h yielding a dark brown suspension. The solution was filtered through Celite yielding a clear red solution. The resultant gel-like solid was redissolved in 80 mL of a 50/50 dichloromethane/hexane mixture and re-dried on the rotovap three times which changed the texture of the solid from a gel to a yellow-emissive powder. The dried solid was dissolved in ethanol and the filtrate was collected via vacuum filtration. Water was added to the ethanol solution which caused the precipitation of a yellow powder. The yellow powder was vacuum filtered and washed with methanol which afforded  $Cu_{BCz}^{PAC}$  as a yellow powder (40 mg, 8% yield). The relatively low yield is likely due to the unconventional workup; the cMa complexes are not typically isolated by precipitation from ethanol using water. The product is also quite soluble in methanol which was used as a rinse solvent.

<sup>1</sup>H NMR (400 MHz, acetone-d6) δ 8.47 (dd, J = 8.0, 1.4 Hz, 1H), 8.01 (td, J = 7.3, 1.9 Hz, 2H), 7.89 – 7.78 (m, 4H), 7.76 (d, J = 7.9 Hz, 2H), 7.62 (d, J = 7.8 Hz, 2H), 6.95 (td, J = 8.8, 8.4, 1.9 Hz, 3H), 5.64 (dd, J = 8.5, 0.6 Hz, 2H), 3.08 (sept, J = 6.8 Hz, 2H), 2.99 (sept, J = 6.8 Hz, 2H), 1.34 (s, 18H), 1.30 – 1.23 (m, 18H), 1.16 (d, J = 6.8 Hz, 6H).

<sup>13</sup>C{<sup>1</sup>H} NMR (100 MHz, acetone-d6) δ 206.3, 206.3, 206.3, 206.3, 206.3, 206.2, 159.7, 149.7, 147.5, 147.2, 142.9, 138.3, 137.5, 137.5, 132.7, 131.6, 129.7, 129.6, 127.2, 126.1, 125.1, 121.4, 120.5, 119.7, 115.5, 115.3, 35.1, 32.9, 30.7, 30.6, 30.4, 30.2, 30.0, 29.8, 29.6, 29.5, 25.4, 24.9, 24.5, 24.3.

## $Ag_{BCz}^{PAC}$ :

A 100 mL Schlenk flask with a stir bar was charged with 145 mg (0.52 mmol) 3,6-di-*tert*-butyl-9H-carbazole and 50 mg (0.52 mmol) sodium *tert*-butoxide and capped with a glass stopper. A vacuum of ~300 mTorr was pulled on the solid followed by backfilling with nitrogen for a total of three cycles. The glass stopper was replaced by a rubber septum and 40 mL of dry THF from our solvent purification system was directly added through the septum. The solids dissolved after 30 minutes of stirring which gave a transparent solution. The rubber septum was removed against positive N<sub>2</sub> pressure and 326 mg (0.49 mmol) of  $Ag_{BF_4}^{PAC}$  was added. The solution was immediately red in color, upon addition of  $Ag_{BF_4}^{PAC}$ . The reaction stirred for an additional 12 h yielding a red suspension. The crude solution was immediately dried on the rotovap. The resultant gel-like solid was redissolved in 80 mL of a 50/50 dichloromethane/hexane mixture and re-dried on the rotovap three times which changed the texture of the solid from a gel to a yellow-emissive powder. The dried yellow solid was dissolved in ether and filtered through celite to yield a bright red solution. The ether solution was dried on the rotovap and the resulting yellow solid was washed copiously with methanol over a vacuum filtration setup to afford  $Ag_{BCz}^{PAC}$  as a yellow powder (116 mg, 28% yield).

<sup>1</sup>H NMR (400 MHz, acetone-d6) δ 8.51 (dd, J = 7.9, 1.3 Hz, 1H), 8.06 (ddd, J = 8.7, 7.3, 1.6 Hz, 1H), 7.96 (t, J = 7.8 Hz, 1H), 7.91 – 7.78 (m, 3H), 7.74 (d, J = 7.8 Hz, 2H), 7.61 (d, J = 7.8 Hz, 2H), 7.48 – 7.36 (m, 1H), 7.09 (d, J = 8.4 Hz, 1H), 7.05 (dd, J = 8.5, 2.0 Hz, 2H), 6.07 (dd, J = 8.5, 0.6 Hz, 2H), 3.07 (sept, J = 7.2 Hz, 2H), 2.95 (sept, J = 6.7 Hz, 2H), 1.38 – 1.07 (m, 42H).

<sup>13</sup>C{<sup>1</sup>H} NMR (100 MHz, acetone-d6) δ 206.3, 206.2, 150.3, 150.2, 147.2, 146.9, 137.8, 137.6, 132.7, 131.6, 130.1, 129.8, 127.1, 126.1, 124.9, 121.5, 120.6, 120.3, 115.6, 115.1, 35.1, 32.9, 30.8, 30.6, 30.4, 30.2, 30.0, 29.8, 29.6, 29.5, 25.3, 24.8, 24.8, 24.6.]

CHN: C: 72.57%; H: 7.48%; N: 4.74%; calculated: C: 73.22%; H: 7.33%; N: 4.93%

## $Au_{BCz}^{PAC}$ :

A 100 mL Schlenk flask with a stir bar was charged with 84 mg (0.30 mmol) 3,6-di-tert-butyl-9H-carbazole and 32 mg (0.33 mmol) sodium *tert*-butoxide and capped with a glass stopper. A vacuum of ~300 mTorr was pulled on the solid followed by backfilling with nitrogen for a total of three cycles. The glass stopper was replaced by a rubber septum and 38 mL of dry THF from our solvent purification system was directly added through the septum. The reaction was stirred for 30 minutes yielding a transparent solution. The rubber septum was removed against positive  $N_2$  pressure and 210 mg (0.30 mmol) of  $Au_{Cl}^{PAC}$  was added. The solution was immediately red in color, upon addition of  $Au_{Cl}^{PAC}$  and was yellow luminescent under the UV lamp. The reaction stirred for an additional 12 h yielding a red suspension. The crude solution was filtered through Celite and concentrated on the rotovap, then precipitated with addition of excess hexane. The resulting yellow solid was washed copiously with methanol over a vacuum filtration setup to afford  $Au_{BCz}^{PAC}$  as a yellow powder (136 mg, 48% yield).

<sup>1</sup>H NMR (400 MHz, acetone-d6) δ 8.48 (ddd, J = 7.9, 1.6, 0.5 Hz, 1H), 8.07 – 7.94 (m, 2H), 7.86 (dt, J = 2.4, 1.2 Hz, 2H), 7.87 – 7.78 (m, 2H), 7.74 (d, J = 7.8 Hz, 2H), 7.60 (d, J = 7.8 Hz, 2H), 7.10 – 7.01 (m, 3H), 6.10 (dd, J = 8.5, 0.7 Hz, 2H), 3.04 (sept, J = 6.8 Hz, 2H), 2.94 (sept, J = 6.9 Hz, 2H), 1.37 – 1.32 (m, 30H), 1.23 (d, J = 6.8 Hz, 6H), 1.14 (d, J = 6.8 Hz, 6H).

 $^{13}C\{^{1}H\}$  NMR (100 MHz, acetone-d6)  $\delta$  206.3, 206.3, 206.3, 206.3, 206.2, 149.2, 147.4, 147.1, 139.2, 132.5, 131.4, 129.6, 126.9, 125.8, 124.9, 121.7, 120.0, 115.7, 114.7, 35.1, 32.8, 30.6, 30.4, 30.2, 30.0, 29.8, 29.6, 29.4, 24.9, 24.8, 24.6, 24.5;

CHN: C: 67.23%; H: 6.67%; N: 4.54%; calculated: C: 66.30%; H: 6.63%; N: 4.46%

## $Cu_{BCz}^{BZAC}$ :

A 100 mL Schlenk flask with a stir bar was charged with 165 mg (0.36 mmol) 3,6-di-tert-butyl-9H-carbazole and 65 mg (0.43 mmol) sodium *tert*-butoxide and capped with a glass stopper. A vacuum of ~300 mTorr was pulled on the solid followed by backfilling with nitrogen for a total of three cycles. The glass stopper was replaced by a rubber septum and 50 mL of dry THF from our solvent purification system was directly added through the septum. The reaction was stirred for 30 minutes yielding a transparent solution. The rubber septum was removed against positive N2 pressure and 375 mg (0.41 mmol) of  $Cu_{cl}^{BZAC}$  was added. The solution immediately became lime green upon addition of  $Cu_{Cl}^{BZAC}$  and was bright green luminescent under the UV lamp. The reaction stirred for an additional 12 h while covered with aluminum foil which yielded a green suspension. The crude solution was immediately dried on the rotovap, then dissolved in diethyl ether and filtered through Celite. The ether phase was dried on the rotovap, then redissolved in 50 mL acetonitrile. Hexane was used to extract the product out of the acetonitrile phase (15 extractions with 50 mL hexane). The hexane phases were combined and dried on the rotovap. The solid was redissolved in 40mL methanol and four additional 20mL hexane extractions were performed, this time keeping the methanol phase and discarding the hexane phases. The methanol phase was dried on the Schlenk line yielding  $Cu_{BCZ}^{BZAC}$  as an off-white powder (26 mg, 6% yield).

<sup>1</sup>H NMR (400 MHz, acetone-d6) δ 7.86 (t, J = 7.8 Hz, 1H), 7.81 – 7.73 (m, 4H), 7.63 (d, J = 7.8 Hz, 2H), 7.58 (d, J = 7.8 Hz, 2H), 7.38 – 7.22 (m, 3H), 6.91 (dd, J = 8.6, 2.1 Hz, 2H), 5.58 (dd, J = 8.6, 0.7 Hz, 2H), 5.06 (s, 2H), 3.54 (sept, J = 6.9 Hz, 2H), 3.33 (sept, J = 6.8 Hz, 2H), 1.42 (d, J = 7.0 Hz, 6H), 1.33 (s, 18H), 1.29 (dd, J = 6.9, 2.0 Hz, 12H), 1.18 (d, J = 6.8 Hz, 6H).

 $^{13}\text{C}\{^{1}\text{H}\}$  NMR (100 MHz, acetone-d6)  $\delta$  206.3, 206.3, 206.3, 206.2, 206.1, 149.3, 148.4, 147.0, 142.0, 138.6, 138.3, 136.0, 131.4, 130.8, 130.1, 128.3, 127.4, 126.5, 124.7, 121.5, 119.2, 117.5, 115.5, 114.6, 52.5, 35.1, 32.9, 30.6, 30.4, 30.2, 30.0, 29.8, 29.7, 29.5, 25.3, 25.2, 25.1, 24.7.

CHN: C: 72.32%; H: 7.76%; N: 4.63%; calculated: C: 72.37%; H: 7.56%; N: 4.78% (CHN-Analysis includes one cocrystalized CH<sub>2</sub>Cl<sub>2</sub> molecule per  $Cu_{BCZ}^{BZAC}$  molecule.)

## $Au_{BCz}^{BZAC}$ :

A 100 mL Schlenk flask with a stir bar was charged with 102 mg (0.36 mmol) 3,6-di-tert-butyl-9H-carbazole and 42 mg (0.43 mmol) sodium tert-butoxide and capped with a glass stopper. A vacuum of ~300 mTorr was pulled on the solid followed by backfilling with nitrogen for a total of three cycles. The glass stopper was replaced by a rubber septum and 50 mL of dry THF from our solvent purification system was directly added through the septum. The reaction was stirred for 30 minutes yielding a transparent solution. The rubber septum was removed against positive N<sub>2</sub> pressure and 285 mg (0.41mmol) of  $Au_{Cl}^{BZAC}$  was added. The solution immediately became lime green upon addition of  $Au_{Cl}^{BZAC}$  and was bright blue luminescent under the UV lamp. The reaction stirred for an additional 12 h while covered with aluminum foil which yielded a green suspension. The crude solution was immediately dried on the rotovap, then dissolved in diethyl ether and filtered through Celite. The ether phase was dried on the rotovap, then redissolved in 50 mL acetonitrile. Hexane was used to extract the product out of the acetonitrile phase (15 extractions with 50 mL hexane). The hexane phases were combined and dried on the rotovap. The solid was redissolved in 40 mL methanol and four additional 20 mL hexane extractions were performed, this time keeping the methanol phase and discarding the hexane phases. The methanol phase was dried on the Schlenk line yielding  $Au_{BCz}^{BZAC}$ : as an off-white powder (82 mg, 24% yield).

<sup>1</sup>H NMR (400 MHz, acetone-d6) δ 7.88 – 7.79 (m, 3H), 7.74 (t, J = 7.8 Hz, 1H), 7.61 (d, J = 7.8 Hz, 2H), 7.56 (d, J = 7.8 Hz, 2H), 7.37 – 7.30 (m, 1H), 7.34 – 7.24 (m, 2H), 7.01 (dd, J = 8.6, 2.1 Hz, 2H), 6.48 – 6.41 (m, 1H), 6.06 (dd, J = 8.5, 0.6 Hz, 2H), 5.13 – 5.08 (m, 2H), 3.50 (sept, J = 6.8 Hz, 2H), 3.28 (sept, J = 6.8 Hz, 2H), 1.45 – 1.36 (m, 18H), 1.33 (s, 18H), 1.17 (d, J = 6.8 Hz, 6H);

<sup>13</sup>C{<sup>1</sup>H} NMR (100 MHz, acetone-d6) δ 205.1, 205.1, 205.1, 205.1, 204.9, 148.2, 147.3, 145.8, 140.9, 137.5, 137.2, 134.8, 130.2, 129.7, 129.0, 127.2, 126.3, 125.3, 123.6, 120.3, 118.1, 116.4, 114.4, 113.5, 51.3, 34.0, 31.7, 29.5, 29.3, 29.1, 28.9, 28.7, 28.5, 28.3, 24.2, 24.0, 24.0, 23.6.

CHN: C: 66.80%; H: 6.94%; N: 4.49%; calculated: C: 67.3%; H: 6.95%; N: 4.53%

## $Au_{Cz}^{PZI}$ :

A 25 mL Schlenk flask with a stir bar with 52 mg (0.311 mmol, 1.1 eq) 1H-carbazole was pump purged and bubble degassed dry THF (10 mL) was added via cannula transfer. 0.155 mL (0.311 mmol, 1.1 eq) 2 M sodium *tert*-butoxide (NaOtBu) solution was added dropwise. After 1h stirring,  $Au_{Cl}^{PZI}$  (190 mg, 0.282 mmol, 1.0 eq) was added and reaction was stirred overnight. Filtration through Celite, washed with dichloromethane and solvent was removed. Product was precipitated from dichloromethane by adding hexanes. Solid was filtered and washed with diethyl ether, yielding to the colorless  $Au_{Cz}^{PZI}$  in 90% yield (205 mg, 0.282 mmol). Under a UV light the solid is orange/green emissive.

<sup>1</sup>H NMR (400 MHz, CDCl<sub>3</sub>) δ 8.59 (s, 2H), 7.95 (ddd, J = 7.7, 1.4, 0.7 Hz, 2H), 7.78 (t, J = 7.9 Hz, 2H), 7.53 (d, J = 7.8 Hz, 4H), 7.07 (ddd, J = 8.2, 7.0, 1.3 Hz, 2H), 6.92 (ddd, J = 7.9, 7.0, 1.1 Hz, 2H), 6.65 (dt, J = 8.1, 0.9 Hz, 2H), 2.48 (sept, J = 6.8 Hz, 4H), 1.33 (d, J = 6.8 Hz, 12H), 1.17 (d, J = 6.9 Hz, 12H).

<sup>13</sup>C NMR (100 MHz, CDCl<sub>3</sub>) δ 149.2, 146.7, 141.1, 140.4, 131.5, 130.4, 124.7, 123.9, 123.5, 119.4, 116.1, 113.4, 65.9, 29.7, 24.3, 24.0, 23.8, 15.3.

CHN: C: 56.63%; H: 5.15%; N: 7.88%; calculated: C: 56.76%; H: 5.22%; N: 7.88% (CHN-Analysis includes one cocrystalized CH<sub>2</sub>Cl<sub>2</sub> molecule per  $Au_{CZ}^{PZI}$  molecule.)

# $Au_{Bim}^{BZAC}$ :

A 100 mL Schlenk flask with a stir bar was charged with 258 mg (1.25 mmol, 1.05 eq) 1H-bim ligand was pump purged and bubble degassed dry THF (50 mL) was added via cannula transfer. 120 mg (1.25 mmol, 0.624 mL, 1.05 eq) sodium *tert*-butoxide (NaOtBu) was added as 2 M solution. After 1 h stirring,  $Au_{Cl}^{BZAC}$  (815 mg, 1.19 mmol, 1.0 eq) was added and reaction was stirred overnight. Filtration through Celite, washing with dichloromethane and removing of solvent yielded to a solid, which was precipitated from dichloromethane /hexanes. If necessary, washing again with pure dichloromethane, dissolves  $Au_{Bim}^{BZAC}$  but does not dissolve remaining bim ligand.  $Au_{Bim}^{BZAC}$  could be isolated as an colorless powder in 88% yield (902 mg, 1.05 mmol). Under a UV light the solid is blue emissive. This compound was crystallized with vapor diffusion of hexanes into a dichloromethane solution of the compound. Crystallographic data can be obtained in the next section.

<sup>1</sup>H NMR (400 MHz, CDCl<sub>3</sub>): δ 7.67 (d, J = 7.8 Hz, 1H), 7.58 (d, J = 8.4 Hz, 2H), 7.53 – 7.45 (m, 4H), 7.41 (d, J = 7.8 Hz, 2H), 7.23 – 7.19 (m, 2H), 7.18 – 7.11 (m, 2H), 6.98 (dd, J = 7.5, 1.2 Hz, 1H), 6.90 (dd, J = 7.5, 1.5 Hz, 2H), 6.51 – 6.46 (m, 1H), 6.05 (dd, J = 7.4, 1.6 Hz, 1H), 4.94 (s, 2H), 3.32 (d, J = 6.8 Hz, 2H), 3.13 (d, J = 6.8 Hz, 2H), 1.44 (dd, J = 6.8, 3.4 Hz, 12H), 1.40 (d, J = 6.8 Hz, 6H), 1.16 (d, J = 6.8 Hz, 6H).

<sup>13</sup>C{<sup>1</sup>H} NMR (101 MHz, CDCl<sub>3</sub>) δ 194.5, 162.5, 149.3, 146.7, 145.4, 145.3, 140.4, 136.8, 135.0, 130.6, 130.1, 129.3, 128.4, 127.1, 126.7, 126.5, 125.6, 121.1, 120.6, 117.4, 117.2, 117.1, 116.5, 113.5, 109.1, 108.9, 51.7, 29.0, 28.9, 25.1, 24.9, 24.6.

# $Au_{Bim}^{BZI}$ :

A 50 mL Schlenk flask with a stir bar with 56.5 mg (0.25 mmol, 1.0 eq) 1H-bim ligand was pump purged and bubble degassed dry THF (20 mL) was added via cannula transfer. 24 mg (0.25 mmol, 1.0 eq) sodium *tert*-butoxide (NaOtBu) was added as 2M solution. After 1 h stirring,  $Au_{Cl}^{BZI}$  (167 mg, 0.25 mmol, 1.0 eq) was added and reaction was stirred overnight. Filtration through Celite, washing with dichloromethane and recrystallization from dichloromethane with layered pentane yielded to the colorless  $Au_{Bim}^{BZI}$  in 84% yield (110 mg, 0.21 mmol). Under a UV light the solid is blue emissive.

<sup>1</sup>H NMR (400 4MHz, CDCl<sub>3</sub>) δ 7.68 (t, J = 7.8 Hz, 2H), 7.62 (d, J = 7.7 Hz, 1H), 7.58 (d, J = 7.5 Hz, 1H), 7.53 – 7.40 (m, 7H), 7.15 (dq, J = 6.1, 3.5, 2.8 Hz, 3H), 7.06 – 6.87 (m, 3H), 6.38 (d, J = 7.9 Hz, 1H), 2.54 (sept, J = 6.7 Hz, 4H), 1.40 (d, J = 6.9 Hz, 13H), 1.14 (d, J = 6.8 Hz, 13H).

<sup>13</sup>C{<sup>1</sup>H} NMR (101 MHz, CDCl<sub>3</sub>) δ 183.0, 162.3, 148.7, 146.8, 145.4, 135.0, 131.5, 131.3, 128.3, 127.0, 125.5, 125.0, 121.5, 121.0, 117.7, 117.1, 117.0, 113.5, 112.2, 109.2, 29.3, 24.9, 24.1.

CHN: C: 62.54%; H: 5.52%; N: 8.29%; calculated: C: 62.78%; H: 5.51%; N: 8.32%

# $Au_{Bim}^{CAAC}$ :

A 50 mL Schlenk flask with a stir bar with 60 mg (0.29 mmol, 1.0 eq) 1H-bim ligand was pump purged and bubble degassed dry THF (20 mL) was added via cannula transfer. 28 mg (0.29 mmol, 1.0 eq) sodium *tert*-butoxide (NaOtBu) was added as 2 M solution. After 1 h stirring,  $Au_{Cl}^{CAAC}$  (180 mg, 0.29 mmol, 1.0 eq) was added and reaction was stirred overnight. Filtration through Celite, washing with dichloromethane and recrystallization in hot acetone yielded to the colorless  $Au_{Bim}^{CAAC}$  in 77% yield (192 mg, 0.31 mmol). Under a UV light the solid is blue emissive. This compound was crystallized with vapor diffusion of hexanes into a dichloromethane solution of the compound. Crystallographic data can be obtained in the next section.

<sup>1</sup>H NMR (400 MHz, CDCl<sub>3</sub>)  $\delta$  7.66 – 7.60 (m, 2H), 7.58 (dd, J = 7.9, 1.1 Hz, 2H), 7.40 (d, J = 7.8 Hz, 2H), 7.18 (dd, J = 7.7, 1.2 Hz, 1H), 7.04 (dd, J = 7.5, 1.1 Hz, 1H), 6.95 (dd, J = 7.5, 1.1 Hz, 1H), 6.86 (dd, J = 7.6, 1.3 Hz, 1H), 5.89 (d, J = 7.8 Hz, 1H), 4.28 (d, J = 12.9 Hz, 2H), 3.48 (s, 1H), 2.87 (sept, J = 6.7 Hz, 2H), 2.54 (s, 1H), 2.43 (s, 2H), 2.04 (d, J = 24.3 Hz, 7H), 1.91 (s, 3H), 1.43 (s, 6H), 1.35 (dd, J = 13.8, 6.7 Hz, 12H).

<sup>13</sup>C{<sup>1</sup>H} NMR (126 MHz, CDCl<sub>3</sub>) δ 149.2, 145.9, 145.2, 136.6, 129.9, 128.5, 127.2, 125.4, 121.4, 121.2, 117.8, 116.8, 113.6, 110.0, 109.3, 109.1, 77.7, 64.2, 59.8, 48.2, 39.2, 37.1, 35.7, 34.5, 29.5, 29.4, 29.2, 29.1, 28.9, 28.8, 28.6, 28.0, 27.5, 26.0, 22.7, 20.0, 13.7;

# $Au_{Bim}^{MAC}$ :

A 25 mL Schlenk flask with a stir bar with 43 mg (0.206 mmol, 1.0 eq) 1H-bim ligand was pump purged and bubble degassed dry THF (10 mL) was added via cannula transfer. 0.10 mL (0.206 mmol, 1.0 eq) 2M sodium *tert*-butoxide (NaOtBu) solution was added dropwise. After 1h stirring,  $Au_{Cl}^{MAC}$  (140 mg, 0.206 mmol, 1.0 eq) was added and reaction was stirred overnight. Filtration through Celite, washing with dichloromethane and removing solvent. Product was purified by layered recrystallization of dichloromethane and pentane. Removing of solvent yielded to the lightly yellow  $Au_{Bim}^{MAC}$  in 85% yield (148 mg, 0.174 mmol). Under a UV light the solid is sky-blue emissive.

<sup>1</sup>H NMR (400 MHz, CDCl<sub>3</sub>) δ 7.64 – 7.54 (m, 3H), 7.48 (dd, J = 7.5, 1.4 Hz, 1H), 7.43 (dd, J = 8.0, 1.0 Hz, 1H), 7.39 (dd, J = 7.8, 1.1 Hz, 4H), 7.14 (dd, J = 7.8, 1.2 Hz, 1H), 6.98 (dd, J = 7.6, 1.1 Hz, 1H), 6.90 (td, J = 7.6, 1.4 Hz, 1H), 6.85 (td, J = 7.6, 1.4 Hz, 1H), 5.95 (dd, J = 7.7, 1.3 Hz, 1H), 3.86 (s, 2H), 3.25 (sept, J = 6.9 Hz, 2H), 3.01 (sept, J = 6.8 Hz, 2H), 1.62 (s, 6H), 1.44 (d, J = 6.8 Hz, 6H), 1.39 (dd, J = 6.9, 3.7 Hz, 12H), 1.24 (d, J = 6.8 Hz, 6H);

<sup>13</sup>C{<sup>1</sup>H} NMR (101 MHz, CDCl<sub>3</sub>) δ 203.9, 171.4, 162.2, 149.0, 145.7, 145.1, 144.5, 140.1, 135.8, 130.7, 130.5, 128.4, 127.1, 125.8, 124.9, 121.3, 120.8, 117.5, 117.2, 116.8, 113.4, 109.1, 109.0, 62.1, 38.1, 29.5, 29.1, 25.0, 24.7, 24.5, 23.9;

# $Au_{Bim}^{PAC}$ :

A 25 mL Schlenk flask with a stir bar with 62 mg (0.300 mmol, 1.05 eq) 1H-bim ligand was pump purged and bubble degassed dry THF (12 mL) was added via cannula transfer. 0.150 mL (0.300 mmol, 1.05 eq) 2M sodium *tert*-butoxide (NaOtBu) solution was added dropwise. After 1h stirring,  $Au_{Cl}^{PAC}$  (200 mg, 0.285 mmol, 1.0 eq) was added and reaction was stirred overnight. Filtration through Celite, washing with dichloromethane and removing solvent. Product was purified by layered recrystallization of dichloromethane and pentane. Removing of solvent yielded to the yellow  $Au_{Bim}^{PAC}$  in 75% yield (186 mg, 0.214 mmol). Under a UV light the solid is green emissive.

<sup>1</sup>H NMR (400 MHz, acetone-d6) δ 8.49 (ddd, J = 7.9, 1.6, 0.5 Hz, 1H), 8.05 (ddd, J = 8.6, 7.3, 1.6 Hz, 1H), 7.86 (td, J = 7.6, 1.1 Hz, 1H), 7.79 (ddt, J = 8.3, 7.4, 0.5 Hz, 1H), 7.69 (ddd, J = 7.8, 1.3, 0.7 Hz, 1H), 7.67 – 7.60 (m, 4H), 7.51 (d, J = 7.8 Hz, 2H), 7.36 (ddd, J = 8.0, 1.1, 0.6 Hz, 1H), 7.13 – 7.05 (m, 2H), 6.99 – 6.87 (m, 3H), 6.31 – 6.25 (m, 1H), 3.03 (sept, J = 6.8 Hz, 2H), 2.92 (sept, J = 6.8 Hz, 2H), 1.45 (dd, J = 15.1, 6.8 Hz, 12H), 1.22 (d, J = 6.8 Hz, 6H), 1.12 (d, J = 6.8 Hz, 6H), 0.14 (d, J = 6.6 Hz, 4H).

<sup>13</sup>C{<sup>1</sup>H} NMR (100 MHz, CDCl<sub>3</sub>) δ 158.7, 145.3, 145.1, 141.7, 135.9, 131.6, 130.6, 129.4, 128.3, 125.9, 124.9, 121.1, 120.6, 118.8, 118.5, 117.4, 117.0, 116.6, 113.3, 109.0, 108.9, 77.2, 29.4, 29.1, 24.5, 24.4, 24.3, 23.9, 1.0;

# $Au_{Bim}^{iPr}$ :

A 25 mL Schlenk flask with a stir bar with 70 mg (0.337 mmol, 1.05 eq) 1H-bim ligand was pump purged and bubble degassed dry THF (10 mL) was added via cannula transfer. 0.17 mL (0.338 mmol, 1.05 eq) 2M sodium *tert*-butoxide (NaOtBu) solution was added dropwise. After 1h stirring,  $Au_{Cl}^{iPr}$  (200 mg, 0.322 mmol, 1.0 eq) was added and reaction was stirred overnight. Filtration through Celite, washing with dichloromethane and removing solvent. Product was first washed with Diethyl ether and then dissolved in as little dichloromethane as possible. Remaining bim ligand, does not dissolve. Removing of solvent yielded to the colorless  $Au_{Bim}^{iPr}$  in 80% yield (205 mg, 0.259 mmol). Under a UV light the solid is blue emissive.

<sup>1</sup>H NMR (400 MHz, acetone-d6) δ 7.92 (s, 2H), 7.73 – 7.65 (m, 2H), 7.60 (ddd, J = 8.3, 7.2, 0.5 Hz, 2H), 7.50 – 7.44 (m, 4H), 7.29 (ddd, J = 8.0, 1.2, 0.7 Hz, 1H), 7.06 (ddd, J = 8.0, 7.3, 1.3 Hz, 1H), 6.97 – 6.87 (m, 3H), 6.68 – 6.59 (m, 1H), 2.83 (sept, J = 6.8 Hz, 4H), 1.46 (d, J = 6.9 Hz, 12H), 1.30 (d, J = 6.9 Hz, 12H).

<sup>13</sup>C NMR (100 MHz, CDCl<sub>3</sub>) δ 207.0, 145.8, 145.6, 134.1, 130.8, 124.5, 124.3, 123.5, 121.4, 120.8, 117.5, 116.9, 116.8, 113.3, 109.0, 77.2, 30.9, 29.0, 28.8, 24.5, 24.1, 24.0.

CHN: C: 60.75%; H: 5.59%; N: 8.73%; calculated: C: 60.68%; H: 5.60%; N: 8.85%

# $Au_{Bim}^{PZI}$ :

A 25 mL Schlenk flask with a stir bar with 65 mg (0.311 mmol, 1.1 eq) 1H-bim ligand was pump purged and bubble degassed dry THF (10 mL) was added via cannula transfer. 0.155 mL (0.311 mmol, 1.1 eq) 2M sodium *tert*-butoxide (NaOtBu) solution was added dropwise. After 1 h stirring,  $Au_{Cl}^{PZI}$  (190 mg, 0.282 mmol, 1.0 eq) was added and reaction was stirred overnight. Filtration through Celite, washed with dichloromethane and solvent was removed. Product was precipitated from dichloromethane by adding hexanes. Solid was filtered and washed with diethyl ether, yielding to the colorless  $Au_{Bim}^{PZI}$  in 76% yield (182 mg, 0.216 mmol). Under a UV light the solid is green emissive.

<sup>1</sup>H NMR (400 MHz, acetone-d6) δ 8.76 (s, 2H), 7.81 - 7.66 (m, 4H), 7.61 (d, J = 7.8 Hz, 4H), 7.33 (d, J = 7.9 Hz, 0H), 7.09 (td, J = 7.9, 1.2 Hz, 1H), 7.01 - 6.92 (m, 3H), 6.58 - 6.49 (m, 1H), 2.67 (sept, J = 6.9 Hz, 4H), 1.45 (d, J = 6.8 Hz, 12H), 1.15 (d, J = 6.8 Hz, 12H).

<sup>13</sup>C NMR (100 MHz, acetone-d6) δ 161.7, 148.7, 146.9, 144.7, 142.2, 140.3, 131.5, 130.7, 128.1, 126.7, 124.7, 121.4, 121.3, 118.1, 116.9, 116.7, 112.9, 109.2, 109.2, 29.2, 23.9, 23.7, 23.3, 23.2.

CHN: C: 59.83%; H: 5.24%; N: 11.56%; calculated: C: 59.78%; H: 5.26%; N: 11.62%

# $Au_{MeBim}^{BZI}$ :

A 25 mL Schlenk flask with a stir bar with 33 mg (0.149 mmol, 1.0 eq) 1H-Mbim ligand was pump purged and bubble degassed dry THF (10 mL) was added via cannula transfer. 0.075 mL (0.149 mmol, 1.0 eq) 2 M sodium *tert*-butoxide (NaOtBu) solution was added dropwise. After stirring for 1 h,  $Au_{Cl}^{BZI}$  (100 mg, 0.149 mmol, 1.0 eq) was added and reaction was stirred overnight. Filtration through Celite, washing with dichloromethane and recrystallization in hot acetone yielded to the colorless  $Au_{MeBim}^{BZI}$  in 76% yield (116 mg, 0.217 mmol). Under a UV light the solid is blue emissive. This compound was crystallized with vapor diffusion of hexanes into a dichloromethane solution of the compound. Crystallographic data can be obtained in the next section. The NMR spectra showed a 50/50 mixture of both possible tautomers. The proton integrations are for a mixture of both tautomers.

<sup>1</sup>H NMR (400 MHz, CDCl<sub>3</sub>) δ 7.68 (t, J = 7.8 Hz, 2H), 7.62 (d, J = 7.7 Hz, 1H), 7.57 (d, J = 7.0 Hz, 1H), 7.53 – 7.40 (m, 7H), 7.15 (dq, J = 6.1, 3.5, 2.8 Hz, 3H), 7.06 – 6.87 (m, 3H), 6.38 (d, J = 7.2 Hz, 1H), 5.30 (s, 1H), 2.54 (sept, J = 6.7 Hz, 4H), 1.40 (d, J = 6.9 Hz, 13H), 1.14 (d, J = 6.8 Hz, 13H).

 $^{13}C\{^{1}H\}$  NMR (101 MHz, CDCl<sub>3</sub>)  $\delta$  183.0, 162.3, 148.7, 146.8, 145.4, 135.0, 131.5, 131.3, 128.3, 127.0, 125.5, 125.0, 121.5, 121.0, 117.7, 117.1, 117.0, 113.5, 112.2, 109.2, 29.3, 24.9, 24.1

# $Au_{MeOBim}^{BZI}$ :

A 25 mL round-bottom flask with stir bar was charged with  $Au_{Cl}^{BZI}$  (200 mg, 0.30 mmol, 1.0 eq), 71 mg (0.30 mmol, 1.0 eq) 1H-Obim ligand and fine ground K<sub>2</sub>CO<sub>3</sub> (125 mg, 0.9 mmol, 3.0 eq) was dissolved in minimal acetone and stirred for 24 h at room temperature. Solution was filtered through Celite, washed with dichloromethane and dried under vacuum. Sonicating in diethylether and collecting the precipitate yielded to the colorless  $Au_{MeOBim}^{BZI}$  in 85% yield (140 mg, 0.255 mmol). Under a UV light the solid is blue emissive. The NMR spectra showed a 50/50 mixture of both possible tautomers. The proton integrations are for a mixture of both tautomers.

[¹H NMR (400 MHz, CDCl₃)  $\delta$  7.67 (t, J = 7.8 Hz, 1H), 7.62 – 7.56 (m, 2H), 7.53 – 7.45 (m, 4H), 7.41 (d, J = 7.8 Hz, 2H), 7.23 – 7.19 (m, 2H), 7.18 – 7.11 (m, 2H), 6.98 (td, J = 7.5, 1.2 Hz, 1H), 6.90 (pd, J = 7.4, 1.5 Hz, 2H), 6.51 – 6.46 (m, 1H), 6.05 (dd, J = 7.4, 1.6 Hz, 1H), 4.94 (s, 2H), 3.32 (sept, J = 6.8 Hz, 2H), 3.13 (sept, J = 6.8 Hz, 2H), 1.44 (dd, J = 6.8, 3.4 Hz, 12H), 1.40 (d, J = 6.8 Hz, 6H), 1.16 (d, J = 6.8 Hz, 6H).

<sup>13</sup>C{<sup>1</sup>H} NMR (101 MHz, CDCl<sub>3</sub>) δ 194.5, 162.5, 149.3, 146.7, 145.4, 145.3, 140.4, 136.8, 135.0, 130.6, 130.1, 129.3, 128.4, 127.1, 126.7, 126.5, 125.6, 121.1, 120.6, 117.4, 117.2, 117.1, 116.5, 113.5, 109.1, 108.9, 51.7, 29.0, 28.9, 25.1, 24.9, 24.6.;

CHN: C: 61.79%; H: 5.56%; N: 7.96%; calculated: C: 61.99%; H: 5.55%; N: 8.03%

#### Structural data

All crystals were grown by recrystallization. Vapor diffusion of hexanes or pentane into a solution of the compound in dichloromethane. A Cryo-Loop was used to mount the sample with Paratone oil.

All single crystal structures were determined at 100K with Rigaku Xta LAB Synergy S, equipped with an HyPix-600HE detector and an Oxford Cryostream 800 low Temperature unit, using Cu  $K_{\alpha}$  PhotonJet-S X-ray source. The frames were integrated using the SAINT algorithm to give the hkl files. Data were corrected for absorption effects using the multi-scan method (SADABS) with Rigaku CrysalisPro. The structures were solved by intrinsic phasing and refined with the SHELXTL Software Package. If necessary, the disordered solvent treatment method BYPASS for co-crystalizing solvent molecules, was implemented and marked in the CCDC entry.

All cif files and report data including atom position, bond lengths and bond angle can be downloaded from the CCDC database, using the database number in the right column of the following table. Furthermore, the following table is giving the most important bond lengths, angles and the torsion angle around the metal center. The conformer ratio represents the ratio of two different disordered conformations of the molecule. Only  $Au_{CZ}^{BZAC}$  crystallized with two molecules in the asymmetric unit, therefore the parameters were given for both molecules in the asymmetric unit. All others crystalized with one molecule in the asymmetric unit.

<u>Table S1:</u> Selected bond lengths and angles for the(carbene)M(amide) complexes.

compound	C-M (A)	M-N (A)	C-M-N (°)	Torsion (°) NC-M-NC	Conformer ratio	CCDC#
$Au_{Cz}^{BZAC}$	2.004(7) 1.984(8)	2.020(6) 1.999(7)	179.1(3) 1.79.5(3)	3.7	100/0	2168084
$Cu_{BCz}^{PAC}$	1.879(2)	1.854(2)	173.9(1)	6.1	100/0	2170320
$Au_{bim}^{BZAC}$	2.005(1)	2.025(7)	176.1(4)	2.7	100/0	2182717
$Au_{bim}^{\mathit{CAAC}}$	1.974(4)	2.014(3)	178.1(2)	7.2	100/0	2155241
$Au_{bim}^{MAC}$	1.992(7)	2.023(6)	178.8(3)	4.0	90/10	2167514
$Au_{bim}^{PAC}$	1.995(3)	2.018(3)	178.6(2)	7.3	100/0	2170000
$Au_{Mbim}^{BZI}$	2.005(7)	2.031(6)	174.1(3)	0.7	84/16	2168086

<u>Table S2:</u> Crystallographic parameters for BZAC-Au-Cz, PAC-Cu-BCz, BZAC-Au-bim and CAAC-Au-bim.

Identification code	BZAC-Au-Cz PAC-Cu-BCz		BZAC-Au-bim	CAAC-Au-bim	
Empirical formula	$C_{176}H_{192}Au_4N_{12}$	$C_{104}H_{124}Cu_2N_6O_2$	C45H48AuN5	C <sub>40</sub> H <sub>47</sub> AuN <sub>4</sub>	
Formula weight	191.96	1613.16 855.883		780.78	
Temperature/K	293(2)	100.00(10)	100.01(10)	107(11)	
Crystal system	triclinic	triclinic	orthorhombic	monoclinic	
Space group	P-1	P-1	Fdd2	I2/a	
a/Å	9.0083(2)	16.5805(2)	57.2043(10)	23.3536(3)	
b/Å	19.3190(3)	17.3257(2)	30.8094(5)	9.61920(10)	
c/Å	23.0688(2)	20.0203(2)	8.8252(1)	33.2792(4)	
$lpha/^\circ$	82.1710(10)	68.7580(10)	90	90	
β/°	80.8960(10)	72.6580(10)	90	100.5580(10)	
γ/°	83.406(2)	62.0990(10)	90	90	
Volume/Å <sup>3</sup>	3909.28(11)	4679.32(11)	15553.8(4)	7349.37(15)	
Z	2	2	16	8	
$\rho_{calc}g/cm^3$	1.386	1.145	1.462	1.411	
$\mu/\text{mm}^{-1}$	7.306	0.934	7.389	7.752	
F(000)	1648	1724	6870.6	3152	
Crystal size/mm <sup>3</sup>	$0.549 \times 0.058 \times 0.029$	$0.25 \times 0.195 \times 0.135$	$0.118 \times 0.025 \times 0.015$	$0.138 \times 0.098 \times 0.029$	
Radiation	Cu K $\alpha$ ( $\lambda = 1.54184$ )	Cu K $\alpha$ ( $\lambda = 1.54184$ )	Cu K $\alpha$ ( $\lambda = 1.54184$ )	Cu K $\alpha$ ( $\lambda = 1.54184$ )	
2Θ range for data collection/°	5.694 to 163.426	5.984 to 161.91	6.18 to 160.66	5.402 to 161.006	
Index ranges	$-11 \le h \le 11,$ $-24 \le k \le 24,$ $-27 \le 1 \le 29$	$-21 \le h \le 21,$ $-21 \le k \le 22,$ $-25 \le 1 \le 25$	$-68 \le h \le 72$ , $-39 \le k \le 37$ , $-7 \le l \le 10$	$-29 \le h \le 29$ , $-12 \le k \le 8$ , $-42 \le 1 \le 42$	
Reflections collected	92189	301930	24795	60195	
Independent reflections	$16775[R_{int} = 0.1410, R_{sigma} = 0.0759]$	$20281[R_{int} = 0.0668, R_{sigma} = 0.0231]$	$6414[R_{int} = 0.0343, R_{sigma} = 0.0274]$	$7981[R_{int} = 0.0901, R_{sigma} = 0.0472]$	
Data/restraints/parameters	16775/0/882	20281/0/1055	6414/1/468	7981/0/412	
Goodness-of-fit on F <sup>2</sup>	1.14	1.052	1.038	1.085	
Final R indexes [I>=2σ (I)]	$R_1 = 0.0791, wR_2 = 0.2219$	$R_1 = 0.0675, wR_2 = 0.1654$	$R_1 = 0.0359$ , $wR_2 = 0.0946$	$R_1 = 0.0364, wR_2 = 0.0915$	
Final R indexes [all data]	$R_1 = 0.0911, wR_2 = 0.2383$	$R_1 = 0.0725, wR_2 = 0.1689$	$R_1 = 0.0377, wR_2 = 0.0953$	$R_1 = 0.0431, wR_2 = 0.0960$	
Largest diff. peak/hole / e Å <sup>-3</sup>	4.79/-3.15	1.59/-1.48	2.12/-1.16	2.49/-1.83	
#CCDC	2168084	2170320	2182717	2155241	

<u>Table S3:</u> Crystallographic parameters for MAC-Au-bim, PAC-Au-bim and BZI-Au-Mbim.

Identification code	MAC-Au-bim	PAC-Au-bim	BZI-Au-Mbim	
Empirical formula	$C_{43}H_{50}AuN_5O$	C <sub>45</sub> H <sub>46</sub> AuN <sub>5</sub> O	C <sub>45</sub> H <sub>48</sub> AuN <sub>5</sub>	
Formula weight	849.876	869.83	855.85	
Temperature/K	123(30)	100.5(8)	100(90)	
Crystal system	monoclinic	monoclinic	monoclinic	
Space group	C2/c	P2 <sub>1</sub> /n	P2 <sub>1</sub> /c	
a/Å	15.9731(1)	13.61560(10)	8.91960(10)	
b/Å	22.6254(2)	18.11870(10)	29.5199(5)	
c/Å	21.5638(2)	16.34850(10)	15.2229(3)	
α/°	90	90	90	
β/°	93.533(1)	109.8980(10)	99.193(2)	
γ/°	90	90	90	
Volume/Å <sup>3</sup>	7778.30(11)	3792.35(5)	3956.79(11)	
Z	8	4	4	
$\rho_{calc}g/cm^3$	1.451	1.523	1.437	
$\mu$ /mm <sup>-1</sup>	7.4	7.609	7.263	
F(000)	3419.4	1752	1728	
Crystal size/mm <sup>3</sup>	$0.27 \times 0.14 \times 0.13$	$0.104 \times 0.083 \times 0.043$	$0.29 \times 0.059 \times 0.032$	
Radiation	Cu K $\alpha$ ( $\lambda = 1.54184$ )	Cu K $\alpha$ ( $\lambda = 1.54184$ )	Cu K $\alpha$ ( $\lambda = 1.54184$ )	
2Θ range for data collection/°	6.78 to 161.6	7.33 to 160.548	5.988 to 176.412	
Index ranges	$-20 \le h \le 20$ , $-28 \le k \le 28$ , $-24 \le 1 \le 27$	$-17 \le h \le 16,$ $-23 \le k \le 23,$ $-20 \le l \le 20$	$-9 \le h \le 11$ , $-37 \le k \le 37$ , $-19 \le 1 \le 19$	
Reflections collected	132598	128799	80685	
Independent reflections $ 8489 \ [R_{int} = 0.0702, R_{sigma} = 0.0200] $		8259 [R <sub>int</sub> = 0.0596, R <sub>sigma</sub> = 0.0195]	8698 [R <sub>int</sub> = 0.1226, R <sub>sigma</sub> = 0.0429]	
Data/restraints/parameters	8489/0/471	8259/0/477	8698/0/476	
Goodness-of-fit on F <sup>2</sup>	0.945	1.178	1.128	
Final R indexes [I>= $2\sigma$ (I)]	$R_1 = 0.0634, wR_2 = 0.1472$	$R_1 = 0.0314, wR_2 = 0.0852$	$R_1 = 0.0622, wR_2 = 0.1347$	
Final R indexes [all data]	$R_1 = 0.0639, wR_2 = 0.1474$	$R_1 = 0.0334, wR_2 = 0.0863$	$R_1 = 0.0701, wR_2 = 0.1549$	
Largest diff. peak/hole / e Å <sup>-3</sup>	2.20/-2.14	1.10/-1.51	2.41/-2.89	
#CCDC	2167514	2170000	2168086	

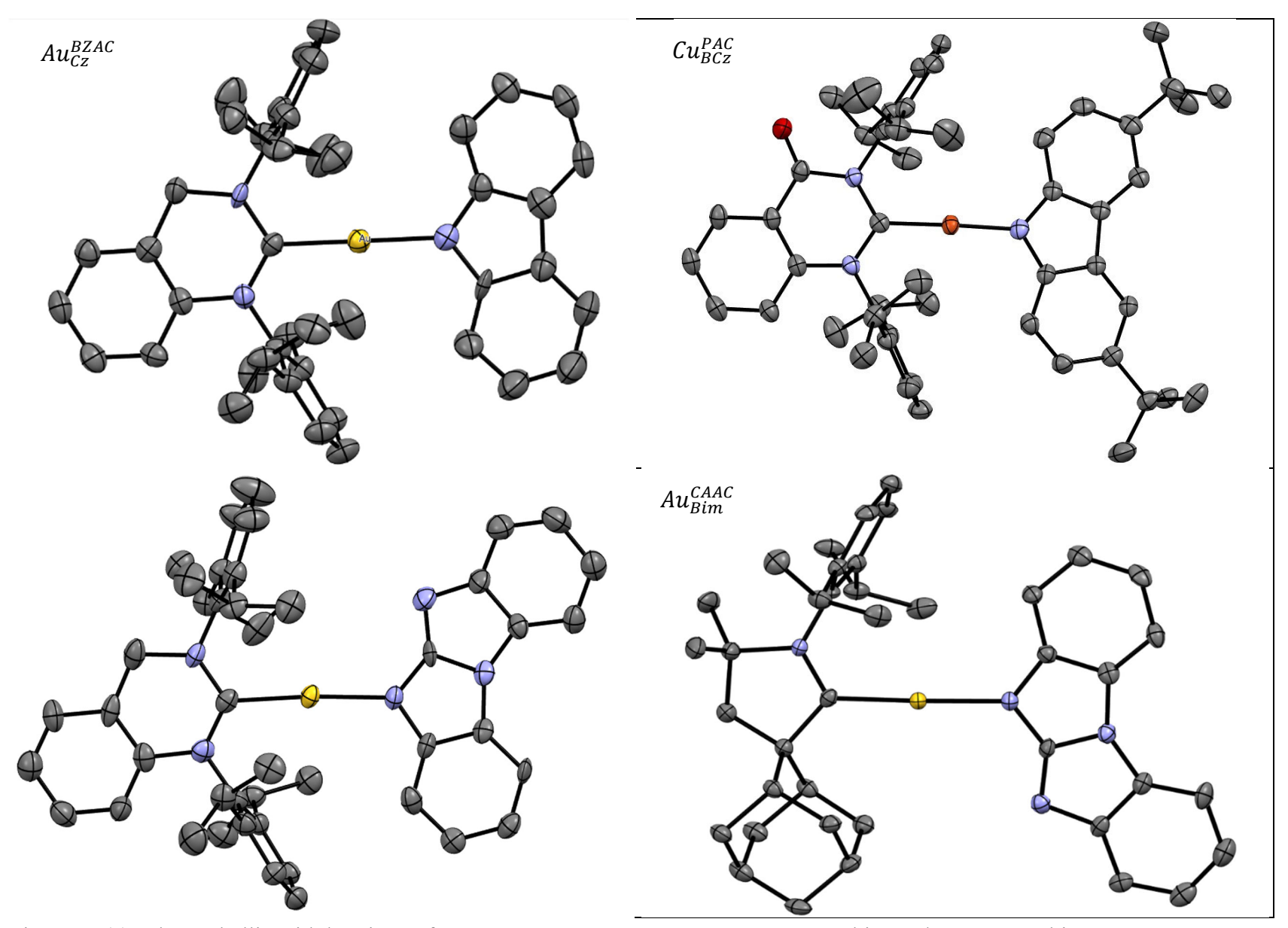


Figure S2(a): Thermal ellipsoid drawings of BZAC-Au-Cz, PAC-Cu-BCz-, BZAC-Au-bim and CAAC-Au-bim.

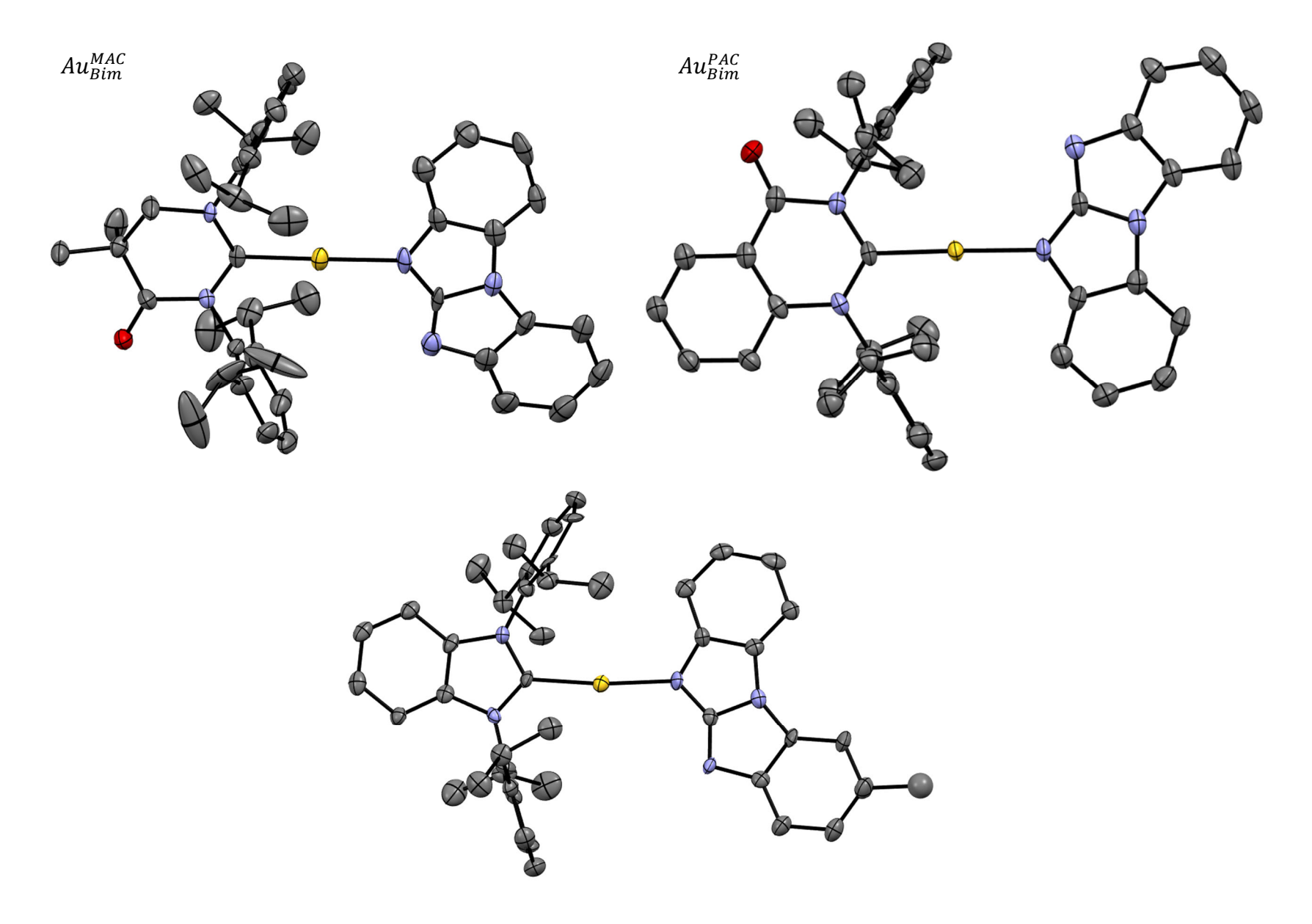
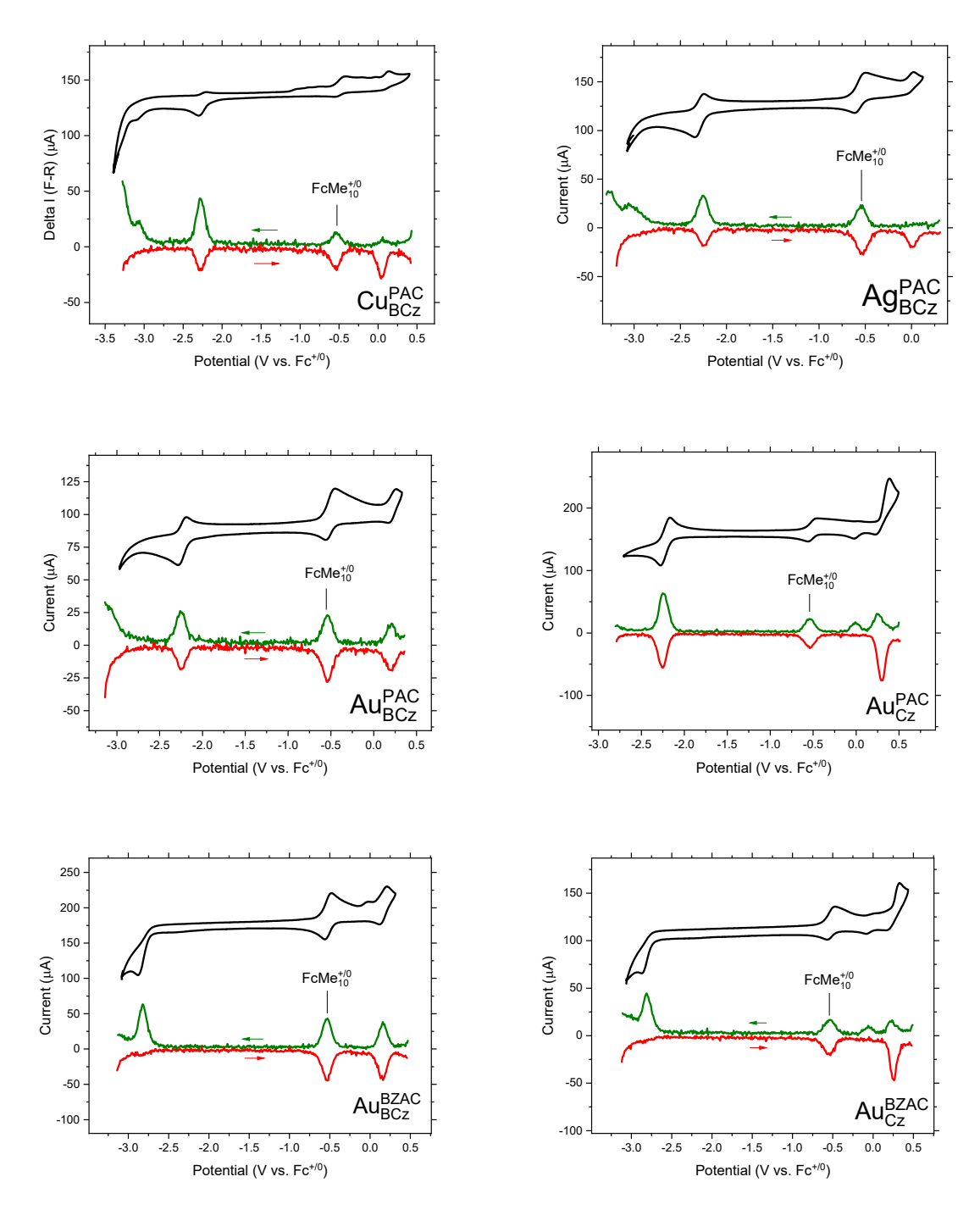


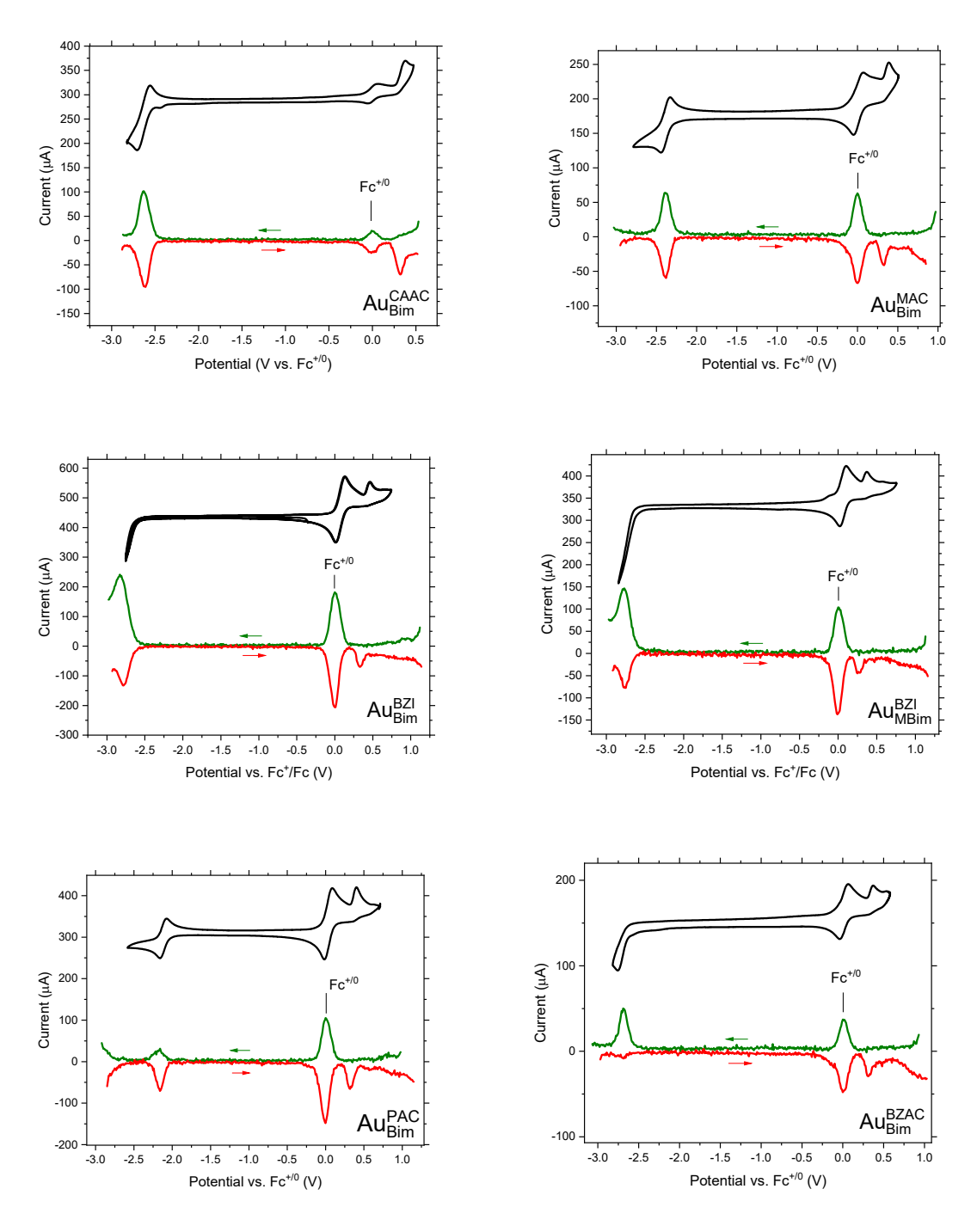
Figure S2 (b): Thermal ellipsoid drawings of MAC-Au-bim, PAC-Au-bim and BZI-Au-Mbim.

#### **Electrochemistry**

Cyclic voltammetry (CV) and differential pulsed voltammetry (DPV) were performed using a VersaSTAT potentiostat. CV scans were measured at 100 mVs<sup>-1</sup>, and DPV was measured at 10 mVs<sup>-1</sup>. All measurements were carried out in dry dimethylformamide using a glassy carbon working electrode, platinum counter electrode, and silver wire pseudo-reference electrode, with 0.1 M (*n*-butyl)<sup>4</sup> PF<sub>6</sub> as an electrolyte, and ferrocene or decamethylferrocene as an internal standard. The potentials given in Table S4 were referenced to the ferrocene +/0 redox couple by setting decamethylferrocene's first oxidation to -0.54 V vs. Fc<sup>+/0</sup>,<sup>5</sup> or ferrocene's first oxidation to 0 V.



<u>Figure S3:</u> CV and DPV traces of cMa complexes collected in DMF with 0.1 TBAPF<sub>6</sub> as an electrolyte.



<u>Figure S3 (continued):</u> CV and DPV traces of cMa complexes collected in DMF with 0.1 TBA PF6 as an electrolyte.

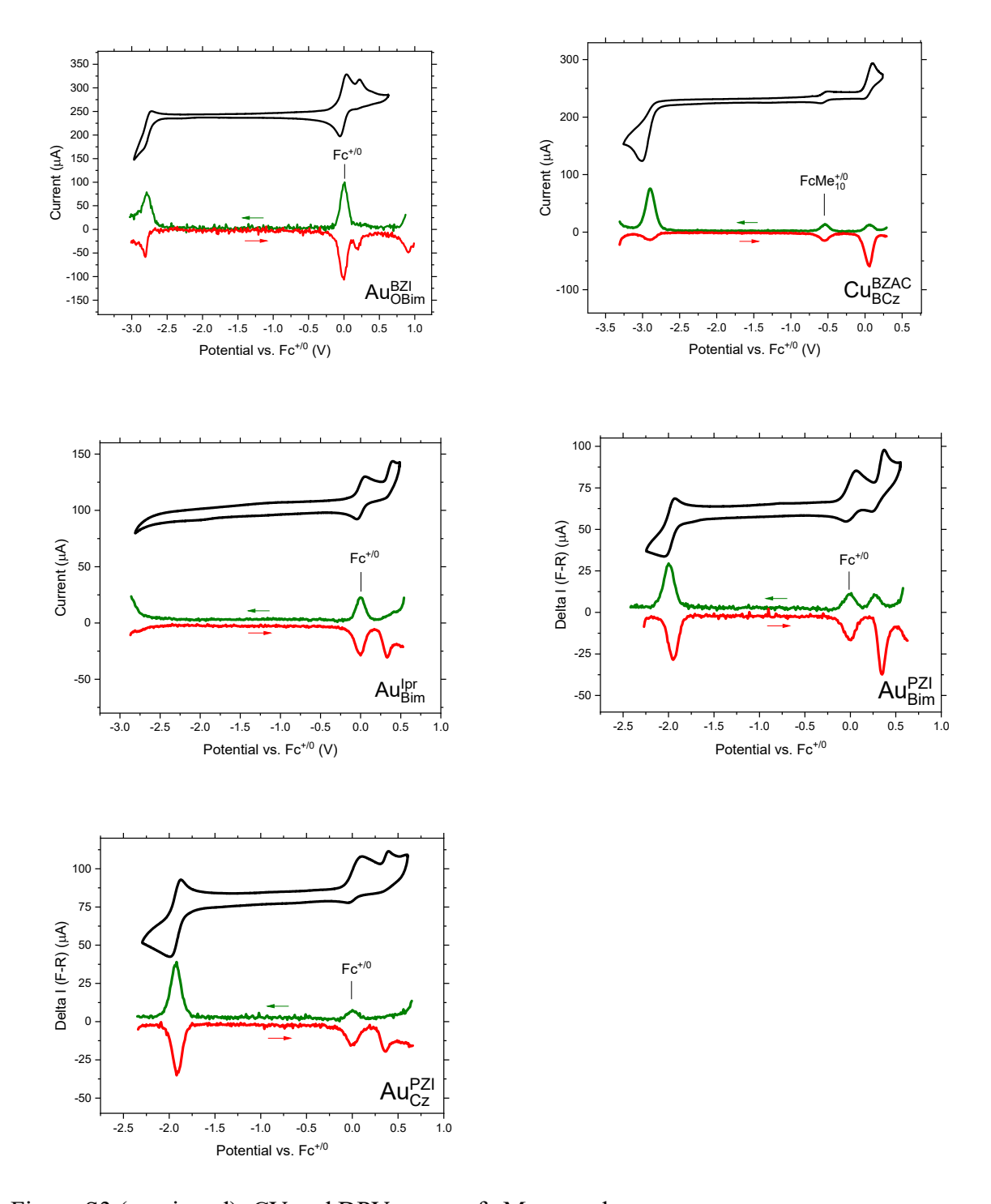


Figure S3 (continued): CV and DPV traces of cMa complexes

<u>Table S4:</u> Electrochemical data. Electrochemical measurements were carried out in DMF solution with 0.1 M NBu<sub>4</sub>PF<sub>6</sub> electrolyte, and the potentials are listed relative to a ferrocene internal reference. The absorption edge is taken as the point where ICT absorbance has dropped to 10% of the peak absorbance for a toluene solution of the cMa.

Complex	$E_{\text{ox}}\left(\mathbf{V}\right)$	Ered (V)	$\Delta E_{ m redox}$ (V)	Abs. edge (eV)
$Cu_{BCz}^{BZAC}$	0.06	-2.90	2.96	2.74
$Au_{BCz}^{BZAC}$	0.15	-2.83	2.98	2.77
$Au_{Cz}^{BZAC}$	0.26	-2.81	3.07	2.89
$Cu_{BCz}^{PAC}$	0.12	-2.28	2.40	2.25
$Ag_{BCz}^{PAC}$	0.02	-2.24	2.26	2.27
$Au_{BCz}^{PAC}$	0.21	-2.24	2.45	2.33
$Au_{Cz}^{PAC}$	0.29	-2.24	2.53	2.49
$Au_{Cz}^{PZI}$	0.29	-1.99	2.30	2.36
$Au_{bim}^{PZI}$	0.36	-1.92	2.28	2.38
$Au_{bim}^{PAC}$	0.32	-2.16	2.48	2.52
$Au_{bim}^{MAC}$	0.33	-2.37	2.70	2.65
$Au_{bim}^{CAAC}$	0.32	-2.62	2.94	2.86
$Au_{bim}^{BZAC}$	0.31	-2.69	3.00	2.99
$Au_{bim}^{BZI}$	0.33	-2.79	3.12	3.08
$Au_{Mbim}^{BZI}$	0.26	-2.75	3.01	3.00
$Au_{Obim}^{BZI}$	0.18	-2.81	2.99	2.93
$Au_{bim}^{Ipr}$	0.33	*	*	3.59

<sup>\*</sup> The reduction potential of  $Au_{bim}^{lpr}$  was outside of the solvent window. This is consistent with it having the largest optical LUMO of all compounds in this study.

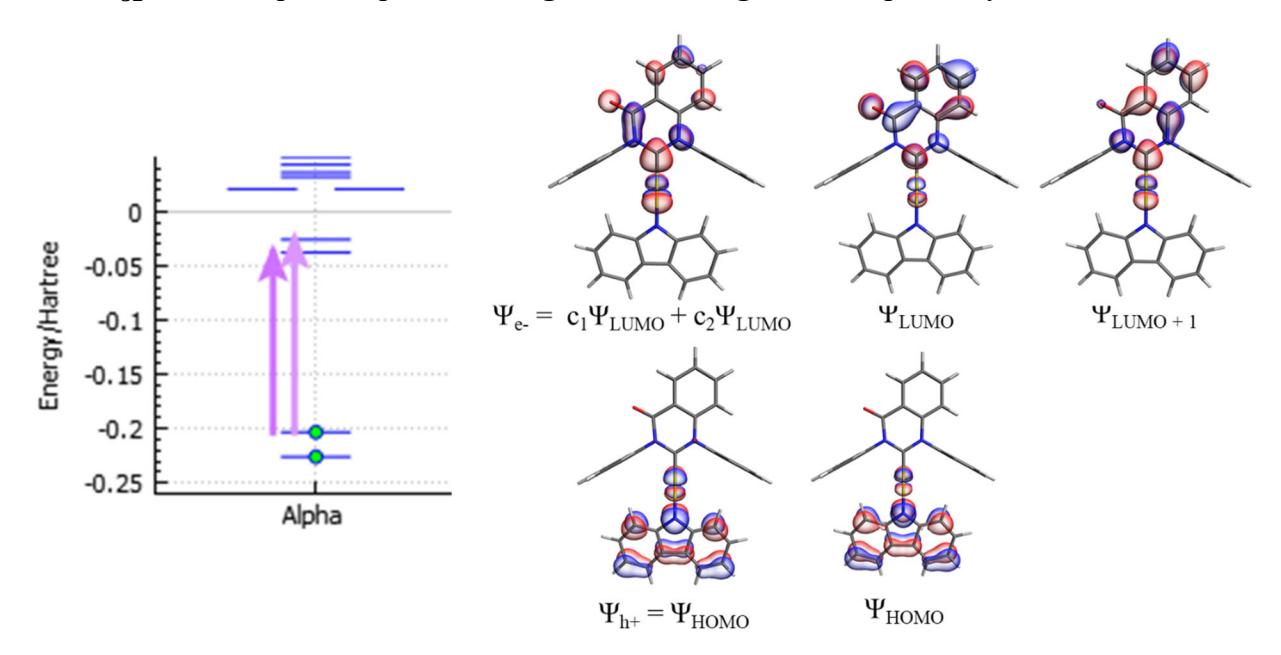
### Molecular modeling

#### General Methodology

The electronic properties of the complexes were modelled in Q-Chem using Density Functional Theory (DFT) and Time Dependent DFT (TDDFT).<sup>6</sup> The electronic properties of the complexes were modeled using Density Functional Theory (DFT) and Time Dependent DFT (TDDFT). First, a geometry optimization was performed using the B3LYP functional and LACVP basis set which accounts for molecules containing transition metals. TDDFT calculations were performed on the ground-state optimized structures to estimate the  $S_0 \rightarrow S_1$  transition energies and corresponding oscillator strengths. The TDDFT calculations were performed using the LACVP basis, the CAMB3LYP exchange, the fit-LACVP effective core potential, the random phase approximation, and the omega value set to 0.2 arbitrary units.

#### **NTOs**

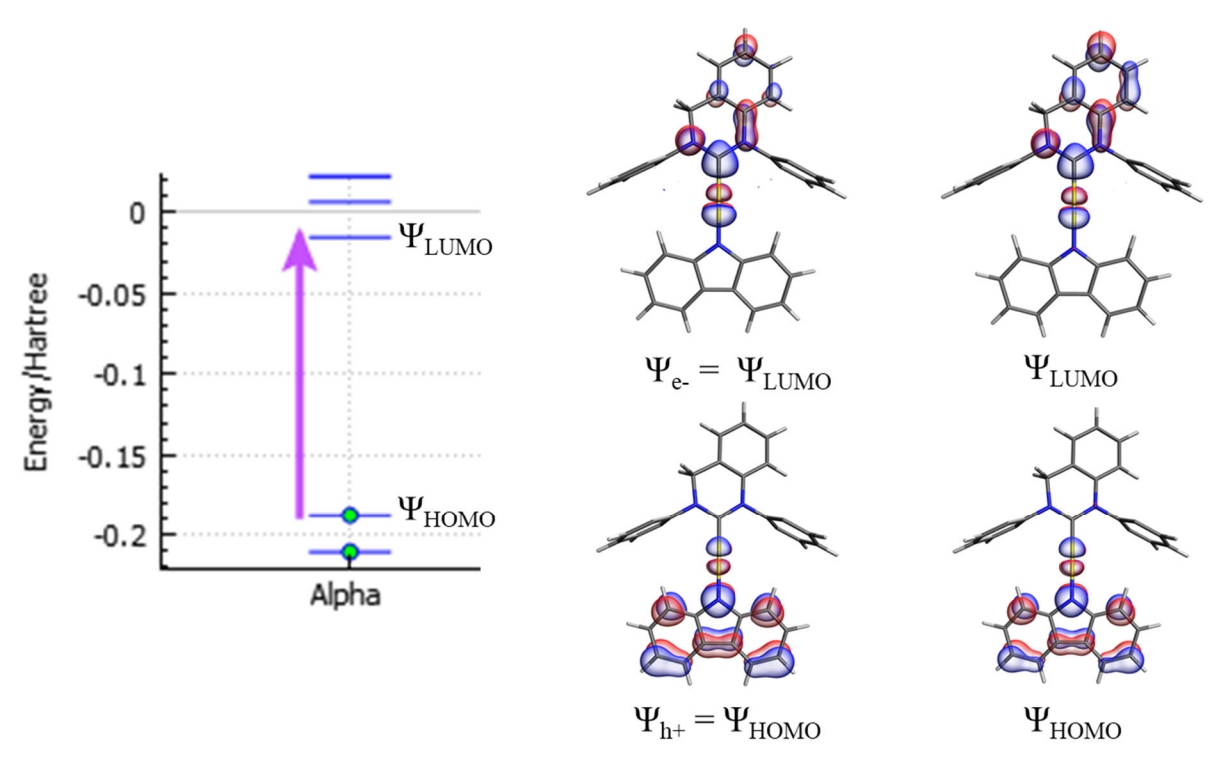
Natural transition orbitals were generated by performing a singular value decomposition on the transition density matrix using the Q-Chem software package. The resultant eigenstates are a linear combination of molecular orbitals involved in the  $S_0 \rightarrow S_n$  transition which are separated into hole and electron pairs. The advantage of NTOs is that electronic transitions are often composed of more than two molecular orbitals (i.e., HOMO to LUMO). Interestingly, the HOMO and LUMO of the compounds in this work make up >99.9% of the  $S_0 \rightarrow S_1$  transition, aside from the PAC complexes which mix the LUMO + 1 into the electron NTO. This is demonstrated with  $Au_{CZ}^{BZAC}$  and  $Au_{CZ}^{PAC}$  as example compounds in **Figure S4** and **Figure S5** respectively.



<u>Figure S4.</u> The S<sub>0</sub> $\rightarrow$ S<sub>1</sub> transition of  $Au_{Cz}^{PAC}$  involves an electron moving from the HOMO to LUMO and HOMO to LUMO + 1. The hole and electron NTOs ( $\Psi_{h^+}$  and  $\Psi_{e^-}$ ) are appropriate visualizations

of the hole and electron wavefunctions corresponding to this transition. One can see that the electron NTO is made up of a linear combination of the  $\Psi_{LUMO}$  and  $\Psi_{LUMO+1}$ . The isopropyl groups are omitted from the diisopropylphenyl groups for clarity.

All PAC compounds give a mixed LUMO/LUMO+1 behavior in the electron NTO which is consistent with the electron NTO being consistent for a given carbene across different metals and donors. However, the Ipr, CAAC, BZAC, BZI, and MAC complexes all have  $S_1 \rightarrow S_0$  NTOs that are described purely by the HOMO and LUMO, localized on the amide and carbene ligands, respectively.



<u>Figure S5.</u> The S<sub>0</sub> $\rightarrow$ S<sub>1</sub> transition of  $Au_{Cz}^{BZAC}$  involves an electron moving from the HOMO to LUMO and HOMO to LUMO + 1. The hole and electron NTOs ( $\Psi_{h+}$  and  $\Psi_{e-}$ ) are appropriate visualizations of the hole and electron wavefunctions corresponding to this transition. One can see that the electron NTO is made up of a linear combination of the  $\Psi_{LUMO}$  and  $\Psi_{LUMO+1}$ . The isopropyl groups are omitted from the diisopropylphenyl groups for clarity.

Further, all compounds in this study are described by a single hole and electron NTO pair. This simplifies overlap integral calculations which will be described in the next section.

## Overlap

The spatial NTO overlap integrals  $\Lambda_{NTO}$  were calculated for these compounds using a script that draws from the integration methods developed by G. Herman, *et al.*, <sup>7</sup> and S. G. P. Castro, *et al.*, <sup>8</sup> using a method reported previously. <sup>5, 9</sup> This makes use of the integral in Equation S1. which computes a weighted average of spatial overlap of all NTO pairs that contribute to the excited state

$$\Lambda_{NTO} \approx \frac{\sum_{k} c_{k} \iiint |\varphi_{k,h+}| |\varphi_{k,e-}| d\tau}{\sum_{k} c_{k}}$$
 (S1)

As aforementioned, all compounds in the study only require one electron/hole NTO pair to describe the excited state which simplifies the integral to equation 3 in the main text. However, it should be noted that all computed integrals were performed rigorously using equation S1, and not the simplified version seen in equation 3 of the manuscript. The overlap calculations reveal the drawbacks of relying on isovalue representations of the wavefunction. All NTO/MO visualizations with isovalue = 0.1 suggest that the hole and electron wavefunctions have very poor spatial overlap, and that most of the overlap comes from the metal d orbital. Certainly, one would not expect the calculated  $\Lambda_{NTO}$  values of 26-43% based on the wavefunction images in Figure S4 and S5. Thus, iso-value representations must be viewed with caution because the viewer does not know the probability of finding an electron within that surface, but only the isosurface corresponding to a probability per unit volume. In the case of cMa complexes, the volume within isovalue = 0.1 only contains 15% probability of finding an electron within the surface, which explains why the overlap integral can be large despite the isovalue = 0.1 visualization.

While overlap integrals give a more quantitative and accurate picture of the spatial overlap of hole and electron NTOs, it still fails to be a reliable parameter in predicting the parameters that account for the TADF rate  $k_r(S_1)$  and  $\Delta E_{ST}$ . The problem is that the integrals that govern  $k_r(S_1)$  and  $\Delta E_{ST}$  are not purely overlap integrals of  $\Psi_{h+}$  and  $\Psi_{e-}$ . For example, the Strickler-Berg relationship<sup>10</sup> is related to the transition dipole between two states by<sup>11</sup>

$$k_r(\Psi_1 \to \Psi_2) = \frac{8\pi^2 \langle \tilde{\nu}_f \rangle^3}{3h^2} |\langle \Psi_1 | \hat{\mu} | \Psi_2 \rangle|^2 \tag{S2}$$

and  $\Delta E_{\rm ST}$  is governed by the exchange integral

$$\Delta E_{ST} = 2 \left\langle \Psi_1 \middle| \frac{1}{r} \middle| \Psi_2 \right\rangle \tag{S3}$$

Many research groups identify the integrals in S2 and S3 and make the assumption that they trend well with the ordinary overlap integral  $\Lambda_{NTO}$ . However, this is only true in the limit of complete charge separation, where equation S1, S2, and S3 all converge to 0. Since the overlap calculations for two-coordinate cMa complexes with coplanar ligands is typically between 23-46%, this assumption cannot be made.

## Center of Charge and +/- separation

The integrals in equations S2 and S3 both have operators that completely change the outcome of integration. Integration relies heavily on symmetry and operators, thus a more straightforward parameter is desirable to predict  $k_r(S_1)$  and  $\Delta E_{ST}$ , and  $k_r(TADF)$ . We opted to reduce the problem to the center of charge of the hole and electron wavefunctions. The center of charge for the hole and electron NTOs of a given transition are extracted from the position expectation values of the respective wavefunctions

$$\langle r_{h+} \rangle = \langle \Psi_{h+} | \hat{r} | \Psi_{h+} \rangle \tag{S4}$$

$$\langle r_{e-} \rangle = \langle \Psi_{e-} | \hat{r} | \Psi_{e-} \rangle \tag{S5}$$

where  $|\Psi_{h+}\rangle$  and  $|\Psi_{e-}\rangle$  represent the hole and electron NTO wavefunctions. This can be calculated component-wise to extract the vectors

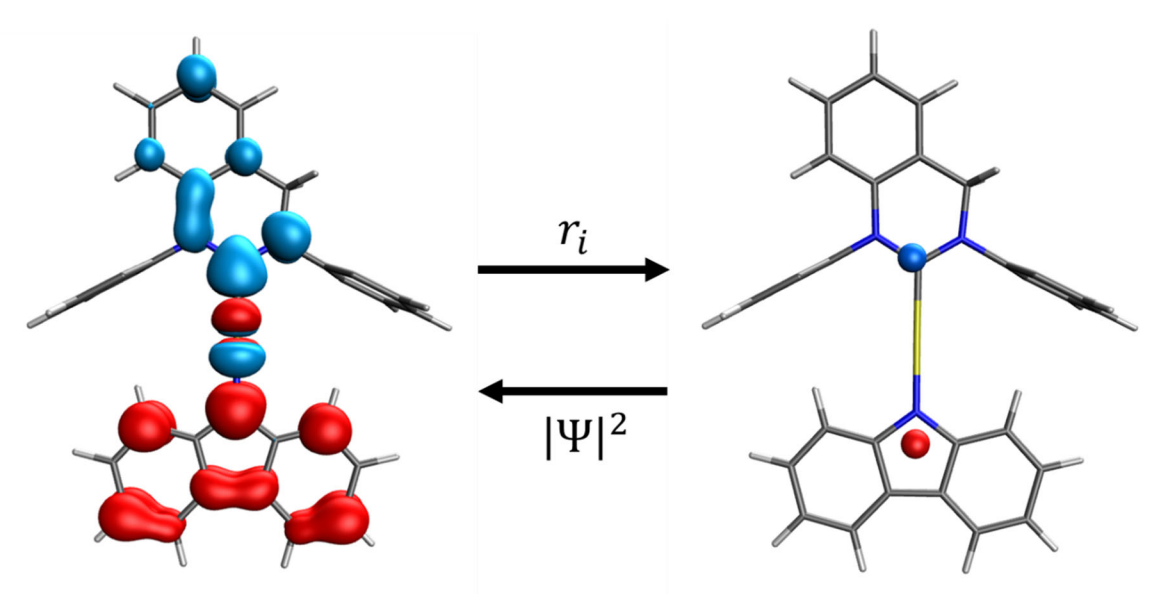
$$\vec{r}_{h+} = \sum_{j} \langle \Psi_{h+} | \hat{r}_{j} | \Psi_{h+} \rangle | j \rangle \tag{S6}$$

$$\vec{r}_{e-} = \sum_{i} \langle \Psi_{e-} | \hat{r}_{j} | \Psi_{e-} \rangle | j \rangle \tag{S7}$$

Where j represents a direction in a coordinate system. The  $\pm$ -separation is the difference of equation 6 and 7

$$d(h^+, e^-) = |\vec{r}_{h+} - \vec{r}_{e-}| \tag{S8}$$

which describes the separation between the hole and electron charges that constitute the exciton. Equations S6 and S7 are useful for visualizing the charges because a pseudo-particle can be imposed on the corresponding molecule by letting  $|j\rangle$  represent molecular coordinates as demonstrated in Figure S6. Again, the centers of charge are readily determined with the QChem software package. Center of charge descriptions are a much simpler parameter to understand compared to the wavefunction overlap  $\Lambda_{NTO}$ . We expect similar behavior; as the +/- separation increases, the exchange integral (equation S3) and the Einstein radiative rate (equation S2) should decrease. The utility of the center of charge descriptor is that it simply describes where the wavefunctions are centered, rather than integrating their products.



<u>Figure S6.</u> The NTO (left) and center of charge representation (right) for the hole and electron wavefunctions of (BZAC)Au(Cz). The isopropyl groups from the diisopropylphenyl substituents have been deleted for clarity. The iso value was set to 0.1 and the phase information omitted for the wavefunction visualization. The red density represents the hole wavefunction and the blue density represents the electron wavefunction respectively. A red dummy atom was placed at the  $r_{h+}$  coordinate and a blue dummy atom was placed at the  $r_{e-}$  coordinate.

<u>Table S5:</u> <u>Hole/electron separation distances for (carbene)Au(amide) complexes.</u>

Au <sup>Carbene</sup> amide	d(h <sup>+</sup> ,e <sup>-</sup> ) (Å)		
	Cz	bim	
Ipr	3.94	4.31	
BZI	5.15	5.51	
BZAC	5.08	5.36	
CAAC	4.43	4.74	
MAC	5.16	5.47	
PAC	5.55	5.86	
PZI	6.54 6.96		

Figure S7: HOMO/LUMO images for all cMa complexes studied here.

	НОМО	LUMO
$Cu^{BZAC}_{Cz}$		
$Cu_{Cz}^{MAC}$		
$Cu_{Cz}^{PAC}$		
$Ag_{Cz}^{PAC}$		
$Au^{PZI}_{Cz}$		

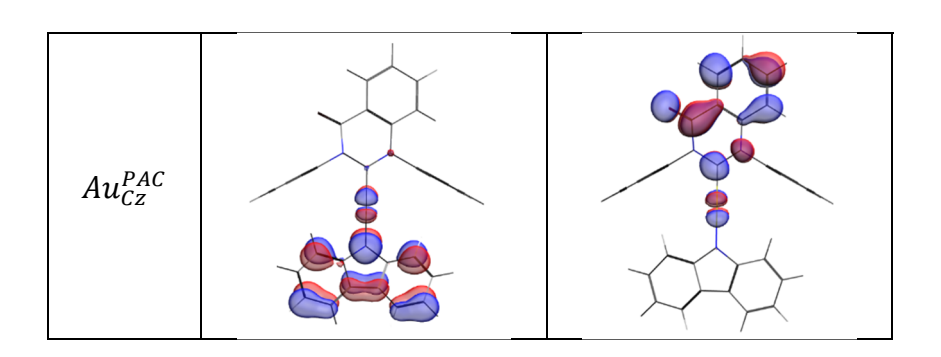


Figure S7 (continued): HOMO/LUMO images for all cMa complexes studied here.

$Au_{Cz}^{MAC}$		
$Au^{\mathit{CAAC}}_{\mathit{Cz}}$		
$Au^{BZAC}_{Cz}$		
$Au_{Cz}^{BZI}$		
$Au^{Ipr}_{Cz}$		LUMO+6

Figure S7 (continued): HOMO/LUMO images for all cMa complexes studied here.

Au <sup>PZI</sup>	
$Au_{bim}^{PAC}$	
$Au_{bim}^{MAC}$	
$Au_{bim}^{\mathit{CAAC}}$	
$Au_{bim}^{BZAC}$	

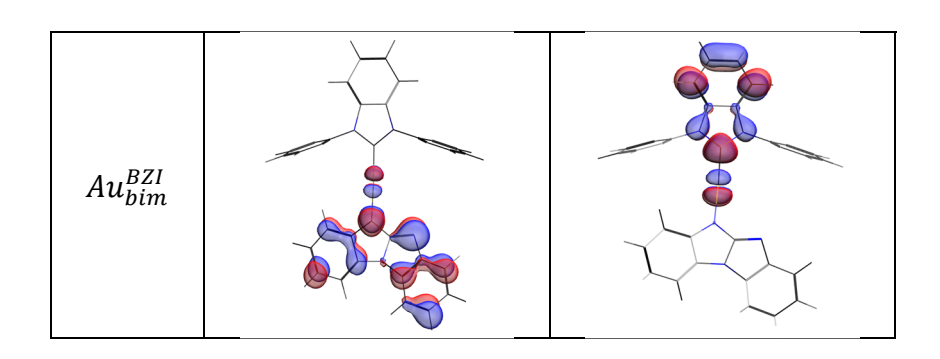
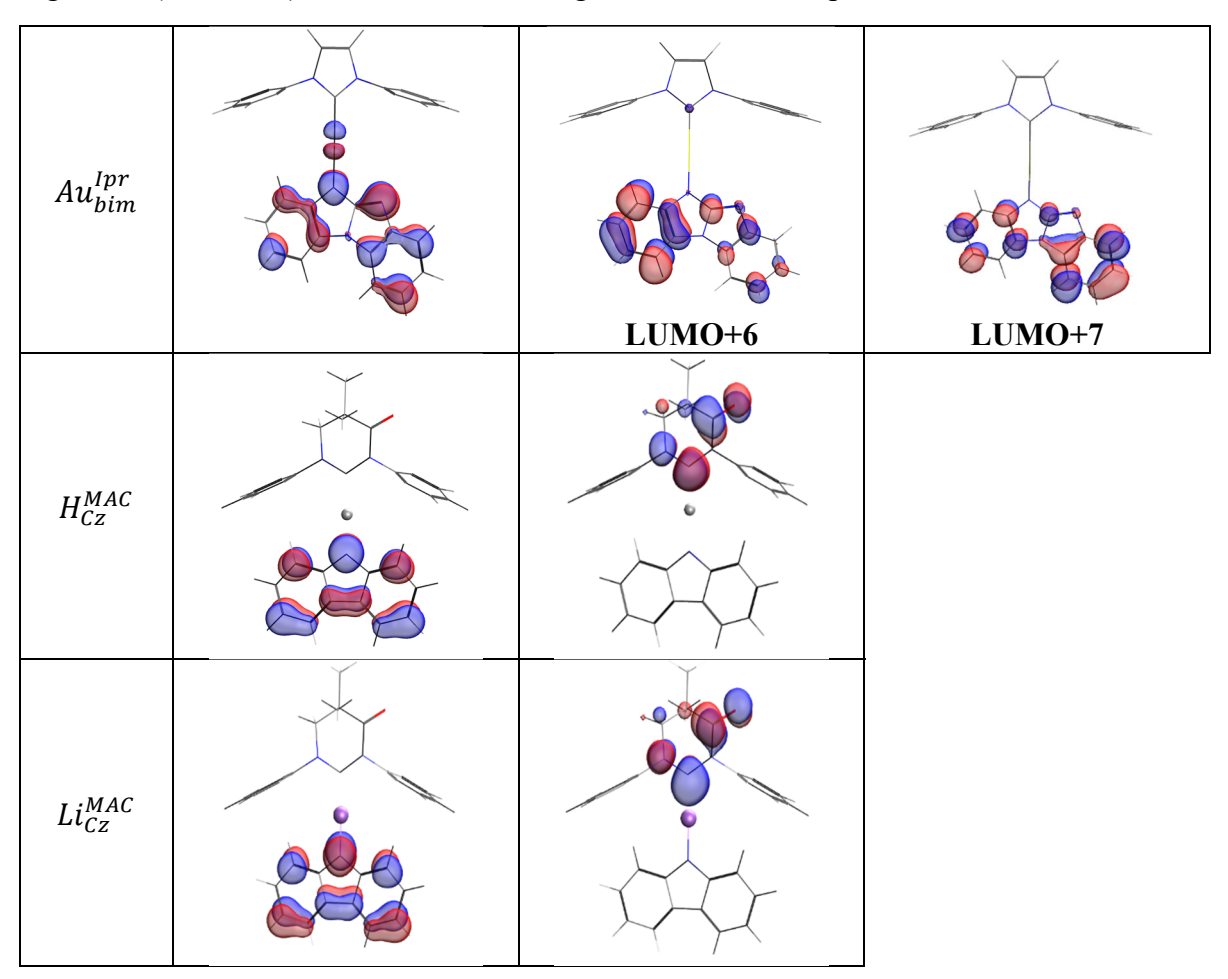


Figure S7 (continued): HOMO/LUMO images for all cMa complexes studied here.



<u>Table S5:</u> Compositions of the  $S_1$  and  $T_1$  states for the cMa complexes. The percent composition was calculated by normalizing square of the relative amplitudes of MOs involved in the transition to the sum of the squares of the relative amplitudes.

	S <sub>1</sub> Decomposition	T <sub>1</sub> Decomposition	
$Cu_{Cz}^{BZAC}$	110110 11110 1000/	HOMO → LUMO: 94%	
	HOMO → LUMO: 100%	HOMO → LUMO+6: 6%	
$Cu_{Cz}^{MAC}$	HOMO → LUMO: 100%	HOMO → LUMO: 100%	
$Cu_{Cz}^{PAC}$	HOMO → LUMO: 70%	HOMO → LUMO: 58%	
$cu_{Cz}$	$HOMO \rightarrow LUMO+1: 30\%$	$HOMO \rightarrow LUMO+1: 42\%$	
$Ag_{Cz}^{PAC}$	HOMO → LUMO: 73%	HOMO → LUMO: 63%	
$Hy_{Cz}$	HOMO → LUMO+1: 27%	HOMO → LUMO+1: 37%	
$Au_{Cz}^{PAC}$	HOMO → LUMO: 72%	HOMO → LUMO: 59%	
	HOMO → LUMO+1: 28%	HOMO → LUMO+1: 41%	
$Au_{Cz}^{MAC}$	HOMO → LUMO: 100%	HOMO → LUMO: 100%	
$Au_{Cz}^{CAAC}$	HOMO → LUMO: 100%	HOMO → LUMO: 100%	
$Au_{Cz}^{BZAC}$	HOMO → LUMO: 100%	HOMO → LUMO: 94%	
$Hu_{CZ}$	110MO → LUMO. 100/6	HOMO → LUMO+6: 6%	
$Au_{Cz}^{BZI}$	HOMO → LUMO: 100%	HOMO → LUMO: 93%	
Au <sub>Cz</sub>	110MO - LOMO. 10076	HOMO → LUMO+6: 7%	
$Au_{Cz}^{Ipr}$	HOMO → LUMO: 100%	HOMO → LUMO: 54%	
Au <sub>Cz</sub>	TIOMO -7 LOMO. 10070	HOMO → LUMO+6: 45%	
$Au_{bim}^{PAC}$	HOMO → LUMO: 72%	HOMO → LUMO: 62%	
	HOMO → LUMO+1: 28%	HOMO → LUMO+1: 38%	
$Au_{bim}^{MAC} \ Au_{bim}^{CAAC} \ Au_{bim}^{CAAC} \ Au_{bim}^{BZAC}$	HOMO → LUMO: 100%	HOMO → LUMO: 100%	
$Au_{bim}^{CAAC}$	HOMO → LUMO: 100%	HOMO → LUMO: 100%	
$Au_{bim}^{BZAC}$	HOMO → LUMO: 100%	HOMO → LUMO: 100%	
$Au_{bim}^{BZI}$	HOMO → LUMO: 100%	HOMO → LUMO: 100%	
		$HOMO-2 \rightarrow LUMO+11: 11\%$	
_		HOMO-1→ LUMO+6: 7%	
$Au_{bim}^{Ipr}$	HOMO → LUMO: 100%	HOMO-1→ LUMO+7: 9%	
		HOMO → LUMO+6: 38%	
		HOMO → LUMO+7: 35%	
$H_{Cz}^{MAC}$	HOMO → LUMO: 100%	HOMO → LUMO+1: 87%	
		HOMO → LUMO+2: 6%	
		HOMO → LUMO+3: 6%	
$Li_{Cz}^{MAC}$	HOMO → LUMO: 100%	HOMO → LUMO: 100%	

<u>Table S6:</u> Dipole moments of the ground, S<sub>1</sub> and T<sub>1</sub> states. These values were determined form DFT and TDDFT modeling studies. Ground state dipoles are oriented along the M-N bond, from the metal toward the amide. Excited state dipoles are oriented in the opposite direction, toward the carbene.

	μ - S <sub>0</sub> (D)	μ - S <sub>1</sub> (D)	μ - T <sub>1</sub> (D)	Δμ (S <sub>0</sub> -S <sub>1</sub> ) (D)	Δμ (S <sub>0</sub> -T <sub>1</sub> ) (D)
$Cu_{Cz}^{BZAC}$	11.6	-12.4	-10.4	24	22
$Cu_{Cz}^{MAC}$	10.1	-15.3	-13.6	25.4	23.7
$Cu_{Cz}^{PAC}$	10.4	-16.8	-14.4	27.2	24.8
$Ag_{Cz}^{PAC}$	11.9	-19.3	-17.7	31.2	29.6
$Au_{Cz}^{PAC}$	10.0	-17.6	-15.2	27.6	25.2
$Au_{Cz}^{MAC}$	9.8	-15.9	-14.5	25.7	24.3
$Au_{Cz}^{CAAC}$	15.3	-10.1	-8.84	25.4	24.14
$Au_{Cz}^{BZAC}$	11.4	-12.8	-10.7	24.2	22.1
$Au_{Cz}^{BZI}$	11.2	-13.4	-10.7	24.6	21.9
$Au_{bim}^{PAC}$	8.2	-20.2	-17.8	28.4	26
$Au_{bim}^{MAC}$	10.3	-18.3	-16.8	28.6	27.1
$Au_{bim}^{CAAC}$	10.6	-12.7	-11.0	23.3	21.6
$Au_{bim}^{BZAC}$	10.7	-15.0	-12.5	25.7	23.2
$Au_{bim}^{BZI}$	10.8	-15.8	-13.1	26.6	23.9
$Au_{bim}^{Ipr}$	11.0	-9.9	12.3*	20.9	-1.3
$H_{Cz}^{MAC}$	11.6	-18.2	-15.8	29.8	NA
$Li_{Cz}^{MAC}$	11.5	-15.7	-15.4	27.2	NA

<sup>\*</sup> The  $T_1$  for  $Au_{bim}^{Ipr}$  is not an ICT state but is localized on the bim ligand.

# Photophysical data

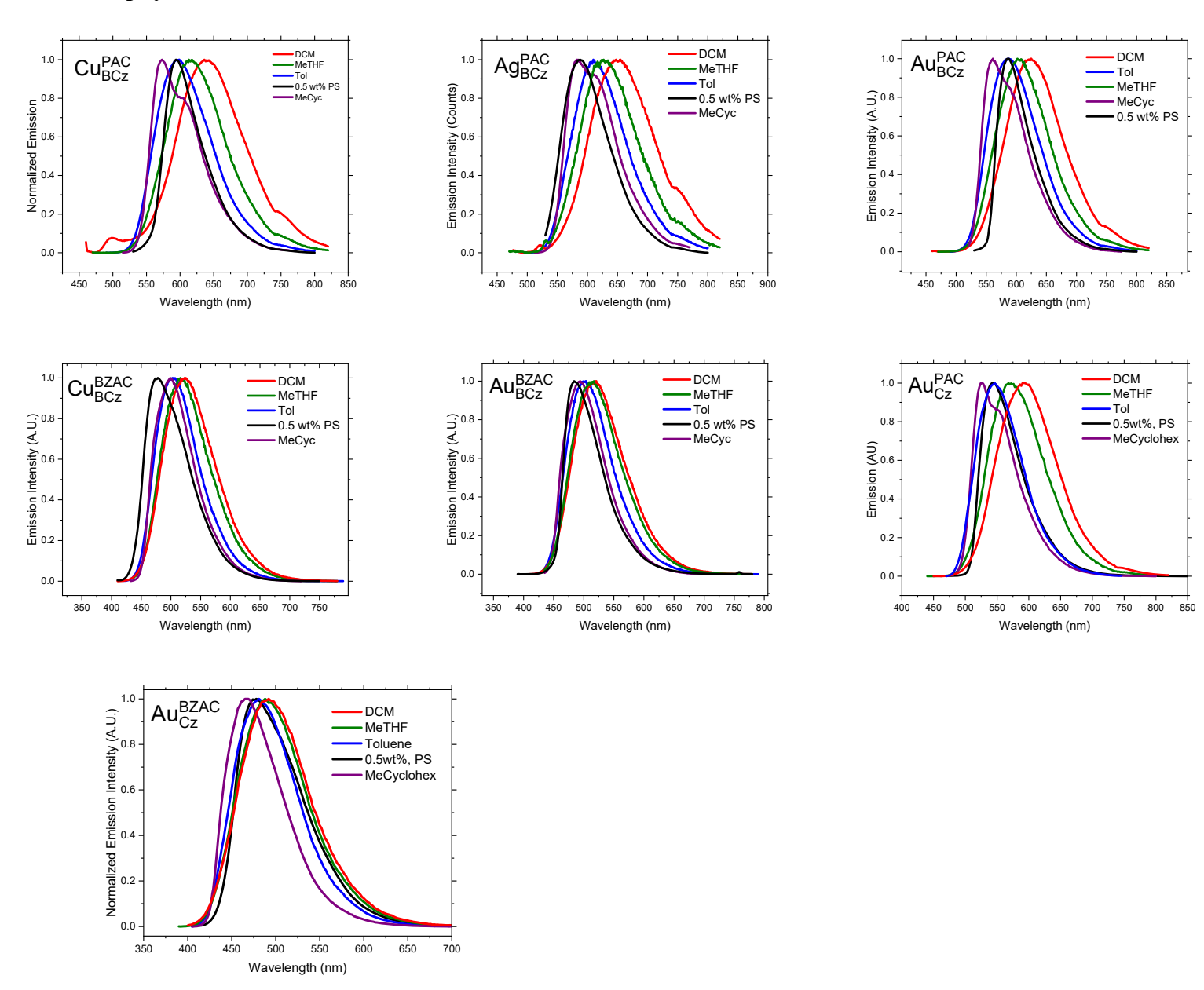
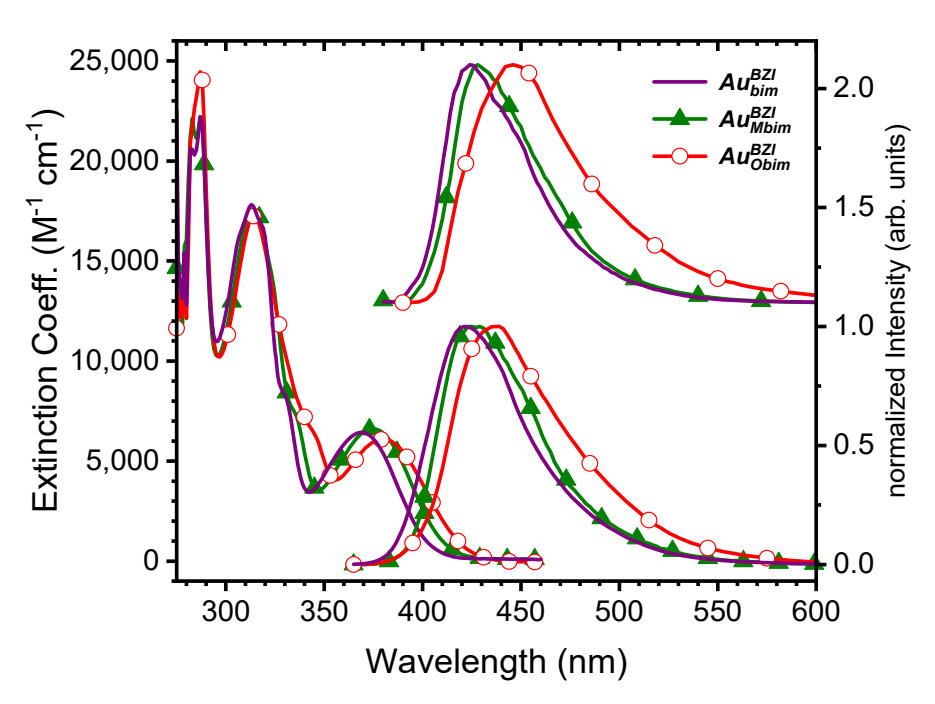
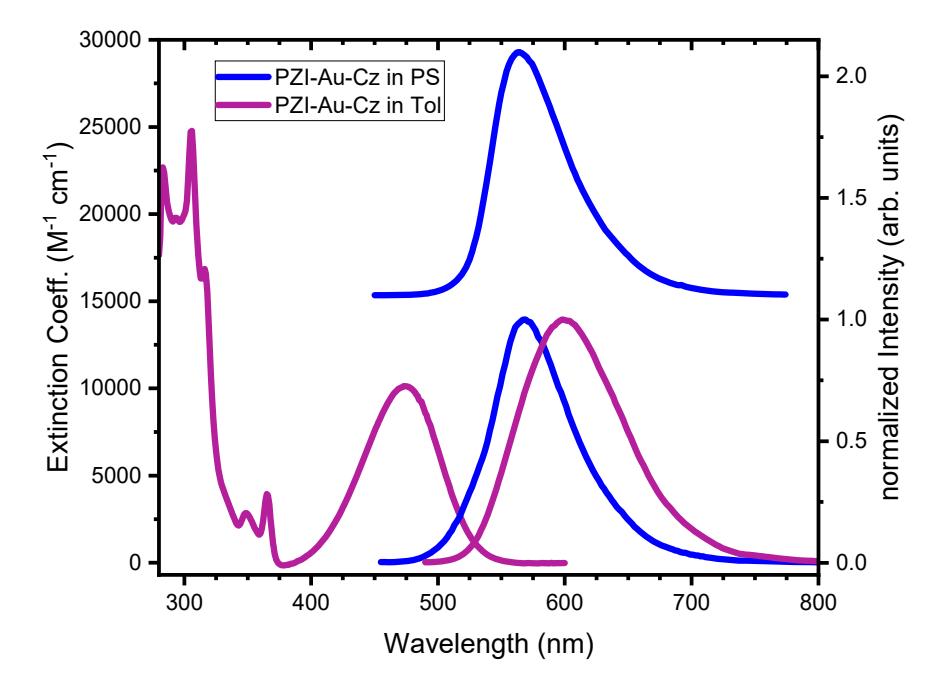


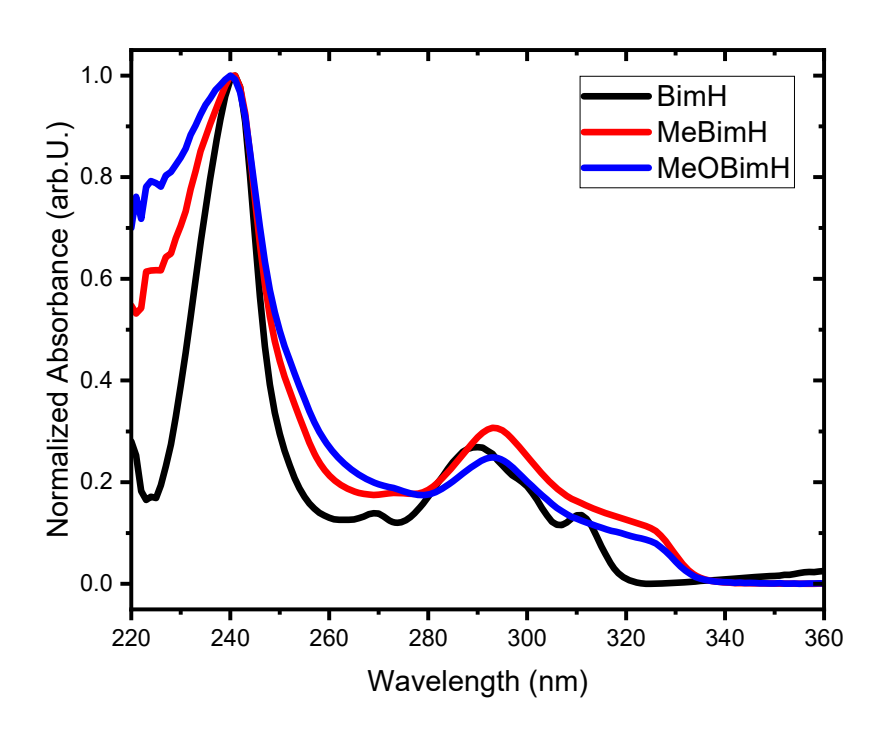
Figure S8: Emission solvatochromism plots of cMa complexes.

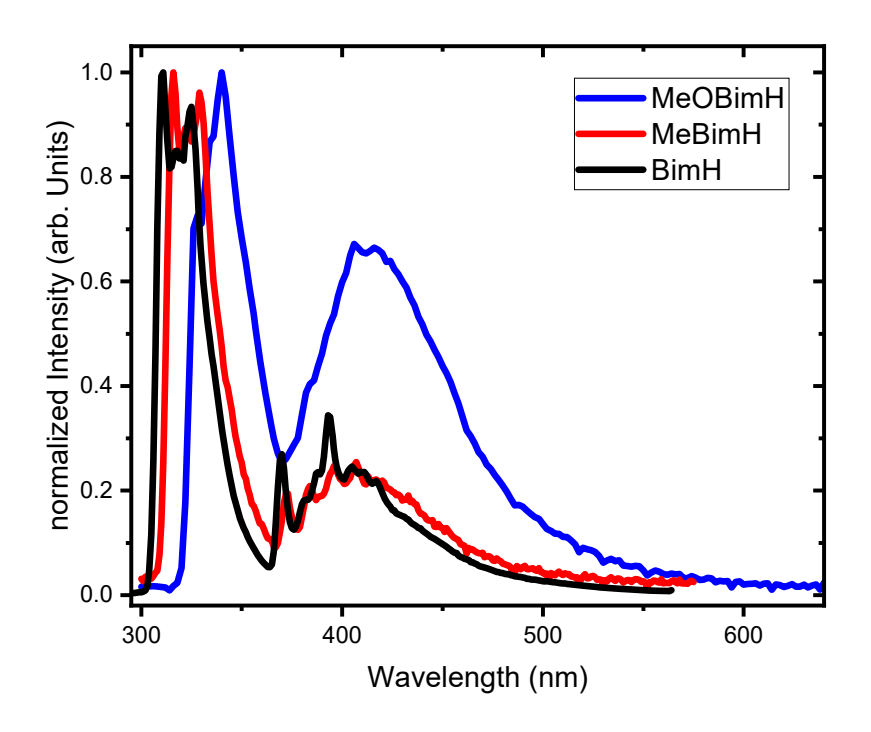


<u>Figure S9:</u> Absorption and emission spectra for (BZI)Au(amide), amide = bim, Mbim and Obim. Extinction spectra are recorded in toluene solution (bottom) and emission spectra in 1% doped polystyrene thin films (top).

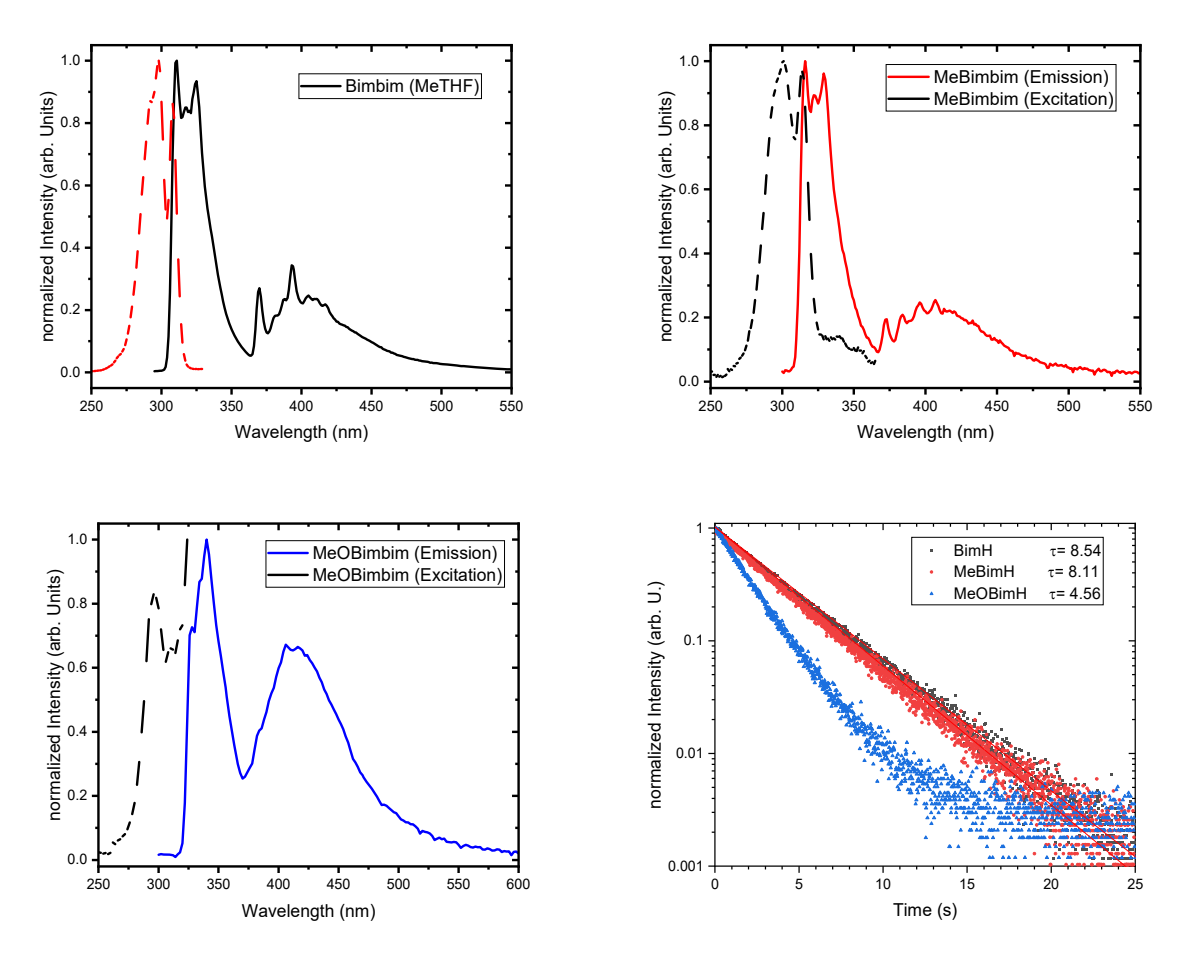


<u>Figure S10:</u> Absorption and emission spectra for (PZI)Au(Cz), extinction spectra are recorded in toluene solution and emission spectra in 1% doped thin polystyrene (PS) films or toluene (Tol) as indicated. Emission spectra were recorded in polystyrene at 298 K (bottom) and 77 K (top).





<u>Figure S11:</u> Absorption spectra in toluene (top) and emission spectra in 2-MeTHF (bottom) of BimH, MebimH and ObimH (the free ligands).



<u>Figure S12:</u> Excitation, emission and gated emission (phosphorescence) spectra of BimH, MeBimH and OBimH in 2-MeTHF.

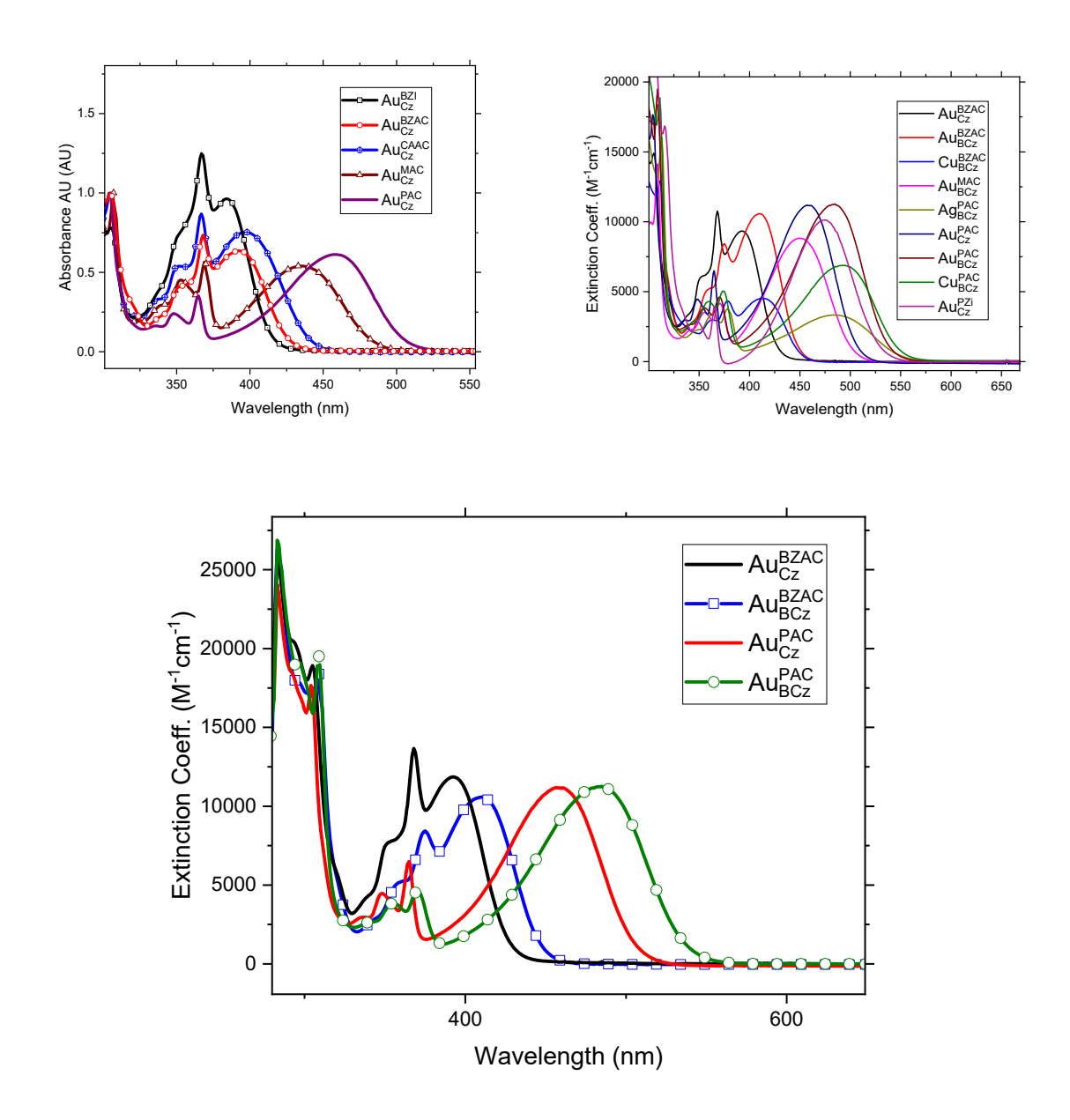


Figure S13. Absorption spectra for (carbene)Au(Cz) and (carbene)Au(BCz) in toluene comparing (carbene)Au(Cz) to (carbene)AuB(Cz). The spectra show that BCz does not significantly perturb the extinction coefficient. This is important when discussing  $k_r$  in (BZAC)Au(Cz) versus (BZAC)Au(BCz) in polystyrene films.

### Temperature dependent photophysics and Boltzmann fitting

Cryogenic photophysical measurements were carried out on a Janis SHI-4-2 cryostat with a Lakeshore 335 Temperature controller and evacuated by an Drytel 31 Turbomolecular pump to  $1.2 \times 10^{-4}$  mTorr. Doped polystyrene thin films spin coated on a round sapphire substrate were used for good thermal conductivity. Experiments showed that the thermal conductivity of the quartz substrates was too low and only sapphire is thermally conductive enough to effectively reach 4 K inside the polystyrene film. This was checked by measuring the lifetime of *fac*-Ir(ppy)<sub>3</sub> doped into polystyrene and PMMA films and cross checked with the data published by Yersin et.al.<sup>12</sup>

The original sample holder was modified in a way, that the emitted light can be collected from the side of the sapphire substrate, as the outcoupling efficiency is highest and the unwanted collected excitation light is minimal in this set-up geometry. See the following figure for the modified sample holder:



The emitted light was collimated by an Edmund Optics 45-716 Lens (Focus: 75mm, Ø 50 mm, VIS-NIR coating for 400-1000nm) and focused with an Edmund Optics 47-393 Lens (Focus: 125mm, Ø 50 mm, VIS-NIR coating for 400-1000nm) Lens onto a Thorlabs BF13LSMA02 (400-2200 nm, Ø 1.3 mm) optical fiber connected to a Thorlabs bifurcated fiber BF19Y2LS02 (250-1200 nm, 19 Fiber, Ø 200  $\mu$ m) with 10 fibers ending in the TCSPC and 9 fibers in the fluorimeter.

Emission spectra were collected with a Photon Technology International QuantaMaster spectrofluorimeter. As Excitation source a 365nm LED (Thorlabs M365L3 365nm LED, 1000 mW) equipped with the Thorlabs SM1U25-A Adjustable Collimation Adapter and driven with a Thorlabs LEDD1B driver.

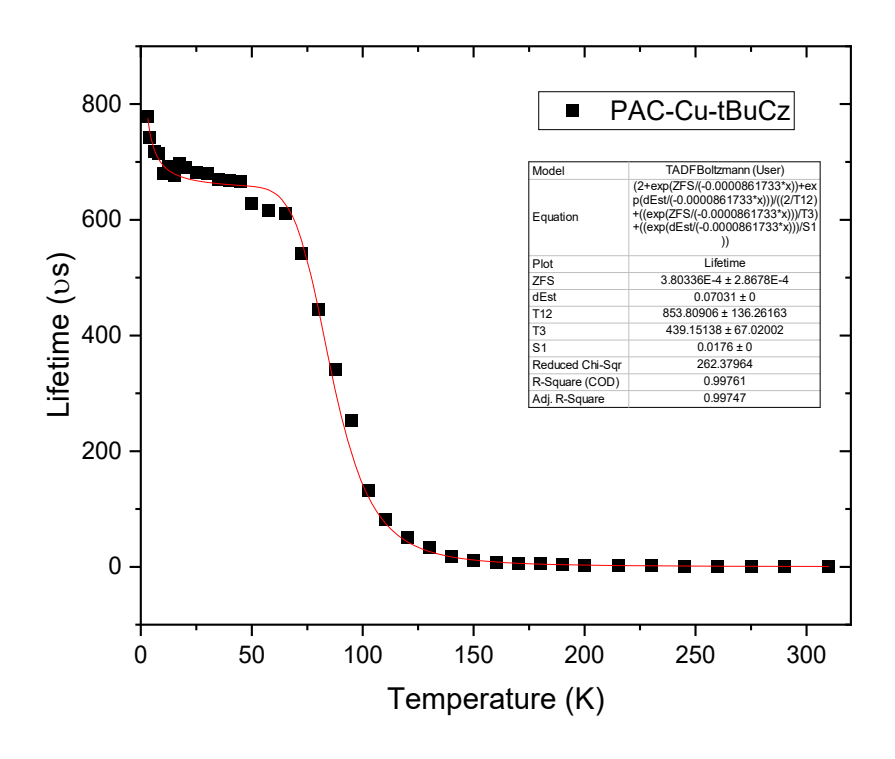
For luminescence lifetime studies a Horibia Fluorohub+ with a Horiba Jobin Yvon detector with monochromator was used. As excitation source a NanoLED 407N (405 nm) or IBH SpectraLED S-03 (372 nm) was used.

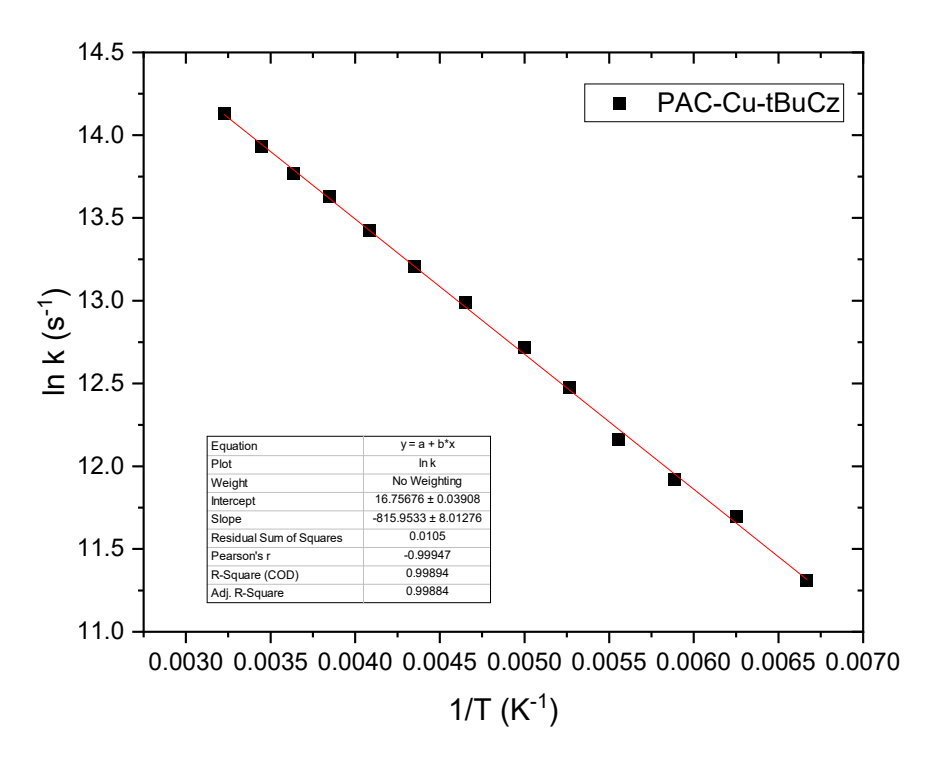
Values for the measured lifetime were plotted against temperature to obtain the plots in the following figures. High temperature data from 150 K – 300 K were fitted to an Arrhenius equation according to Hamze, et al.<sup>13</sup> The plots of  $ln(k_{TADF})$  vs. 1/T are given below with their linear fit values.  $\Delta E_{ST}$  and  $\tau_{SI}$  was obtained from the slope and intercept respectfully.

Zero-Field Splitting (ZFS) and  $\tau_{T3}$  was obtained from Boltzmann fits of the plots lifetime vs. temperature using the following equation:

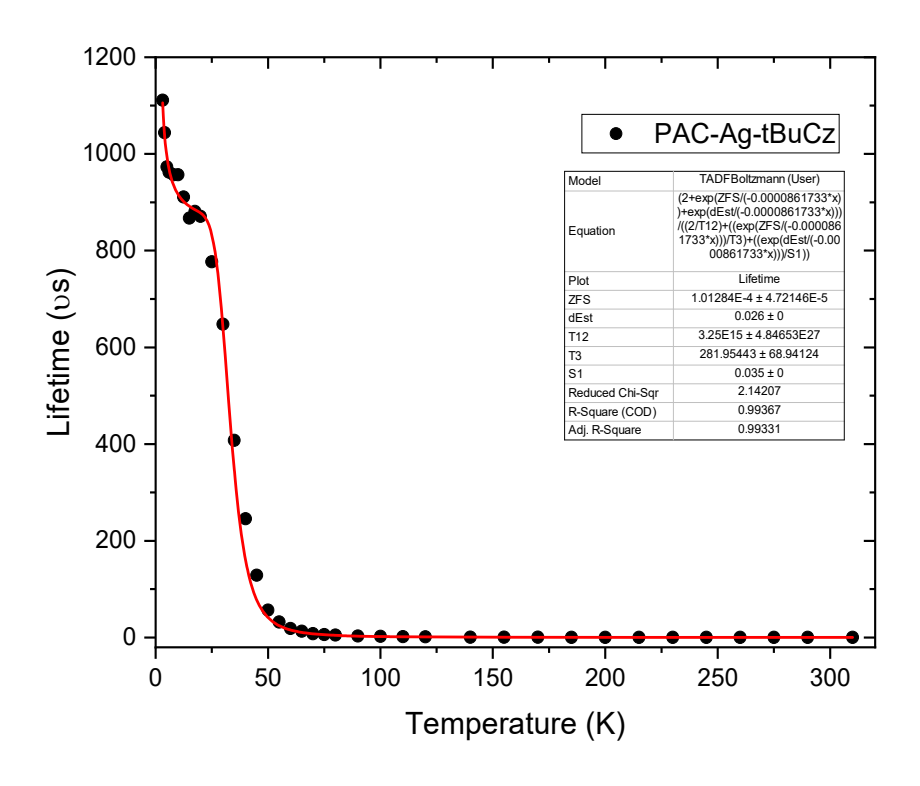
$$\tau = \frac{2 + e^{-\frac{\Delta E(III - I,II)}{k_B T}} + e^{-\frac{\Delta E(S_1 - I,II)}{k_B T}}}{2(\frac{1}{k_{I,II}}) + (\frac{1}{k_{III}})e^{-\frac{\Delta E(III - I,II)}{k_B T}} + (\frac{1}{k_{fl}})e^{-\frac{\Delta E(S_1 - I,II)}{k_B T}}}$$

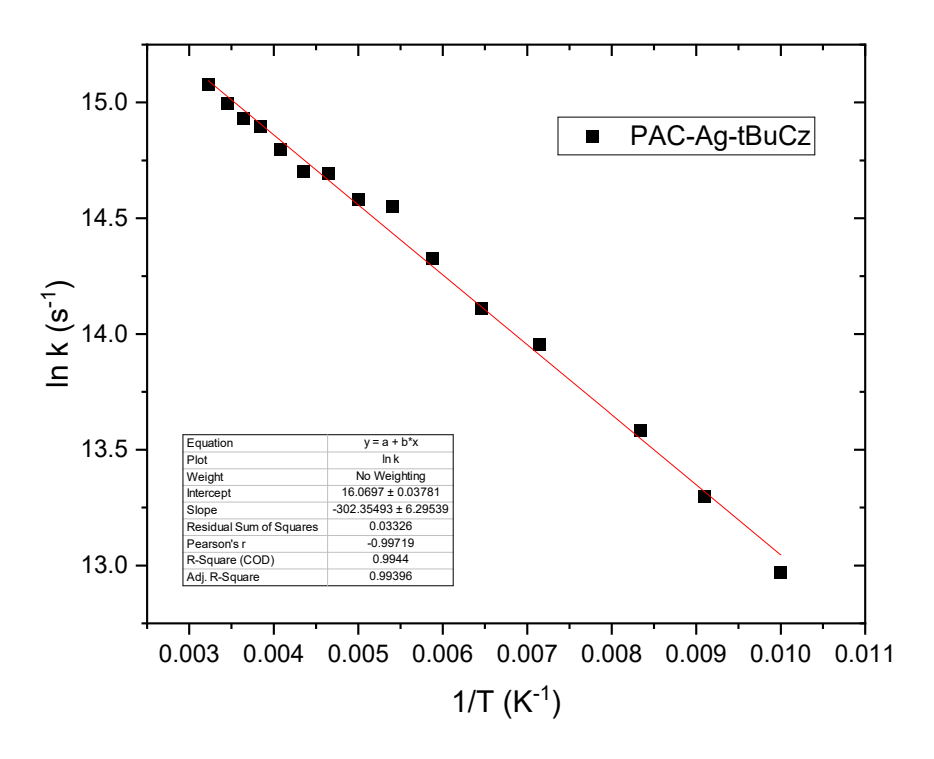
Statistical weighing was used in fits to prevent a higher contribution of long lifetimes. The previously determined  $\Delta E_{\rm ST}$  and  $\tau_{\rm SI}$  were used as fixed parameters in the equation.  $\tau_{\rm T1,2}$  could not be reliably determined due to insufficient data below 4 K.



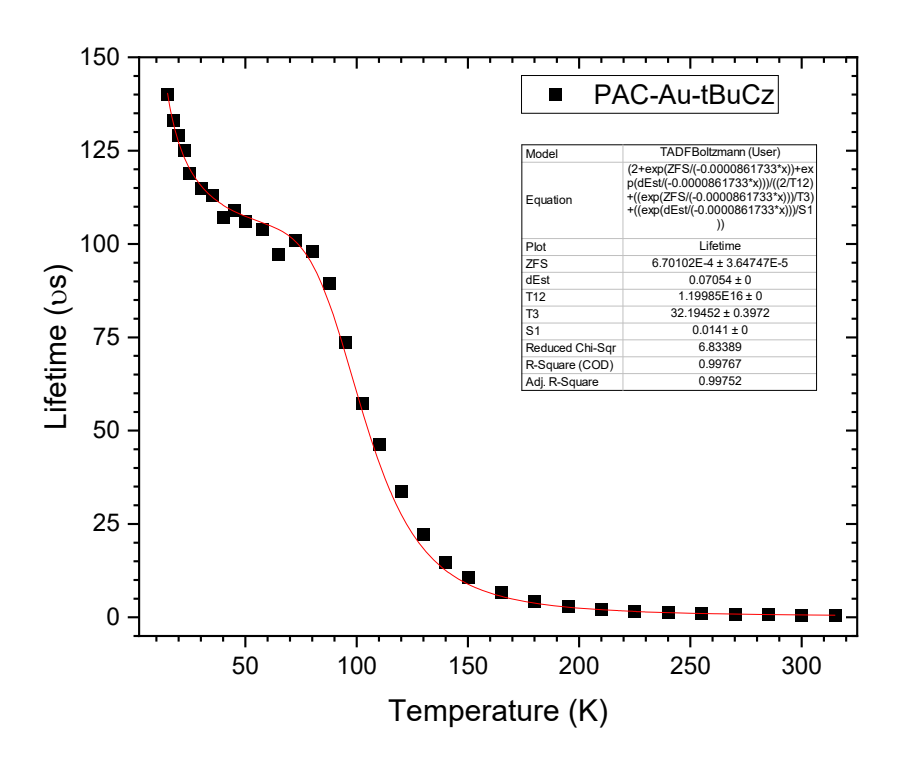


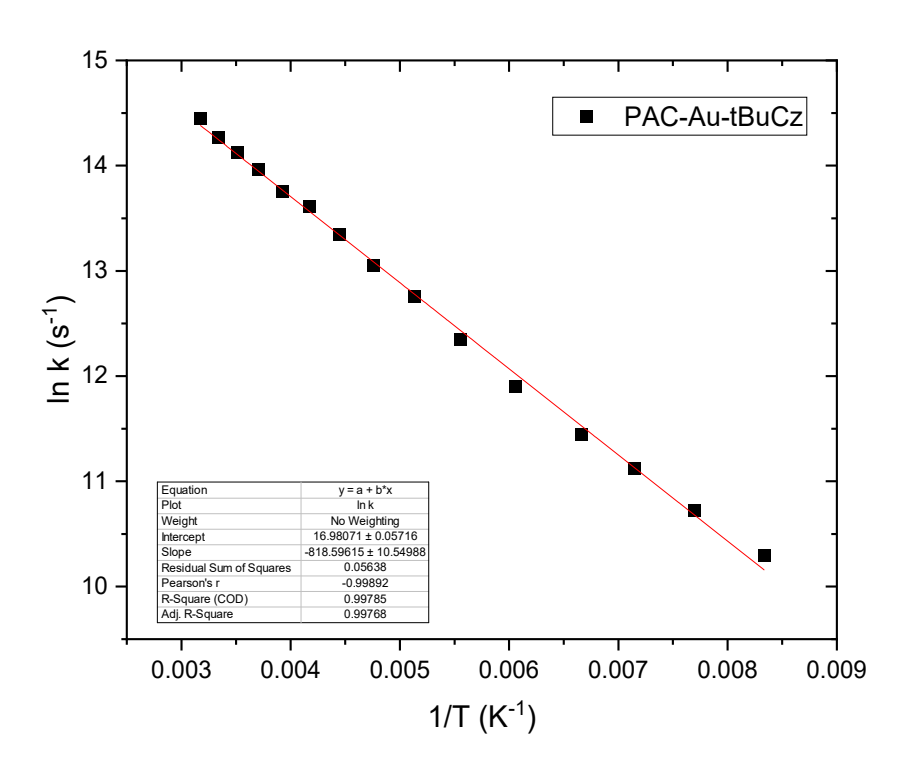
<u>Figure S14:</u> Temperature dependent lifetime for (PAC)Cu(BCz) in PS. Boltzmann fit (top) and Arrhenius plot (bottom).



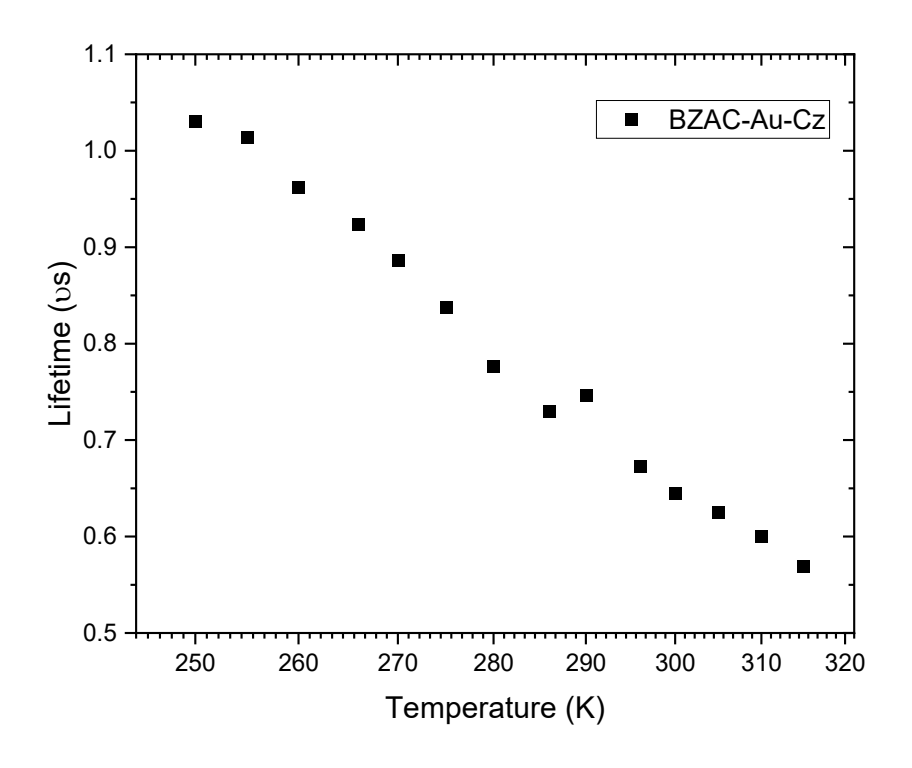


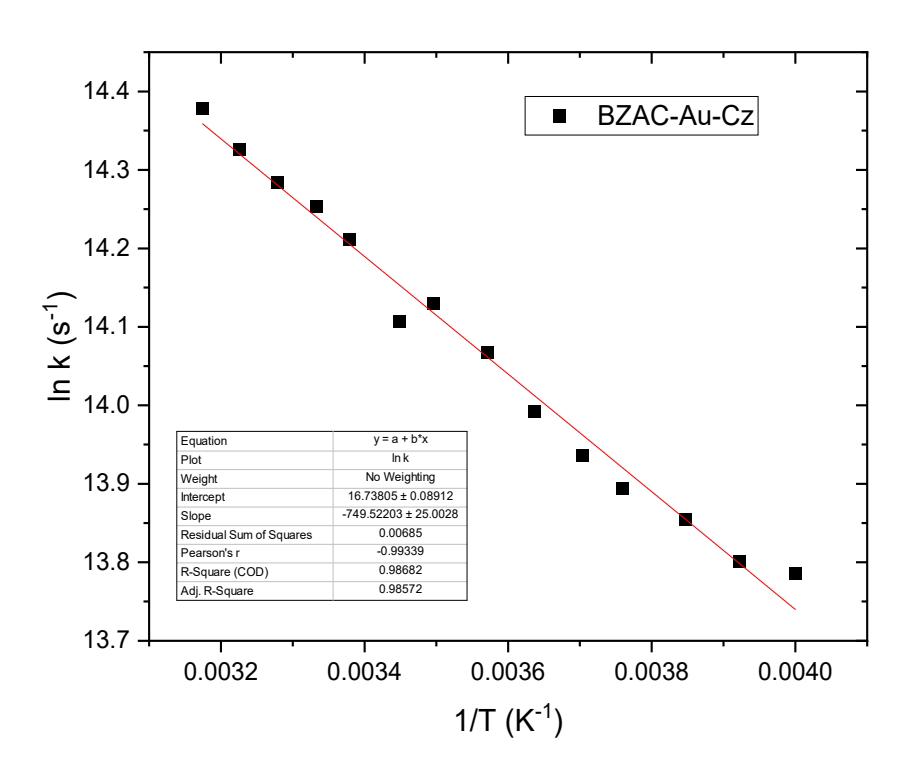
<u>Figure S15:</u> Temperature dependent lifetime for (PAC)Ag(BCz) in PS. Boltzmann fit (top) and Arrhenius plot (bottom).



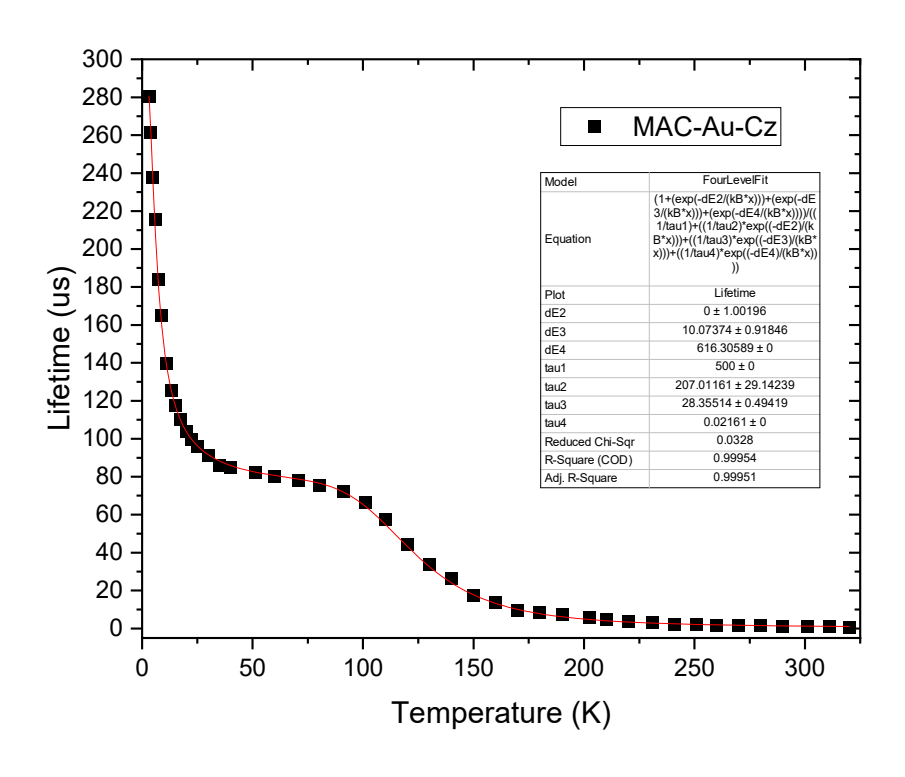


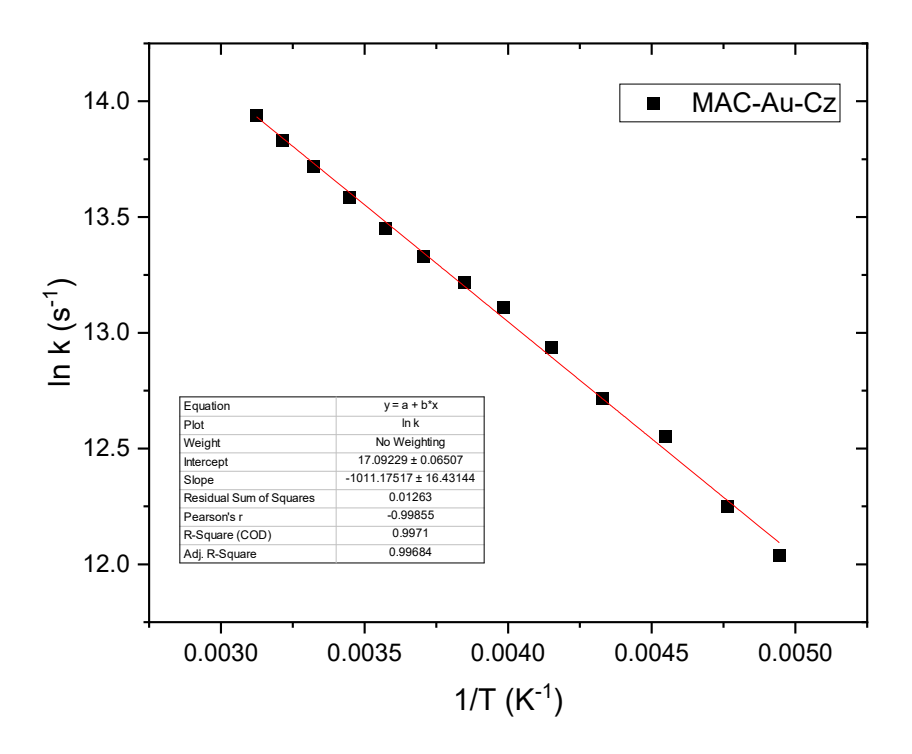
<u>Figure S16:</u> Temperature dependent lifetime for (PAC)Au(BCz) in PS. Boltzmann fit (top) and Arrhenius plot (bottom).



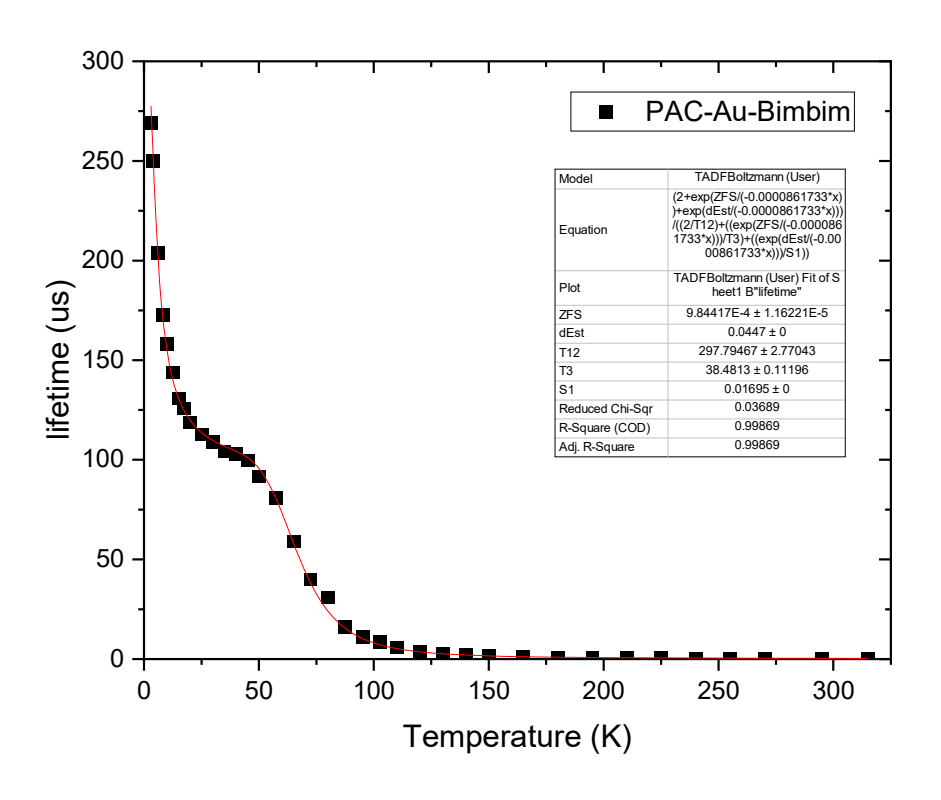


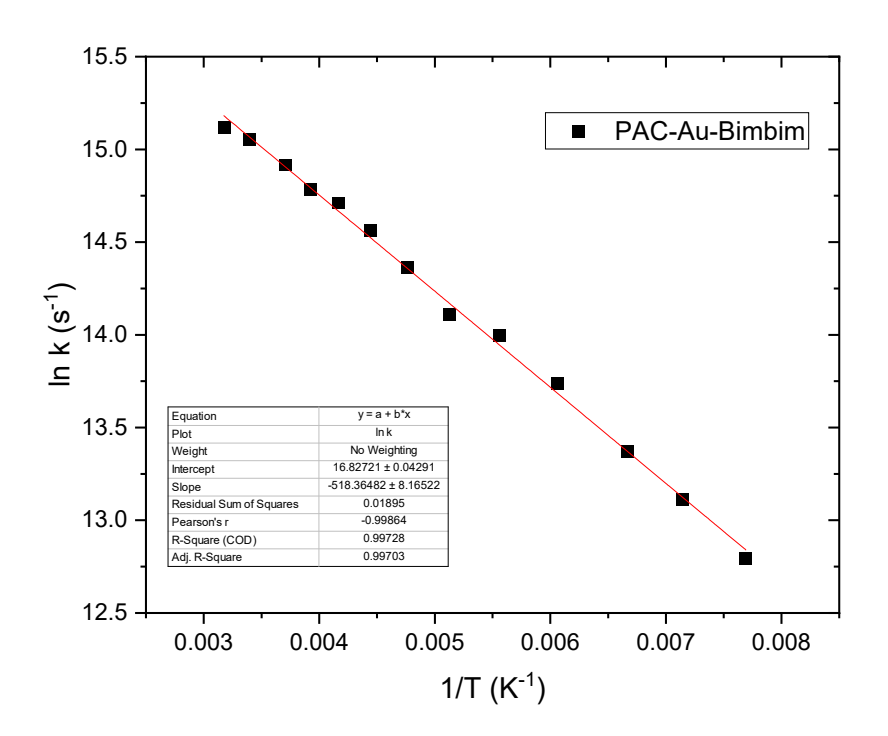
<u>Figure S17:</u> Temperature dependent lifetime for (BZAC)Au(Cz) in PS. Boltzmann fit (top) and Arrhenius plot (bottom).



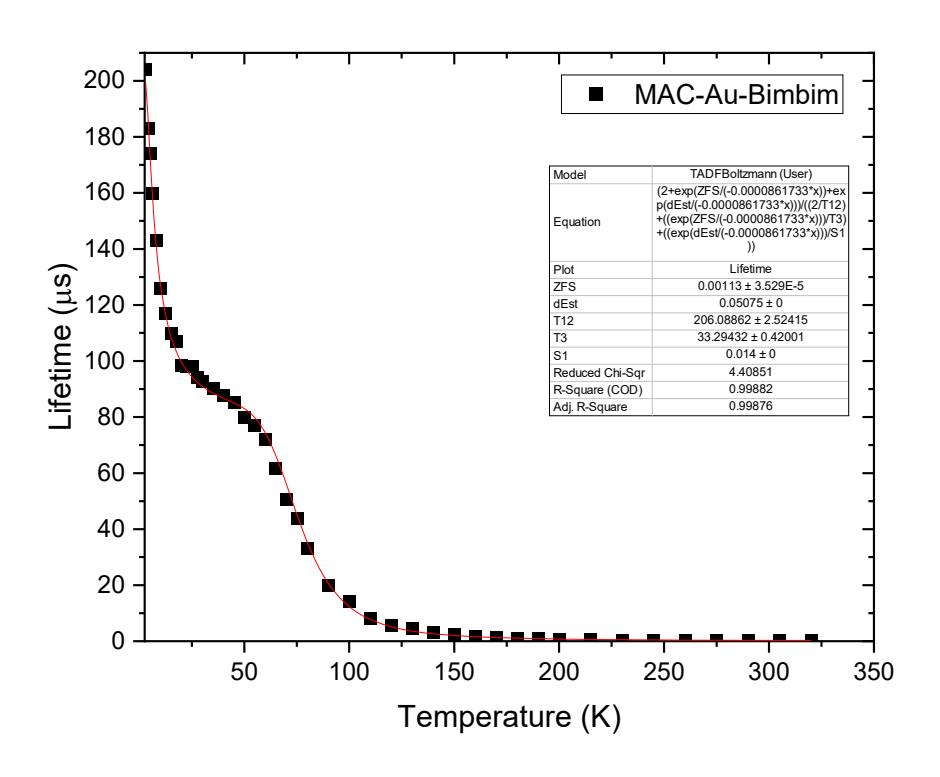


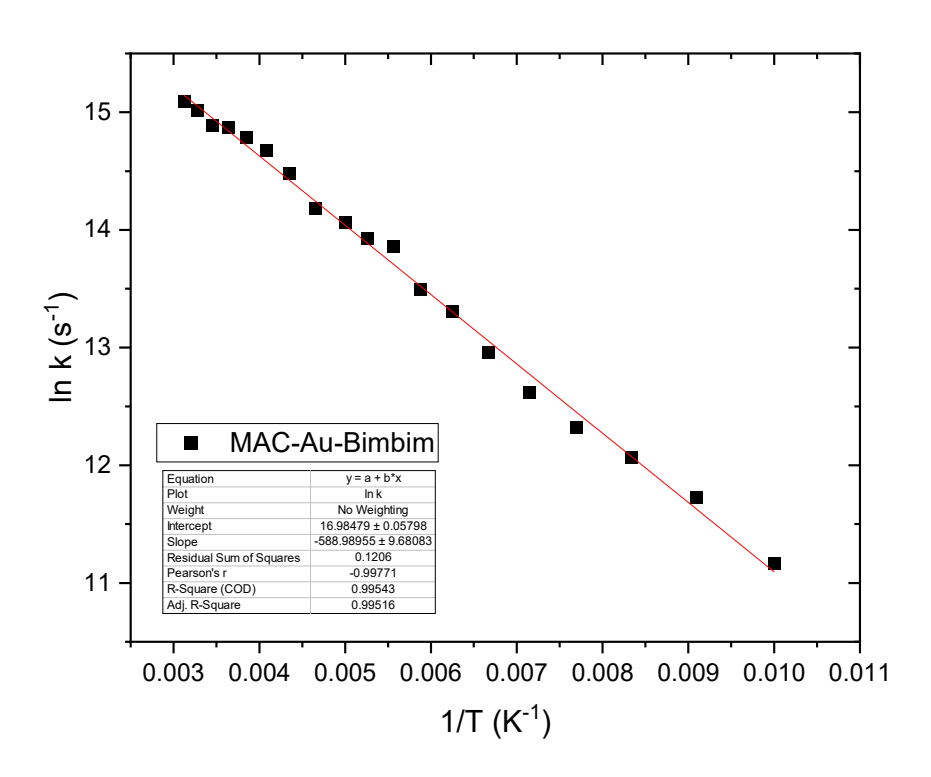
<u>Figure S18:</u> Temperature dependent lifetime for (MAC)Au(Cz) in PS. Boltzmann fit (top) and Arrhenius plot (bottom).



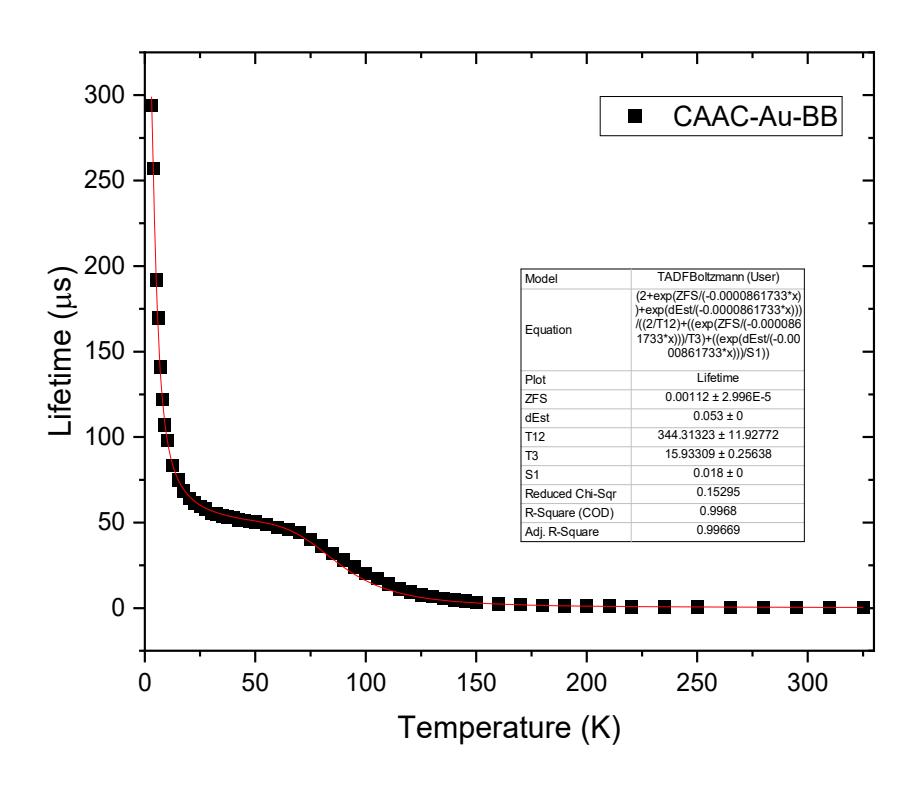


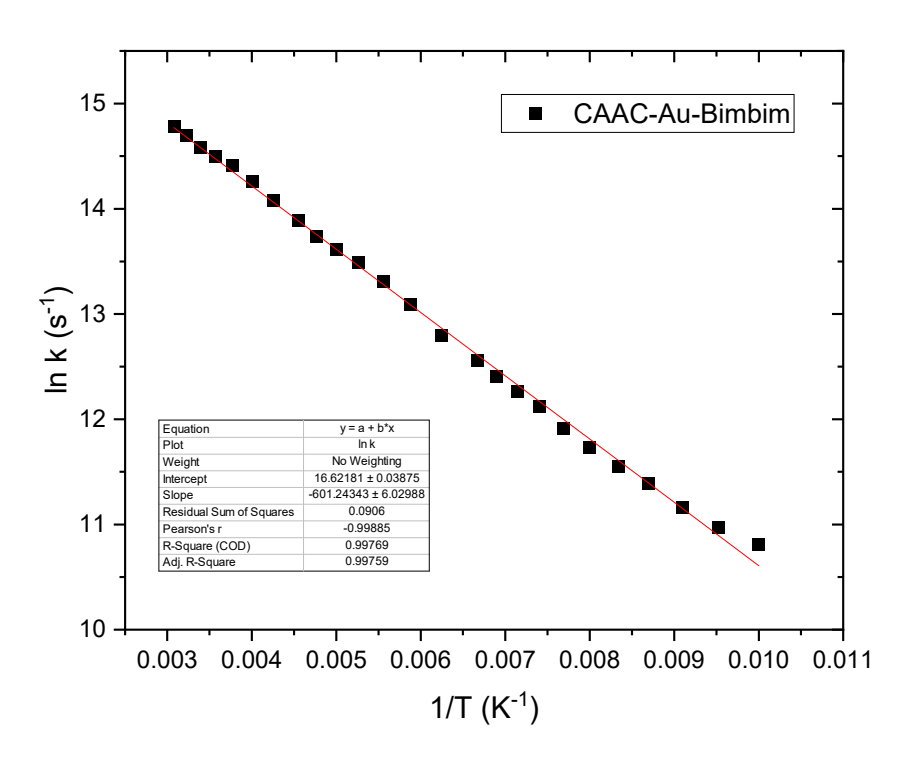
<u>Figure S19:</u> Temperature dependent lifetime for (PAC)Au(Bim) in PS. Boltzmann fit (top) and Arrhenius plot (bottom).



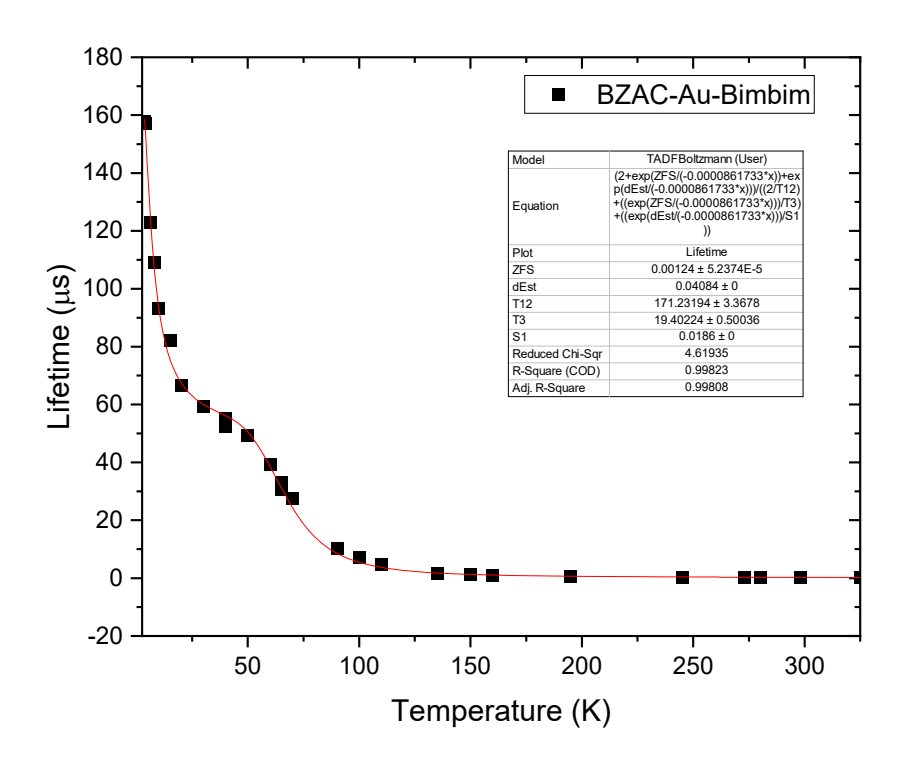


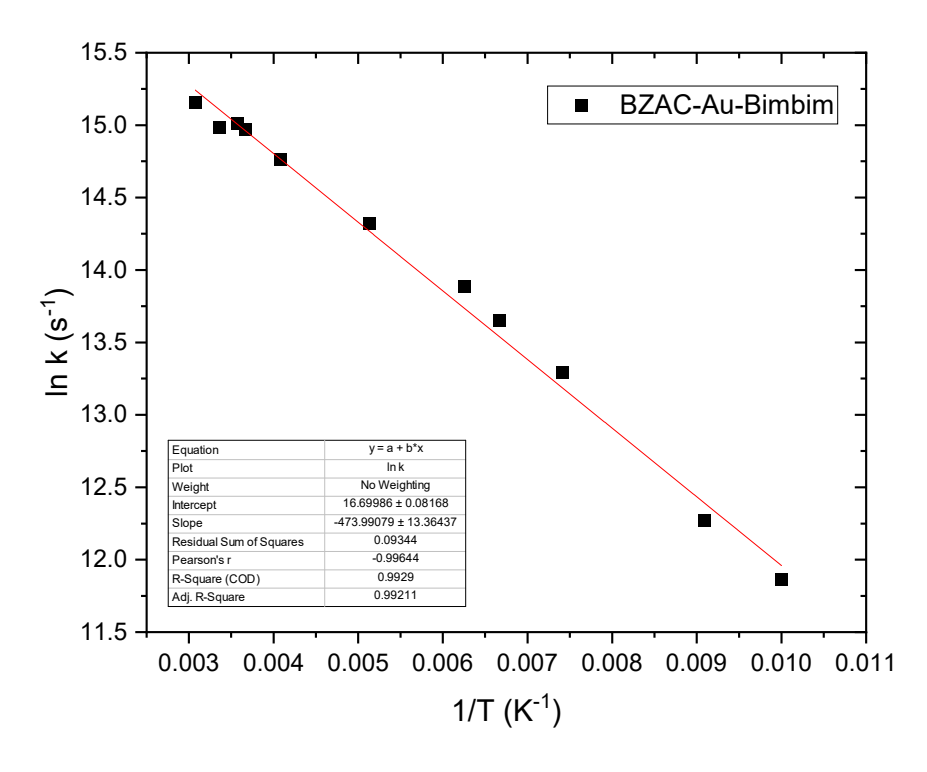
<u>Figure S20:</u> Temperature dependent lifetime for (MAC)Au(Bim) in PS. Boltzmann fit (top) and Arrhenius plot (bottom).



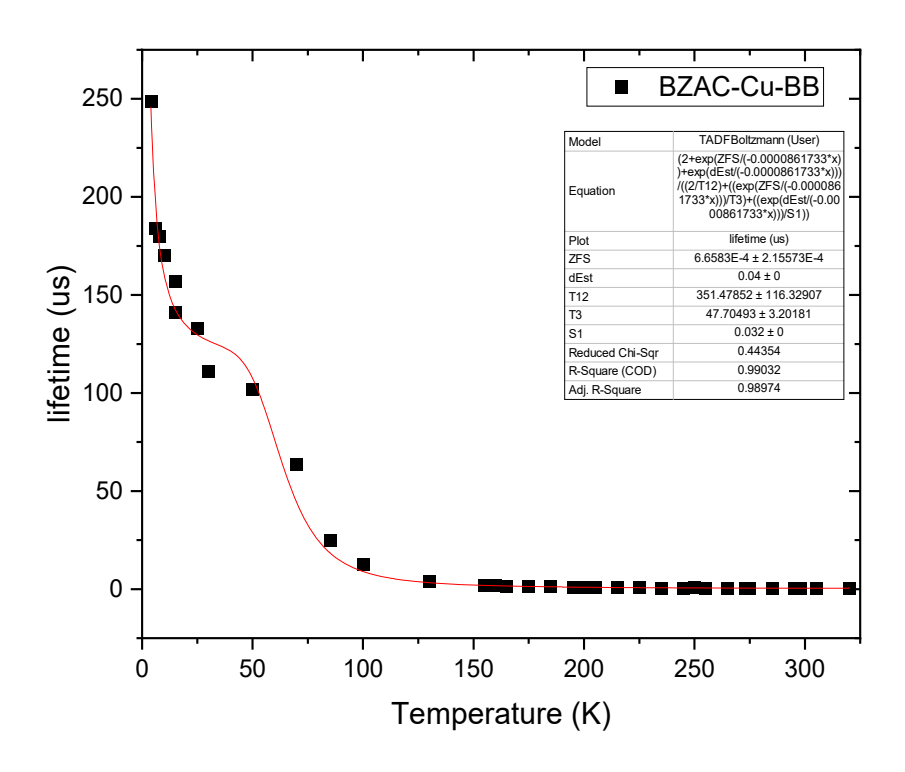


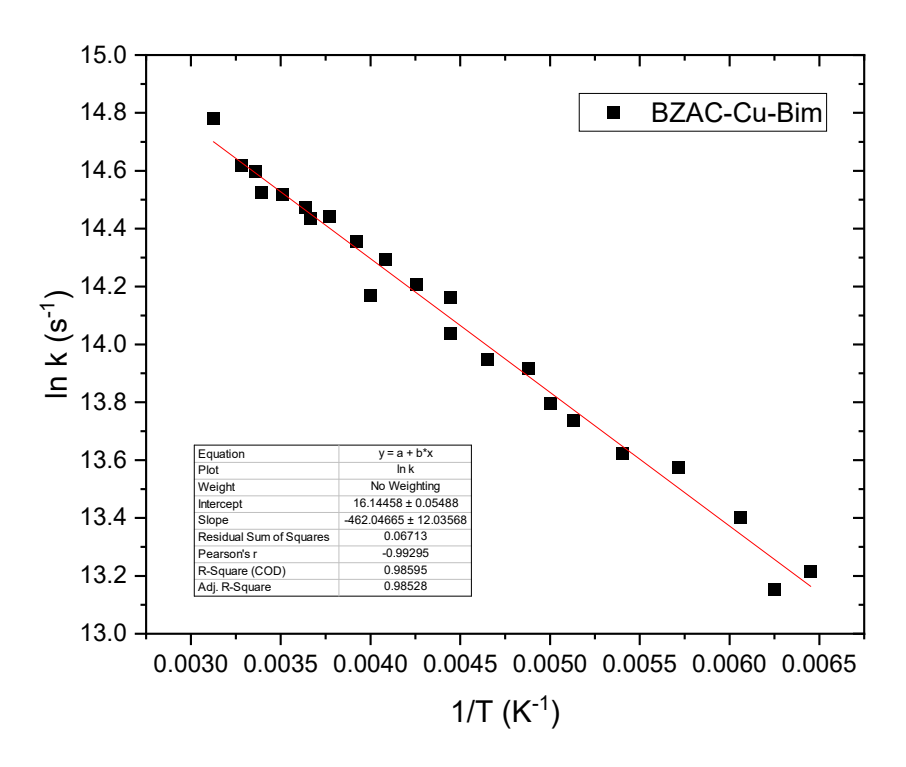
<u>Figure S21:</u> Temperature dependent lifetime for (CAAC)Au(Bim) in PS. Boltzmann fit (top) and Arrhenius plot (bottom).



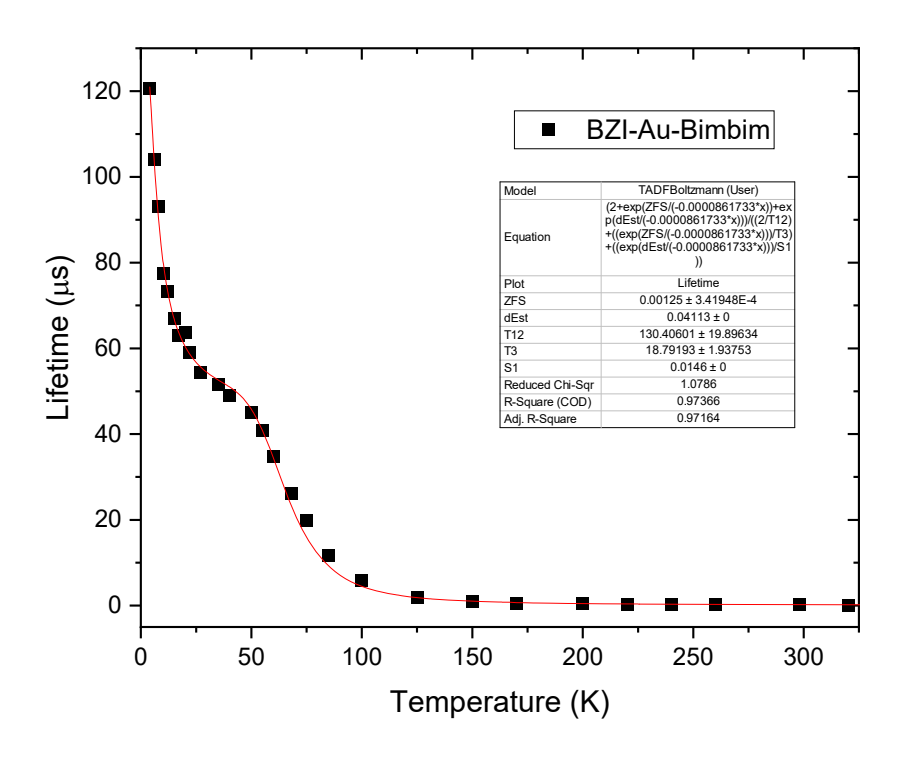


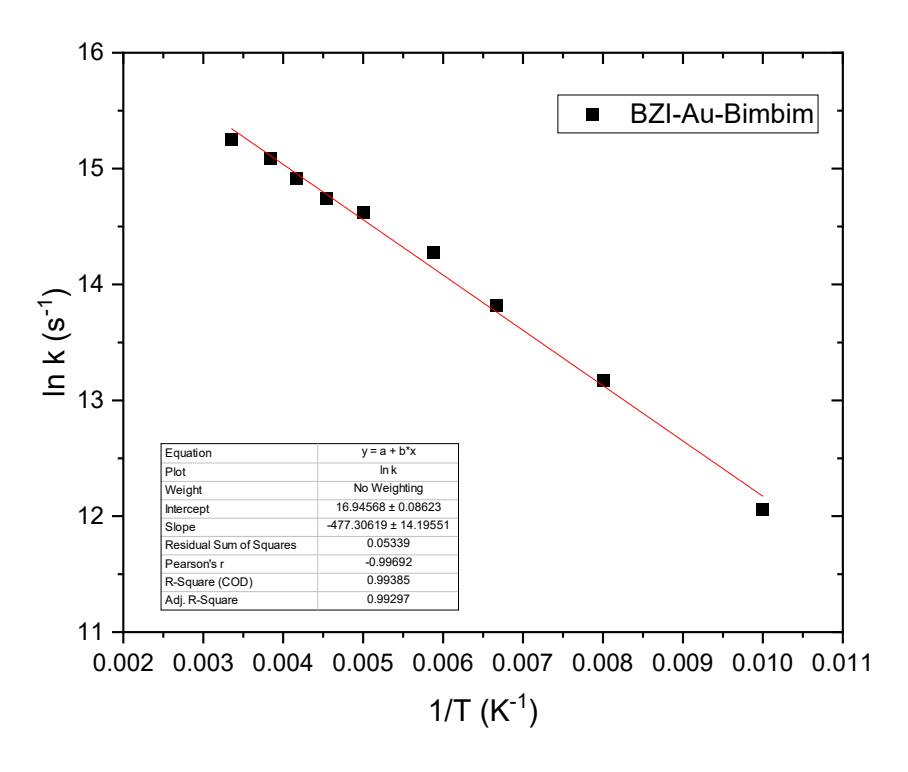
<u>Figure S22:</u> Temperature dependent lifetime for (BZAC)Au(Bim) in PS. Boltzmann fit (top) and Arrhenius plot (bottom).



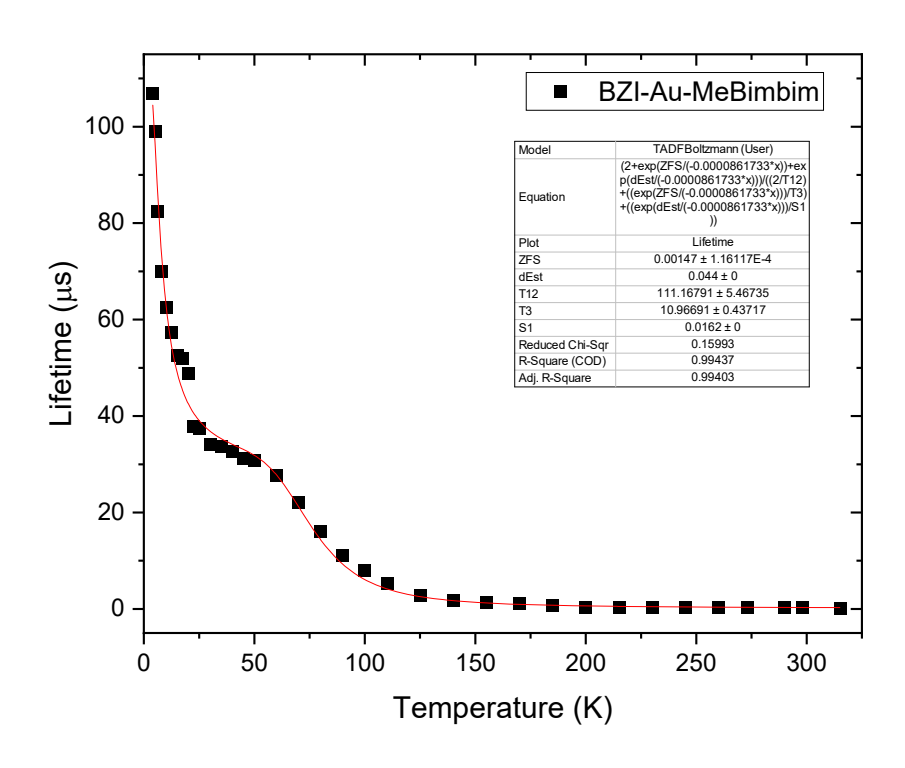


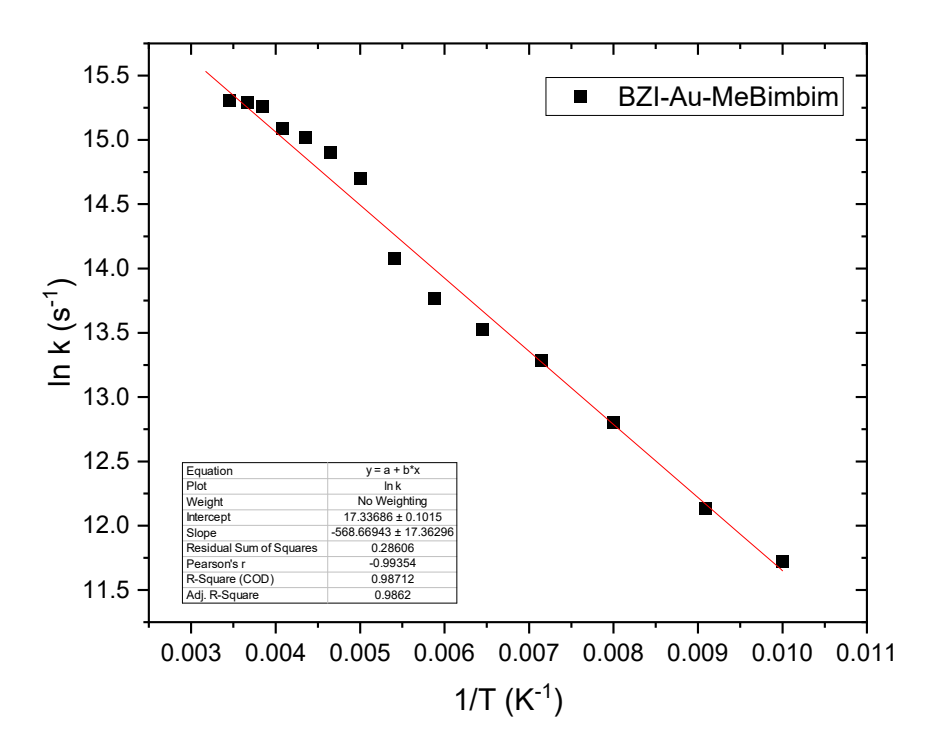
<u>Figure S23:</u> Temperature dependent lifetime for (BZAC)Cu(Bim) in PS. Boltzmann fit (top) and Arrhenius plot (bottom).



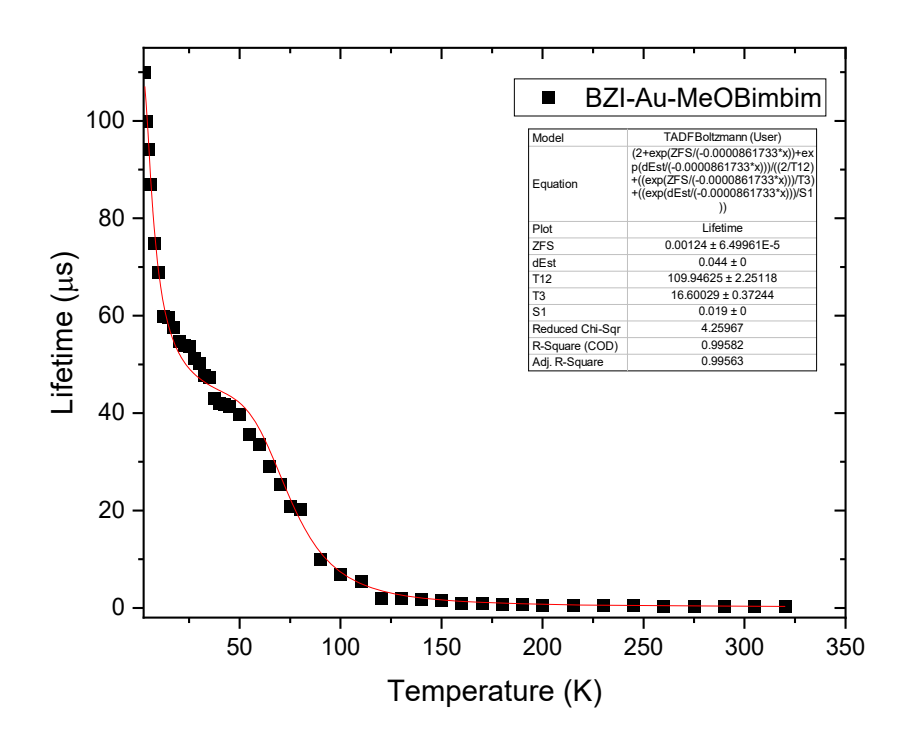


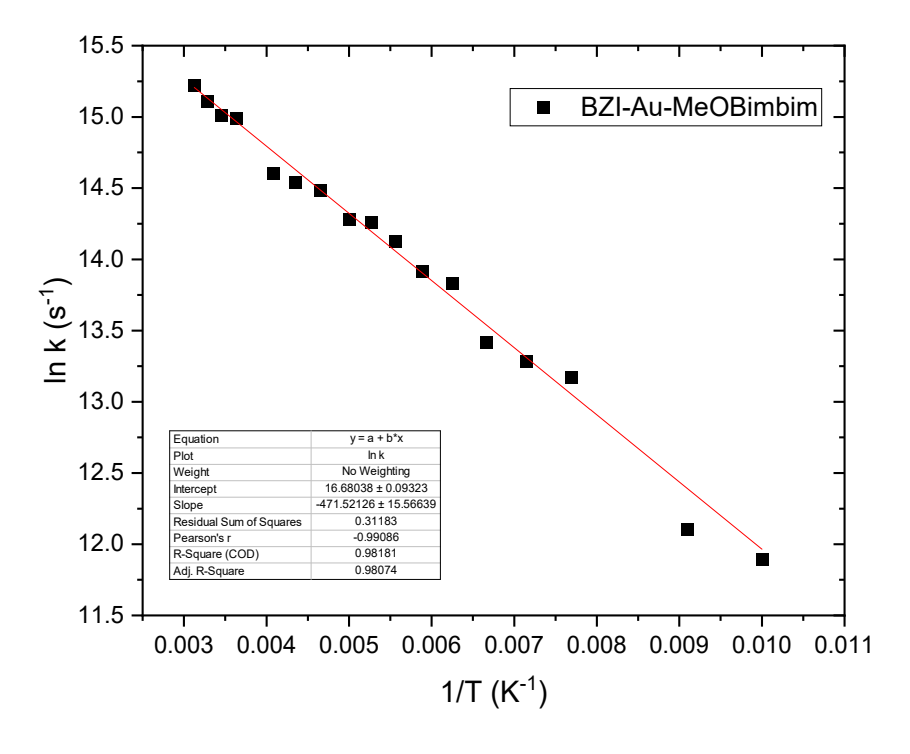
<u>Figure S24:</u> Temperature dependent lifetime for (BZI)Au(Bim) in PS. Boltzmann fit (top) and Arrhenius plot (bottom).



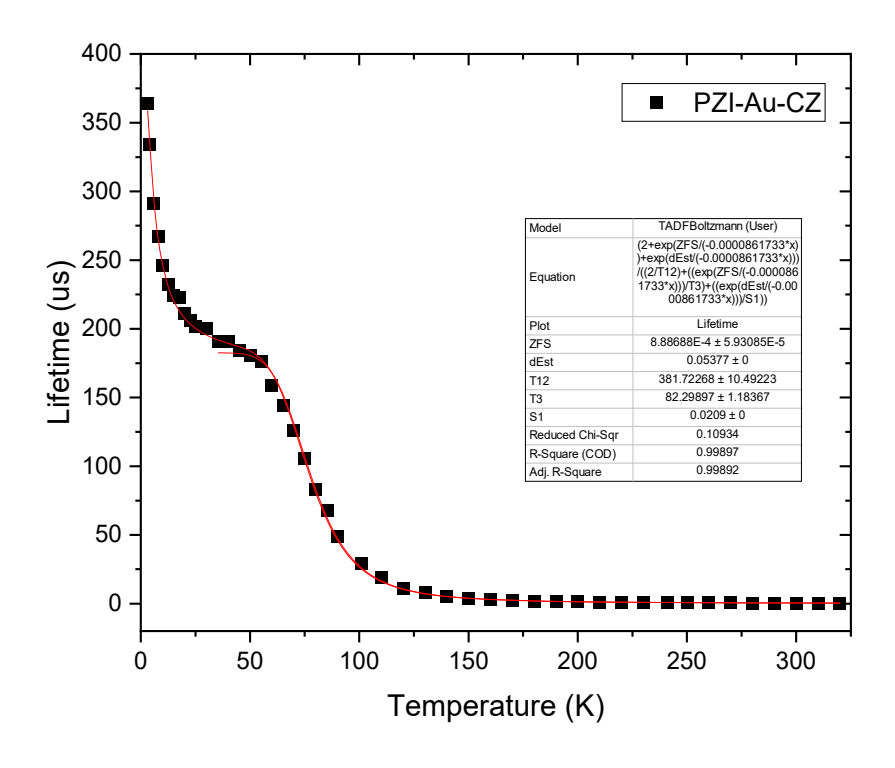


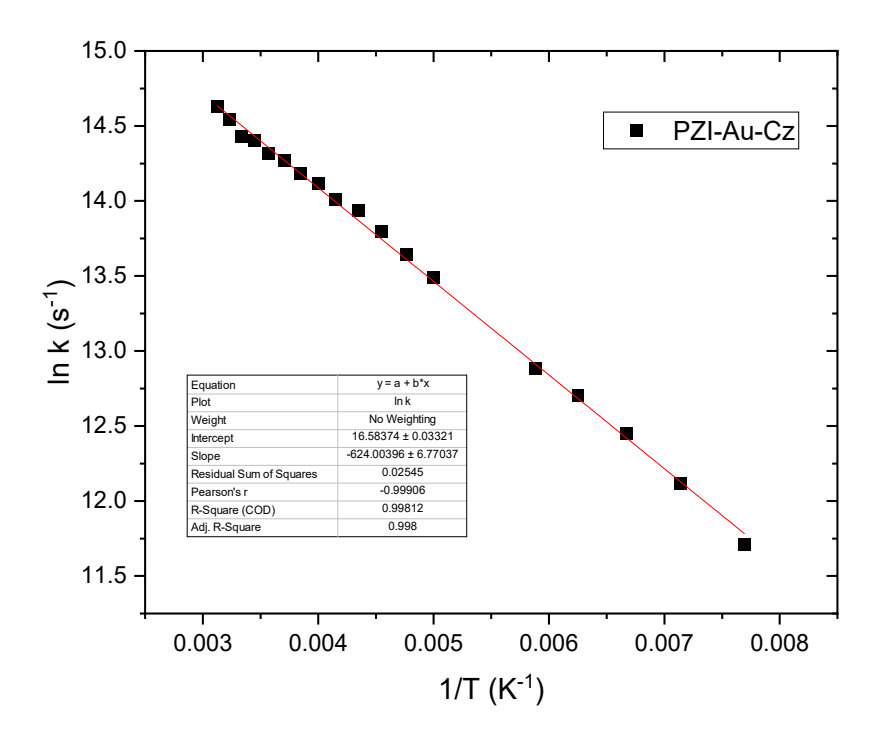
<u>Figure S25:</u> Temperature dependent lifetime for (BZI)Au(MBim) in PS. Boltzmann fit (top) and Arrhenius plot (bottom).



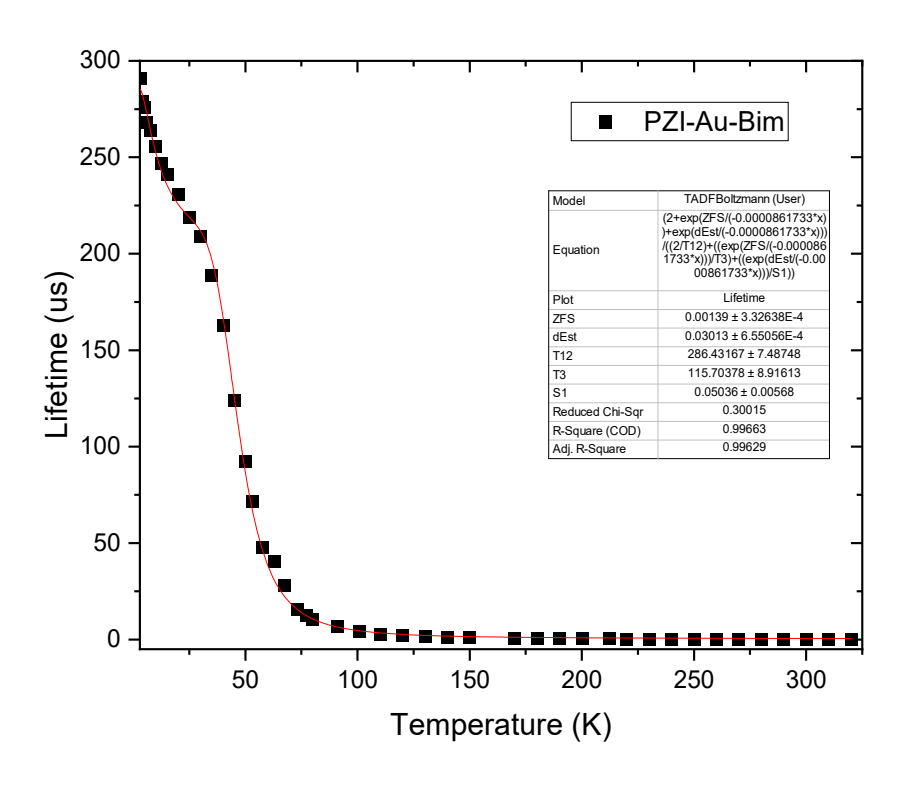


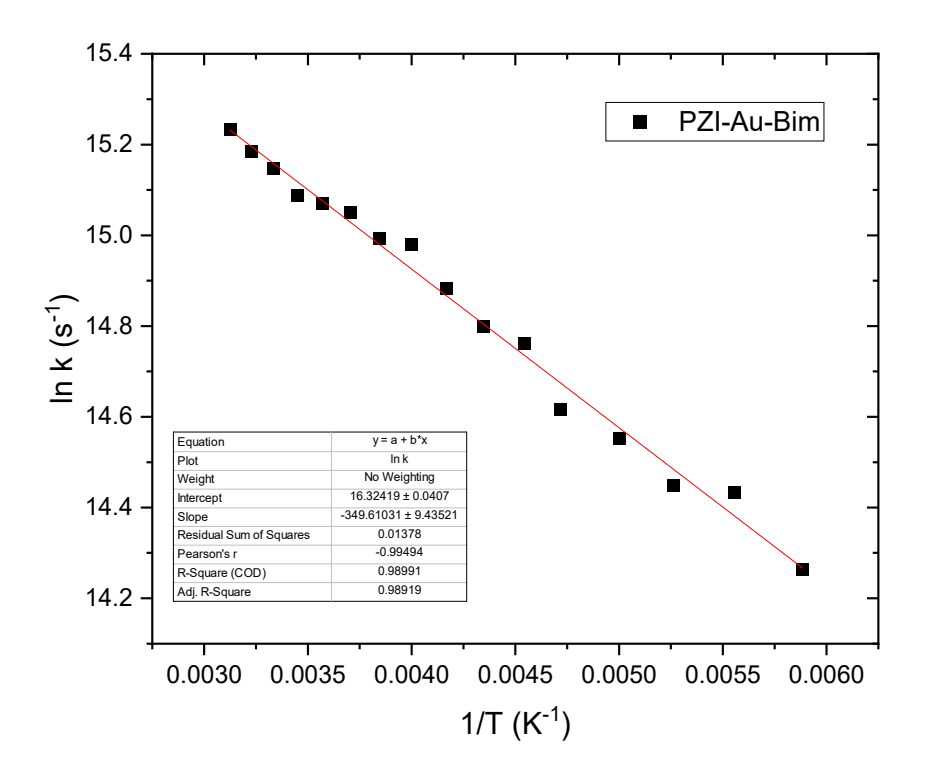
<u>Figure S26:</u> Temperature dependent lifetime for (BZI)Au(OBim) in PS. Boltzmann fit (top) and Arrhenius plot (bottom).





<u>Figure S27:</u> Temperature dependent lifetime for (PZI)Au(Cz) in PS. Boltzmann fit (top) and Arrhenius plot (bottom).





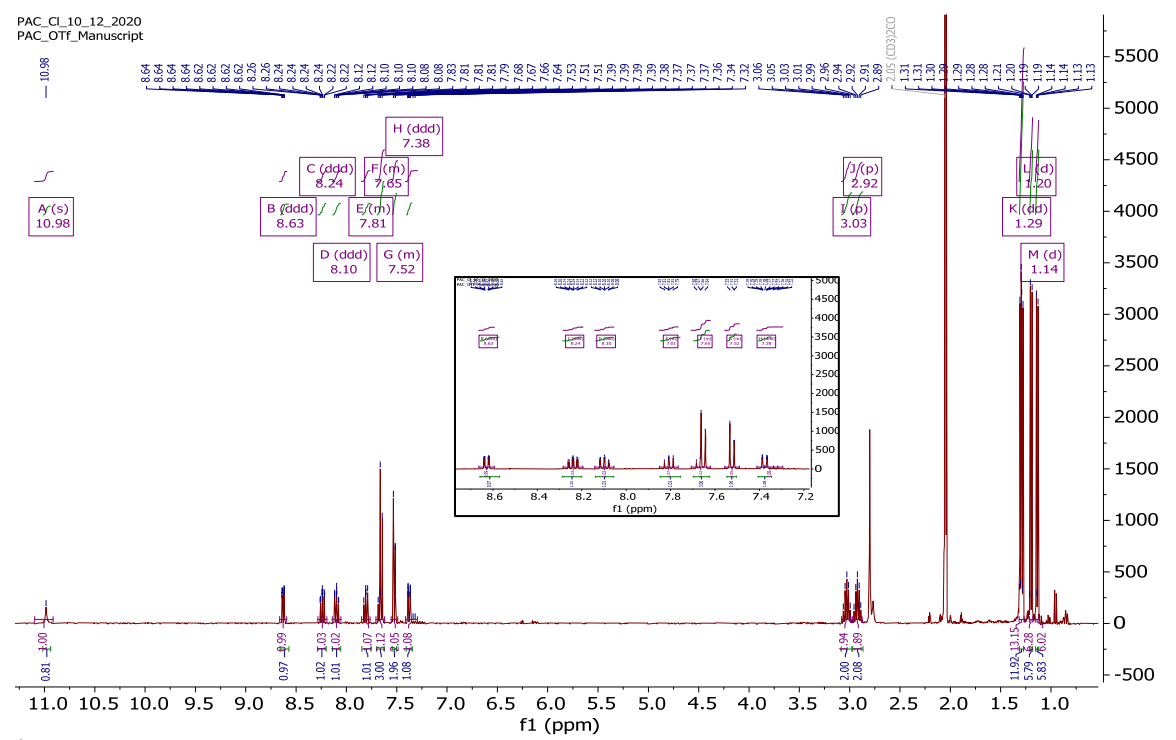
<u>Figure S28:</u> Temperature dependent lifetime for (PZI)Au(Bim) in PS. Boltzmann fit (top) and Arrhenius plot (bottom).

# <sup>1</sup>H, <sup>13</sup>C NMR and MALDI experimental

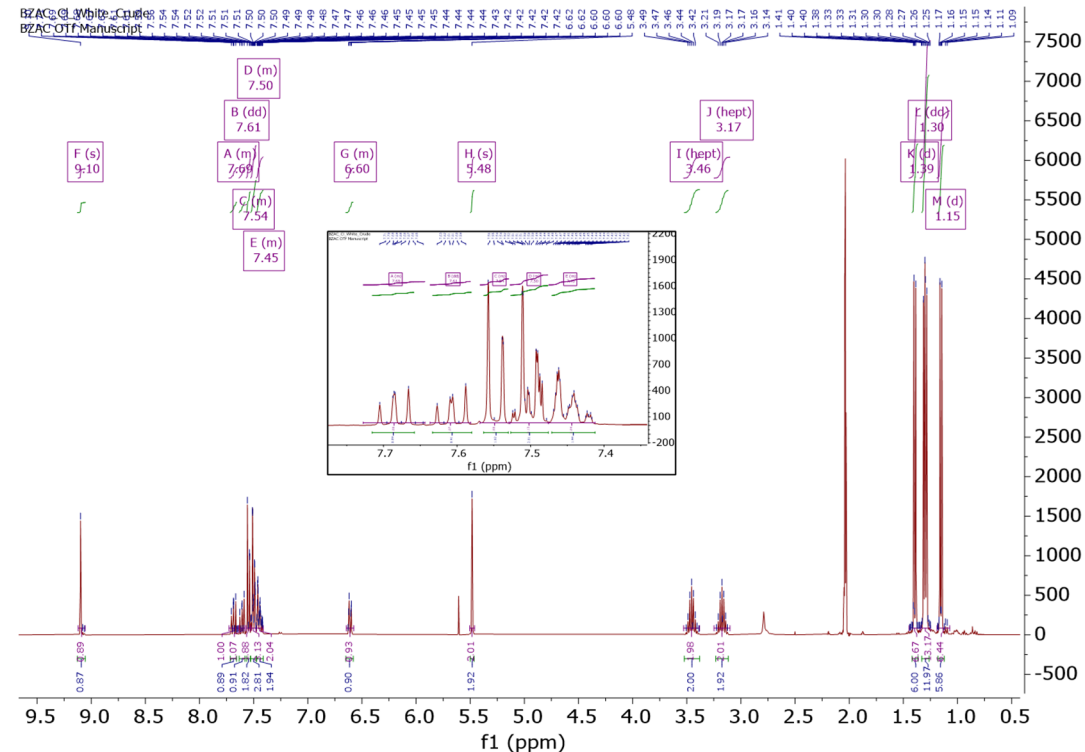
All NMR measurements were performed with a Varian 400-MR 2-Channel NMR spectrometer.

MALDI TOF experiments were performed using a Bruker Auto Flex Speed MALDI. The Bruker peptide calibration standard II with the HCCA matrix was used as an internal callibrant. Measurements were performed in a reverse positive method. The instrument was calibrated for each compound using the peptide standard and was double-checked after each analyte was measured to confirm that no drift occurred during the measurement. All compounds displayed a clear match between calculated and experimental isotope patterns. The weighted average of all isotope signals was compared to the calculated molecular weight and reported below.

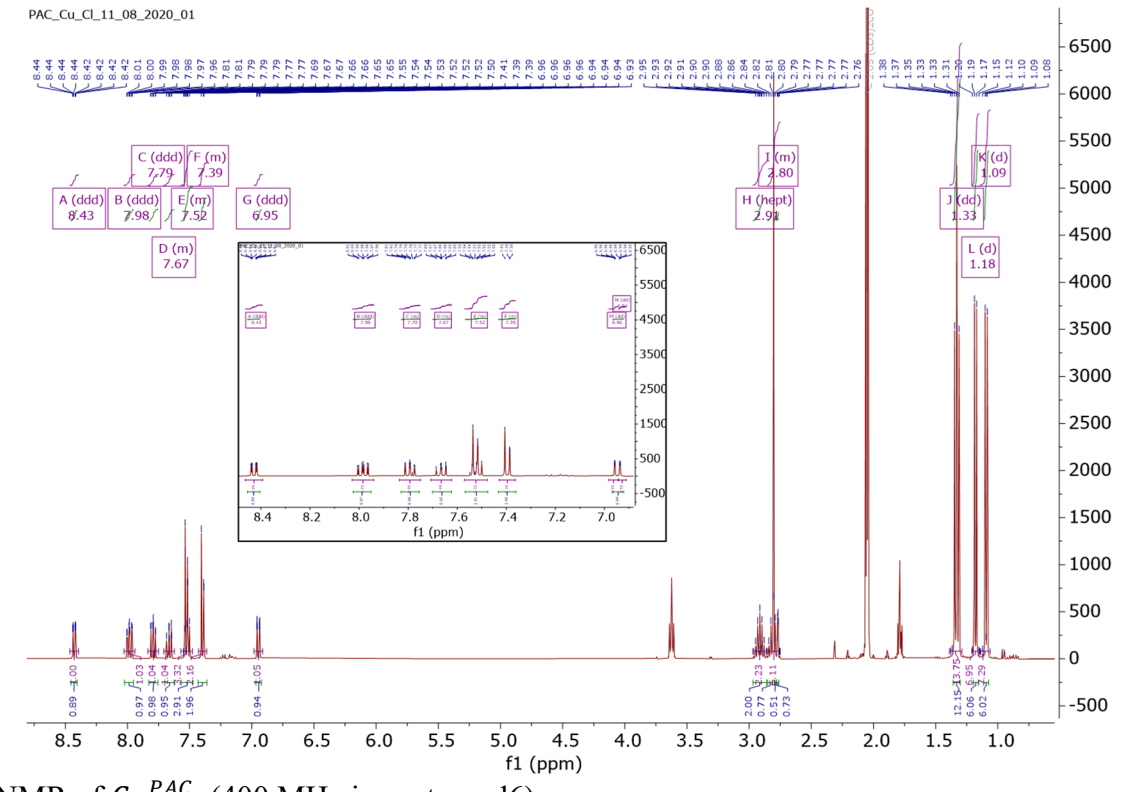
<sup>1</sup>H, <sup>13</sup>C NMR and MALDI spectra or each cMa compound

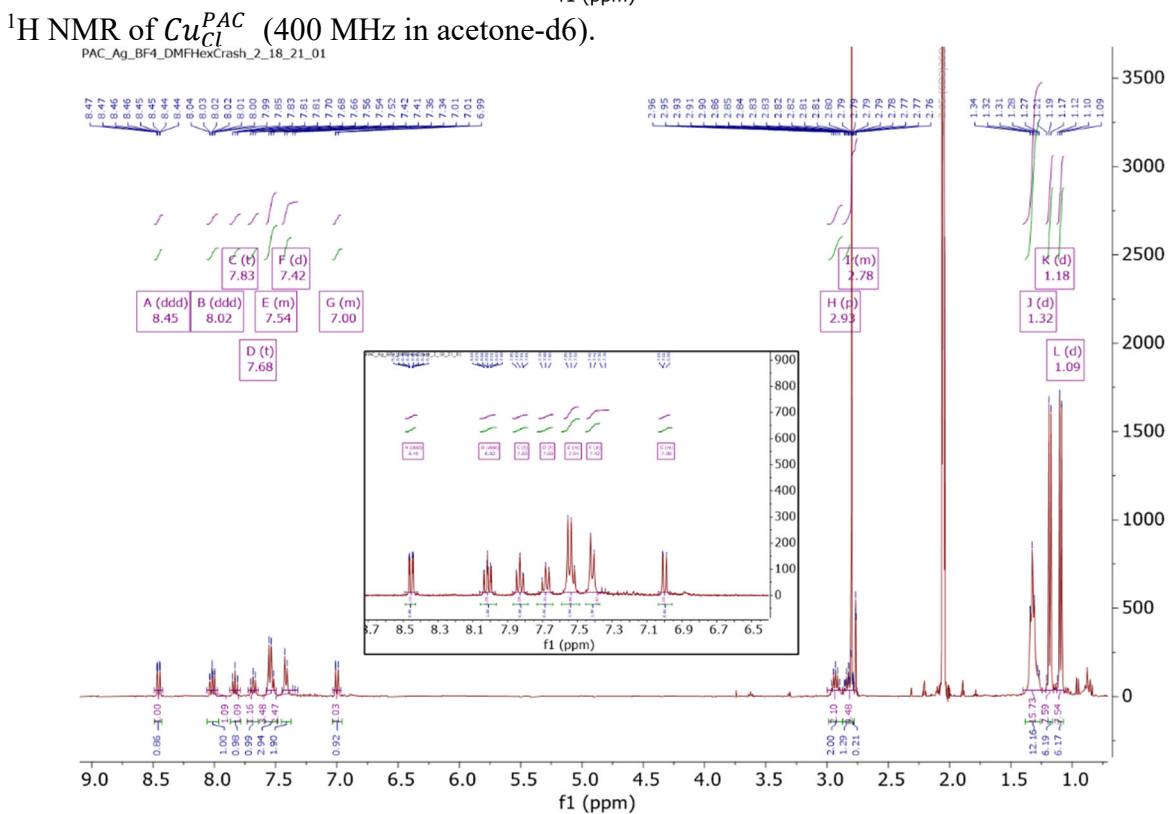


<sup>1</sup>H NMR of PAC OTf in acetone-d6.

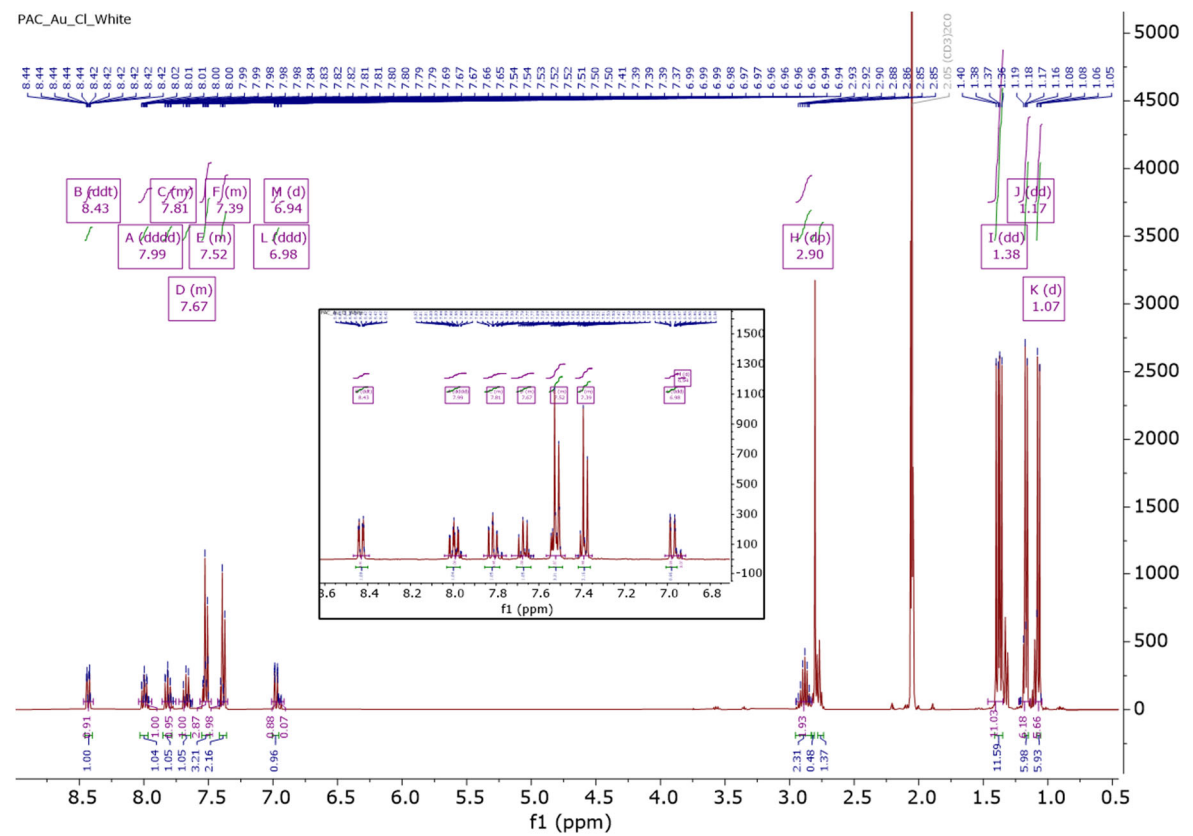


<sup>1</sup>H NMR of BZAC OTf (400 MHz in acetone-d6).

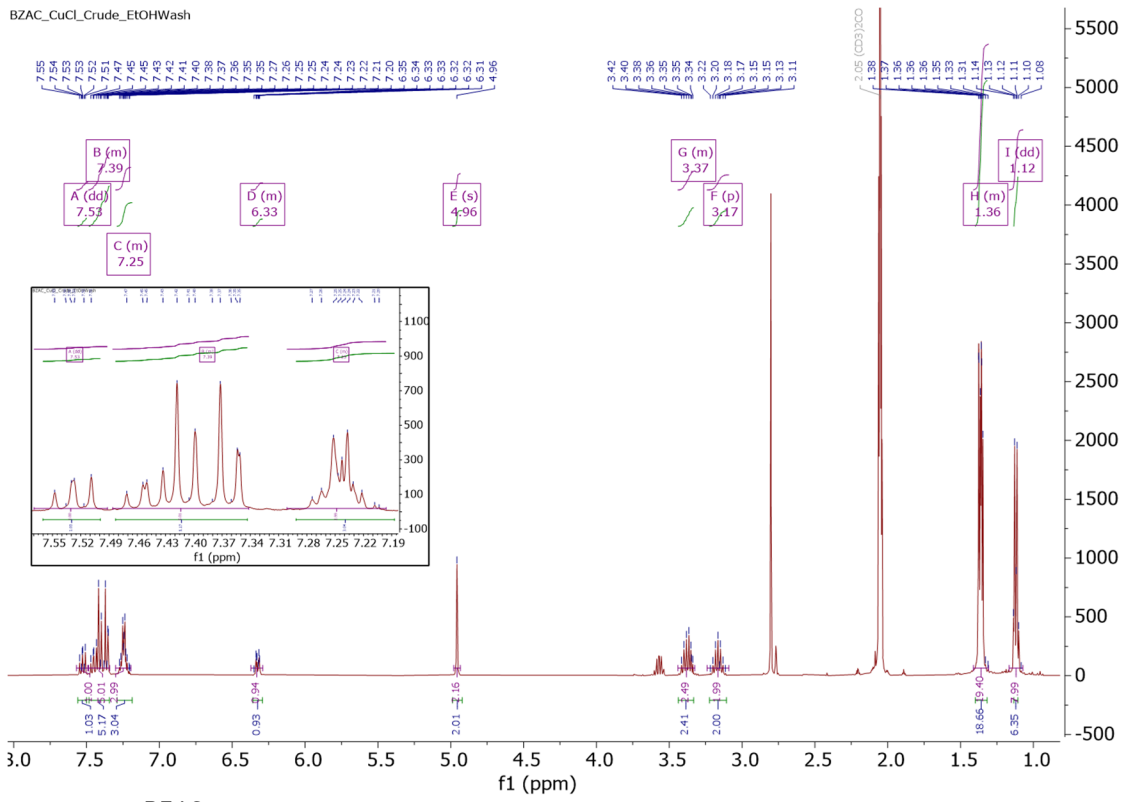




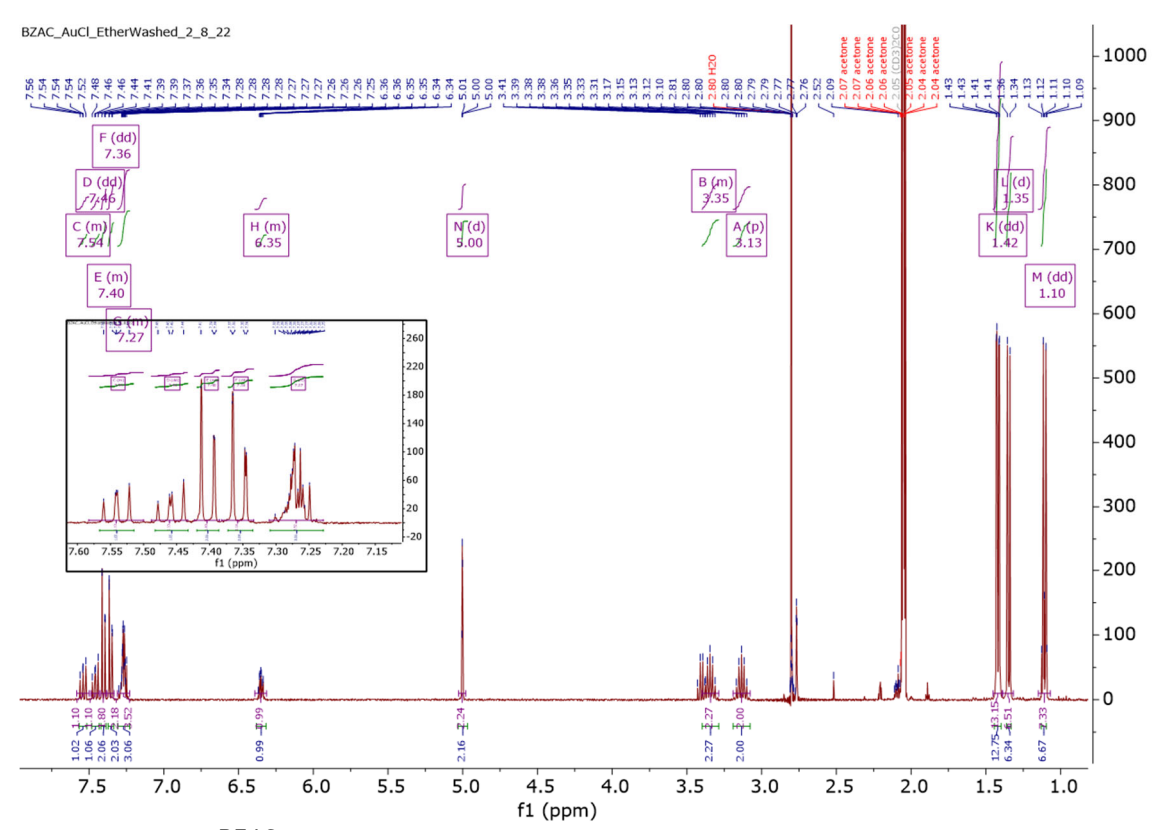
<sup>1</sup>H NMR of  $Ag_{BF_4}^{PAC}$  (400 MHz in acetone-d6).



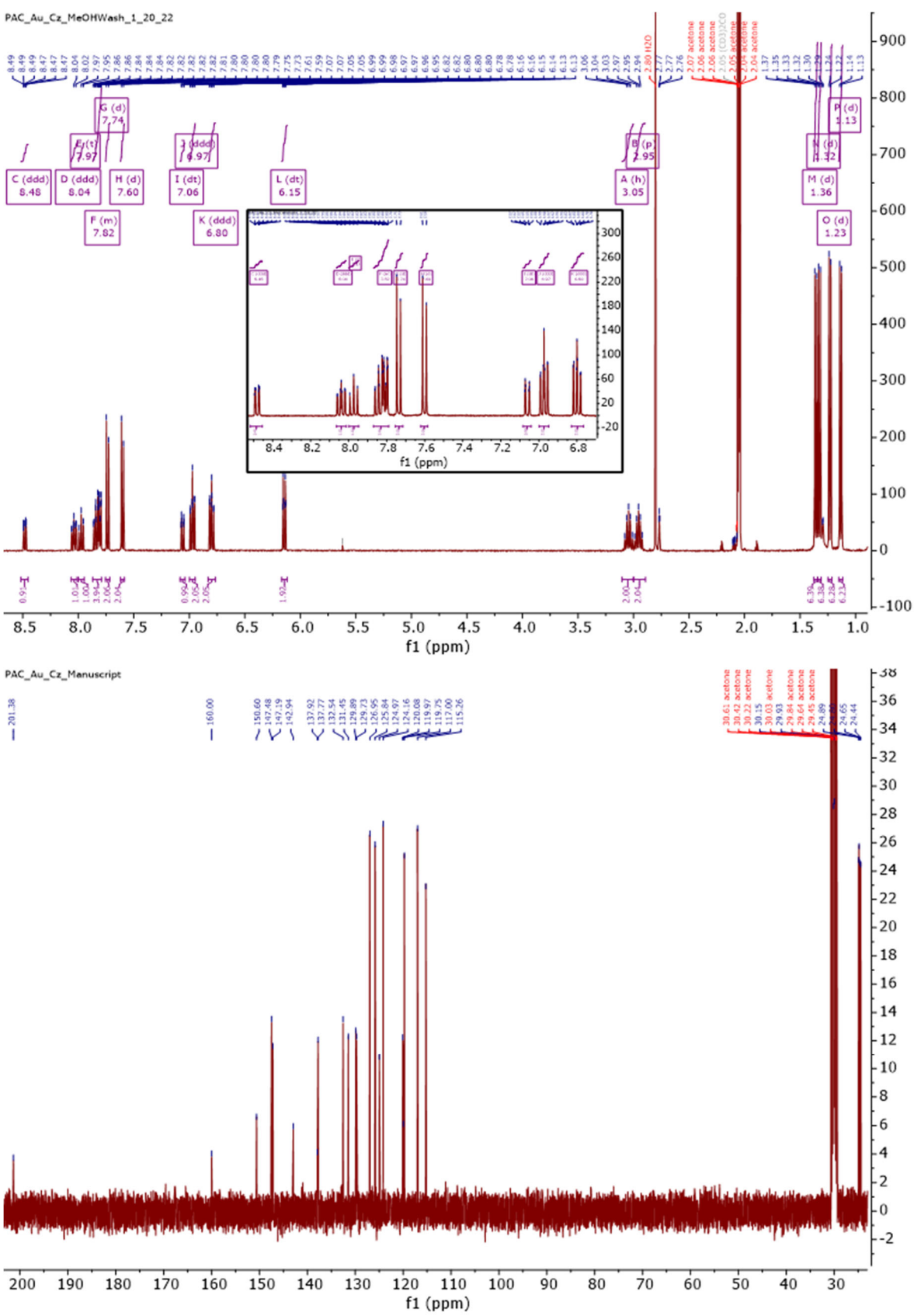




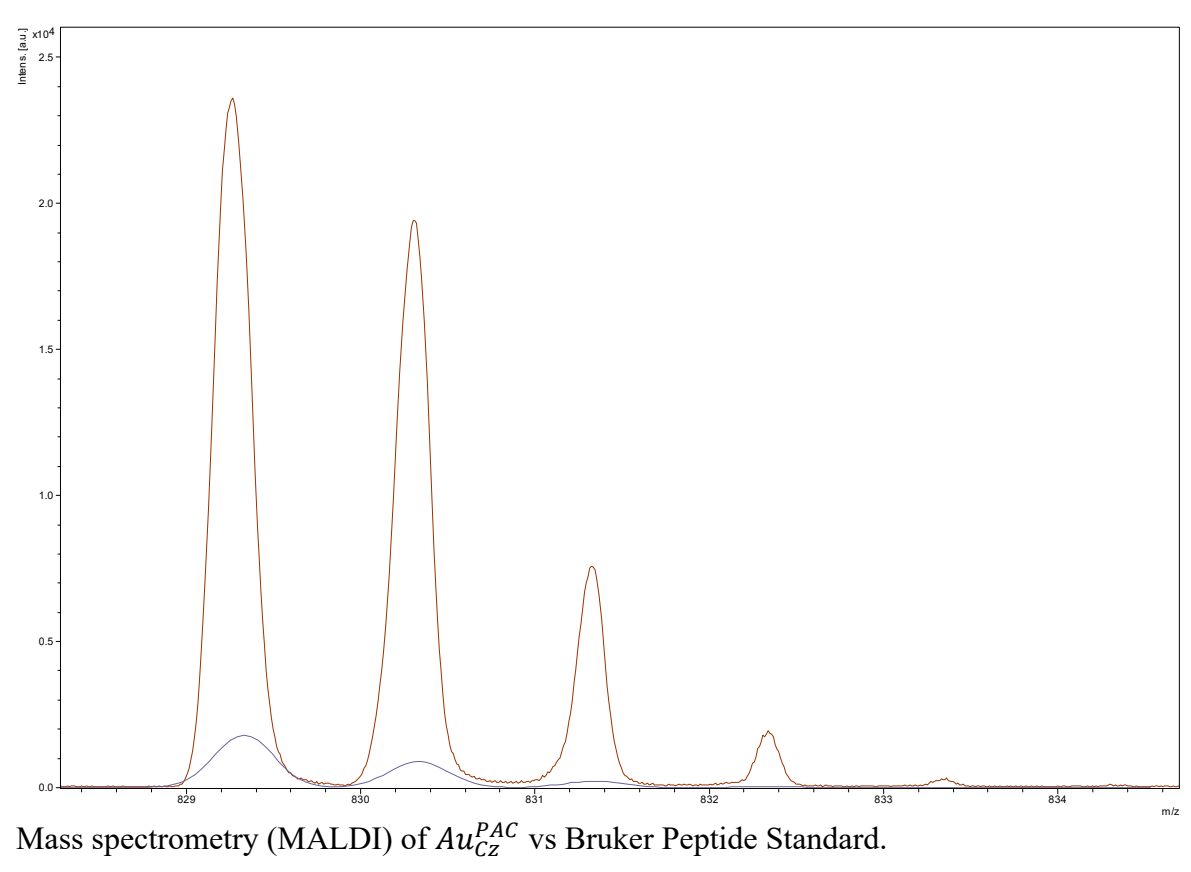
<sup>1</sup>H NMR of  $Cu_{Cl}^{BZAC}$  (400 MHz in acetone-d6).

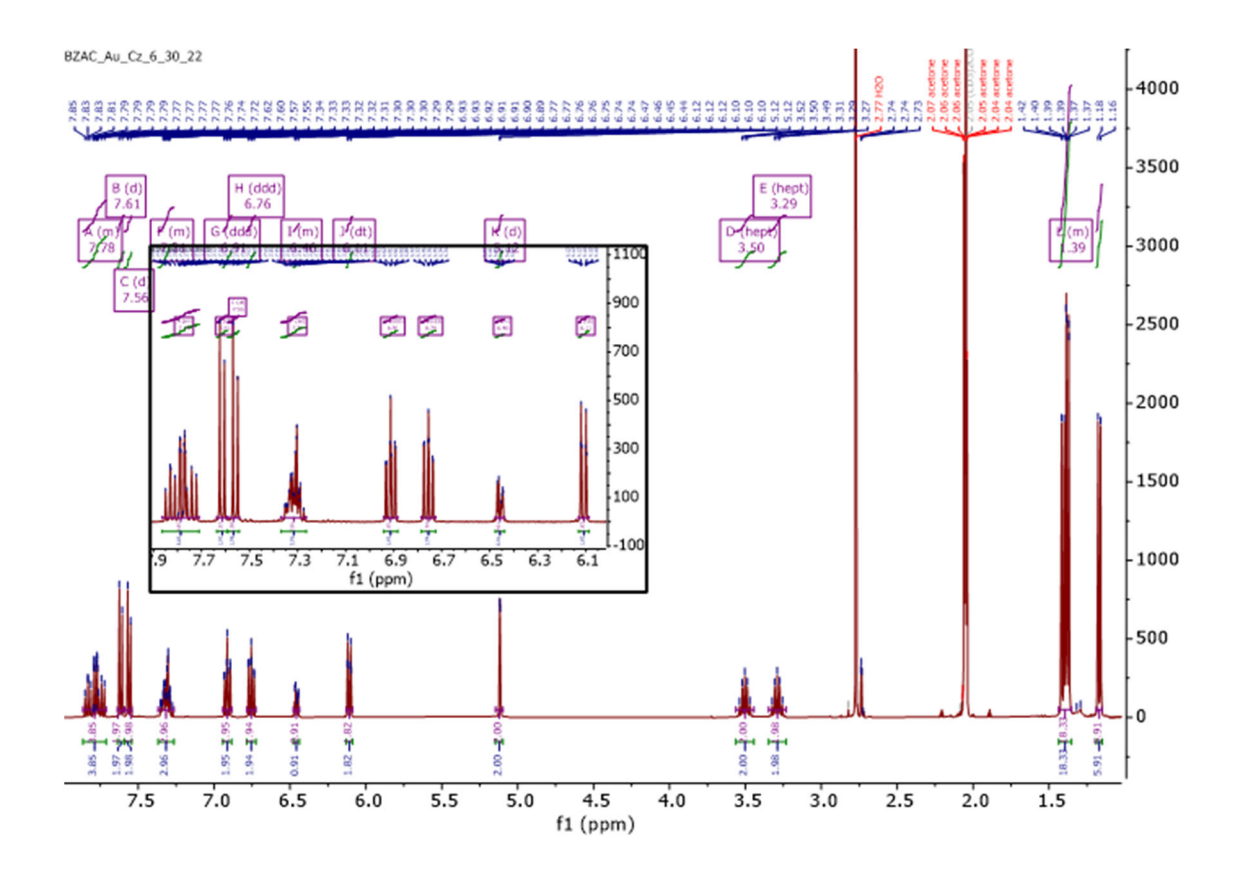


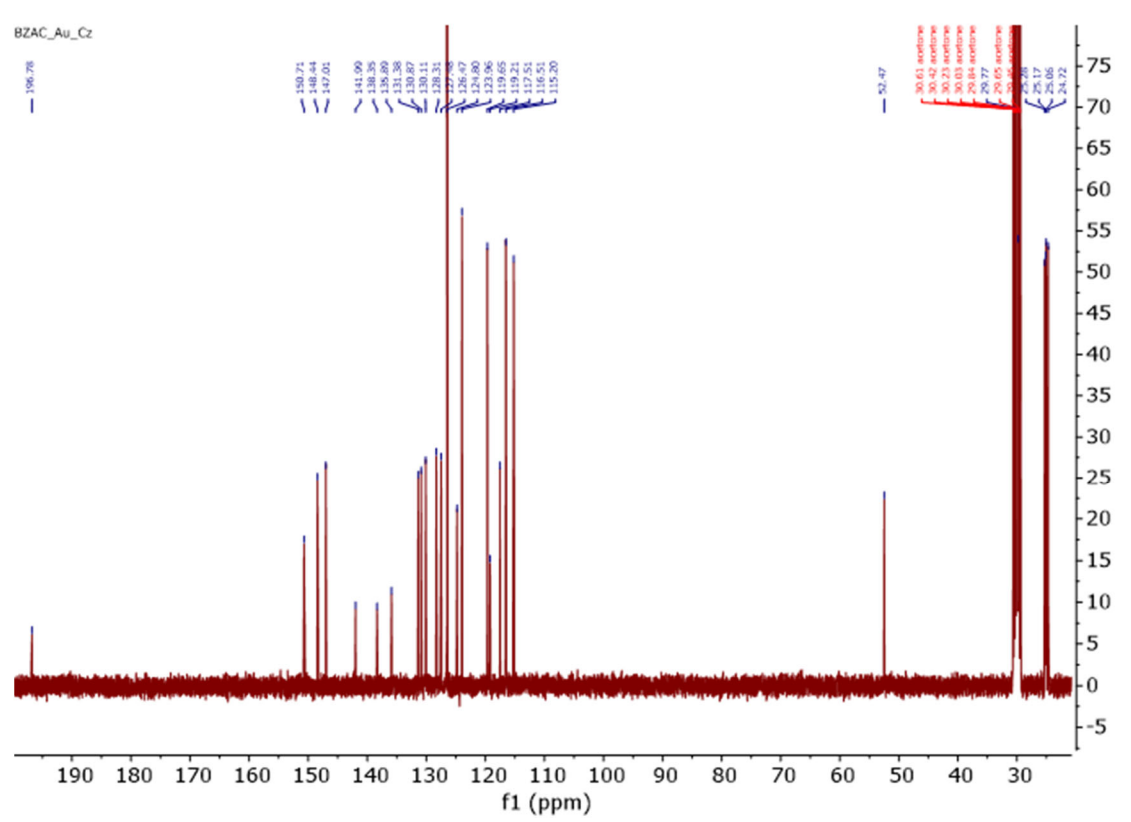
<sup>1</sup>H NMR of  $Au_{cl}^{BZAC}$  (400 MHz in acetone-d6).



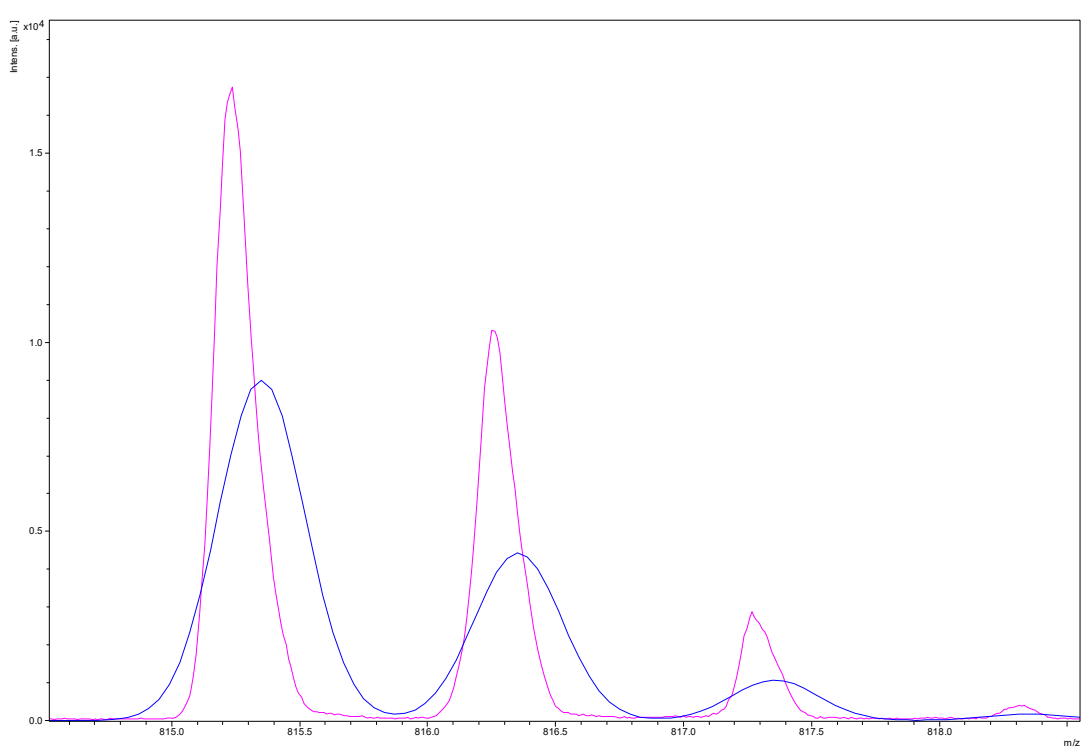
 $^{1}$ H and  $^{13}$ C $\{^{1}$ H $\}$  NMR of  $Au_{Cz}^{PAC}$  (400 MHz in acetone-d6).



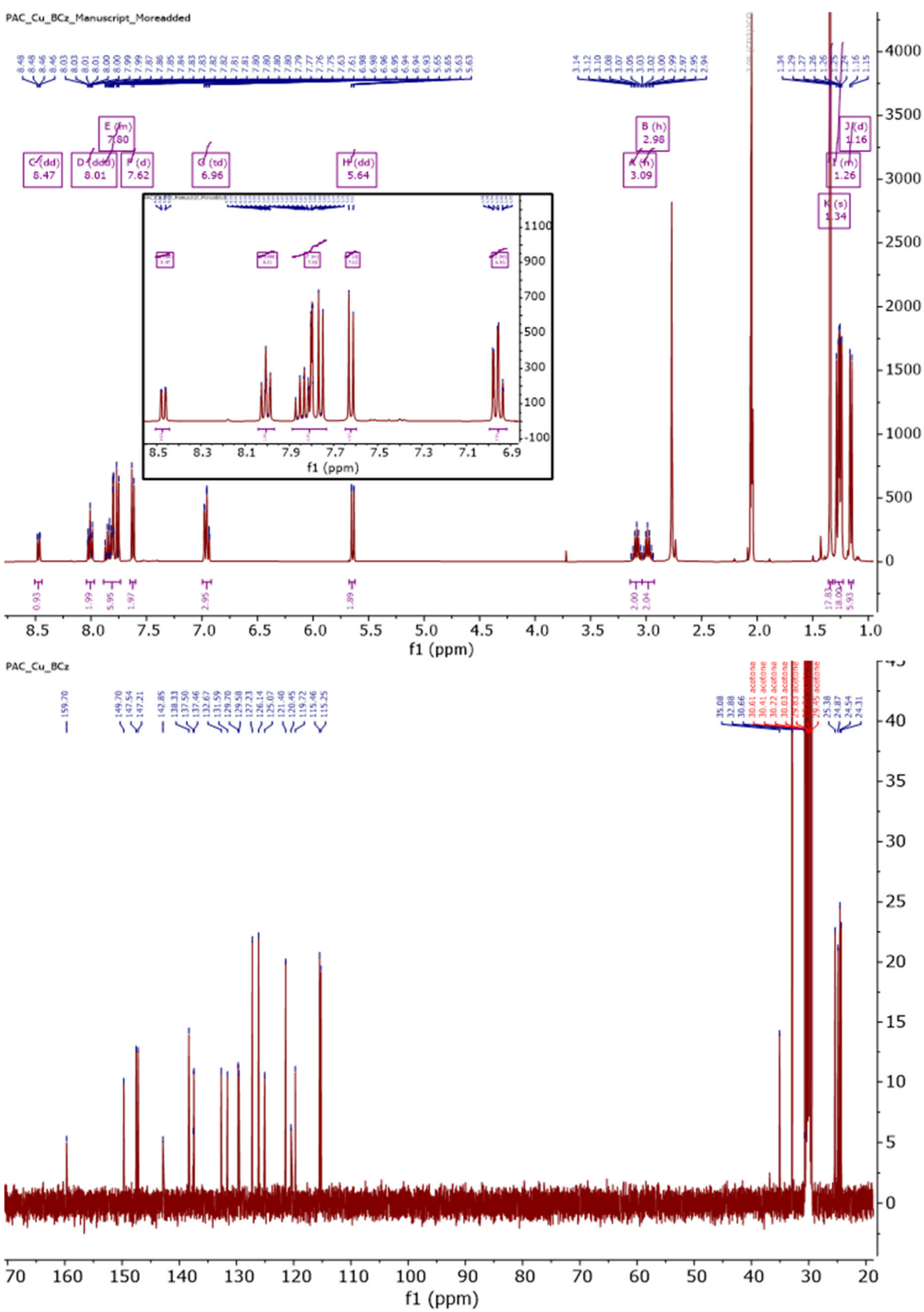




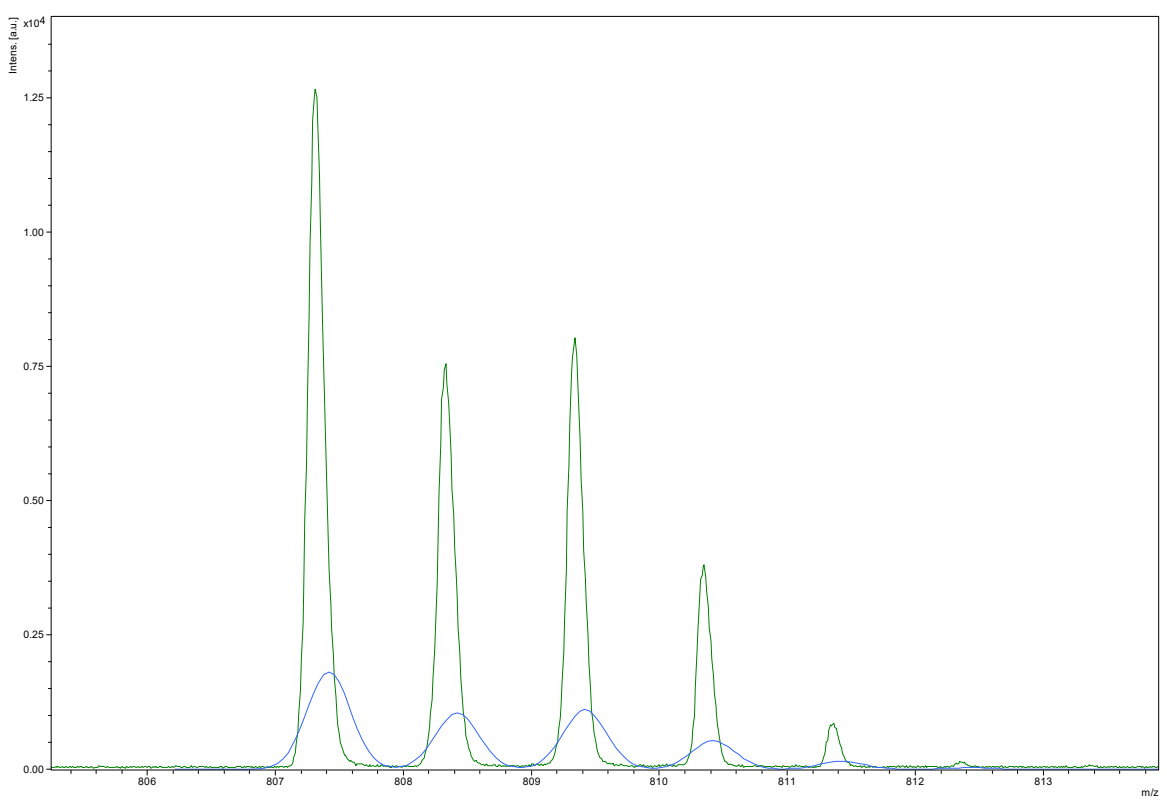
 $^{1}$ H and  $^{13}$ C{ $^{1}$ H} NMR of  $Au_{Cz}^{BZAC}$  (400 MHz in acetone-d6).



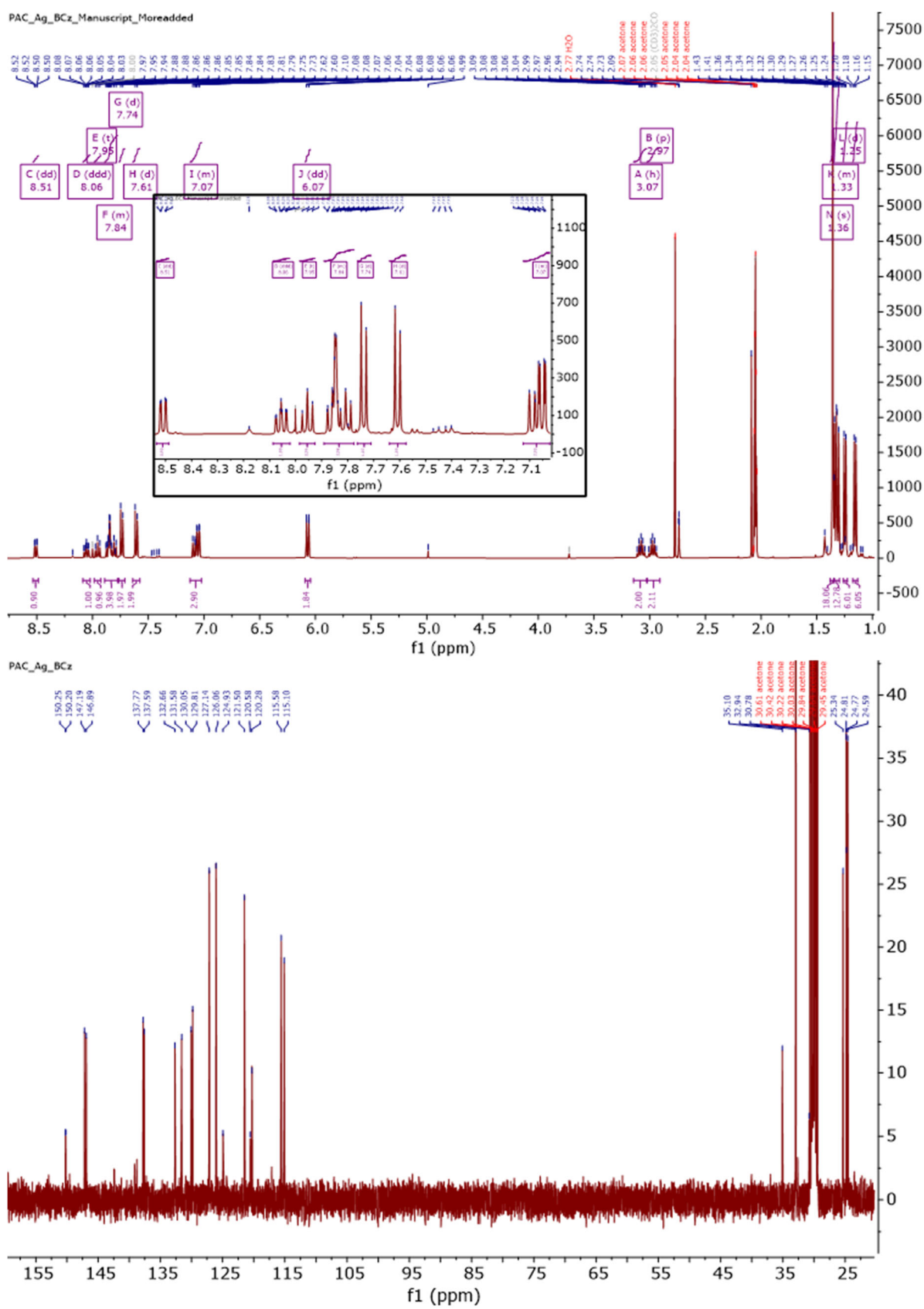
Mass spectrometry (MALDI) of  $Au_{Cz}^{BZAC}$  vs Bruker Peptide Standard.



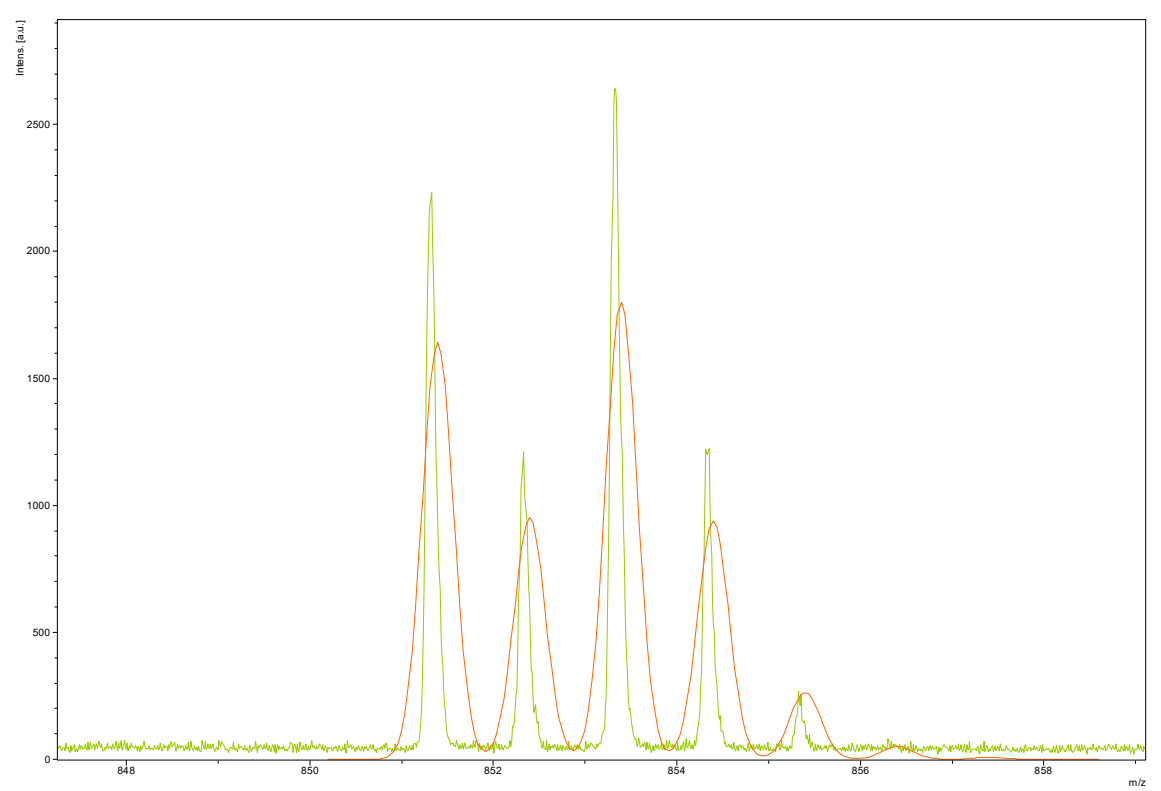
 $^{1}$ H and  $^{13}$ C{ $^{1}$ H} NMR of  $Cu_{BCz}^{PAC}$  (400 MHz in acetone-d6).



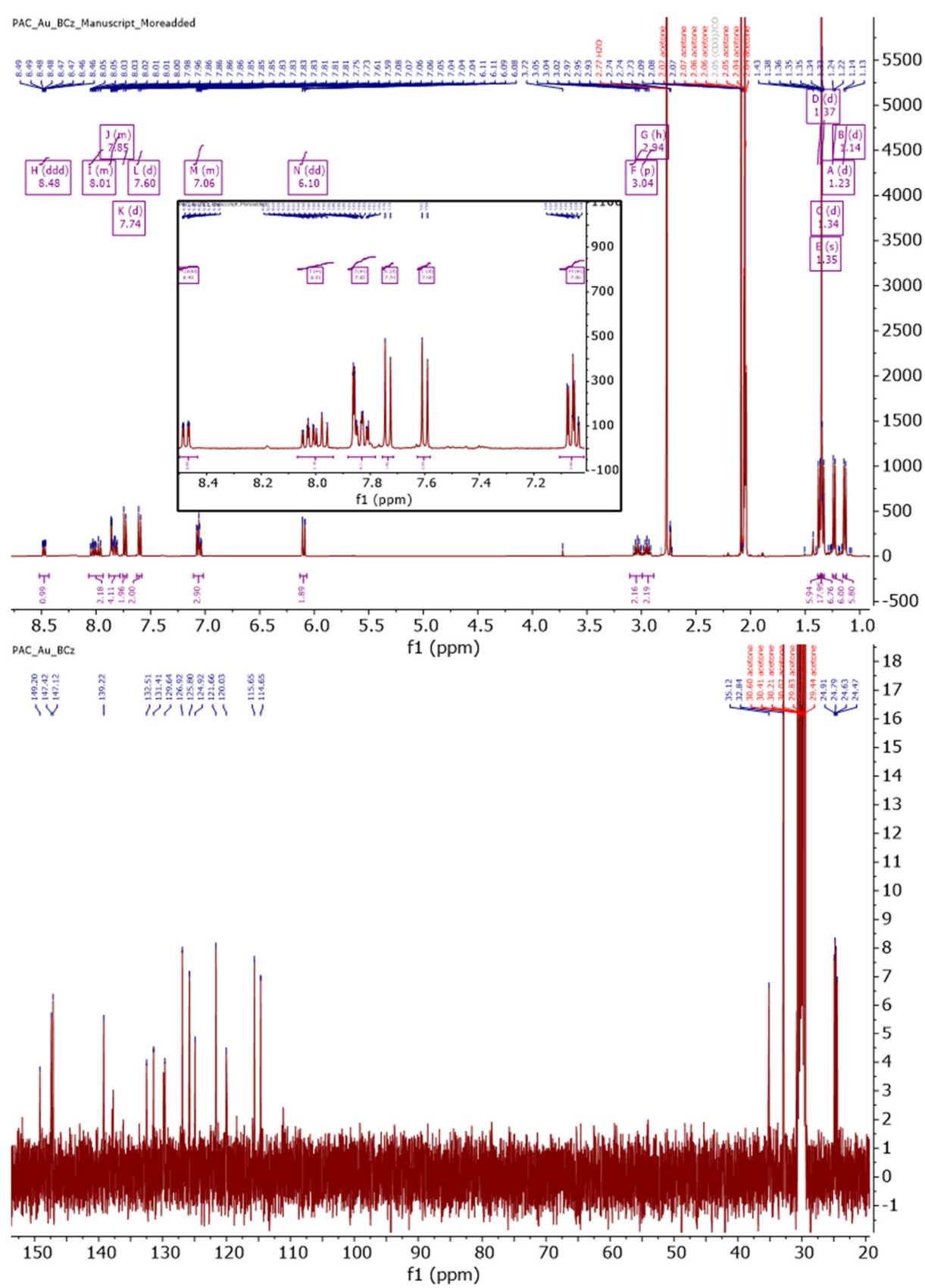
Mass spectrometry (MALDI) of  $Cu_{BCz}^{PAC}$  vs Bruker Peptide Standard.



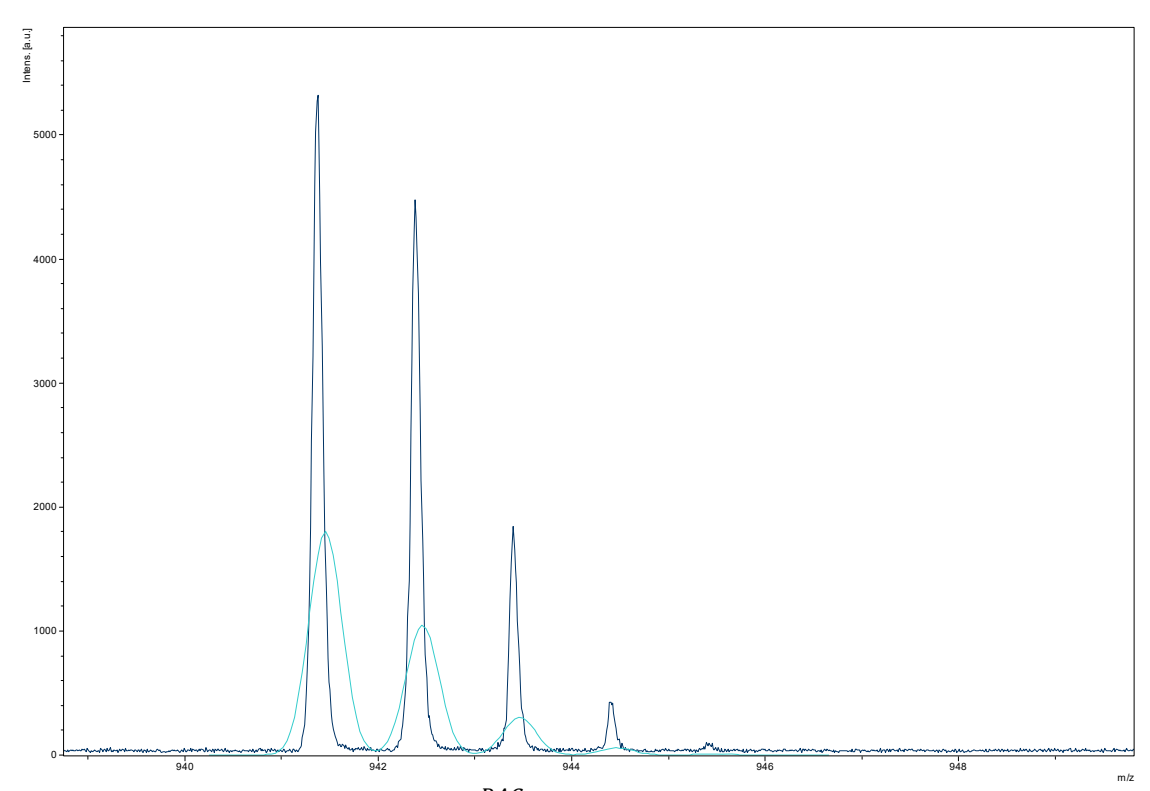
 $^{1}$ H and  $^{13}$ C{ $^{1}$ H} NMR of  $Ag_{BCz}^{PAC}$  (400 MHz in acetone-d6).



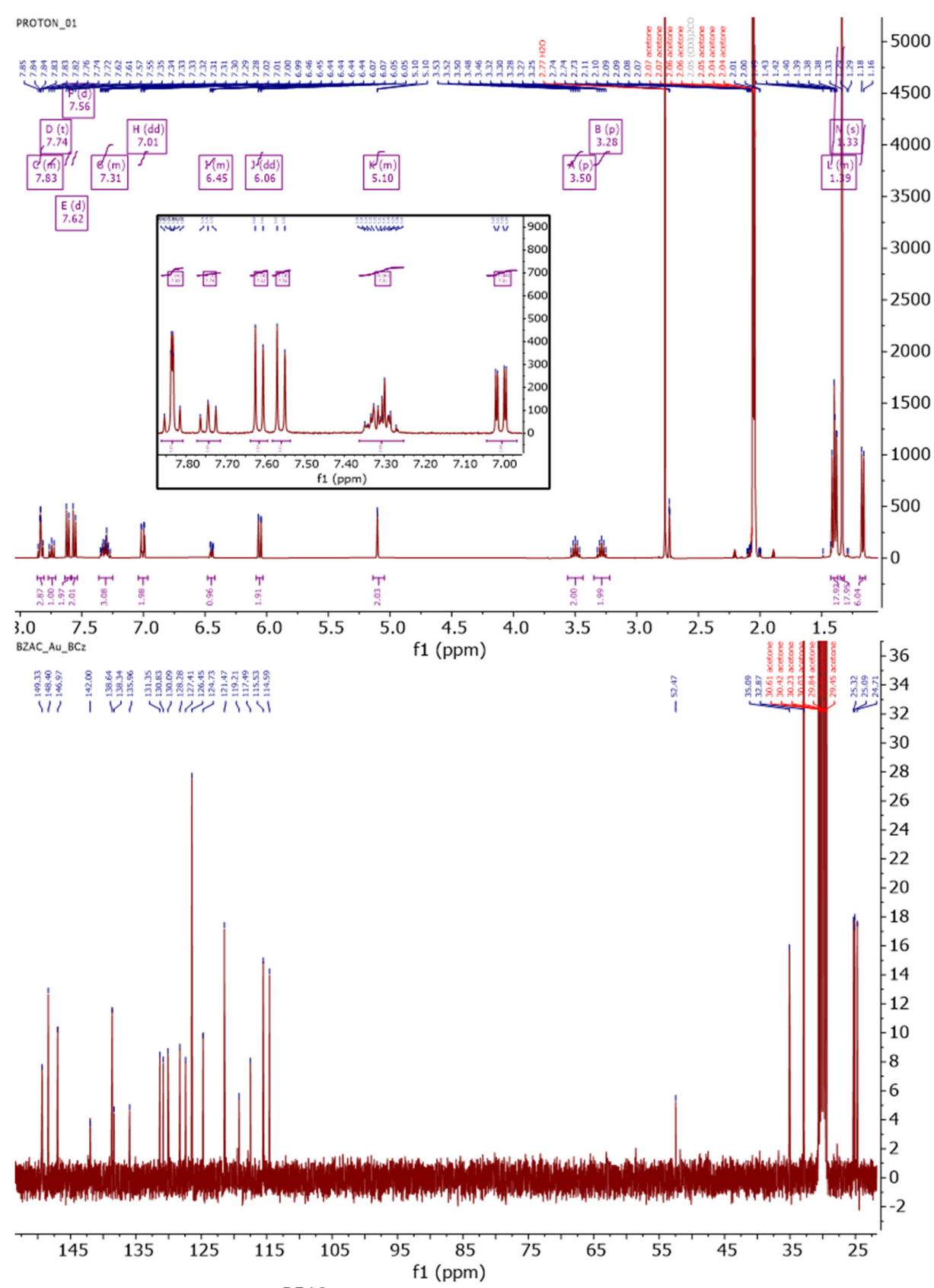
Mass spectrometry (MALDI) of  $Ag_{BCz}^{PAC}$  vs Bruker Peptide Standard.



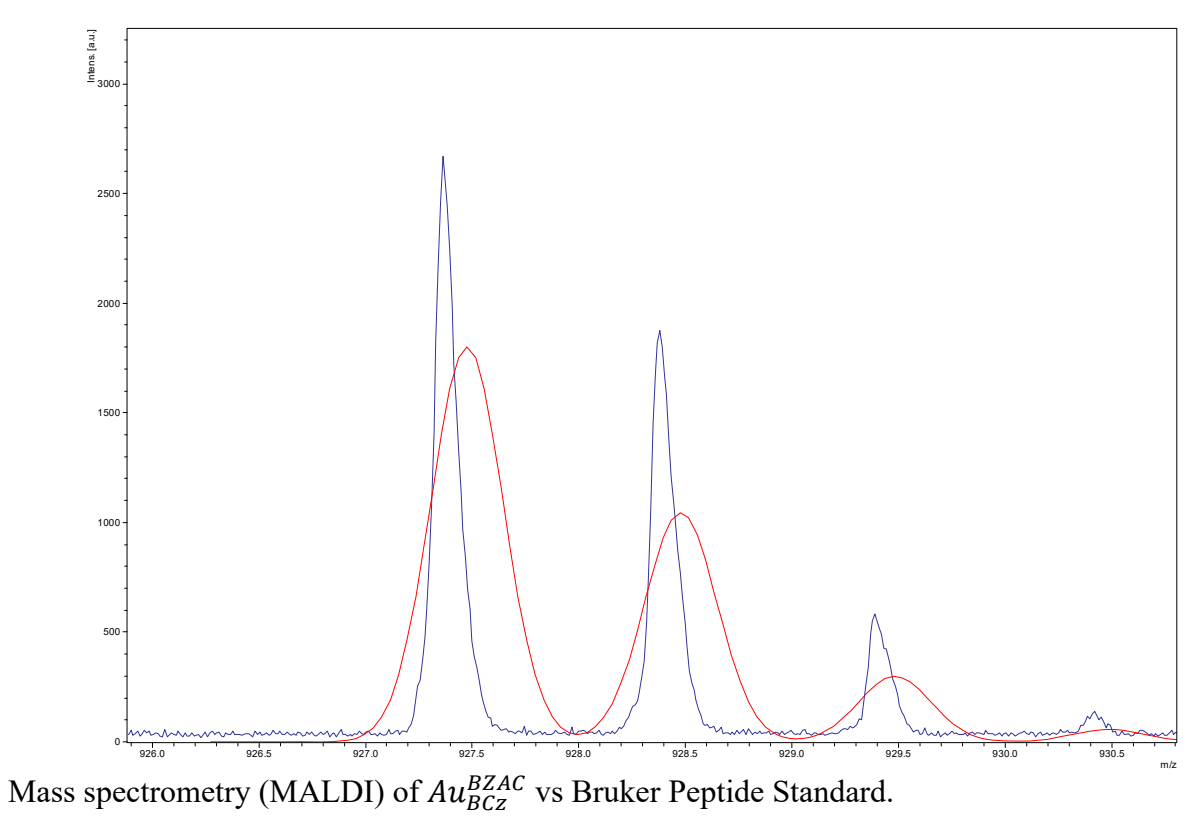
 $^{1}$ H and  $^{13}$ C{ $^{1}$ H} NMR of  $Au_{BCz}^{PAC}$  (400 MHz in acetone-d6).

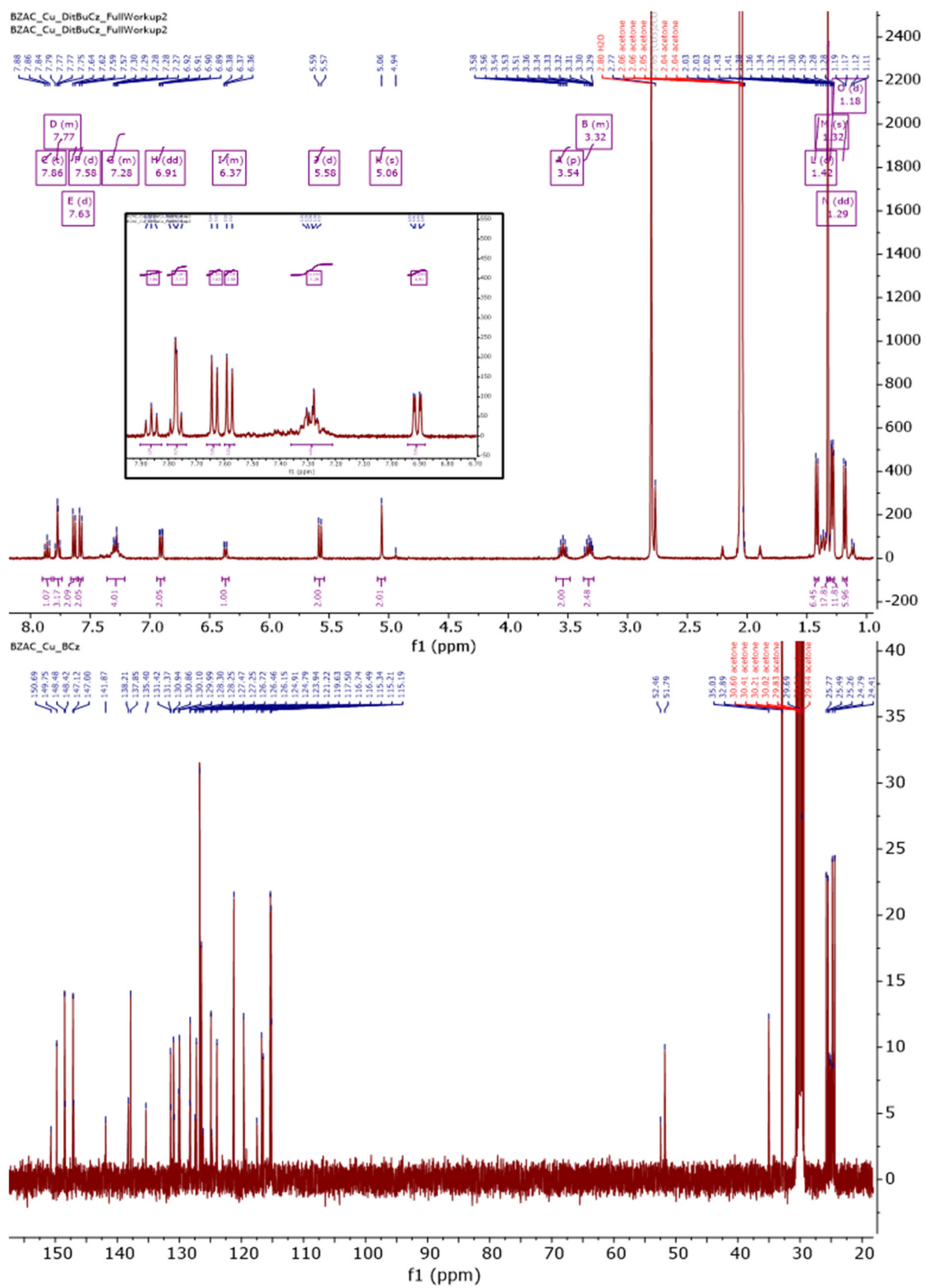


Mass spectrometry (MALDI) of  $Au_{BCz}^{PAC}$  vs Bruker Peptide Standard.

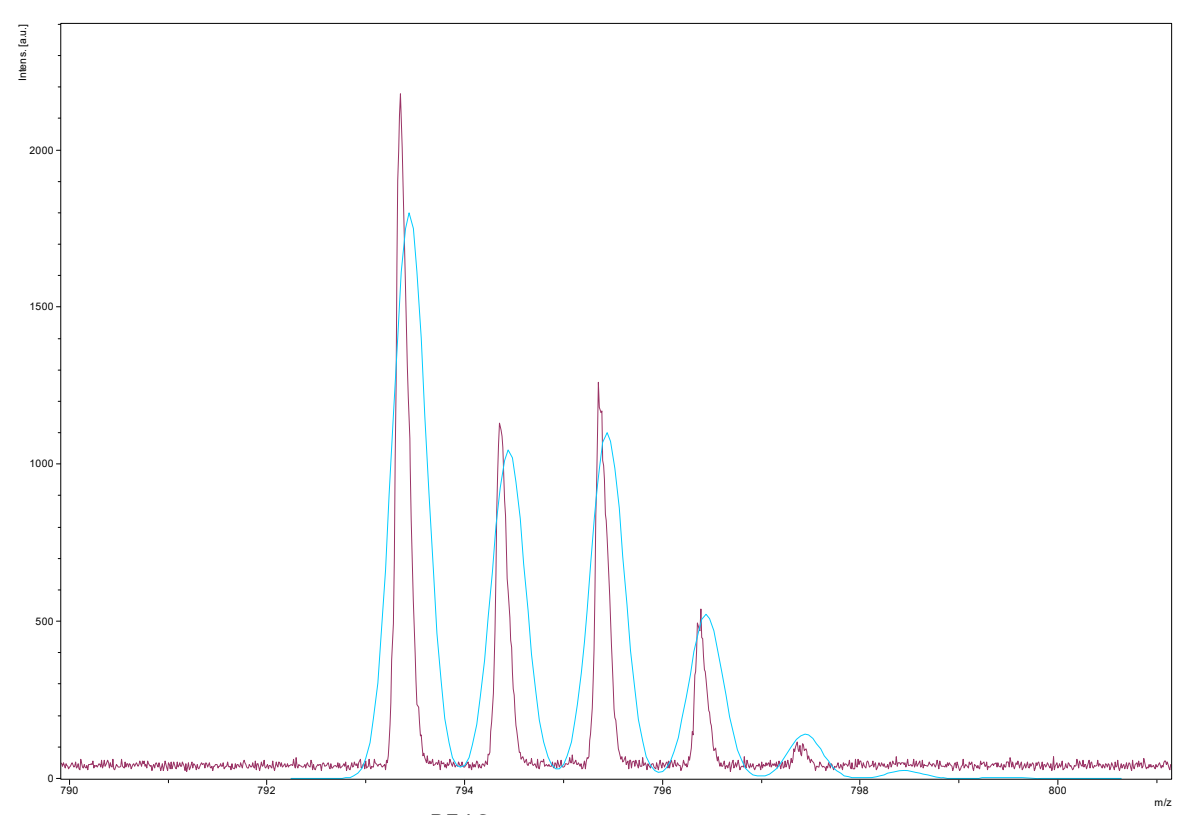


 $^{1}$ H and  $^{13}$ C{ $^{1}$ H} NMR of  $Au_{BCz}^{BZAC}$  (400 MHz in acetone-d6).

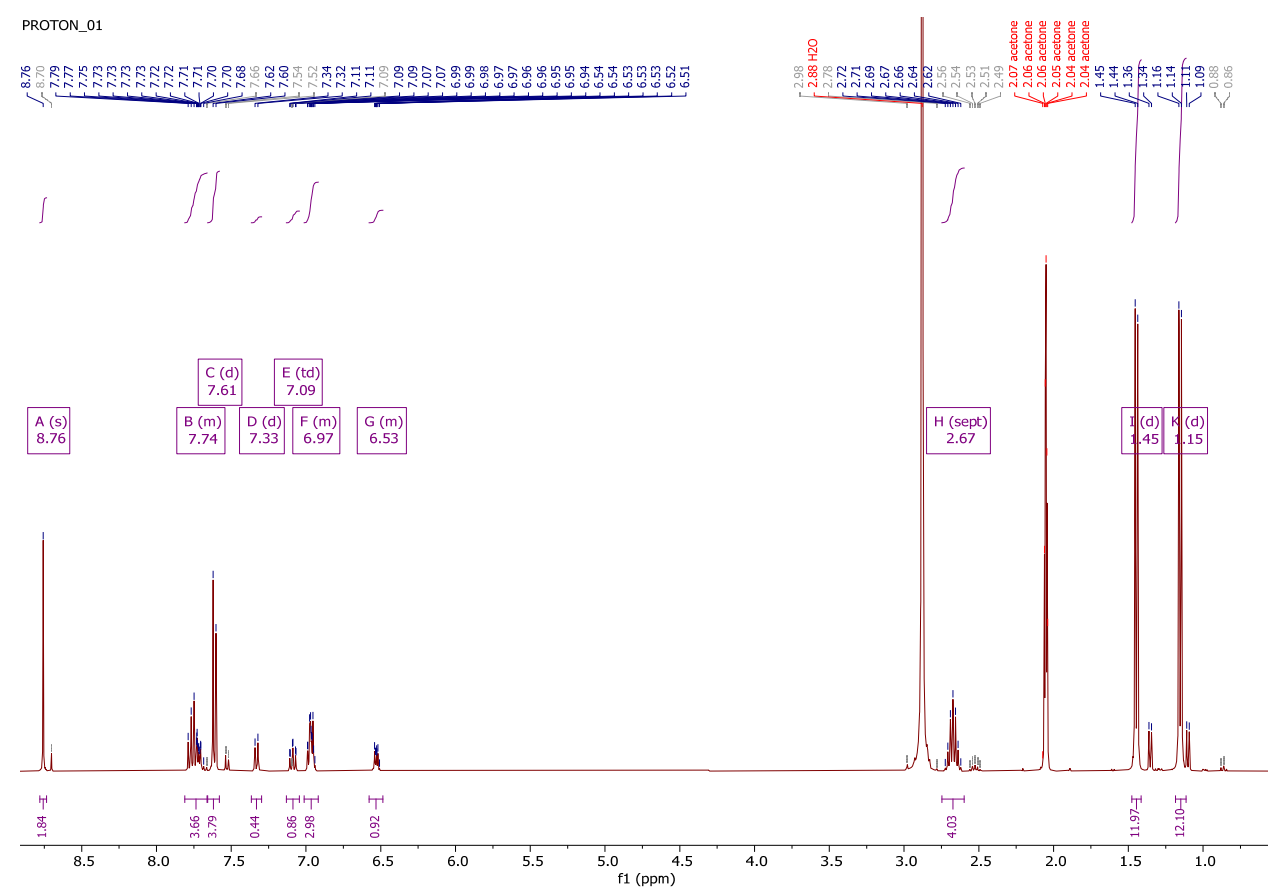




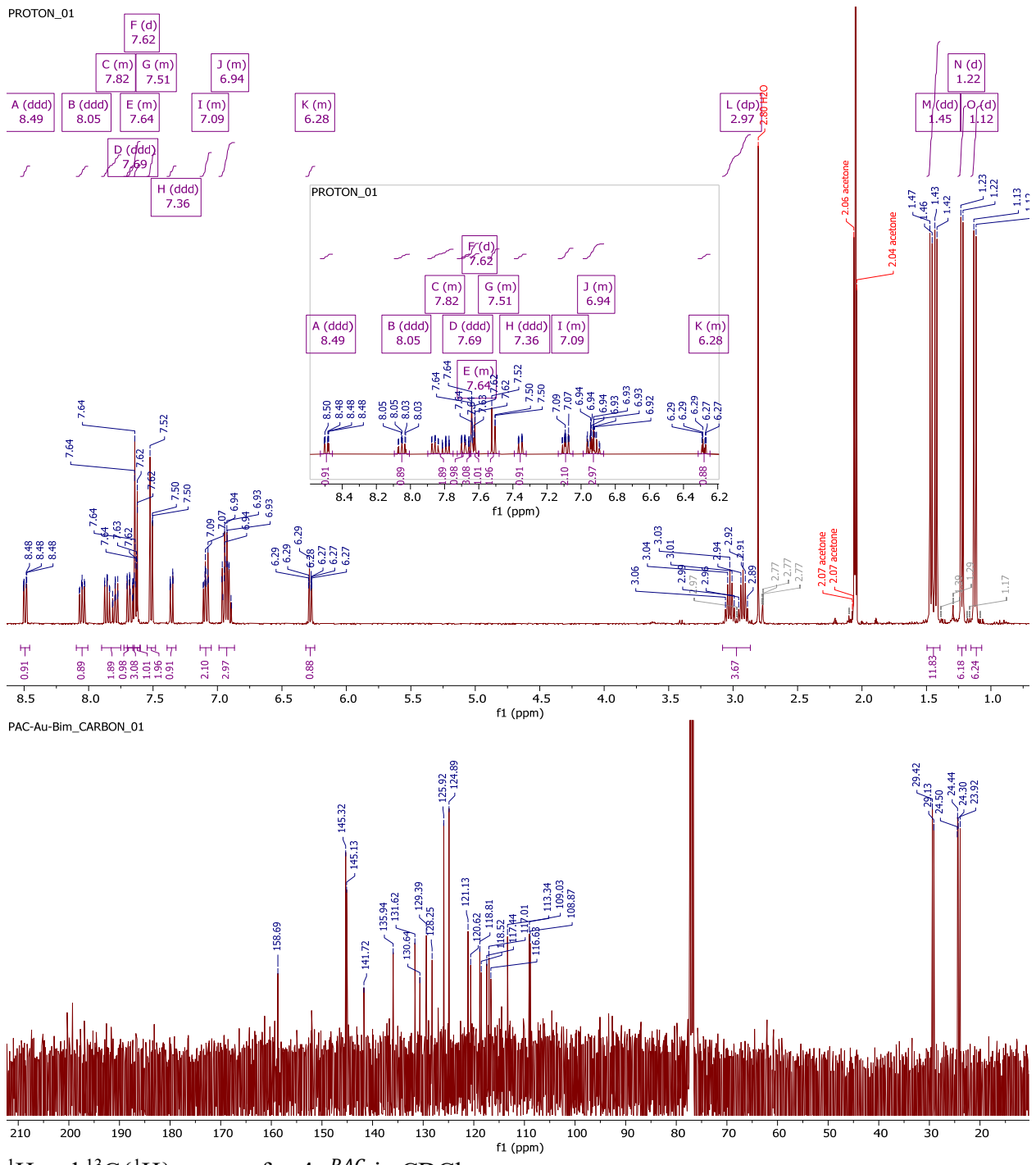
 $^{1}$ H and  $^{13}$ C{ $^{1}$ H} NMR of  $Cu_{BCz}^{BZAC}$  (400 MHz in acetone-d6).



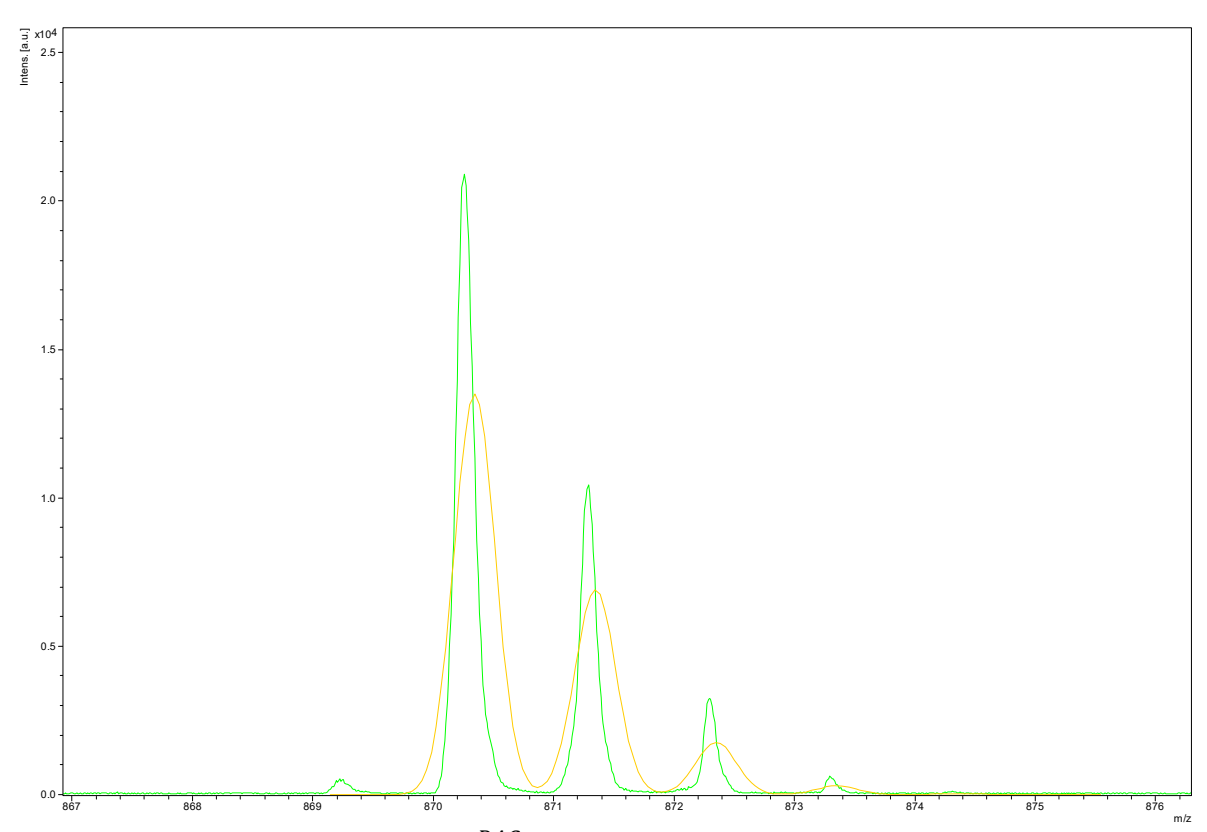
Mass spectrometry (MALDI) of  $\mathcal{C}u^{BZAC}_{BCz}$  vs Bruker Peptide Standard.



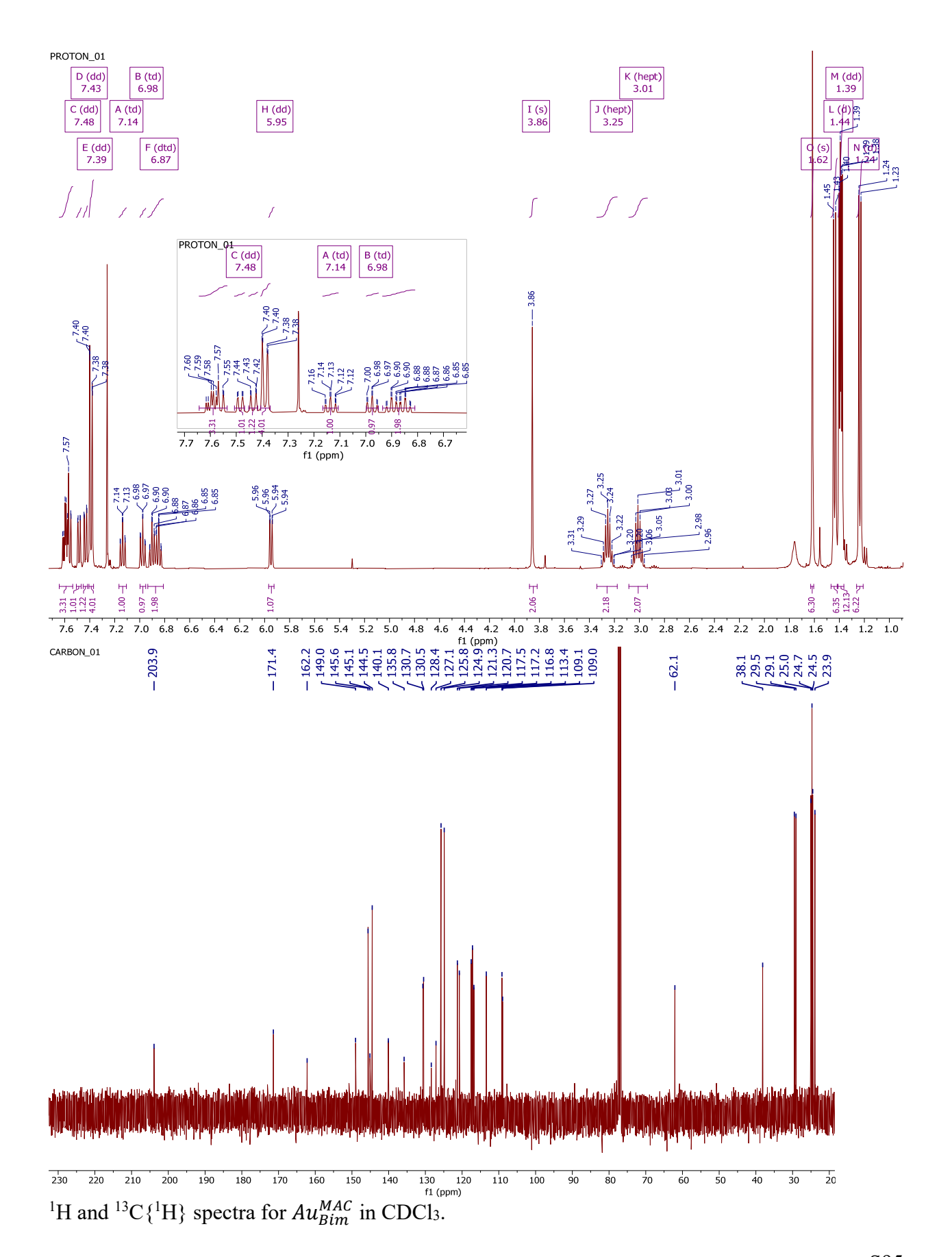
<sup>1</sup>H and <sup>13</sup>C{<sup>1</sup>H} spectra for  $Au_{Bim}^{PZI}$  in acetone-d6.

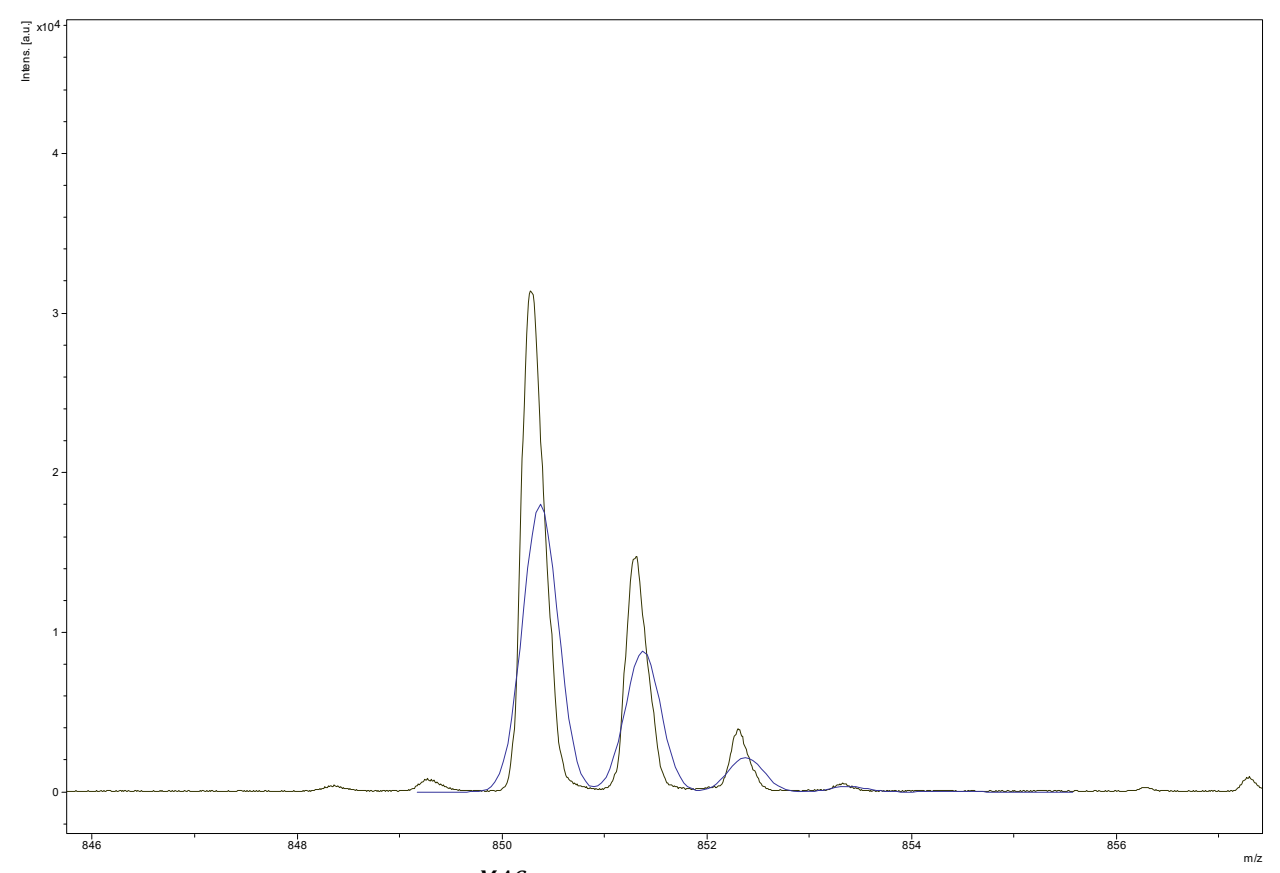


 $^{1}\mathrm{H}$  and  $^{13}\mathrm{C}\{^{1}\mathrm{H}\}$  spectra for  $Au_{Bim}^{PAC}$  in CDCl<sub>3</sub>.

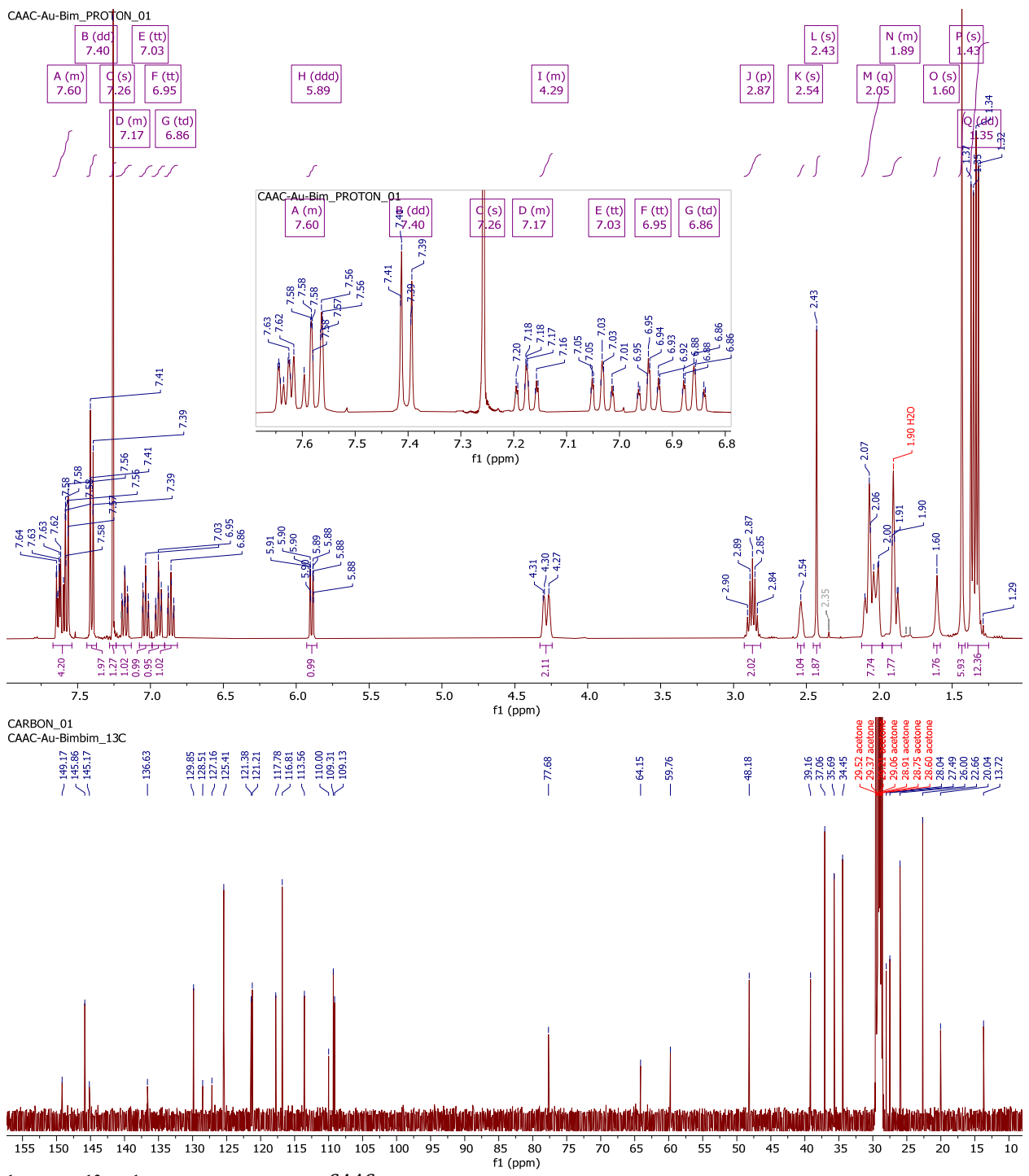


Mass spectrometry (MALDI) of  $Au_{Bim}^{PAC}$  vs Bruker Peptide Standard.

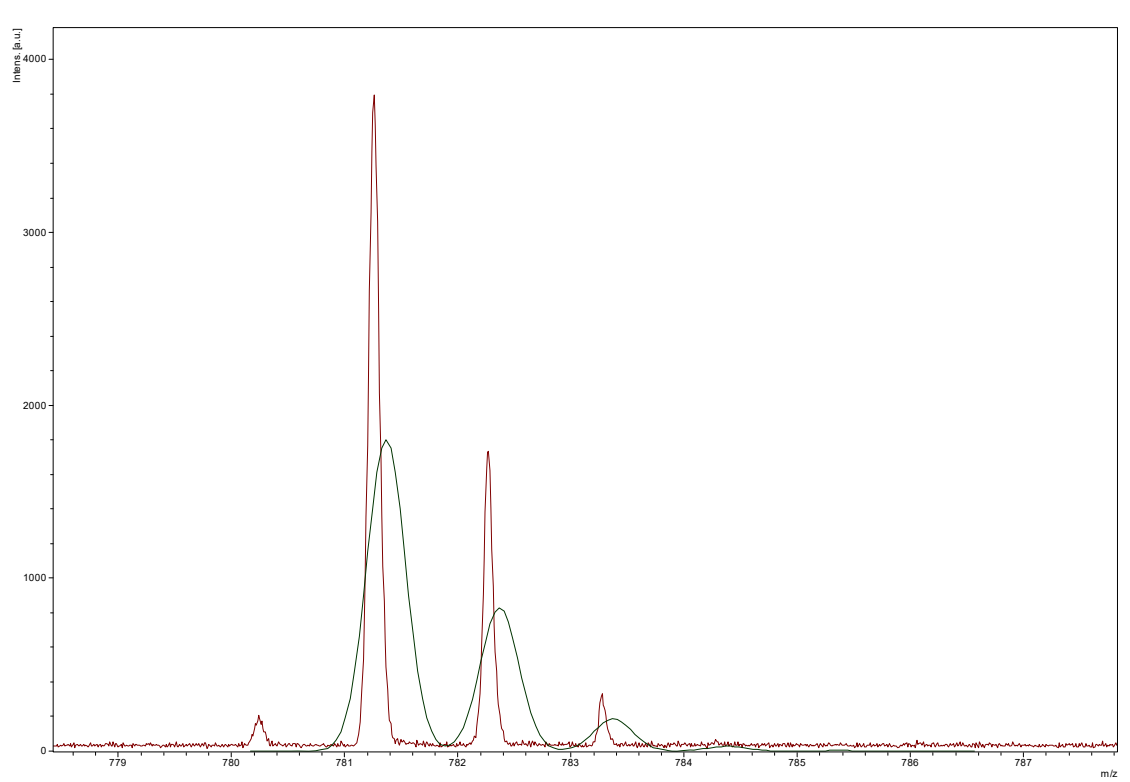




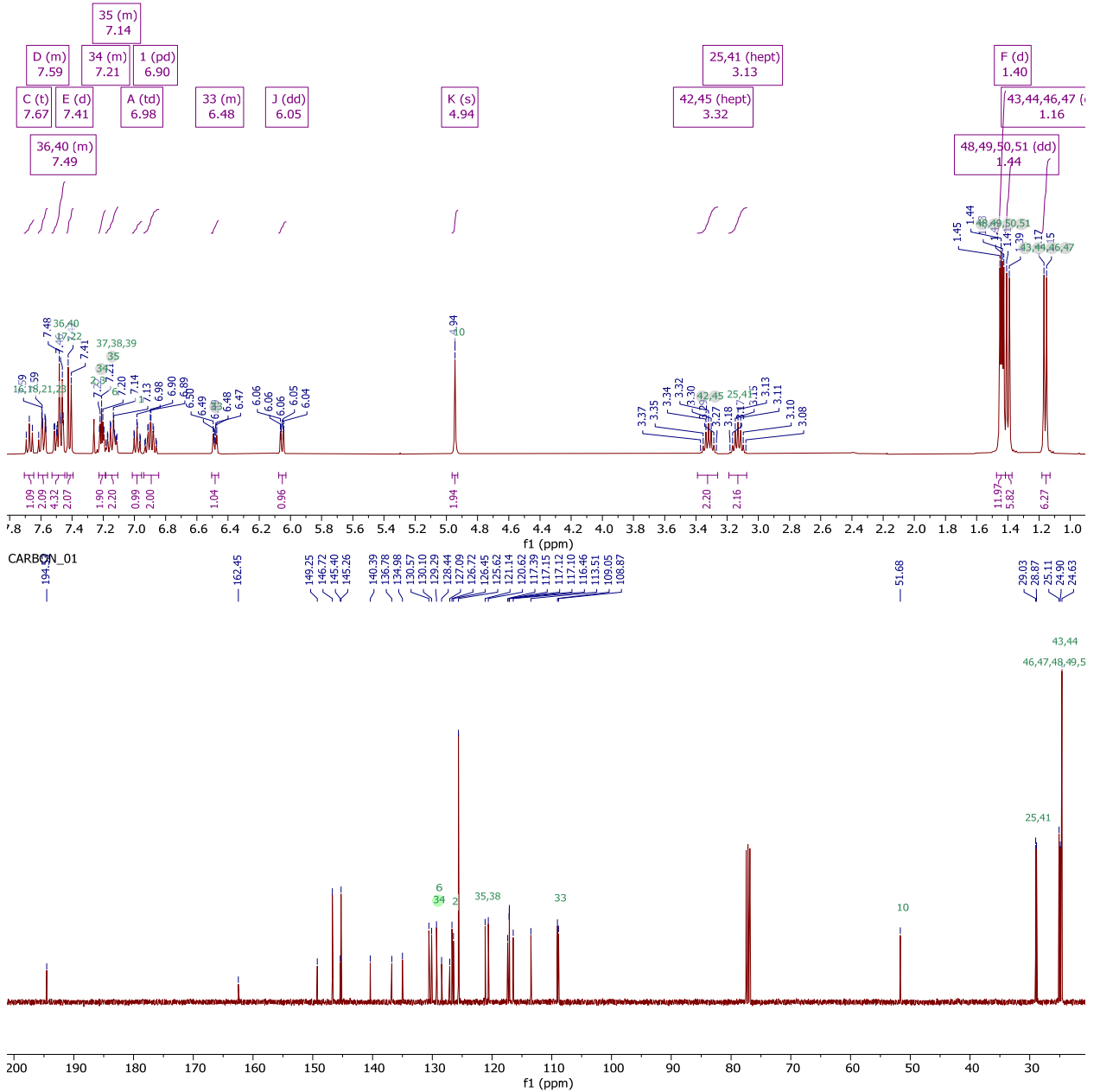
Mass spectrometry (MALDI) of  $Au_{Bim}^{MAC}$  vs Bruker Peptide Standard.



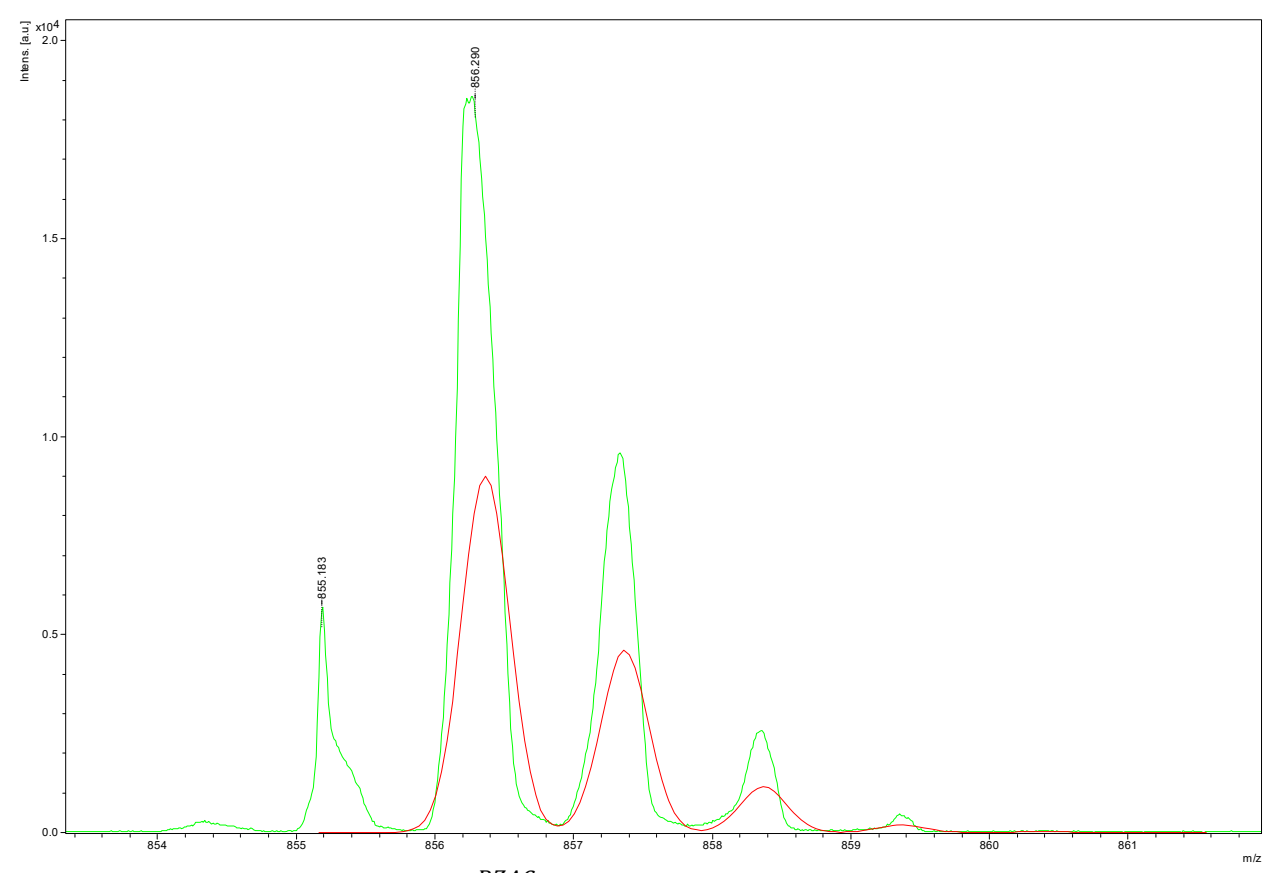
 $^{1}\mathrm{H}$  and  $^{13}\mathrm{C}\{^{1}\mathrm{H}\}$  spectra for  $Au_{Bim}^{CAAC}$  in CDCl<sub>3</sub>.



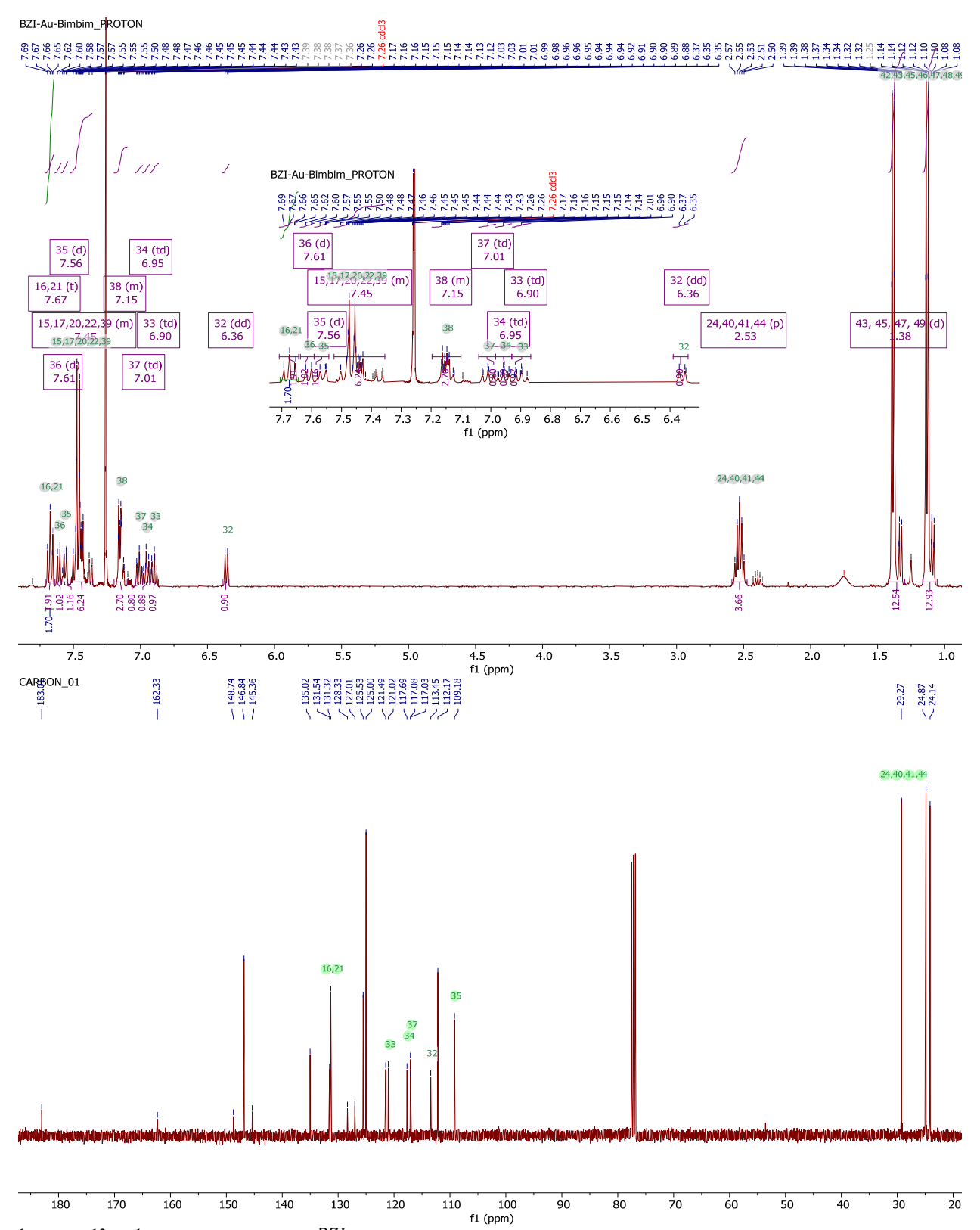
Mass spectrometry (MALDI) of  $Au_{Bim}^{CAAC}$  vs Bruker Peptide Standard.

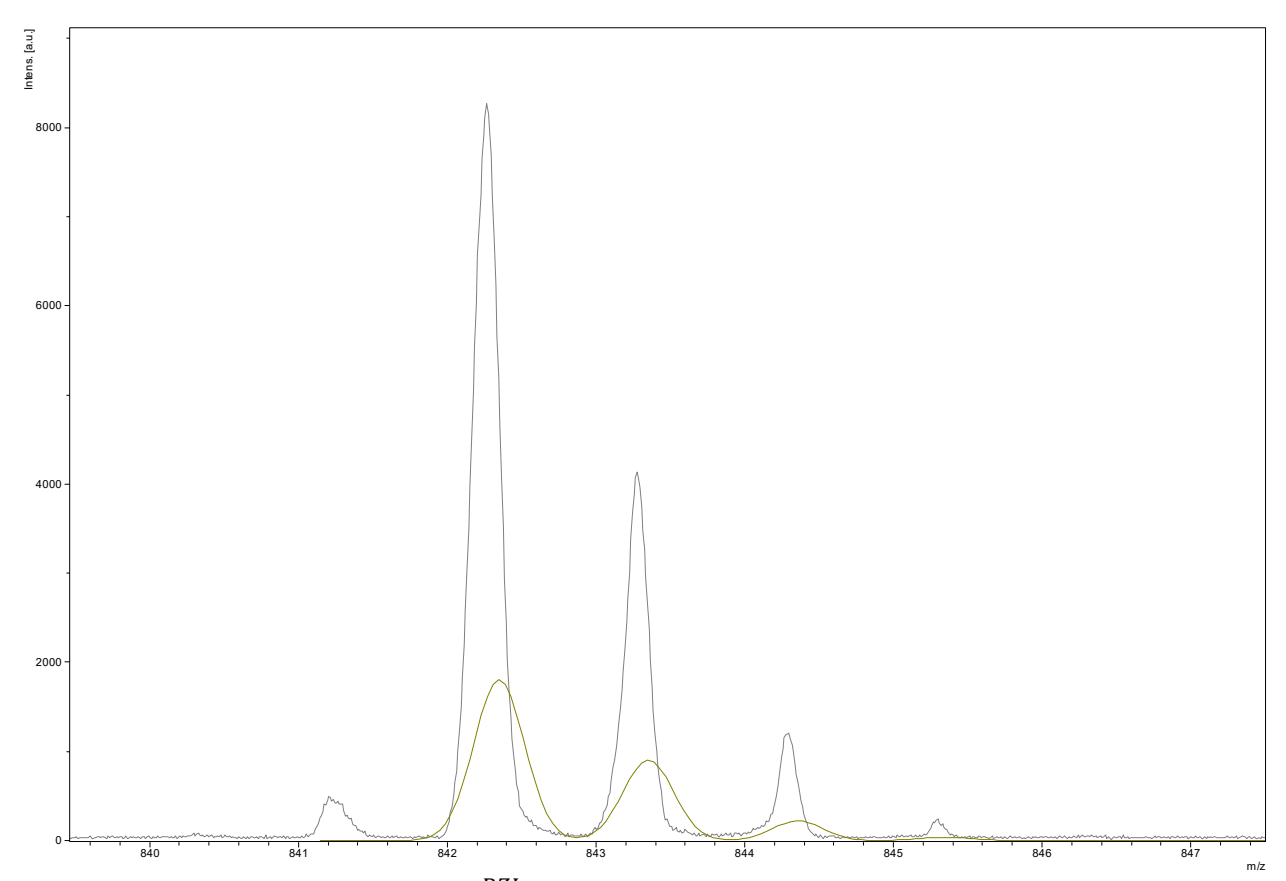


 $^{1}\mathrm{H}$  and  $^{13}\mathrm{C}\{^{1}\mathrm{H}\}$  spectra for  $Au_{Bim}^{BZAC}$  in CDCl<sub>3</sub>.

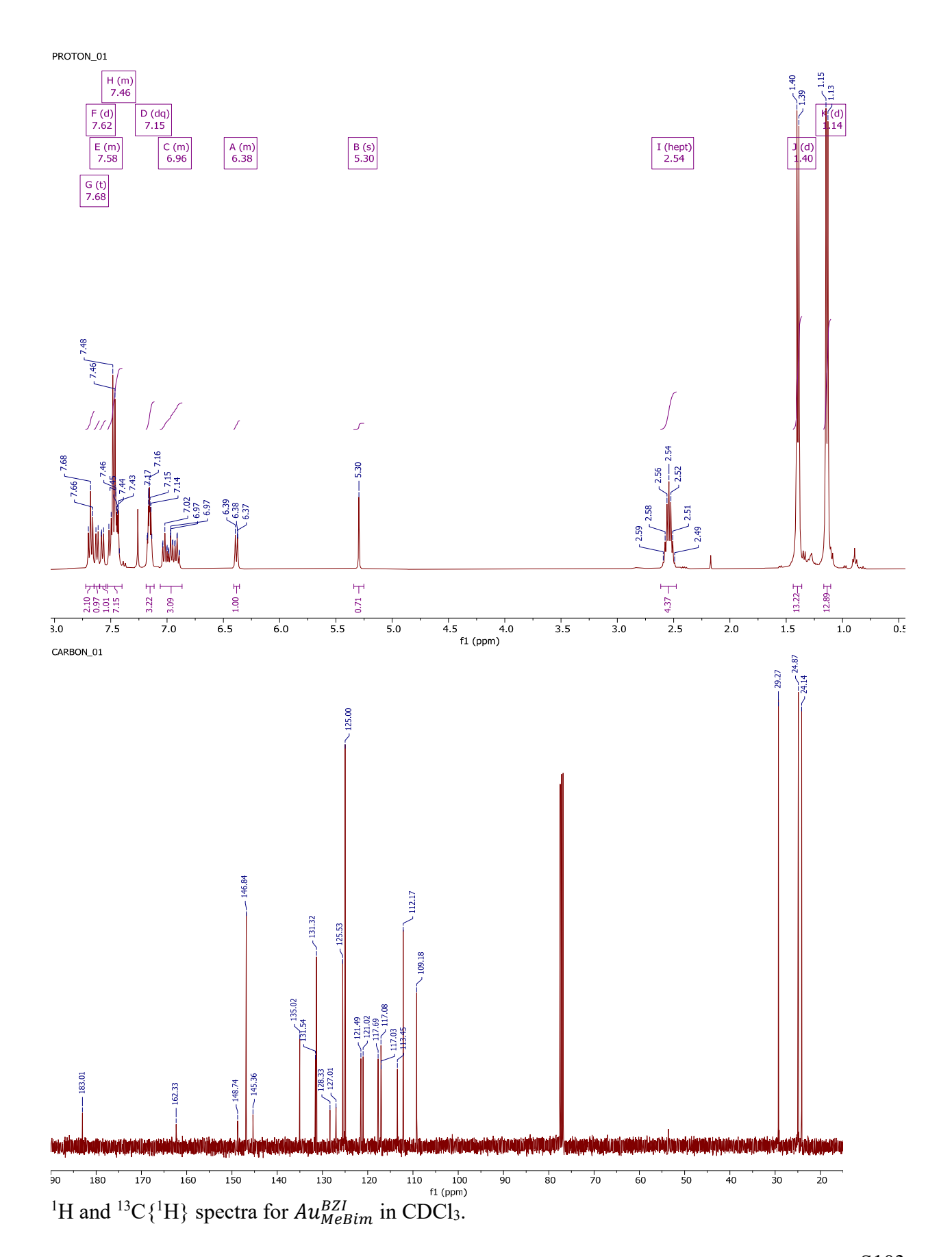


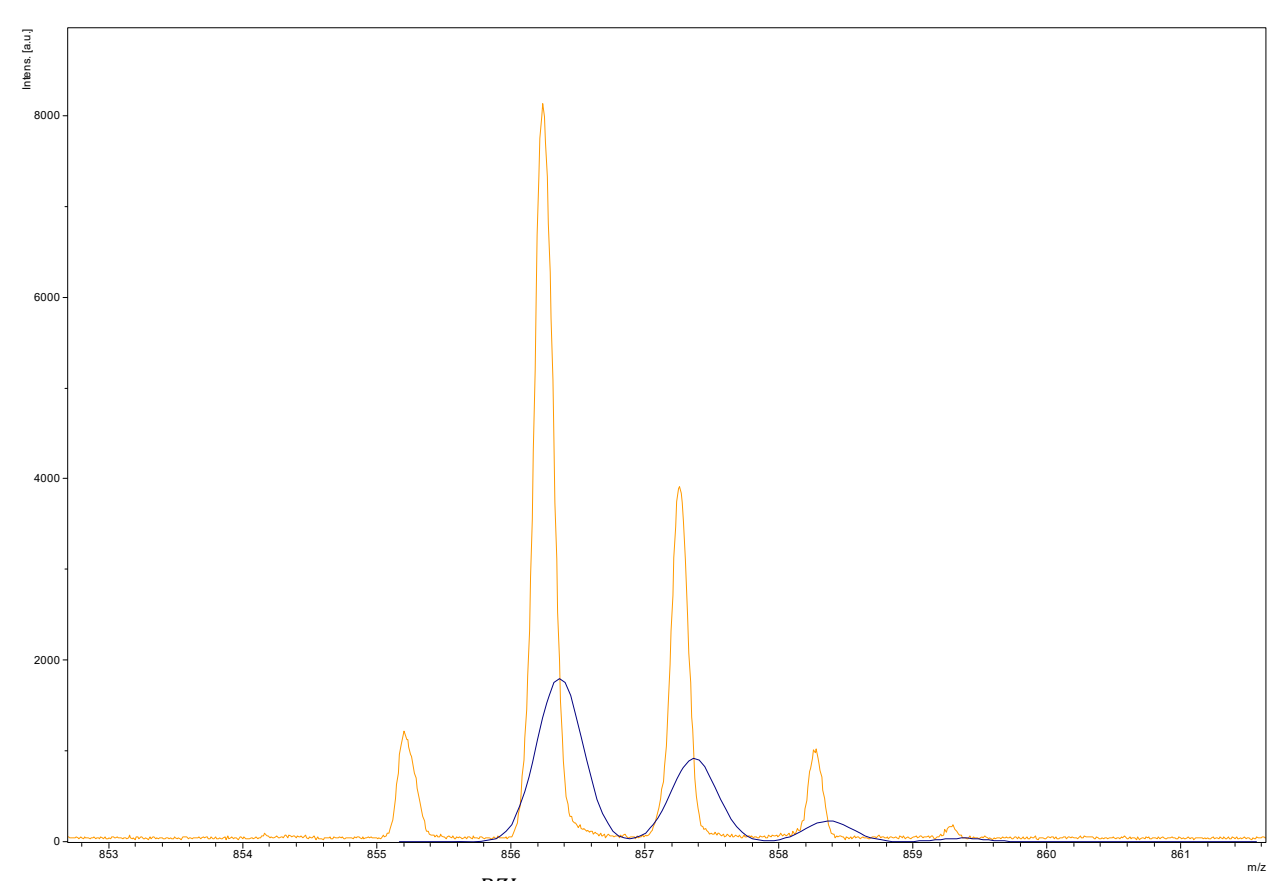
Mass spectrometry (MALDI) of  $Au_{Bim}^{BZAC}$  vs Bruker Peptide Standard.



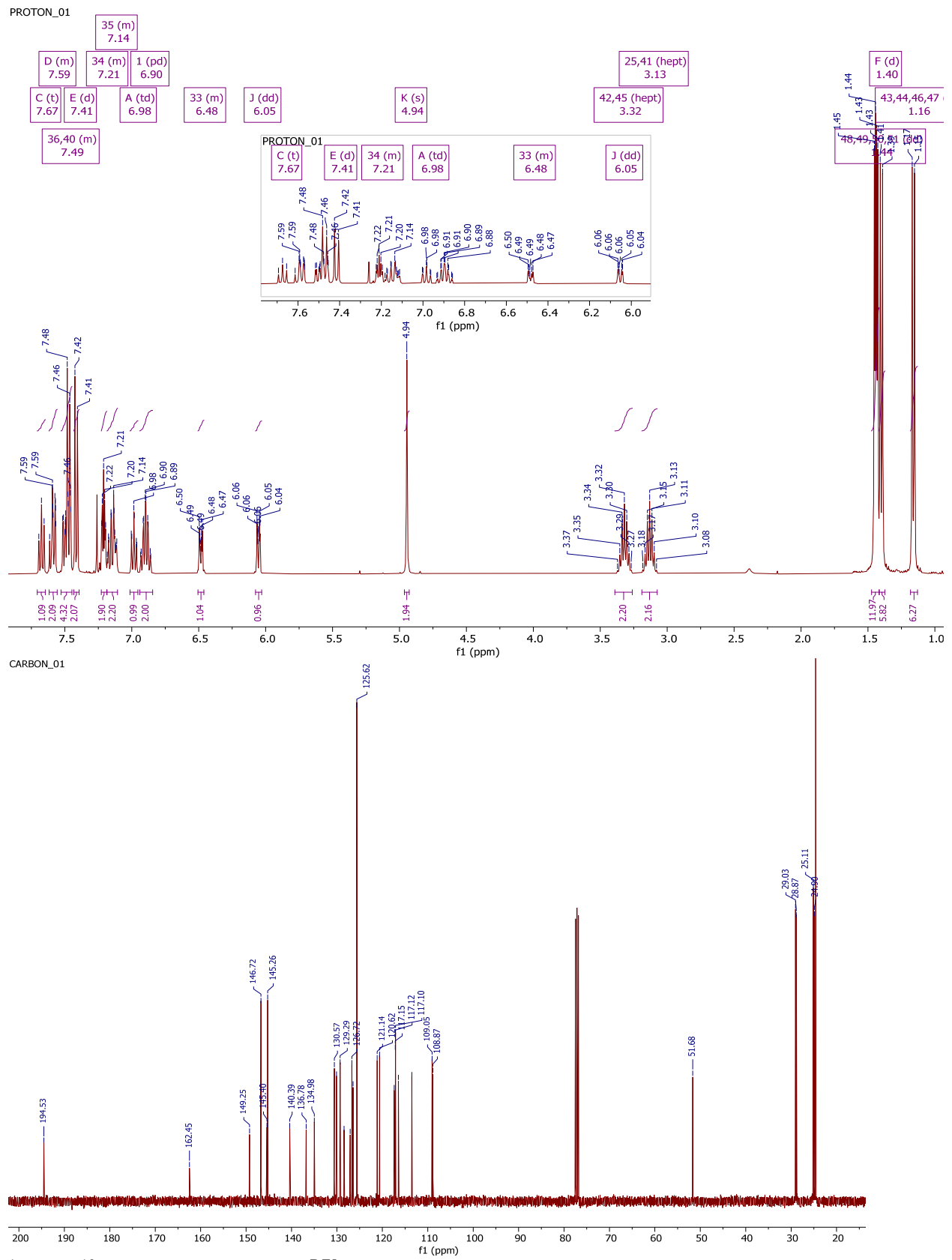


Mass spectrometry (MALDI) of  $Au_{Bim}^{BZI}$  vs Bruker Peptide Standard.

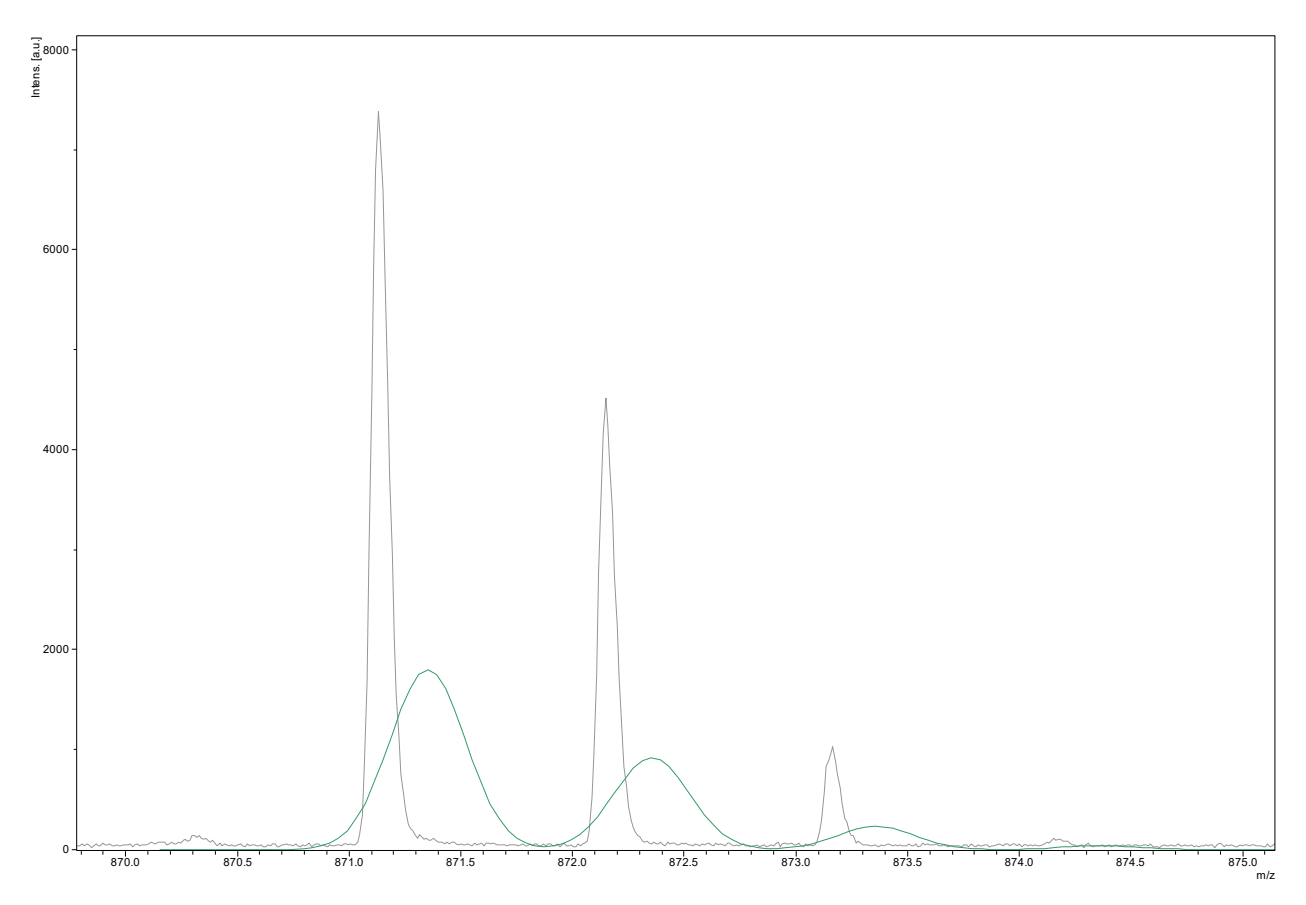




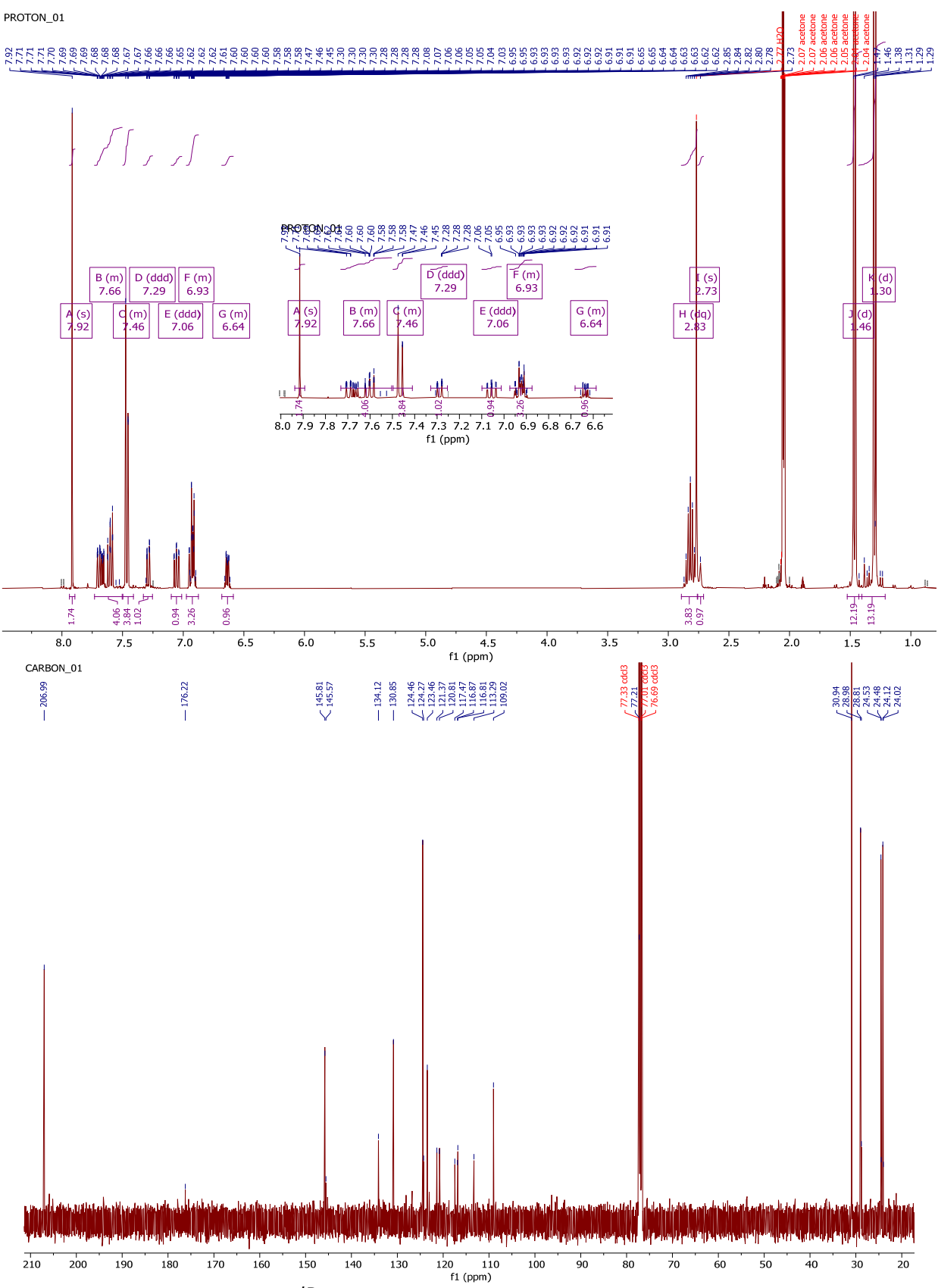
Mass spectrometry (MALDI) of  $Au_{MeBim}^{BZI}$  vs Bruker Peptide Standard.



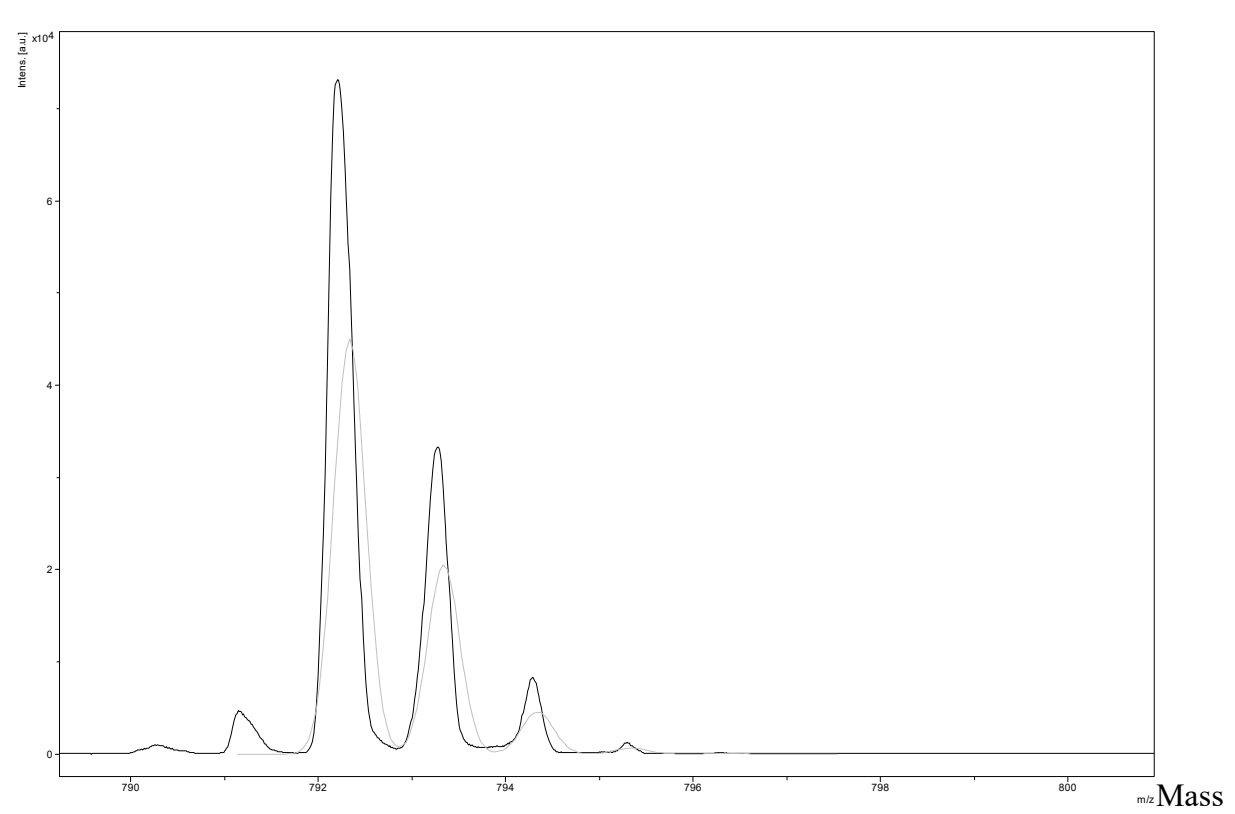
<sup>1</sup>H and <sup>13</sup>C{1H} spectra for  $Au_{MeOBim}^{BZI}$  in CDCl<sub>3</sub>.



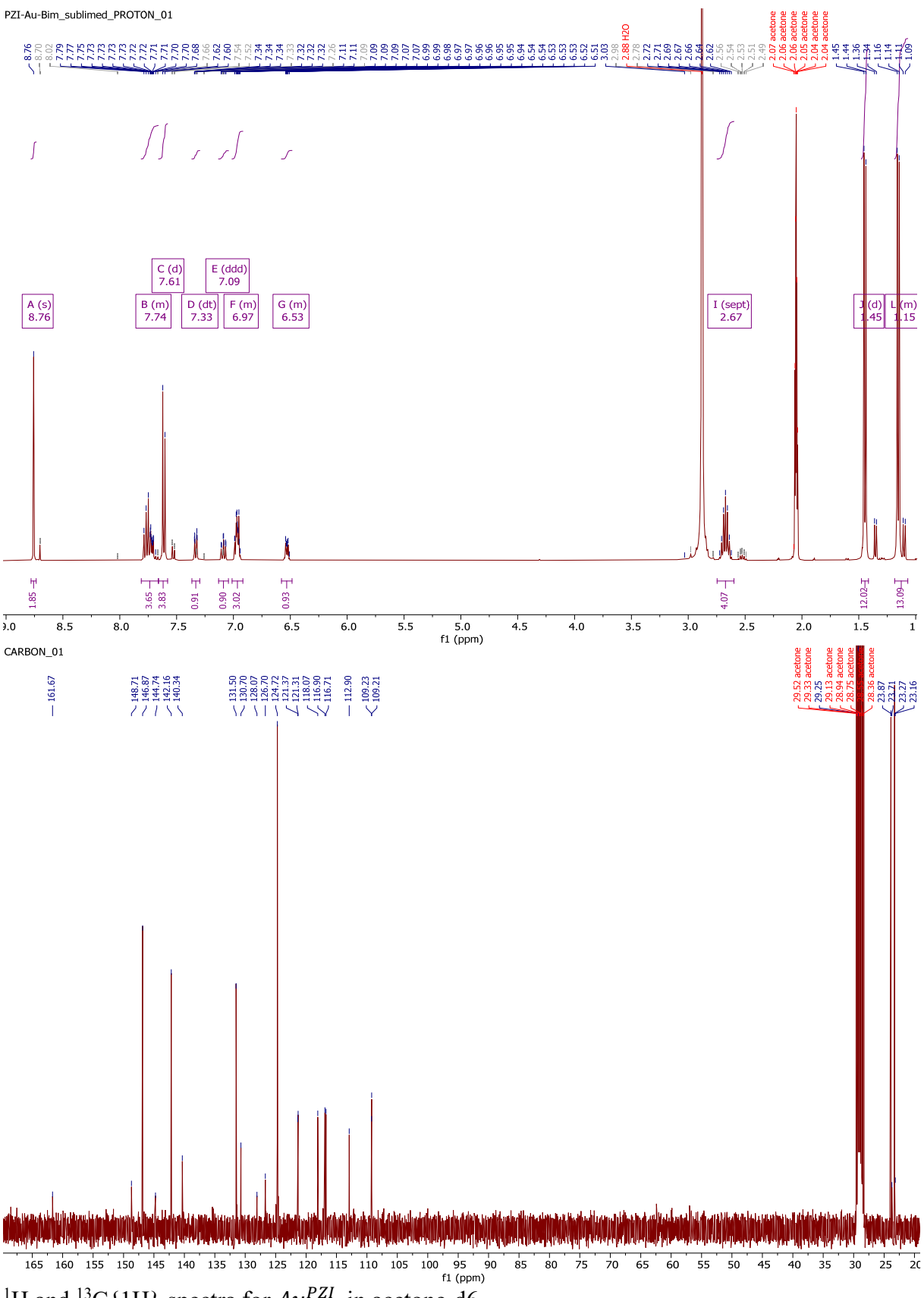
Mass spectrometry (MALDI) of  $Au^{BZI}_{MeOBim}$  vs Bruker Peptide Standard.



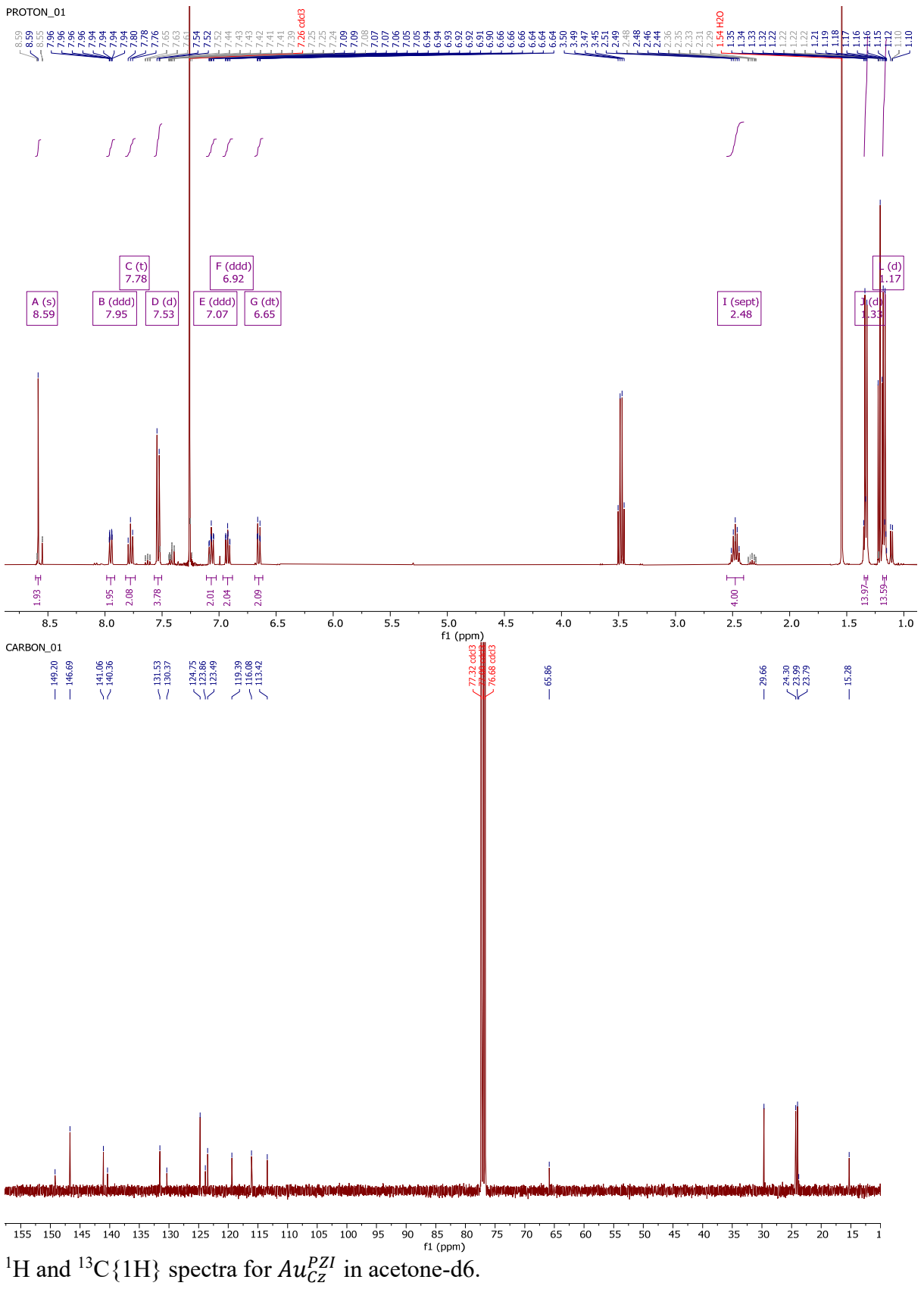
 $^{1}$ H and  $^{13}$ C{1H} spectra for  $Au_{MeBim}^{iPr}$  in CDCl<sub>3</sub>.



spectrometry (MALDI) of  $Au_{Bim}^{iPr}$  vs Bruker Peptide Standard.



 $^{1}\text{H}$  and  $^{13}\text{C}\{1\text{H}\}$  spectra for  $Au_{Bim}^{PZI}$  in acetone-d6.



## References

- 1. Shen, W.; Li, J.; Zhang, C.; Shi, M.; Zhang, J., Copper, Silver and Sodium Salt-Mediated Quaternization by Arylation: Syntheses of N-Heterocyclic Carbene Precursors and 6-H-Phenanthridine Derivatives. *Chem. Asian J.* **2016**, *11* (13), 1883-6.
- 2. Tang, R.; Xu, S.; Lam, T.-L.; Cheng, G.; Du, L.; Wan, Q.; Yang, J.; Hung, F.-F.; Low, K.-H.; Phillips, D. L.; Che, C.-M., Highly Robust CuI-TADF Emitters for Vacuum-Deposited OLEDs with Luminance up to 222 200 cd m-2 and Device Lifetimes (LT90) up to 1300 hours at an Initial Luminance of 1000 cd m-2. *Angewandte Chemie International Edition* **2022**, *61* (33), e202203982.
- 3. Greff, M.; Peter, B.; Stumpf, R. PROCESS FOR THE PREPARATION OF BENZIMIDAZO[1,2-AJBENZIMIDAZOLES. 2017.
- 4. Sheldrick, G., Crystal structure refinement with SHELXL. *Acta Crystallographica Section C* **2015**, *71* (1), 3-8.
- 5. Li, T.-y.; Schaab, J.; Djurovich, P. I.; Thompson, M. E., Toward rational design of TADF two-coordinate coinage metal complexes: understanding the relationship between natural transition orbital overlap and photophysical properties. *Journal of Materials Chemistry C* **2022**, *10* (12), 4674-4683.
- 6. Shao, Y.; Gan, Z.; Epifanovsky, E.; Gilbert, A. T. B.; Wormit, M.; Kussmann, J.; Lange, A. W.; Behn, A.; Deng, J.; Feng, X.; Ghosh, D.; Goldey, M.; Horn, P. R.; Jacobson, L. D.; Kaliman, I.; Khaliullin, R. Z.; Kuś, T.; Landau, A.; Liu, J.; Proynov, E. I.; Rhee, Y. M.; Richard, R. M.; Rohrdanz, M. A.; Steele, R. P.; Sundstrom, E. J.; Woodcock, H. L.; Zimmerman, P. M.; Zuev, D.; Albrecht, B.; Alguire, E.; Austin, B.; Beran, G. J. O.; Bernard, Y. A.; Berquist, E.; Brandhorst, K.; Bravaya, K. B.; Brown, S. T.; Casanova, D.; Chang, C.-M.; Chen, Y.; Chien, S. H.; Closser, K. D.; Crittenden, D. L.; Diedenhofen, M.; DiStasio, R. A.; Do, H.; Dutoi, A. D.; Edgar, R. G.; Fatehi, S.; Fusti-Molnar, L.; Ghysels, A.; Golubeva-Zadorozhnaya, A.; Gomes, J.; Hanson-Heine, M. W. D.; Harbach, P. H. P.; Hauser, A. W.; Hohenstein, E. G.; Holden, Z. C.; Jagau, T.-C.; Ji, H.; Kaduk, B.; Khistyaev, K.; Kim, J.; Kim, J.; King, R. A.; Klunzinger, P.; Kosenkov, D.; Kowalczyk, T.; Krauter, C. M.; Lao, K. U.; Laurent, A. D.; Lawler, K. V.; Levchenko, S. V.; Lin, C. Y.; Liu, F.; Livshits, E.; Lochan, R. C.; Luenser, A.; Manohar, P.; Manzer, S. F.; Mao, S.-P.; Mardirossian, N.; Marenich, A. V.; Maurer, S. A.; Mayhall, N. J.; Neuscamman, E.; Oana, C. M.; Olivares-Amaya, R.; O'Neill, D. P.; Parkhill, J. A.; Perrine, T. M.; Peverati, R.; Prociuk, A.; Rehn, D. R.; Rosta, E.; Russ, N. J.; Sharada, S. M.; Sharma, S.; Small, D. W.; Sodt, A.; Stein, T.; Stück, D.; Su, Y.-C.; Thom, A. J. W.; Tsuchimochi, T.; Vanovschi, V.; Vogt, L.; Vydrov, O.; Wang, T.; Watson, M. A.; Wenzel, J.; White, A.; Williams, C. F.; Yang, J.; Yeganeh, S.; Yost, S. R.; You, Z.-Q.; Zhang, I. Y.; Zhang, X.; Zhao, Y.; Brooks, B. R.; Chan, G. K. L.; Chipman, D. M.; Cramer, C. J.; Goddard, W. A.; Gordon, M. S.; Hehre, W. J.; Klamt, A.; Schaefer, H. F.; Schmidt, M. W.; Sherrill, C. D.; Truhlar, D. G.; Warshel, A.; Xu, X.; Aspuru-Guzik, A.; Baer, R.; Bell, A. T.; Besley, N. A.; Chai, J.-D.; Dreuw, A.; Dunietz, B. D.; Furlani, T. R.; Gwaltney, S. R.; Hsu, C.-P.; Jung, Y.; Kong, J.; Lambrecht, D. S.; Liang, W.; Ochsenfeld, C.; Rassolov, V. A.; Slipchenko, L. V.; Subotnik, J. E.; Van Voorhis, T.; Herbert, J. M.; Krylov, A. I.; Gill, P. M. W.; Head-Gordon, M., Advances in molecular quantum chemistry contained in the Q-Chem 4 program package. Molecular Physics 2015, 113 (2), 184-215.

- 7. Hermann, G.; Pohl, V.; Tremblay, J. C.; Paulus, B.; Hege, H.-C.; Schild, A., ORBKIT: A modular python toolbox for cross-platform postprocessing of quantum chemical wavefunction data. *J. Comput. Chem.* **2016**, *37* (16), 1511-1520.
- 8. Castro, S. G. P. L., A.; et al. 2021 Python wrapper for Cubature: adaptive multidimensional integration, Version 0.14.8; 2021.
- 9. Tadle, A. C.; El Roz, K. A.; Soh, C. H.; Sylvinson Muthiah Ravinson, D.; Djurovich, P. I.; Forrest, S. R.; Thompson, M. E., Tuning the Photophysical and Electrochemical Properties of Aza-Boron-Dipyridylmethenes for Fluorescent Blue OLEDs. *Adv. Funct. Mater.* **2021**, *31* (27), 2101175.
- 10. Strickler, S. J.; Berg, R. A., Relationship between Absorption Intensity and Fluorescence Lifetime of Molecules. *The Journal of Chemical Physics* **1962**, *37* (4), 814-822.
- 11. Birks, J. B., *Photophysics of aromatic molecules*. Wiley-Interscience: London, 1970.
- 12. Hofbeck, T.; Yersin, H., The Triplet State of fac-Ir(ppy)3. *Inorganic Chemistry* **2010**, 49 (20), 9290-9299.
- 13. Hamze, R.; Shi, S.; Kapper, S. C.; Muthiah Ravinson, D. S.; Estergreen, L.; Jung, M.-C.; Tadle, A. C.; Haiges, R.; Djurovich, P. I.; Peltier, J. L.; Jazzar, R.; Bertrand, G.; Bradforth, S. E.; Thompson, M. E., "Quick-Silver" from a Systematic Study of Highly Luminescent, Two-Coordinate, d10 Coinage Metal Complexes. *Journal of the American Chemical Society* **2019**, *141* (21), 8616-8626.